Interaction between deformation sources & implications for numerical modelling of magma storage

Karen Pascal

Submitted in accordance with the requirements for the degree of
Doctor of Philosophy

The University of Leeds
School of Earth and Environment
April 2013

Declaration of Authorship

The candidate confirms that the work submitted is her own, except where work which has formed part of jointly authored publications has been included. The contribution of the candidate and the other authors to this work has been explicitly indicated below. The candidate confirms that appropriate credit has been given within the thesis where reference has been made to the work of others.

Chapters 4 & 5 contain work from the publication Pascal, K., Neuberg, J. & Rivalta, E., *In Review*. On precisely modelling surface deformation due to interacting magma chambers and dikes. *Geophys. I. Int.*. All the sections and appendices of this paper were prepared by K. Pascal, the text and figures were written and done by K. Pascal, with comments from all co-authors.

Acknowledgements

As I am spending my last moments both working on this thesis and in Leeds, I would first of all like to express my sincere thanks to my two supervisors Dr Eleonora Rivalta and Prof Jürgen Neuberg for the help, and for the moral and financial support they have always provided when needed. Additionally, I would like to thank Eleonora and Locko for having opened doors for me, either introducing me to other researchers, offering me to be part of other teaching or research projects, or mentioning my name for a work placement, but much more importantly thanks to them and their family for having opened the doors of their own home.

At the Institute of Geophysics and Tectonics, I would also like to thank in particular Prof Tim Wright, part of my Research Committee, who has spent a significant amount of time helping me with some work presented in Chapter 5 and has provided some of the codes employed in this thesis. I would also like to extend these thanks to the members of the Volcanology group as well as to Prof Greg. Houseman, for fruitful discussions who improved this work.

In the sinuous, 16 years long path which led me here, I have met a lot of inspiring people and I would like to thank here Christian Honthaas, Frank Donnadieu and Regis Doucelance for their friendship, encouragements and for awakening my curiosity to geology, geophysics, and to modelling. My time at the University of Leeds and in Lanzarote would not have been enjoyable without the time spent in company of Hannah, Stephanie, Barbara (twice) and Mark. Thanks also to Hannah, Sandra and Becky for helping out printing and handing in the final version of this thesis. I would also like to thank here the staff of the Montserrat Volcano Observatory, who made my time in Montserrat an unforgettable experience, and would like to particularly thank here Sonja, Richard and Adam for their friendship and motivational speeches.

For willing to share, help me going through, and laugh about the PhD experience, I would like to give my warmest thanks to my closest friends, most of them also the furthest, Aurelia, Carole, Gwenn, Marie, Fanny, Hanika, Pascaline, Carolina, my friends from the Picture House for socializing with a scientist and for great escapes, my dear housemates Larisa and Paula, and of course also to Dulce who shared so many nights with me at the office.

Most of all, I want to thank my parents, for their constant love and support, both moral and financial, and for offering me the wonderful gift of having the possibility to satisfy my curiosity in other fields and to take the time to find a profession which will make me happy. Finally, my last thoughts go to those who have made me feel warm and who left before I could make them proud, my grand-fathers Louis and Lucien, my uncles Dominique, Alain and Jean-Bernard, and my grand-mother Julie, as well as all the children who have extended my family and friends' families. May they always be able to follow their dreams, not stick to social etiquette, and be unreasonable.

Abstract

Volcano ground deformation due to magma movement in the subsurface is commonly modelled using simple point (Mogi) or dislocation (Okada) sources, embedded in a homogeneous, isotropic, elastic half-space, and representing respectively a magma chamber and a dike. When datasets are too complex to be explained by a single deformation source, the magmatic system is often represented by a combination of these sources and their displacements fields are simply summed. By doing so, the assumption of homogeneity in the half space is violated and the resulting interaction between sources is neglected.

This thesis seeks to determine the limits in which the combination of analytical sources is justified, by testing the analytical surface displacements against the solutions of corresponding 3D finite element models, which account for the interaction between sources. For models with dike and magma chamber aligned vertically or along the dike-strike direction, the calculated discrepancies, and therefore the source interaction, are insignificant ($< 5\%$), independently of the source separation. Although the discrepancies depend on the physical model parameters and can not be generalized, for models with a magma chamber next to a dike (in the direction perpendicular to the dike-strike), or for horizontally or vertically aligned pressurized magma chambers, care must be taken for source separation of less than 4 times the radius of the magma chamber as the discrepancies can reach 20% at a wall-to-wall distance of 0.5 source radii. Furthermore, a statistical study of the retrieved source parameters employing an inversion scheme (based on analytical solutions, hence neglecting the source interaction), demonstrates the difficulty of solving the structure of vertically layered magmatic system without additional, *e.g.* petrological, constraints. Finally, modelling the dike employing various FE methods has pointed out the fact that the rheology of the magma needs to be integrated in future numerical modelling approaches.

Contents

List of Figures

List of Tables

Chapter 1

Introduction

1.1 Volcanic ground deformation

One of the first theories linking volcano deformation and subsurface processes is attributable to the geologist C. von Buch. In 1815, following observations at basaltic shields in the Canary islands, von Buch proposed the 'crater of elevation' theory, where an inflating deep magmatic source would induce the uplift of originally horizontal lava flows, the related expansion leading to the collapse of a summit caldera (Celâl Sengôr, 2003, p.83). From the early nineteen hundreds onwards, deformation surveys in volcanic areas have become more and more common, due to the development of both ground- and space-based geophysical methods such as trilateration or the Global Positioning System (GPS). The deformation time series gathered, in few instances spanning over 50 years (*e.g. ca.* 100 years at Aira caldera, Japan and Kilauea, Hawaii, Dvorak and Dzurisin, 1997), has concurred to a better understanding of magmatic processes in general, to a better knowledge of the magmatic plumbing system of specific volcanoes, hereby improving their monitoring. In the following sections, I first consider some potential sources of deformation in volcanic areas and the techniques employed to monitor the deformation at the surface. Then, after describing common displacement patterns observed, I introduce modelling methods of the ground deformation, aiming at retrieving the source parameters. Finally, I state the aims of this thesis and give an overview of Chapter 2-6.

1.1.1 Potential sources of surface deformation

Ground deformation in volcanic areas reflects the response of the host rock to stress changes within the crust. The stress changes can be due to:

1. Isostatic adjustments, regional or local uplift/subsidence due *e.g.* to melting ice-caps, mantle plumes, or lava (un)loading of the edifice (Grapenthin et al., 2010; Sparks, 2003).

2. Tectonic processes, modulated by the volcano activity, *e.g.* regional displacements due to plate tectonics, etc. (Roman et al., 2008).

3. Surface processes related in particular to magma extrusion (*e.g.* dome building, lava flows) or gravitational effect (*e.g.* flank collapse, edifice subsidence).

4. Magma transfers into/from a magmatic reservoir (Decker et al., 1983; Dvorak and Dzurisin, 1997; Segall, 2010; Tryggvason, 1986).

5. Exsolution of the volatiles in a stagnating, cooling, magma within the magma chamber or conduit (Anderson et al., 2010; Huppert and Woods, 2002; Sparks, 2003; Voight et al., 1999).

6. Hydrothermal activity (Camacho et al., 2011; Peltier et al., 2009; Price, 2004).

Amongst the relatively local subsurface processes listed above (processes *(4)-(6)*), magma transfers contribute the most to surface deformation. When the magma fills or departs from a magma reservoir, when it propagates through horizontal sills or sub-vertical dikes and conduits, sometimes reaching the surface, the surrounding crust must accommodate the volume change and the related pressure change exerted at the magma/crust interface by deforming. Depending on the intrusion rates and rock temperature, the deformation behaviour of an elastic crust can be either brittle (high intrusion rate, low temperature), or linear-elastic and ductile (low intrusion rate, high temperature). In the following chapters, a 'linear-elastic' behaviour will simply be referred to as 'elastic'. Examples of brittle and elastic surface deformation patterns include, respectively, normal faulting and graben formation in rift zone (Dzurisin, 2000; Pollard et al., 1983), and edifice inflation/deflation (*e.g.* Bianchi et al., 1987; Bonforte et al., 2008; Decker et al., 1983; Dvorak and Dzurisin, 1997; Genco and Ripepe, 2010; Janssen, 2007; Mogi, 1958; Palano et al., 2012; Segall, 2010; Wadge et al., 2006). In the latter example, inflation and deflation patterns usually correspond, respectively, to the pressurization and depressurization either of the magma chamber or within the hydrothermal system. Magma chamber pressurization can be attributed, as mentioned above, to the intrusion of new magma. However the magma chamber volume increase

can be also related to the exsolution of the volatiles (mostly H_2O) of a stagnating, cooling, magma within the chamber. Similarly, surface inflation can be measured when fluids of the hydrothermal system become entrapped and pressurized in a layer sealed by mineral deposits, close to the magma/rock interface (Dvorak and Dzurisin, 1997; Peltier et al., 2009). In all cases, when the stresses applied on the magma chamber or sealed aquifer walls overcome the confining, lithostatic pressure, fracturing occurs and magma and volatiles are released via magmatic intrusions, magmatic conduit, or fumaroles. This depressurization of the system is associated with a surface deflation. More recent studies have also shown that shear stresses produced either on the conduit wall as the magma ascends towards the surface (Green et al., 2006; Anderson and Segall, 2011), or in a magma chamber, can also contribute to the deformation measured at the surface (Anderson and Segall, 2011). Finally, it is worth mentioning, that ground deformation does not always accompany the transfer of magma between reservoirs, *e.g.* when there is no volume imbalance between the magma entering and leaving a specific part of the magmatic system, hence no net surplus or deficit.

1.1.2 Monitoring methods

The diversity of the deformation sources is echoed in the diversity and complexity of the surface deformation patterns measured in volcanic settings. In addition, the amplitude and extent of the surface deformation field also depend on the mechanical properties of the crust and on the topography. Various geodetic monitoring methods are used, both ground- and space-based, to allow the detection of slight and slow displacements, or covering a broad area in space and time (Table 1.1).

Standard volcano deformation techniques record temporal variations in either:

- benchmark locations, using GPS (episodic and continuous stations), and InSAR;
- relative distances (horizontal and vertical), using Electronic Distance Measurements (EDM), precise levelling, strainmeters, extensometers measuring the opening of fractures (Schmid et al., 2012, Piton de la Fournaise, Réunion);
- angles, using tiltmeters.

GPS, tilt and strain measurements can be made either episodically or continuously, their datasets being in general streamed towards a centre where they are processed,

Method	Achievable accuracy	Common network extent
EDM	<1 cm	<50 km
	Iwatsubo and Swanson (1992); Stiros et al. (2010)	
Precise levelling	<5 mm	<100 km
	Murray and Wooller (2002); Dzurisin (1992a)	
Strainmeter	10^{-12}	<50 km
	Sparks (2003); Linde et al. (2010)	
Tiltmeter	0.1 μrad	<10 km
	Dzurisin (1992b); Voight et al. (1998)	
GPS	cm to <1 cm	<100 km
Segall and Davis (1997); Janssen (2007); Bonforte et al. (2008); Shepherd et al. (1998)		
InSAR	cm to <1 cm	>100 km
	Lu et al. (2000); Pritchard and Simons (2002)	

Table 1.1: Standard methods of detection of the deformation signal: achievable accuracies and common network extent. InSAR accuracy is given in the direction of the line-of-sight. The achievable spatial coverage of the deformation signal varies depending on the signal itself (*i.e.* as well as its source), on the sensitivity of the instrument, and on environmental factors such as topography, weather conditions, etc.

e.g. in volcano observatories. More recently, InSAR has been increasingly used in volcano monitoring. Indeed, this remote sensing method presents the advantage of detecting small displacements over large areas, however with a very low sampling rate. On the other hand, GPS has a high sampling rate, but low spatial coverage. Combining these two methods allows us improving potentially the ability to forecast eruptions (Massonnet et al., 1995; Lu et al., 2002; Dzurisin, 2003; Pritchard and Simons, 2002). Ideally, volcano deformation surveys must take into account the process studied, the accumulated knowledge about the specific volcanic system, in order to constrain the expected deformation spatially and temporally and consequently choose the appropriate method(s) and equipment(s).

Theoretically, modern methods like GPS or InSAR allow detecting displacements associated with small-moderate eruptions (Volcanic Explosivity Index of 1-2, Dzurisin, 2000). However, in reality, measurements of surface displacements in volcanic areas are hindered by difficult access or financial limitations. Hence, ground deformation monitoring is often greatly improved by combining several of the methods mentioned above (Palano et al., 2007; Segall, 2013; Dzurisin, 2003; Voight et al., 1999), and by complementing it with other geophysical (seismology, gravity or resistivity surveys), geological, petrological and geochemical datasets for a better understanding of the

evolution of the magmatic system.

1.1.3 Surface displacement patterns

As volcano-seismicity or gas monitoring, surface displacements monitoring is a common method to measure and forecast the short-term activity of the volcano. Surface deformation is not systematically observed prior or during an eruption (*e.g.* Mount St Helens, 2004-2010 eruption, Palano et al., 2012; Lascar volcano, Chile, eruptions between 1993-2000, Pritchard and Simons, 2002). When observed, however, surface deformation points towards potentially active volcanoes. For instance Pritchard and Simons (2002) have detected a 'background level' deformation of ≈2 cm/yr at various South American volcanoes. Sometimes detectable months before the onset of the eruption, surface deformation is also one of the earliest signs of volcanic unrest (Dzurisin, 2003; Dvorak and Dzurisin, 1997; Sparks, 2003; Linde et al., 1993), *e.g.* significant deformation has been observed at Mount Peulik volcano, Alaska, considered a dormant volcano, at least a year before the first earthquake swarm (Lu et al., 2002).

Volcanic deformation patterns are usually complex and irregular, however many eruptions are characterized by regular pressure-cycles such as inflation-deflation patterns (Figure 1.1). Prior to an eruption, a radial inflation pattern is likely to be the surface expression of the magma chamber pressurization, with the maximum amplitude located above the deformation source. The period of inflation can vary in duration from few weeks to months (Dvorak and Dzurisin, 1997), even at the same volcano. The inflation rate ranges from 0.1 to 100 cm/yr (Fournier et al., 2010, 2012), and the maximum amplitude can reach more than 100 m, *e.g.* during the intrusion of a cryptodome like at Mount St Helens in 1980 (Lipman et al., 1981, p.122). In contrast, deflation rates can be rapid relative to the inflation rates, *e.g.* 10-100 mm/day but only a few mm/day, respectively, at Kilauea, Hawaii (Dvorak and Dzurisin, 1997). Deflation is assumed to reflect the depressurization of the magma chamber, and the propagation of the magma through dikes or a preexisting conduit. Dikes up to tens of kilometres length and few meters wide can be emplaced in less than a few hours (Dvorak and Dzurisin, 1997). They produce at the surface a characteristic 'ridge-trough-ridge' pattern (Pollard et al., 1983), with deflation above the dike encompassed by two inflating areas. If, and when, the magma withdrawn from the magma chamber reaches the surface, either via a dike

(*i.e.* fissure eruption) or a conduit, the deflation rate decreases rapidly together with the rate of pressurization of the magma chamber. For instance, a drop in extension rate from 25 to 4 cm/yr was observed at Pu'u O'o, Hawaii, when the activity passed from intrusive to extrusive (Cayol et al., 2000).

While at stratovolcanoes significant displacements tend to be localized within few meters to kilometers from the vent (Dvorak and Dzurisin, 1997), they can, at calderas, be detected as well over a much broader area of more than 100 km^2 (Dvorak and Dzurisin, 1997). With the improvement of equipment (amongst which is InSAR technology) and the increasing duration of the ground deformation datasets, inflation-deflation cycles have been revealed at many magmatic system (Figure 1.1). These exhibit periods ranging from few minutes (Genco and Ripepe, 2010), few hours or days (Voight et al., 1998; Anderson et al., 2010) to several years (Mattioli et al., 2010). The inflation and deflation rates are related to the pressure difference between the deeper (feeding) reservoir and the shallower (fed) chamber (Dvorak and Dzurisin, 1997). Many volcanoes inflate rapidly at first, then inflation levels out before a rapid deflation occurs.

When deformation monitoring help predicting the short-term eruptive behaviour of a volcano, deformation modelling attempts to image the plumbing system and predict the evolution of the volcanic system in the future.

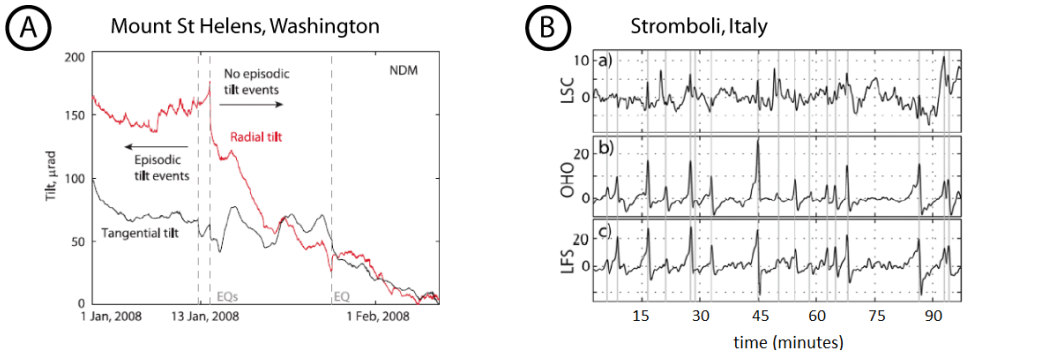
A
Mount St Helens, Washington
No episodic tilt events
NDM
Radial tilt
Episodic tilt events
Tangential tilt
Tilt, µrad
EQs
EQ
1 Jan, 2008
13 Jan, 2008
1 Feb, 2008
B
Stromboli, Italy
LSC
OHO
LFS
time (minutes)

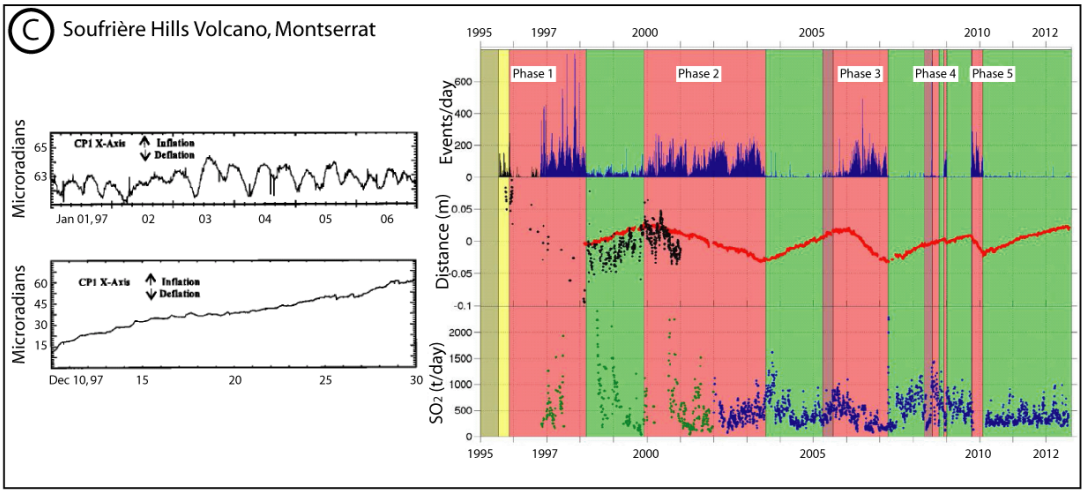
C
Soufrière Hills Volcano, Montserrat
Microradians
CPI X-Axis
Inflation
Deflation
Jan 01, 97
Dec 10, 97
Phase 1
Phase 2
Phase 3
Phase 4
Phase 5
Events/day
Distance (m)
SO2 (t/day)

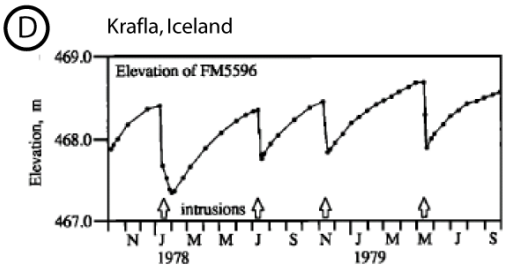
D
Krafla, Iceland
Elevation of FM5596
Elevation, m
intrusions
1978
1979

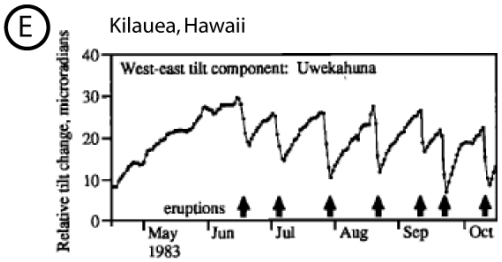
E
Kilauea, Hawaii
West-east tilt component: Uwekahuna
Relative tilt change, microradians
eruptions
May
1983
Jun
Jul
Aug
Sep
Oct

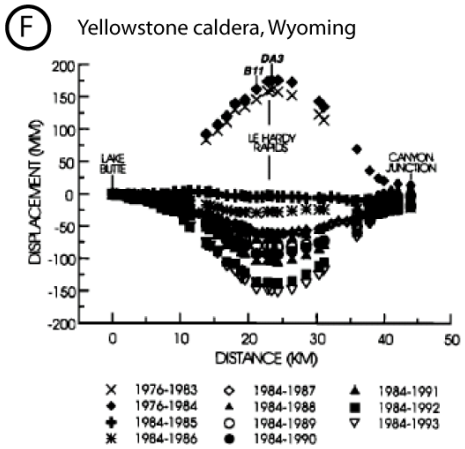
F
Yellowstone caldera, Wyoming
DISPLACEMENT (MM)
DISTANCE (KM)
LAKE BUTTE
CANYON JUNCTION
1976-1983
1976-1984
1984-1985
1984-1986
1984-1987
1984-1988
1984-1989
1984-1990
1984-1991
1984-1992
1984-1993

1.2 Modelling of volcanic ground deformation

Mathematical models are a simplification of a natural process or system, represented by a set of equations. In volcano deformation studies, much efforts have been made to develop mathematical models in order to determine the geometry, depth and physical parameters of the deformation source such as pressure change. More recently, the short-period deformation signals such as tilt and strain (Voight et al., 1998) have also been modelled in relationship with the release of the volatiles of the magma and with the stresses exerted by the rising magma on the conduit walls (Green et al., 2006; Watson et al., 2000; Nishimura, 2009; Iguchi et al., 2008; Albino et al., 2011). Analytical and numerical modelling are two different yet complementary possible approaches. On the one hand, analytical models are very efficient computing-time wise, and the source parameters retrieved with inversion schemes are accurate enough relatively to the spatial and temporal accuracy of the data available. On the other hand, numerical models are often more realistic, can integrate several physical processes (Currenti et al., 2011; Albino et al., 2011; Collinson and Neuberg, 2012), and can be inverted for sources whose geometry is not defined *a priori* (Trasatti et al., 2011).

Analytical models of volcano deformation are available for sources of various simple geometries generally embedded in a homogeneous, isotropic, elastic half-space. Magma

Figure 1.1 *(preceding page)*: Cyclic inflation-deflation ground deformation patterns in various volcanic settings and at different time-scales. **A. Mount St Helens, Washington.** Inflation-deflation cycles, with period of few hours, as observed at the NDM tiltmeter in early 2008, showing episodic tilt activity only before mid-January (modified after Anderson et al., 2010; **B. Stromboli volcano, Italy.** Inflation-deflation cycles, with period of few minutes, recorded at the LSC, OHO and LFS tilt stations, showing inflation before the explosive onset, marked by gray lines (modified after Genco and Ripepe, 2010; **C. Soufrière Hills Volcano, Montserrat.** Short-term tilt cycles with period of few hours recorded between January 1-6, 1997 and trend leading up January 1, 1997 (*left, modified after Voight et al., 1998*) and long-term inflation-deflation cycles since 1998, with period of few months-years, measured by radial component of MVO1 GPS continuous station (*red*) and by vertical component of HARR GPS station (black), compared with seismic and SO_2 flux measured with COSPEC (*green*) and DOAS (*blue*) (*right, modified after Cole et al., 2012*); **D. Krafla caldera, Iceland.** Elevation change of benchmark FM5596 situated in the middle of the caldera with comparison to a benchmark located 12 km to the South. Cycles last few months and are limited by eruption (modified after Dvorak and Dzurisin, 1997); **E. Kilauea volcano, Hawaii.** Tilt cycles of few days recorded between May and October 1983 (modified after Dvorak and Dzurisin, 1997); **F. Yellowstone caldera, Wyoming.** Inflation-deflation profiles between Lake Butte and Canyon Junction measured in 1976 and from 1983 to 1993. The deformation rates varied: after a measured uplift at 22 mm/yr during 1976-84, no deformation has been detected during 1984-85, before a deflation occurring between 10-30 mm/yr between 1985-93 (modified after Dvorak and Dzurisin, 1997)

chambers, sills, and pressurized hydrothermal systems are either modelled as a pressurized point source (Mogi, 1958; Okada, 1992) or as finite sources of various shapes, such as a spheroid (McTigue, 1987), a horizontal penny-shaped or elliptical crack (Fialko et al., 2001a), or a saucer-shaped sill (Galland and Scheibert, 2013). Magmatic conduits and dikes are modelled either as vertically elongated ellipsoid (Bonaccorso and Davis, 1999), as vertical or inclined finite elliptical pressurized cracks (Pollard and Holzhausen, 1979; Davis, 1983), or as finite rectangular dislocation sources opening evenly (Okada, 1985, 1992). Finally, some models account for visco-elastic crustal behaviour (Dragoni and Magnanensi, 1989; Piombo et al., 2007).

The following study concentrates on the surface deformation related to volume changes of magma chambers and dikes within an elastic crust. The Mogi point source and Okada rectangular dislocation source, hereafter referred to as 'Mogi' and 'Okada' models, are certainly the most widely used analytical models to calculate surface deformation related to the pressurization of a magma chamber or the opening of a dike (*e.g.* Abidin et al., 2005; Hughes, 2011; Sanderson et al., 2010; Stiros et al., 2010; Sturkell, 2003). This is due to the fact that they explain well many deformation patterns through simple equations governed by only a few parameters (Masterlark, 2007; Dvorak and Dzurisin, 1997). These two analytical models simplify the geometry and physical properties of the magmatic system and its surrounding. The elasticity assumption implies that displacements on the source walls must be small compared to the source main dimensions. The deformation source is embedded in a homogeneous and isotropic elastic half-space, the half-space assumption implying a flat and stress-free surface. For the Mogi source to be considered a point source, it must be located at a depth more than five times its radius (Lisowski, 2007). In this simplified approach, several aspects are neglected: the properties of the magma within the source, such as its compressibility, surface topography, and 3D heterogeneities in the crust.

Several studies comparing numerical and analytical results have quantified the errors introduced when these aspects are neglected. Neglecting the topography or variations in the mechanical properties of the crust can introduce significant errors when predicting the surface deformation and when estimating the volume change of the source or its depth (*e.g.* Cayol and Cornet, 1998; Long and Grosfils, 2009; Lungarini et al., 2005; Masterlark, 2007; de Zeeuw-van Dalfsen et al., 2012; Williams and Wadge, 1998).

In general, the geometry of magmatic systems is often complex, and they are often represented by a combination of several sources if a single source model does not explain a complex dataset. Many magmatic systems are modelled with a magma chamber where the magma originates and propagates either towards the surface or laterally through a dike or conduit. Examples for this set of models are Mt Etna, Sicily (Palano et al., 2008), Stromboli Volcano, Aeolian Islands (Bonaccorso et al., 2008), Kilauea Volcano, Hawaii (Yang and Davis, 1992), Izu islands, Japan (Nishimura et al., 2001). Occasionally, magma chambers are also feeding a juxtaposed dike, *i.e.* side-by-side in the strike-perpendicular direction of the dike, *e.g.* at Krafla Volcano, Iceland (Arnadóttir et al., 1998), or at Kilauea Volcano, Hawaii (Montgomery-Brown et al., 2010). When the magmatic system is modelled with several magma chambers, those are either vertically stacked or more often stacked with a horizontal offset, *e.g.* for Unzen Volcano, Japan (Kohno et al., 2008), Long Valley Caldera, California (Tiampo et al., 2000).

In cases such as those, the different analytical deformation sources are combined, and their respective deformation fields are summed. However, by doing so, the homogeneous half-space assumption is violated, in the sense that the source interaction is neglected. The effect of the source interaction has been addressed in rock mechanics and engineering studies in 2 and 3D. However they focus on cracks, holes or cavities subjected to a far-field tension or compression and on the estimation of the effective crustal elasticity or stress intensity factors (Gdoutos, 1981; Gorbatikh et al., 2007; Grechka and Kachanov, 2006; Kachanov, 1987, 2003). Generalizing for 2D cavities, Jaeger et al. (2007, p.250) indicates that if the cavity is not located too close to any adjacent cavities or other boundaries, such as the ground surface, the infinite rock mass assumption (homogeneous half-space) is reasonable. Accordingly, the nearest distance to another cavity or other type of boundary should be at least three times the characteristic dimension of the cavity in order for this assumption to be met. In the context of volcano deformation however, the effect of source interactions, and for various arrangements of Mogi and Okada sources in 3D, has not been addressed yet. Such interaction introduces uncertainties additional to those eventually caused by neglecting topography and heterogeneities. It is my aim of the present study to isolate and quantify these uncertainties.

1.3 Project aims

This project seeks to determine the limitations of combining several Mogi and Okada sources, to quantify the errors made by violating fundamental assumptions and neglecting the source interactions, and to study the implications for numerical modelling approaches of magma storage. This will be addressed by:

- testing the combined analytical solutions against the comprehensive numerical solutions of several sets of models, summing analytical Mogi and Okada solutions and quantifying the errors induced;
- testing a finite analytical model of a spherical magma chambers (McTigue, 1987), to compare with the discrepancies calculated with the Mogi model;
- modelling the dike with several numerical methods, to investigate how this choice and its physical meaning can influence the discrepancies between analytical and numerical models;
- performing analytical inversions of the numerical solutions, in order to estimate how these uncertainties map into the determination of inverted model parameters.

1.4 Thesis overview

The overall structure of this study takes the form of six chapters, including this introductory chapter. Chapter Two describes and gives the limitations of the analytical models of magma chambers and dikes either used in the combined analytical models (Mogi, 1958; McTigue, 1987; Okada, 1992) or leading to a numerical method (Davis, 1983). Chapter Three presents the various numerical methods employed to model magma chambers and dikes, and their calibration against analytical solutions. Chapters Four and Five are concerned with the main questions of this study. Chapter 4 gives a description of the geometry and physical parameters of the computed models, including three case studies, and quantifies the discrepancies between analytical and numerical models. Chapter Five presents the results of analytical inversions of several of the numerical models performed in Chapter Four, and summarizes the finding of both chapters. Finally, the conclusion gives a brief summary and discussion of the findings, and identifies topics of future research.

Chapter 2

Analytical modelling of dike and magma chamber

Analytical solutions are obtained from sets of equations representing simplified source and medium properties. Many analytical models were developed to account for various source geometries and various crustal rheologies. Because of their simplicity and wide suitability to observed data, the two predominantly used sources are the Mogi (1958) and Okada (1992) models, respectively representing a point source and a rectangular source in an infinite homogeneous and isotropic half-space

2.1 Principles and previous studies

The first volcanological studies relating surface deformation with a magmatic reservoir at depth have used simple point source models embedded within an elastic crust (Anderson, 1936; Mogi, 1958). Since then, the models have been diversified and have become more complex to account for the variety of the magmatic settings, for the complexity of the deformation field, and more recently, supported by the increase in computing-power, for more detailed datasets, with high spatial and temporal resolution. The main advancements in analytical modelling have concerned three main points: the geometry of the deformation sources, the crustal rheology, and the magma properties.

In general, magmatic systems are not yet well understood. This is stressed by the coexistence of the traditional magmatic model, consisting of a big, fluid-filled magma chamber from which dikes or a conduit originate, with more recent models consisting of a system of stacked sill-like bodies with a fluid centre and "mushy" periphery (Figure 2.1). Analytical models cannot account for the complexity of the magmatic

"mush", however solutions for various simple 3D geometries have been found in addition to the earlier point source solution used in particular by Mogi (1958). Amongst those solutions, the most common source geometries include pressurized finite spheres (McTigue, 1987), pressurized prolate or oblate ellipsoids (Davis, 1986; Yang et al., 1988; Bonaccorso and Davis, 1999), pressurized penny-shaped bodies (Fialko et al., 2001b), pressurized rectangular source (Davis, 1983), and rectangular (Okada, 1985, 1992) or cylindrical (Bonaccorso and Davis, 1999; Nishimura, 2009) dislocation sources, which model either magma chambers, sills, dikes or conduits (Figure 2.1). When the surface displacements cannot be explained by a single deformation source, the magmatic system is thought to be more complex, and several of these analytical models are combined. This can also be the case if alternative data sets such as seismic tomography or gravity are jointly considered.

Compared to the diversity of the source geometries now available through analytical models of surface deformation, including a more complex medium or magma rheology quickly leads to equations which can only be solved numerically. However, although almost all analytical models are designed for an elastic homogeneous and isotropic half-space, now analytical expressions have been extended to calculate the deformation field to visco-elastic half-space (Bonafede and Ferrari, 2009; Piombo et al., 2007). Moreover, in order to model the change in elastic properties of the medium directly surrounding the magma chamber, due to its high temperature, Bonafede and Ferrari (2009) have also derived the displacements due to a pressurized magma chamber surrounded by a visco-elastic shell in a homogeneous and isotropic half-space.

Similarly, in the vast majority of analytical models, the magma is considered as an incompressible fluid. However, some authors have expressed the surface uplift in relation with the volume change of a spherical source filled with magma of depth-independent compressibility (Delaney and McTigue, 1994; Johnson, 1992; Johnson et al., 2000), although the expressions to calculate both horizontal and vertical surface displacements caused by the volume change of a compressible magma within a reservoir are not given explicitly. Other authors have focused on the discrepancies in volume change during transfer of compressible magma between sources of different geometries (Rivalta and Segall, 2008). Finally, some studies have recently coupled solid mechanics and conduit flow in order to expand the use of surface deformation data beyond the estimation of location and volume change of magmatic sources and exploit

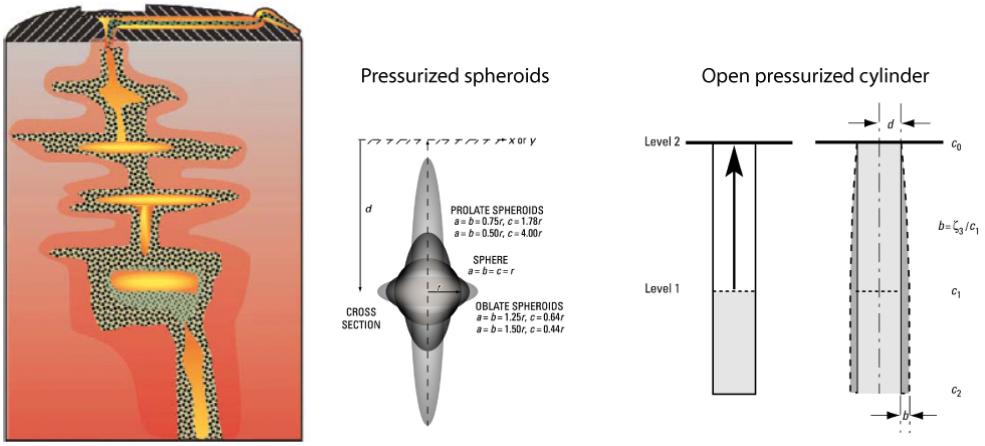

(a) (b)

Figure 2.1: (a) A representation of a magmatic system, the 'magmatic mush column', where colour hotness portrays magma temperature and small black squares depict large crystals. The mush column is characterized by a complex variety of local crystallization environments with different cooling rates (after Zellmer and Annen (2008)). **(b)** Some of the deformation source geometries representing magma chambers, sills, dikes or conduits: oblate to prolate pressurized spheroids (Davis, 1986; Yang et al., 1988; Bonaccorso and Davis, 1999; McTigue, 1987; Mogi, 1958) and open pressurized conduit (Bonaccorso and Davis, 1999) (modified after Lisowski, 2007).

the spatial and temporal richness of recent geodetic datasets. Nishimura (2009) has derived time-dependent equations relating surface displacements due to normal and shear stresses to compressible and incompressible magma rising into a cylindrical conduit. Anderson and Segall (2011) have developed an analytical model to link surface deformation and effusion rate to magma rising from a magma chamber into a cylindrical conduit closed by a plug.

While analytical models have become more diversified in relation to the source geometry, medium rheology and magma properties, yet the Mogi and Okada models are the most widely used. This is due to the simplicity of the equations which are easily inverted. Furthermore, the predicted displacements model appropriately the geodetic datasets. Finally, the available datasets are often too poor to justify the use of more complex models.

2.2 A classic magma chamber model: The Mogi model

2.2.1 Mathematical description

Mogi (1958) is one of the firsts to have applied to a volcanic setting the equations for the deformation induced by a nucleus-of-strain in a homogeneous isotropic elastic half-

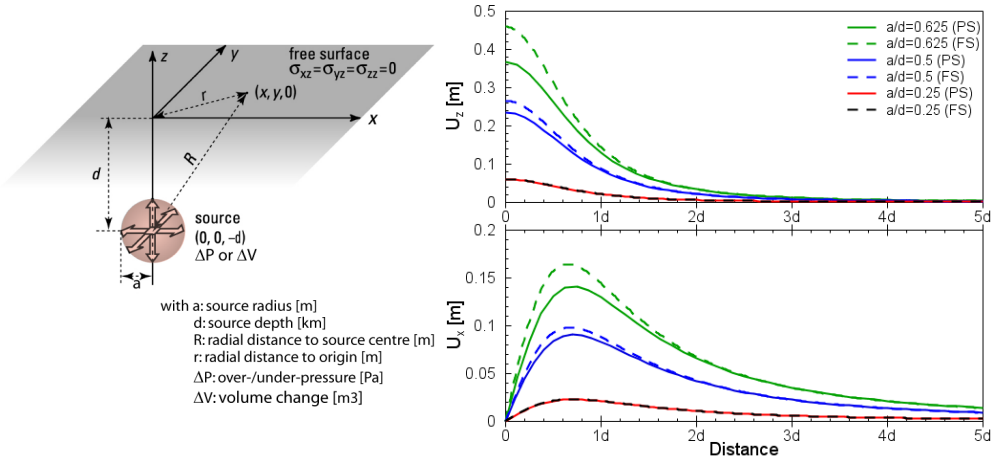

(a) (b)

Figure 2.2: **(a)** Geometry and physical parameters for spherical pressure source models (Mogi, 1958; McTigue, 1987) embedded in an homogeneous isotropic elastic half-space (adapted from Lisowski, 2007). For the Mogi source, the radius-to-depth ratio $a/d < 0.3$ and the Poisson's ratio $\nu = 0.25$. **(b)** Vertical *(top)* and horizontal *(bottom)* profiles calculated with various a/d ratio for the point source model ('PS', Mogi, 1958, in full line) and finite spherical model ('FS', McTigue, 1987, dashed line). The distance from the origin is normalized by the source depth.

space. Instead of giving here the full solution to this problem, solved by Melan (1932), Mindlin (1936), McTigue (1987), and outlined in Segall (2010), I only describe hereafter the principal characteristics of the surface displacements obtained by the Mogi model. For a magma chamber with a radius-to-depth ratio $a/d \ll 1$, and assuming a Poisson's ratio $\nu = 0.25$, the horizontal and vertical surface displacements at the surface location with coordinates (x, y) are given by

$$\begin{pmatrix} U_x \\ U_y \\ U_z \end{pmatrix} = \frac{3a^3 \Delta P}{4GR^3} \begin{pmatrix} x \\ y \\ d \end{pmatrix}, \tag{2.1}$$

where U_x, U_y and U_z are the horizontal and vertical surface displacements, a and d are the radius and depth of the source, ΔP is the pressure difference between the medium and the interior of the source, R is the distance to the source centre, and G is the medium shear modulus (Figure 2.2).

2.2.2 Description of the surface deformation

The surface displacements are axisymmetric relatively to the origin (*i.e.* to the projection at the surface of the source centre), with the strength of the source equal to the

factor

$$\frac{3a^3\Delta P}{4GR^3}, \tag{2.2}$$

The radial displacement $U_r = \sqrt{{U_x}^2 + {U_y}^2}$ at a radial distance r on the surface is given by

$$U_r = \frac{3a^3\Delta P}{4GR^3} r \tag{2.3}$$

Moreover, the peak magnitude of the displacements is proportional to the source volume and pressure change, and inversely proportional to its depth and medium shear modulus, while the displacements wavelength increases with the source depth (Figure 2.3). The maximum vertical displacements occur directly above the source, falling to half at a distance of $\approx 0.7d$. The maximum horizontal displacements occur at a distance of $\pm d/\sqrt{2}$, and exceed the vertical displacements magnitude after a distance of $\pm d$ from the origin. Hence, it is possible to deduce the source depth solely by measuring the vertical displacements, or by comparing radial (*i.e.* horizontal) and vertical displacements, or by calculating the ratio $(U_z/U_r)r$ which equals the source depth d.

2.3 A classic dike model: The Okada model

2.3.1 Crack and Dislocation models

Magmatic dikes are fractures whose length and width are orders of magnitude bigger than the thickness, which allows to consider them as planar features and neglect their surface irregularities and thickness variations (Pollard and Holzhausen, 1979; Kavanagh and Sparks, 2011; Davis, 1983). Two types of analytical solutions have been formulated to compute the deformation field generated by an opening dike in an homogeneous, isotropic, elastic half-space. On the one hand a set of solutions defines the dike as a uniformly pressurized penny-shaped or elliptical 2D slit or 3D crack (Pollard and Holzhausen, 1979). In this case, the dike deforms into an ellipsoid with maximum displacements in its centre if far enough from the free surface, or in proximity to its shallowest tip when close from the free surface (Pollard and Holzhausen, 1979). On the other hand, another set of solutions approximate the dike to a rectangular dislocation source (Okada, 1985; Yang and Davis, 1986; Okada, 1992). Despite the fact that pressurized models are more realistic, Davis (1983) has nevertheless demonstrated that the

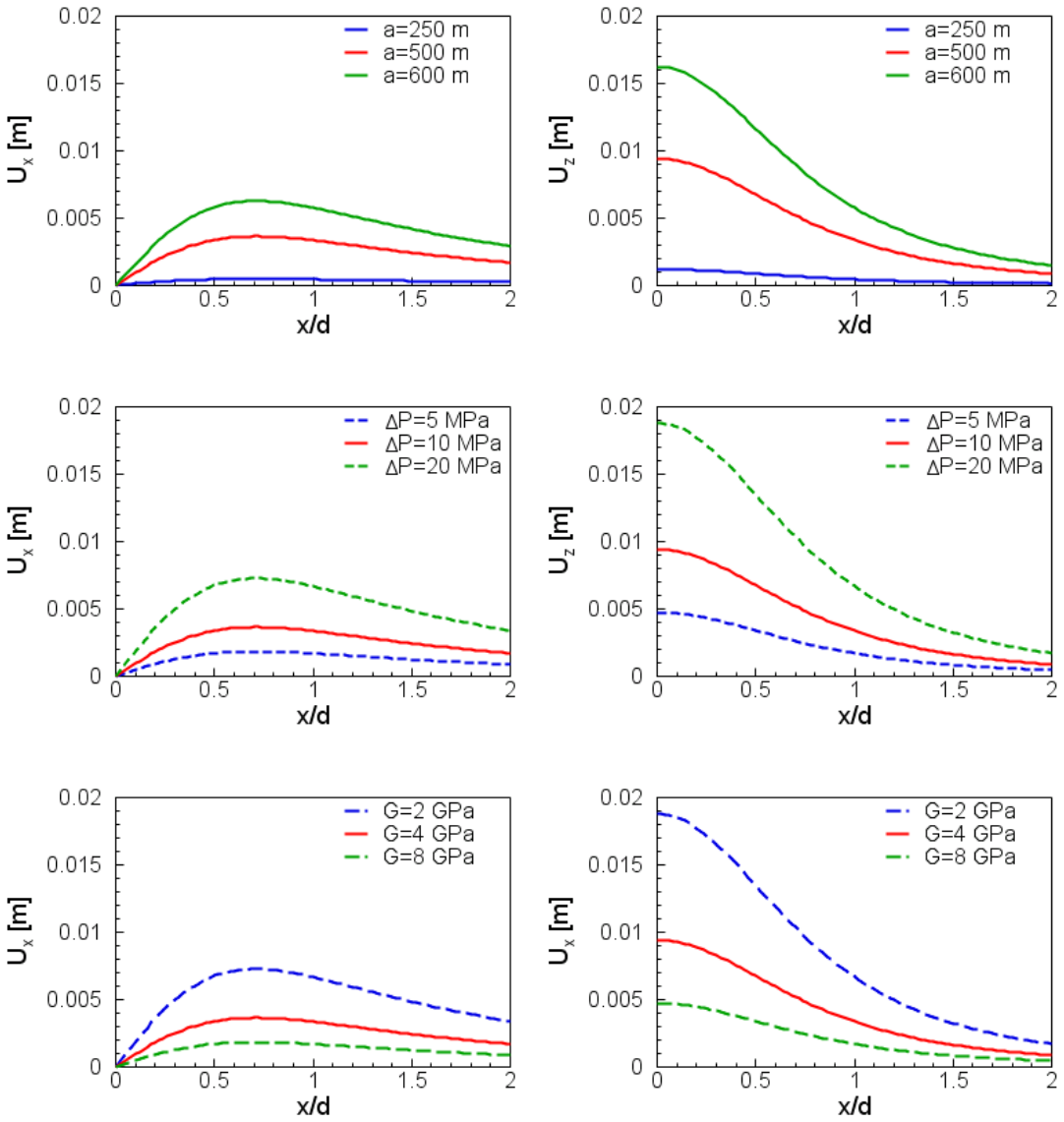

Figure 2.3: Sensitivity of the horizontal (*left*) and vertical (*right*) displacements of a Mogi source to source radius a (*top*), pressure change ΔP (*middle*), and shear modulus G (*bottom*). The source is originally defined with a radius a=500 m at depth d=5 km, overpressurized by ΔP=10 MPa in a medium with shear modulus G=4 GPa and Poisson's ratio $\nu = 0.25$ (*solid red line*)

.

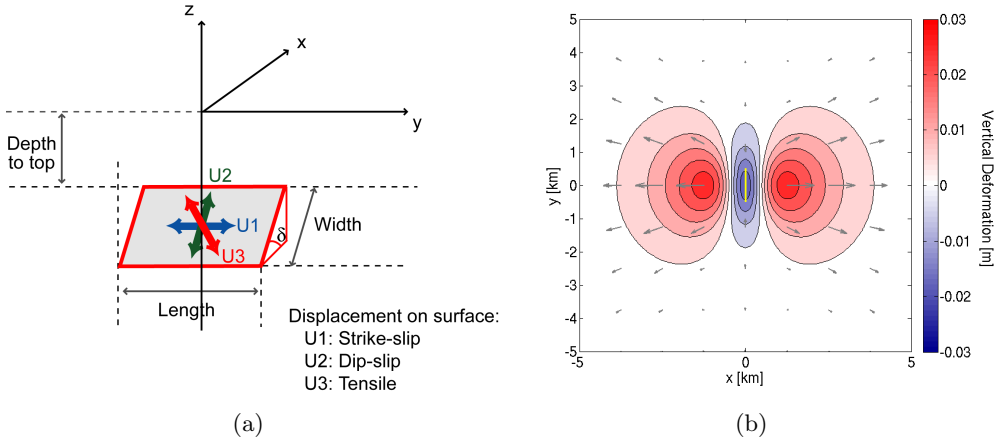

(a) (b)

Figure 2.4: **(a)** Geometry and physical parameters for a rectangular finite dislocation source embedded in an homogeneous isotropic elastic half-space, with Poisson's ratio $\nu = 0.25$ (Okada, 1985, 1992, adapted from Lisowski, 2007). U_1, U_2 and U_3 correspond to the strike-slip, dip-slip and tensile components, respectively. **(b)** Deformation field generated by an Okada source corresponding to a vertical dike opening by 1 m, of width and length equal to 1 km, and with depth-to-top at 1 km. The surface projection of the dike is indicated by the yellow line on the y-axis

discrepancies are negligible between the vertical surface displacements computed for a pressurized elliptical crack compared to a rectangular dislocation source of identical volume, the latter being more computer-efficient. Moreover, the limited quality and quantity of data generally only allow an approximation of the dike parameters through analytical inversions.

2.3.2 Mathematical description

The deformation field induced by dike emplacement is often inverted by means of finite rectangular dislocation source with a tensile component. Basing his work on a previous study by Steketee (1958), Okada (1985, 1992) has integrated the solution of the deformation field due to a point source of dislocation over a finite rectangular source. By doing so, he has formulated the deformation field due to, or to a combination of, a shear, strike-slip and tensile finite dislocation in an elastic homogeneous and isotropic half space with Poisson's ratio $\nu = 0.25$ (Figures 2.4 & 2.5).

For a tensile dislocation, after having defined the dike depth-to-top, width, length, dip and opening, the horizontal and vertical surface displacements U_x, U_y and U_z, are given by (Okada, 1985):

$$\begin{cases} U_x = \dfrac{U_3}{2\pi}\left[\dfrac{q^2}{R(R+\eta)} - I_3 \sin^2\delta\right] \\ U_y = \dfrac{U_3}{2\pi}\left[\dfrac{-\widetilde{d}q}{R(R+\xi)} - \sin\delta\left\{\dfrac{\xi q}{R(R+\eta)} - \tan^{-1}\dfrac{\xi\eta}{qR}\right\} - I_1 \sin^2\delta\right] \\ U_z = \dfrac{U_3}{2\pi}\left[\dfrac{\widetilde{y}q}{R(R+\xi)} + \cos\delta\left\{\dfrac{\xi q}{R(R+\eta)} - \tan^{-1}\dfrac{\xi\eta}{qR}\right\} - I_5 \sin^2\delta\right] \end{cases} \tag{2.4}$$

where U_3 corresponds to tensile component of the dislocation, the length and width of the dike are respectively represented in the variables ξ and η (see Okada, 1985, for details), δ is the dip angle of the dike, (Figure 2.4), λ and μ are the Lamé constants and, for a vertical dike ($\delta = \pm 90$), the remaining coefficients are given by:

$$\begin{cases} I_1 = -\dfrac{\mu}{2(\lambda+\mu)}\dfrac{\eta q}{(R+d)^2} \\ I_3 = \dfrac{\mu}{2(\lambda+\mu)}\left[\dfrac{\eta}{R+\widetilde{d}} + \dfrac{\widetilde{y}q}{(R+\widetilde{d})^2} - \ln(R+\eta)\right] \\ I_4 = -\dfrac{\mu}{\lambda+\mu}\dfrac{q}{R+\widetilde{d}} \\ I_5 = -\dfrac{\mu}{\lambda+\mu}\dfrac{\xi\sin\delta}{R+\widetilde{d}} \end{cases} \tag{2.5}$$

and

$$\begin{cases} p = y\cos\delta + d\sin\delta \\ q = y\sin\delta - d\cos\delta \\ \widetilde{y} = \eta\cos\delta + q\sin\delta \\ \widetilde{d} = \eta\cos\delta - q\cos\delta \\ R^2 = \xi^2 + \eta^2 + q^2 = \xi^2 + \widetilde{y}^2 + \widetilde{d}^2. \end{cases} \tag{2.6}$$

2.3.3 Description of the surface deformation

The surface deformation induced by a vertical opening dike is symmetric relative to the dike axis and characterized by a subsidence directly above it, with a steep gradient at the edges of the dike. Further away, two uplift lobes encompass this central zone of subsidence. The maximum magnitude of the vertical displacements U_z are located at a distance $\approx 0.8d$ from the dike while the horizontal displacements maxima are at a distance $\approx 1.25d$ (Figures 2.4 & 2.5). The wavelength and magnitude of the horizontal and vertical surface displacements are related to both the dislocation type and magnitude, and to the geometry of the dike, that is to its dip, its (horizontal)

length, its depth-to-top and to a lesser extent its (vertical) width (Figure 2.5).

2.4 Assumptions and limitations applying to the Mogi and Okada models

Analytical models are widely used in volcano deformation studies and acknowledging their inherent limitations and particularly their geometric and physical assumptions is necessary for a critical interpretation of their solutions.

2.4.1 A non-unique solution

As shown by the expression of the Mogi source strength (Eq. 2.2) and in Figures 2.3 & 2.5, several combinations of source parameters can give similar surface deformation pattern when employing the expressions derived by Mogi (1958) and Okada (1985, 1992), and source and medium parameters cannot be separated (Figure 2.6).

For the Mogi source, it is common to solve this problem using the volume change of the magma chamber $\Delta V = \pi \Delta P a^3/G$ rather than modelling radius (a) and pressure change (ΔP), as long as it does not correspond to a combination of radius and ΔP which does not overcome the crustal strength. Furthermore, Delaney and McTigue (1994) have proposed expressions to derive the volume change of a finite spherical source from the surface displacements, providing the Poisson's ratio ν is specified, as

$$\frac{\Delta V_{\text{uplift}}}{\Delta V_{\text{injection}}} = 2(1-\nu) \tag{2.7}$$

where $\Delta V_{\text{injection}}$ is the magma chamber volume change, ΔV_{uplift} is the integral of the vertical displacement at the surface, and ν is Poisson's ratio.

Additionally, because of the sparsity and the uncertainties of the deformation data, it is often possible to fit several models to the same datasets, even with deformation patterns as distinctive as those induced by a dike emplacement or when using both horizontal and vertical surface displacements. Finally, heterogeneities in the medium or non-negligible topography such as stratovolcanoes can lead to misinterpretation of the deformation field as induced by a sill-like source rather than by a spherical source (Cayol and Cornet, 1998).

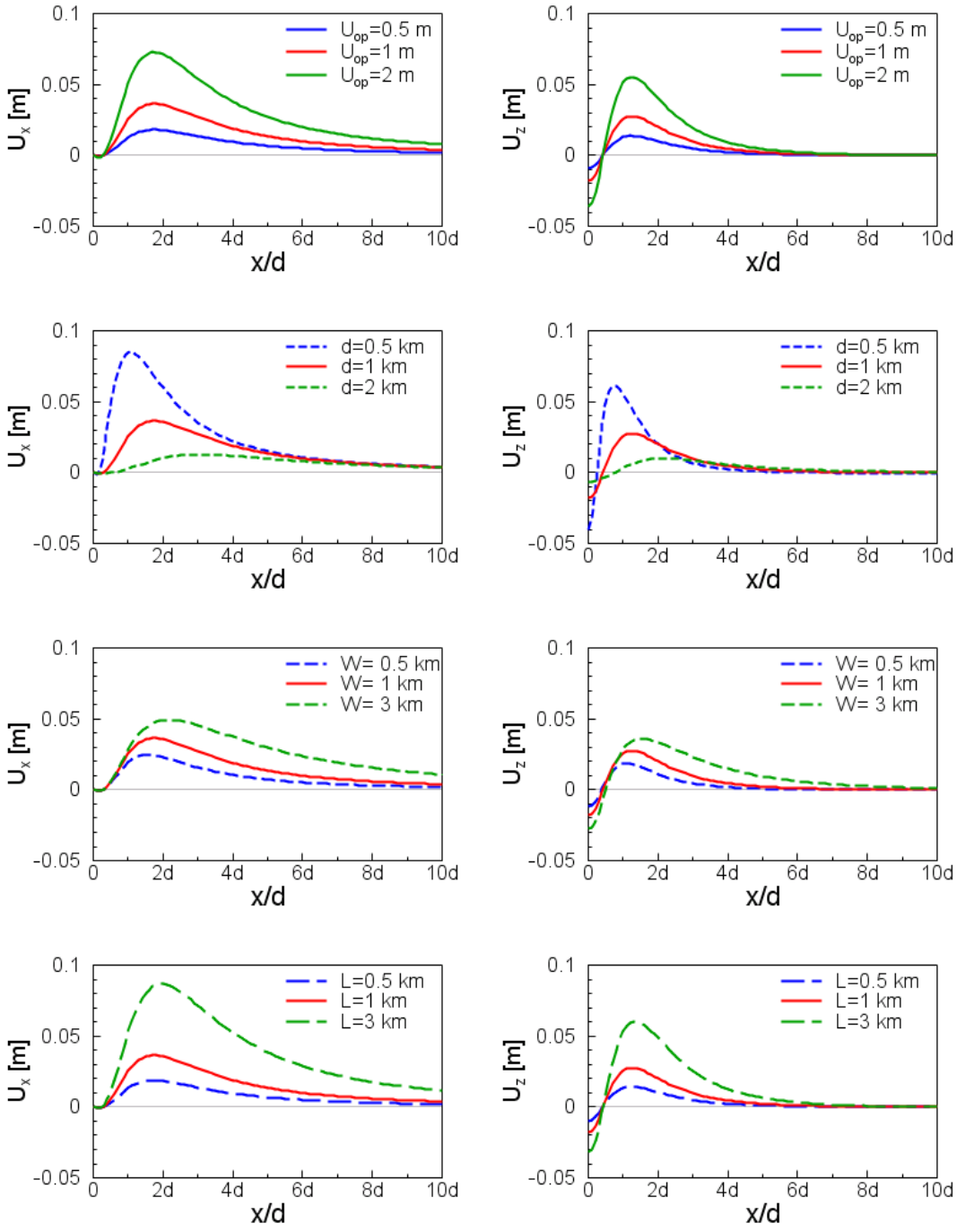

Figure 2.5: Sensitivity of the horizontal (*left*) and vertical (*right*) displacements of a dike (Okada source) to the source opening (*top*), depth-to-top d (2^{nd} *row*), width W (3^{nd} *row*) and to its length L (*bottom*). The source dimensions are originally of 1 km width, 1 km length, it opens by 1 m and is located such that its top reaches 1 km depth (*solid red line*).

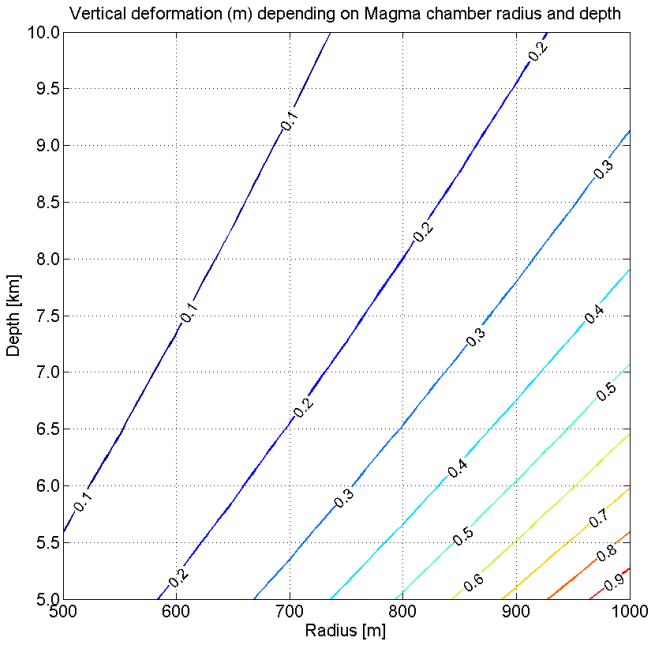

Figure 2.6: Non-uniqueness of the Mogi source: the trade-off between source radius and depth is demonstrated by the identical values of the maximum surface displacement u_{zmax} (normalized by their maximum) which can be obtained for several combinations of radius and depth. The solutions are calculated with a pressurization $\Delta P = 10$ MPa, Shear modulus $G = 4$ GPa, and Poisson's ratio $\nu = 0.25$.

2.4.2 Physical properties of the crust and the impact of the topography

Although tomographic investigations can quantify the shear modulus (G) as well as Poisson's ratio, and image their variations, information on the elastic parameters is lacking at the vast majority of volcanoes. Because of this lack of information and to simplify their equations, most of analytical volcano deformation models assume the crust as an infinite homogeneous isotropic elastic half-space.

Strictly speaking these models apply only to short-term, low temperatures cases, where the strains on the source walls are small. The value of the factor $\Delta P/G$ in the Mogi model (Eq. 2.1) must also reflect an elastic behaviour of the crust and not correspond to large irreversible processes such as caldera collapses (Lisowski, 2007).

Overall, the evaluation of the physical parameters of the crust is not straightforward, and assuming the crust as homogeneous and isotropic is highly questionable in volcanic areas, where the host rock is more likely to be layered, fractured, henceforth having structural and physical properties varying in both lateral and vertical directions. Numerous comparisons between solutions of numerical and analytical models have also

shown the effects of neglecting lateral and vertical structural heterogeneities. Masterlark (2007) and Magni et al. (2008) have shown that the presence of a shallow, low-rigidity layer, increases both horizontal and vertical displacements, especially as the layer is finite in extent like a caldera, rather than an infinite horizontal layer. In fact, Masterlark (2007), who studied the difference between analytical and numerical models, notes that the error induced by regional-scale heterogeneities modelled by infinite superposed layers are insignificant relative to local-scale, caldera-like heterogeneities, and can be neglected for studies at volcano-scale.

Heterogeneities in the physical properties of the crust can also be a consequence of the existing stress field interacting with regional- or local-scale processes such as plate tectonics, crustal loading (Grapenthin et al., 2010), or the presence of other magmatic bodies or aquifers and hence pore fluids. For examples, the undrained and drained Poisson's ratio of a granitic crust are respectively 0.25 (Poisson solid, as assumed by the Mogi model) and 0.34, causing surface displacements predictions to diverge by $\approx 40\%$ (Masterlark, 2007).

While the half-space assumption implies a flat surface, the topography in volcanic areas can be, however, of the order of kilometers (Masterlark, 2007). Cayol and Cornet (1998) have estimated the error induced when neglecting the effect of the topography with the Mogi model at basaltic shield volcanoes for a 10, 20 degrees slopes, and andesitic stratovolcanoes with a 30 degrees slope. They have demonstrated that for an edifice with slopes from 10 to 30 degrees the volume change of the source are overestimated by 10 to 50 %, respectively, and that for stratovolcanoes, the near-field surface displacement pattern differs from the half-space predictions. Assuming a deformation source below the summit and a source radius a, the maximum vertical displacement is not observed at the summit but at a distance of $3a$, and the minimum vertical displacement is located at the summit instead of in the far-field. For volcanoes with a slope > 20 degrees, the tilt sign is reversed compared to the Mogi model predictions within a distance of $3a$ from the summit, which could lead to misinterpreting the deflation of the magma chamber for its inflation. This pattern was also observed by Trasatti et al. (2003) and by Meo et al. (2008), who have used a Digital Elevation Model (D.E.M) of Mount Vesuvius (Italy) topography in place of an axisymmetric volcano model as in Cayol and Cornet (1998). By doing so, they have additionally observed the asymmetry

of the displacement field and that the horizontal components U_x and U_y are not reduced to zero along their y and x axes, respectively.

Several methods have been found to correct the Mogi model solution from the discrepancies induced when neglecting the topography. The source depth computed by inverting the surface displacements is correct if considered from a reference elevation either located at an average altitude (Lisowski, 2007; Williams et al., 2000) instead of from sea level, the latter corresponding to the half-space case, or at the summit of the volcano, in particular for a volcano with steeper topography (Cayol and Cornet, 1998; Williams et al., 2000). Following McTigue and Segall (1988) and Williams and Wadge (1998), Williams et al. (2000) have proposed an analytical method to correct for the topographic effect. Although analytical models are corrected from the topographic effect when the more precise topographic corrections are applied, their solutions fitting with the numerical solutions, the simpler corrections are much more commonly applied (Masterlark, 2007).

2.4.3 Source geometry and magma properties

The point source assumption of the Mogi model limits the application of the model to only a few volcanic systems, where the magma chamber radius is small relatively to its depth. In order to solve this issue, McTigue (1987) applies corrections to suppress the stresses which are added on the magma chamber walls when introducing the free surface of the half-space. These corrections have a common factor of $(a/d)^3$ and become significant when $a/d > 0.3$ (McTigue, 1987; Lisowski, 2007; and Figure 2.2b). The equations of the surface displacements for a finite, spherical, pressurized source in an homogeneous, isotropic, elastic half-space are given by

$$\begin{pmatrix} U_x \\ U_y \\ U_z \end{pmatrix} = a^3 \Delta P \frac{(1-\nu)}{GR^3} \left(1 + \left(\frac{a}{d}\right)^3 \left(\frac{(1+\nu)}{2(-7+5\nu)} + \frac{15d^2(-2+\nu)}{4R^2(-7+5\nu)}\right)\right) \begin{pmatrix} x \\ y \\ d \end{pmatrix} \quad (2.8)$$

where U_x, U_y and U_z are the horizontal and vertical surface displacements, ΔP is the pressure difference between the medium and the interior of the source, a is the radius of the source, d is the depth of the source centre, R is the distance to the source centre, G is the medium shear modulus and ν is its Poisson's ratio (Figure 2.2).

The physics of the intrusion may be more complicated than just one inflating or

deflating source and in general several physical factors should be taken into account in order to constrain the geometry of the sources, for example neither the Mogi nor the Okada models take into consideration mass conservation, and hence, the surface deformation caused by a second reservoir where magma might originate from or migrate to (Trasatti et al., 2011). Moreover, if the mass is conserved, the volume change of the source might be different depending on the shape of the reservoirs (Rivalta and Segall, 2008). Additionally, the absence of shear stresses on the source walls implies that the cavity or dike is fluid-filled before the (de)pressurization of the magma chambers or the dike opening (Trasatti et al., 2011). The Mogi model potentially permits such a scenario if the pressure change is induced by the mere exsolution of volatiles. On the contrary, the Okada model, representing a dislocation source opening evenly, is not a physically realistic model of an opening, propagating dike, which is more likely to have a crack-like shape due the pressurization of its walls.

Furthermore, in both the Mogi and the Okada models the properties of the magma such as its compressibility are ignored. In order to take the magma compressibility into account, Johnson et al. (2000), following Delaney and McTigue (1994) (see Equation 2.7) relates the Mogi source to the induced surface volume changes by

$$\frac{\Delta V_{\text{edifice}}}{\Delta V_{\text{magma}}} = \frac{2(1-\nu)}{1+\dfrac{4G}{3K^*}} \tag{2.9}$$

where G is the medium shear modulus, ν is its Poisson's ratio, $\Delta V_{\text{edifice}}$ and ΔV_{magma} are the uplift volume and the volume of magma (intruded or withdrawn), respectively, and K^* is the effective bulk modulus (incompressibility) of the magma in the reservoir:

$$K^* = K \text{ for } \mathrm{N} < \mathrm{N_s}, \tag{2.10a}$$

$$K^* = \frac{K}{1+\dfrac{KN\rho_m RT}{P^2\omega}} \text{ for } \mathrm{N} > \mathrm{N_s}, \tag{2.10b}$$

where K is the gas-free melt bulk modulus, ρ_m is the bulk magma density, $R = 8.314$ $\mathrm{m^3Pa/mol^\circ K}$ is the gas constant, T is the absolute temperature, P is the average pressure assumed to be lithostatic, and ω is the molar mass of gas. Finally, N is the total weight fraction of a gas phase, exsolved and dissolved, in the magma and N_s the maximum amount of this gas phase which can be dissolved. Although the effect of

the compressibility of the magma is here included, nevertheless Equations 2.9-2.10b do not take into account the expansion of the magma as it progresses towards the surface (Rivalta and Segall, 2008).

2.5 Summary

In this section, I have described the surface displacements pattern induced by the volume change of a spherical magma chamber and by the opening of a dike, as modelled by the Mogi and Okada sources. These two analytical models have the merit of having simple expressions, which can be easily inverted, and which reproduce deformation datasets with uncomplicated symmetry. Moreover, analytical modelling is in general computationally very efficient and many analytical models exist to overcome the various limitations of the Mogi and Okada model assumptions. However, the complexity of the mathematics involved hinders finding analytical expressions that would surmount several of these limitations, possibly simultaneously, in order to represent more complex datasets. In particular, no study has been carried out on the discrepancies introduced when neglecting the interaction between several deformation sources. Moreover, in the Mogi and Okada models, the magma is treated as an incompressible fluid or liquid. Although numerical forward modelling is computationally more expensive, this alternative method of studying volcano deformation allows building more complex models that can integrate several physical processes. In this context, analytical models -in particular very simple ones like the Mogi or Okada sources- can be used for the calibration of the numerical models, as described in Chapter 3, or as first approximations of the deformation source position, shape, and overpressure (Bonaccorso, 2006), but also in cases where the interaction between multiple analytical sources can be neglected; this is investigated in Chapter 4.

Chapter 3

Finite Element modelling of dike and magma chamber

Finite element models are commonly employed in structural analysis, where the physics or the geometry of the problems considered are often too complex to be solved with an exact analytical solution. With numerical studies (*e.g.* Finite Element, FE) it is possible to model magmatic systems where the rheology of the crust is anelastic, where it is inhomogeneous, or where significant topography is present. Here I employ the Finite Element modelling package COMSOL Multiphysics®to assess the errors introduced when neglecting some assumptions of the analytical models such as the Mogi or Okada models. Before evaluating the discrepancies due to the source interaction of several magmatic sources (Chapters 4-5), I describe below the main principles of Finite Element modelling, and I illustrate the design of magma chamber and dike models comparable to the Mogi and Okada analytical sources. I use a common benchmark test to calibrate the numerical models in deformation modelling comparing analytical and numerical solutions of equivalent models.

3.1 Introduction to Finite Element numerical modelling (FEM)

3.1.1 General principles

The analytical models simplify the physical problems and solve the exact equations of elasticity, while satisfying a set of assumptions at the boundaries of an infinite or finite volume. Finite elements models solve the complete set of elasticity equations at certain locations only (*e.g.* at mesh nodes) of a finite volume, satisfying the physical

constraints given by the boundary conditions. The displacement within elements is then interpolated from the nodal displacements. A FE analysis consists of several consecutive steps, once the physical problem to address has been formulated:

1. the definition of the structural problem, *i.e.* of the general geometry, material properties and physical laws of the model;

2. the construction of the computational model, comprising the discretization of the geometry in a mesh of *elements* and the definition of the boundary conditions;

3. the solving step of the problem, expressed as the global system of equation assembling the element equations through a 'shape function';

4. the post-processing system during which the variables of interest are plotted and analysed.

Two types of errors, modelling error and computational error, emerge during a FE analysis. The former is related to the formulation of the physical problem and to the simplifications made compared to the 'real problem', including the restriction from an infinite to a finite domain, and can be reduced by re-defining the problem. The latter consists of the numerical error due to the rounded solutions, in general insignificant compared to the discretization error, which can be reduced with a finer mesh. Once the FE model is built, it is then necessary to validate it against either experimental data or against the equivalent 'exact' analytical solution.

3.1.2 Definition of the structural problems in dike and magma chamber FE analysis (steps 1-2) and computational errors

The deformation field induced by a pressurized magma chamber or opening dike in an elastic crust is a solid mechanics problem. It can be addressed either in 3D or 2D axisymmetric for the case of a magma chamber, or in 3D with or without plane symmetry for the case of a dike. In COMSOL Multiphysics®, this type of model can be built within the 'Solid Mechanics' interface, where the implemented equations solve for the displacements at the model nodes. Although it is possible to build smaller models taking advantage of the axis or plane of symmetry of the model geometry, the models are constructed in 3 dimensions, from the perspective of building more complex models

with no element of symmetry later in the study.

Several issues have to be addressed before an FE model comparable to Mogi and Okada models can be found. Firstly, the homogeneous half-space assumption of the Mogi and Okada models is reproduced in the FE models by a large enough elastic volume and by zero-displacement ('Fixed') conditions on its lateral and bottom boundaries. Alternatively, a 'Roller' condition can be applied on the lateral boundaries, constraining the boundaries only in the normal direction while they can move vertically. If the domain is large enough, the solutions obtained when imposing either a 'Fixed' or 'Roller' condition on the lateral boundaries will be similar. The physical constraints include the definition of the elastic properties of the medium, such as its Young's modulus (E) and Poisson's ratio (ν), either user-defined or loaded from COMSOL Multiphysics®library of commonly used materials (*e.g.* granite, etc). The domain, prismatic, is chosen big enough for these boundary conditions not to distort the numerical solution where the displacement is studied. The surface, *i.e.* the top boundary of the volume, is flat and stress-free.

Secondly, the compromise between the computational capacity and the resolution of the mesh influences the accuracy of the solution, defining the computational error. For both magma chamber and dike models, the elements have to be the smallest, minimizing the inaccuracy due to the discretization, on the deformation sources where the source volume change is imposed, and above the source on the surface where the deformation field amplitude and gradient are the greatest. COMSOL Multiphysics®offers the possibility to create this type of 'user-controlled' mesh, where the number of nodes or their emplacement can be specified. Although quadrilateral 2D meshes (in 3D hexahedra) are more adapted for some physical problems, triangular elements (tetrahedra in 3D) have been chosen for all of the following models, in particular because they are the only elements available for spherical geometries.

The description of the boundary conditions and of the mesh specific to the FE models of a magma chamber and dike, equivalent to the Mogi and Okada analytical models, as well as the model calibrations, are described in Sections 3.2 and 3.3. The calibration of Finite Element models being a case-by-case process, the following validation results cannot be generalized. Nevertheless, the same methodology will be employed in Chapter 4, where discrepancies between analytical and FE models are studied.

3.1.3 Calibration of the FE models: quantifying the numerical error

The solution of the FE models of a magma chamber and of a dike are validated against the 'exact' analytical solutions of the Mogi and Okada source, respectively. In order to estimate the errors, I calculate the mean surface absolute discrepancies ϵ (Equation 3.1) following Currenti et al. (2008), and the local discrepancies Ξ (Equation 3.2) at the maximum ($U\Big|_{\max}$) or the minimum ($U\Big|_{\min}$) of the vertical or horizontal surface displacements. These two estimates have been chosen because ϵ expresses the datafit of the entire dataset, while Ξ links to the modelling process employing a single datapoint at the maximum of the ground deformation.

The average of the absolute discrepancies ϵ [%] is computed at each surface node normalized by the average surface analytical solution $\overline{U^{An}}$,

$$\epsilon_j = \frac{\sum_{i=1}^{N} \frac{|U_{ji}^{An} - U_{ji}^{FE}|}{N}}{\frac{\sum_{i=1}^{N} |U_{ji}^{An}|}{N}} \times 100, \tag{3.1}$$

with U_{ji}^{An} and U_{ji}^{FE} being the analytical or numerical horizontal ($U_{xi},\ U_{yi}$) or vertical (U_{zi}) surface displacements calculated at the surface node i located at coordinates $(x, y, 0)$, with N being the total number of surface nodes.

The local discrepancies (Ξ in [%]) correspond to the normalized difference at the minimum ($\Xi_x\Big|_{\min}$, $\Xi_z\Big|_{\min}$) or maximum ($\Xi_x\Big|_{\max}$, $\Xi_z\Big|_{\max}$) of the analytical and numerical surface displacements. Taking $\Xi_x\Big|_{\min}$ and $\Xi_z\Big|_{\max}$ as examples:

$$\Xi_x\Big|_{\min} = \frac{\text{abs}\left\{U_x^{An}\Big|_{\min} - U_x^{FE}\Big|_{\min}\right\}}{\text{abs}\left\{U_x^{An}\Big|_{\min}\right\}} \times 100 \tag{3.2a}$$

$$\text{or } \Xi_z\Big|_{\max} = \frac{\text{abs}\left\{U_z^{An}\Big|_{\max} - U_z^{FE}\Big|_{\max}\right\}}{\text{abs}\left\{U_z^{An}\Big|_{\max}\right\}} \times 100 \tag{3.2b}$$

3.2 Finite Elements magma chamber model

3.2.1 Geometry, mesh, and physical constraints

The FE model of a spherical magma chamber that I compare to the Mogi model, consists of a pressurized spherical cavity embedded in the elastic domain, with a radius-to-depth ratio of $a/d < 0.3$. For this model, several physical constraints have to be defined:

the elastic properties of the domain, the domain lateral boundary conditions, and the pressure difference applied on the cavity walls. The physical constraints regarding the domain and its lateral boundaries are defined as described previously in Section 3.1.2. Additionally, the difference in pressure between the domain and the interior of the cavity is modelled by a 'Load' boundary condition, either as a 'Pressure' or as 'Force per unit area' applied normal to the cavity surface, and closely enough to prevent the underestimation of surface displacements when compared to the analytical solutions (Table 3.1). The dimensions of the cavity and of the domain differ by more than two orders of magnitude which hinder the implementation of the mesh. Hence an additional, smaller subdomain is introduced at the centre of the domain, encompassing the cavity and creating a central small surface at the origin, where the mesh is finer than for the rest of the surface (Figure 3.1). Two lines are also added to the geometry along the x and y axis in order to define the repartition of the surface mesh nodes, including at the origin, and in order to calculate the maximum local discrepancies $\Xi_x\Big|_{\max}$ and $\Xi_z\Big|_{\max}$.

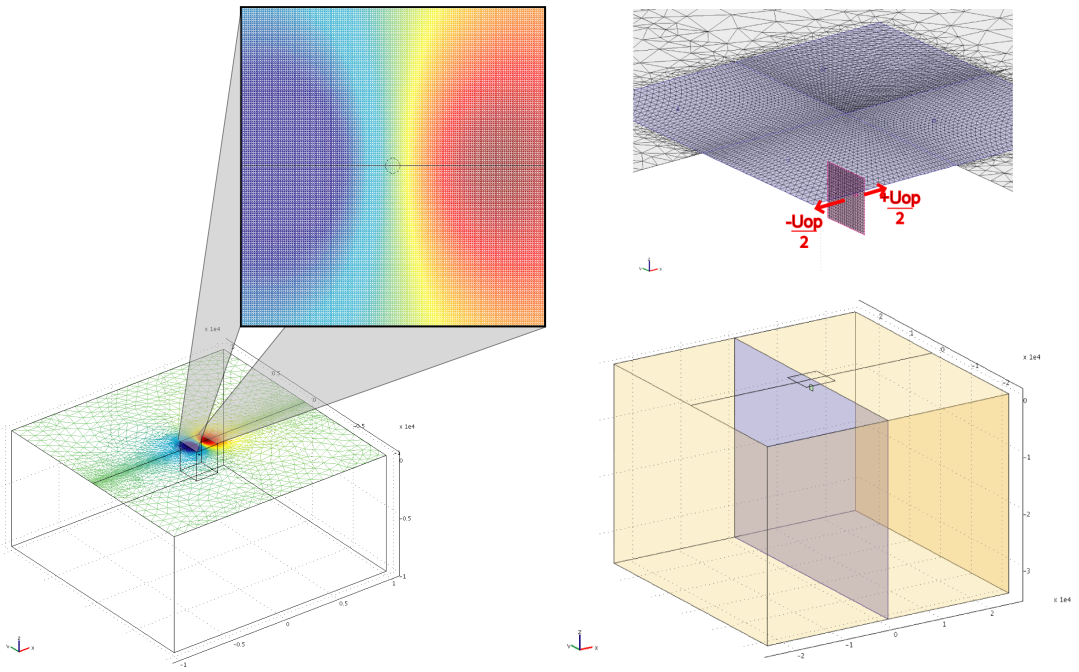

(a) (b)

Figure 3.1: Example of the geometry and mesh employed in FE models of a magma chamber *(a)* and of a dike *(b)*, corresponding to the Mogi and Okada sources. In both cases the mesh is finer on the source walls, and at the surface above the source, where the displacements peak (*e.g.* U_x are plotted in *(a)*). A 'Fixed' or 'Roller' condition is imposed on the lateral boundaries of the domain, while its bottom boundary is fixed and the top surface is left stress-free. For the dike model, the inner boundaries (in blue) are defined as *identity pair* which ensures the continuity of the medium. However, the dike, here modelled with Method 1 (see section 3.3.1), is opening by a total amount of U_x.

Source parameters	Magma chamber	Dike		
		Method 1	Method 2	Method 3
Geometry:				
Radius	50 m	n/a	n/a	n/a
Length×Width	n/a	1×1 km	1×1 km	1×1 km
Depth-to-centre	1 km	n/a	n/a	n/a
Depth-to-top	n/a	1 km	1 km	1 km
Model variables	$dP = 20$ MPa	$u_{op} = 1$ m $u_B = u_{op}/2$ m	$u_{op} = 1$ m $u_{B1} = u^{(2)}$ $u_{B1x} = genext1(u_{B1})$ $u_{B2} = u_{B1x} - u_{op}$	$dP = 12$ MPa
Boundary condition	'Load' $-dP^{(1)}$	'Prescribed displacement' $-u_B^{(1)}$	$-u_{B2}^{(3)}$	'Load' $-dP^{(1)}$

Table 3.1: Summary of the source geometry and boundary conditions applied on the cavity and dike boundaries in the FE models calibrated. The dike is modelled with Methods 1-3 as described in section 3.3.1. $^{(1)}$ indicates that the boundary condition is applied normal to all source boundaries (with positive values going 'out' of the model). For Method 2, a function (genext) is defined to make available the displacements of one boundary on the other while the model is being solved. $^{(2)}$ indicates the definition is applied only on one of the dike boundary (B1) and $^{(3)}$ that the variable is defined, or the boundary condition is applied, on the second dike boundary (B2).

3.2.2 FE model of a magma chamber: calibration methodology

The spherical source considered is 50 m radius with a radius-to-depth ratio $a/d = 0.05$, which is within the Mogi model limitations, and is pressurized by $\Delta P = 20$ MPa (Table 3.1). Although the 50 m source radius is smaller than typical magma chamber radii, ranging from 500 to 7000 m (Marsh, 1989), it allows a first evaluation of the necessary domain and mesh sizes minimizing the computing time. However, the calibration of Finite Element models is a case-by-case process, hence the following validation results cannot be generalized.

Several tests have been carried out, varying the size of the domain and of the inner domain, the size of the mesh, and the constraints on the lateral boundaries. The appropriate geometry and mesh of the model must minimize the differences between the numerical and analytical displacement patterns and amplitudes. Hence for each model I evaluate this misfit qualitatively (*e.g.* Figure 3.3), as well as quantitatively through the surface and maximum discrepancies ϵ and Ξ (Table 3.2, Figure 3.2) as defined in section 3.1.3.

For the calibrated model, the comparison between the displacement patterns and

discrepancies of the various tests emphasizes that:

- the misfit with the analytical solution is acceptably reduced when the lateral extent of the domain is 400 times bigger than the magma chamber radius (*i.e.* 20×20 km, see models #T3b *vs* #T2a), and its vertical extent is 200 times greater than the magma chamber radius that is 10 times than the magma chamber depth (*i.e.* a domain depth of 10 km, see models #T2a *vs* #T4c). An inner domain around the origin with a lateral extent of 40 times the magma chamber radius is suitable (*i.e.* 2 × 2 km, see models #T4a *vs* #T4b);

- constraining the lateral boundaries of the domain with either a 'Fixed' or a 'Roller' condition has no significant impact on the FE solution for a 20×20×10 km domain (models #T2b *vs* #T2c), although it does for smaller domains (models #T3b *vs* #T3c). Additionally, three 20 × 20 × 10 km models were designed with either 4, 10, or 40 nodes on the edges of the domain and applying either a 'Fixed' or 'Roller' condition on the lateral boundaries. To emphasize the influence of the lateral boundary mesh and physical constraints, the pressurization of the source was set to $\Delta P = 100$ MPa (models not listed in Table 3.2). A difference smaller than 0.05% between the misfits calculated for each of these supplementary models confirm that a domain of 20 × 20 × 10 km is large enough;

- a large error can be introduced between analytical and numerical solution if the inner surface mesh is too coarse, due to the interpolation of the FE solution between the nodes (see Figure 3.3*(a1)-(b1)*, model #T2a), but also because there are fewer elements hence the solution is less accurate at the nodes themselves. Similarly, when the mesh of the cavity is too coarse, the pressure is not distributed uniformly on its walls (Figure 3.4). A mesh of ≈ 6000 triangular elements at the surface and of ≈ 13000 triangular elements on the cavity walls reduces the misfit with the Mogi solution to an acceptable level.

Model #		T1a	T1b	T2a	T2b	T2c	T2d	T3a	
Domain dimensions[(1)] [km]		5×5×5	5×5×5	20×20×10	20×20×10	20×20×10	20×20×10	10×10×5	
Inner domain[(1)] [km]		2×2×1.5	2×2×1.5	2×2×1.5	2×2×1.5	2×2×1.5	2×2×1.5	2×2×1.5	
Lateral boundary		Fixed	Fixed	Fixed	Roller	Fixed	Fixed	Fixed	
Mesh statistics	Tetrahedra	4330	7076	7045	242792	242792	568188	6120	
	Surface[(2)]	472	398	526	4070	4070	9582	506	
	Inner Surface[(2)]	150	146	148	2710	2710	6022	148	
	Cavity[(2)]	1	152	152	12732	12732	34612	152	
	A.E.Q[(3)]	0.66	0.63	0.63	0.74	0.74	0.74	0.58	
Degrees of Freedom		21150	31392	31176	1024857	1024857	2410893	26892	
Computing time [s]		3	4	5	490	490	> 1 hour	5	
Bench-marking [%]	$\epsilon_x = \epsilon_y$	78.27	25.30	3.46	0.69	0.84	n/a	9.43	
	ϵ_z	74.74	12.75	2.74	1.13	1.00	n/a	6.21	
	$\Xi_x\big\|_{\min} = \Xi_x\big\|_{\max}$	73.47	7.35	0.96	0.07	0.10	n/a	1.89	
	$\Xi_z\big\|_{\max}$	72.80	4.90	1.39	0.52	0.49	n/a	1.85	

Model #		T3b	T3c	T3d	T3e	T3f	T4a	T4b	T4c
Domain dimensions[(1)] [km]		10×10×10	10×10×10	10×10×10	10×10×10	10×10×10	20×20×15	20×20×15	20×20×2
Inner domain[(1)] [km]		2×2×1.5	2×2×1.5	2×2×1.5	2×2×1.5	2×2×1.5	2×2×1.5	5×5×1.5	2×2×1.5
Lateral boundary		Fixed	Roller	Roller	Roller	Roller	Fixed	Fixed	Fixed
Mesh statistics	Tetrahedra	6143	6143	13732	80209	81791	300000	435634	313785
	Surface[(2)]	506	506	496	3920	4278	9598	20524	11196
	Inner Surface[(2)]	148	148	146	2346	2346	6048	17328	8058
	Cavity[(2)]	152	152	852	852	852	12732	12732	12732
	A.E.Q[(3)]	0.59	0.59	0.59	0.71	0.71	0.73	0.73	0.73
Degrees of Freedom		27429	27429	59634	337095	345882	1271106	435634	1330485
Computing time [s]		3	3	8	77	87	439	581	423
Bench-marking [%]	$\epsilon_x = \epsilon_y$	8.97	7.70	8.62	3.31	4.39	0.86	0.77	5.40
	ϵ_z	4.58	6.13	7.69	2.57	2.76	0.56	1.74	6.89
	$\Xi_x\big\|_{\min} = \Xi_x\big\|_{\max}$	1.87	1.75	3.28	0.79	0.79	0.04	0.11	3.48
	$\Xi_z\big\|_{\max}$	1.48	1.74	4.67	1.19	1.18	0.23	0.48	4.63

Table 3.2: FE model of magma chamber: description of the domain geometry; Models statistics; Benchmarking of the various test models, against theMogi (1958) analytical solution. In all models, the medium elastic parameters are $\nu = 0.25$ and $E = 10$ GPa. The magma chamber is 50 m radius, its centre is located at 1 km depth, and is overpressurized by $\Delta P = 20$ MPa. [(1)]Domain dimensions correspond to Width×Length×Height; [(2)]Elements are triangular; [(3)]'A.E.Q' is the average elements quality, a dimensionless quantity between 0 and 1, where 0 and 1 represent a degenerated and a perfectly regular element, respectively. See also Figure 3.2, Figures 3.3 & 3.4.

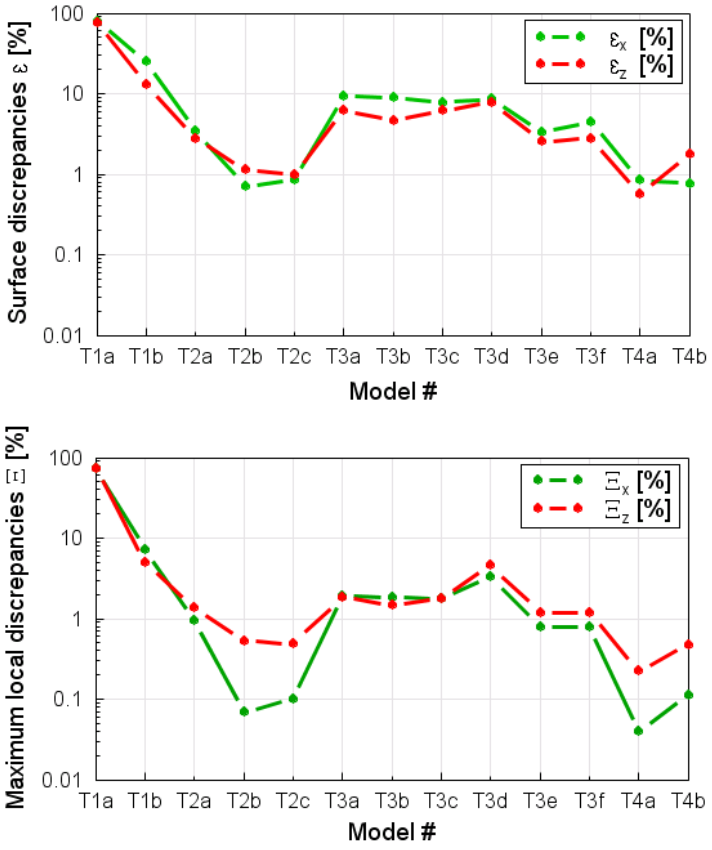

Figure 3.2: Horizontal and vertical surface discrepancies ϵ (*top*) and maximum local discrepancies Ξ (*bottom*) obtained for the domain geometries and meshes of the models tested in Table 3.2, when compared to an equivalent Mogi source solution. The source is located at depth $d = 1$ km, has a radius of $a = 50$ m, is pressurized by $\Delta P = 20$ MPa in a medium with shear modulus $G = 4$ GPa and Poisson's ratio $\nu = 0.25$. See also Table 3.2, Figures 3.3 & 3.4.

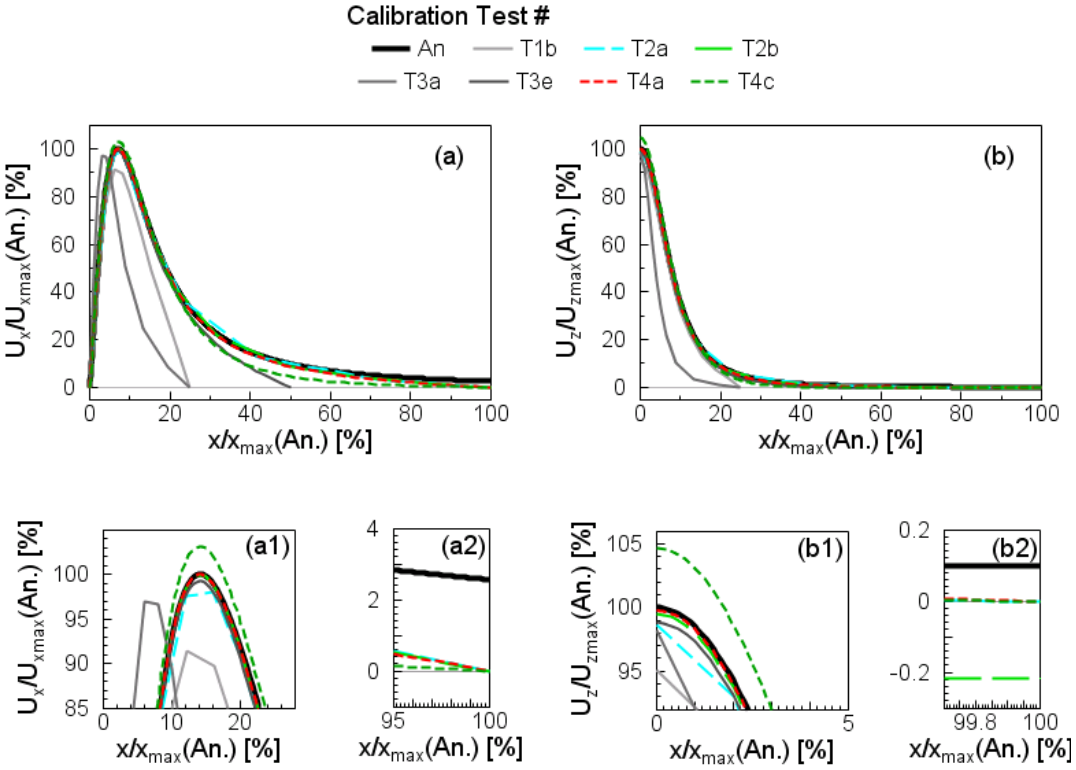

Figure 3.3: Calibration of FE model of a spherical magma chamber: U_x (*a1-3*) and U_z (*b1-3*) profiles along the x-axis for the domain geometry, mesh and lateral boundary conditions tested in some of the models listed in Table 3.2. The analytical solution is represented by a thick solid black line. The FE horizontal and vertical displacements are normalized by the maximum analytical horizontal or vertical displacement, respectively. The distance to the origin is normalized by 10 km, the maximum distance to the origin in the analytical model. The source centre is located at depth $d = 1$ km, has a radius of $a = 50$ m, is overpressurized by ΔP=20 MPa in a medium with shear modulus $G = 4$ GPa and Poisson's ratio $\nu = 0.25$. The effect of the various geometry, mesh and lateral boundary conditions are particularly noticeable at the maximum horizontal and vertical displacement (*(a1)* and *(b1)*) and at the edge of the FE domain (*(a2)* and *(b2)*). See also Table 3.2, Figures 3.2 & 3.4.

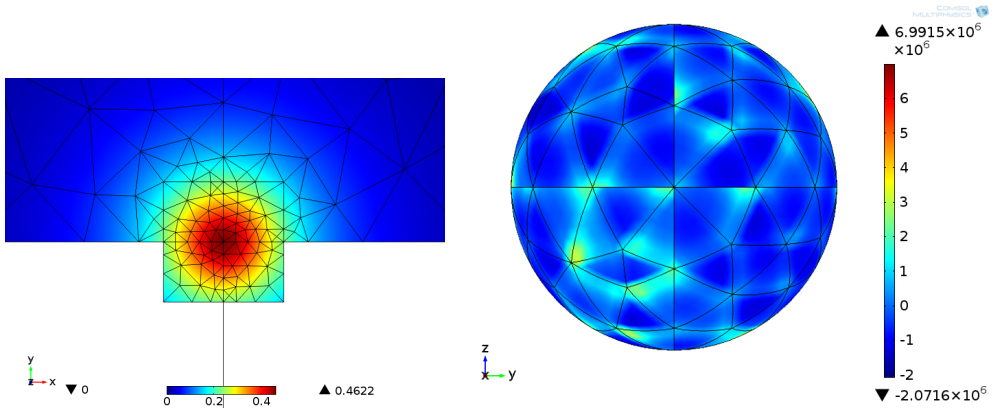

(a) Model T2a: surface mesh

(b) Model T2a: magma chamber mesh

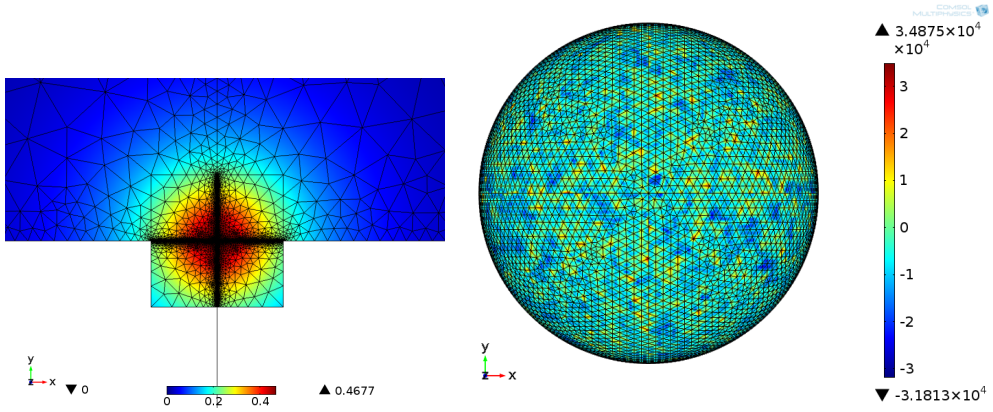

(c) Model T4a: surface mesh

(d) Model T4a: magma chamber mesh

Figure 3.4: Calibration of FE model of a spherical magma chamber: example of meshes at the surface of the domain and on the cavity walls. The colorscales indicate the total surface displacement [mm] (*(a)* and *(c)*), and the variation in [Pa] from the overpressure $\Delta P = 20$ MPa (*(b)* and *(d)*). The edges of the mesh elements are represented in black. In model T2a (*(a)* and *(b)*), the meshes are not fine enough (Table 3.2) resulting in a noticeable departure from the overpressure imposed on the magma chamber walls (*(b)*) and in a misfit with the analytical solution (Figure 3.3). This is quantified by surface discrepancies up to 3.5%, and local maximum discrepancies up to 1.5% (Table 3.2). In model T4a (*(c)* and *(d)*), the meshes are fine, resulting in surface and local maximum misfits only up to 0.9% and 0.2%, respectively (Table 3.2).

3.3 Finite Element dike models

3.3.1 Domain geometry and modelling methods

The FE representation of a dike equivalent to the Okada model consists of a rectangular source embedded in an elastic domain. As for the magma chamber model, the elastic properties of the domain and the lateral boundary conditions are defined as described in section 3.1.2. The overall geometry of the domain is represented in Figure 3.1(b). It is composed of two boxes joined at the $x = 0$ plane where the dike is modelled as a rectangular discontinuity. The same Young's modulus E is imposed in the two boxes as well as a Poisson's ratio of $\nu = 0.25$.

Several approaches can be taken to model a dike numerically. In the three methods tested in this study (Figure 3.5), the deformation source is composed of two rectangular surfaces representing the dike walls, initially welded. An 'identity pair' condition is imposed on the two surfaces surrounding the dike, to ensure the continuity of the deformation field in the elastic medium (Figure 3.1). The boundary conditions applied on the dike walls depend on the method employed.

In the first numerical approach ('Method 1'), a constant normal displacement of $\pm U_{op}/2$ is applied to the wall of a vertical dike , such that U_{op} is the total opening of the dike and the centre of the dike is fixed in space. Although this method is used in numerical modelling (Currenti et al., 2008; Pulvirenti et al., 2009, *e.g.*), note that, in contrast to Method 1, the central plane of an inclined or horizontal Okada source is not fixed, but is shifted towards the free surface (Figure 3.6). Method 1 is hence used for vertical dikes, when the center of the dike is not shifted by other forces in the medium.

In the second approach ('Method 2'), a constant displacement U_{op} is imposed between the two dike walls without fixing their location. Methods 1 & 2 will provide identical results if no second source is employed. However, Method 2 can account for the response of the dike geometry to the stress-field of a secondary source. Finally, Davis (1983) showed that the vertical displacements due to a rectangular tensile source and a pressurized elliptical crack after Pollard and Holzhausen (1979) are similar when their volume change is nearly equal and their depth-to-top is deep enough, *i.e.* at a ratio of depth to half-length of 1.25 (see Figure 3.9 and Table 3.4).

Hence in 'Method 3', I model the dike as a pressurized *tabular* source with a volume change equivalent to the one of the analytical Okada source (Figure 3.5). Note that in

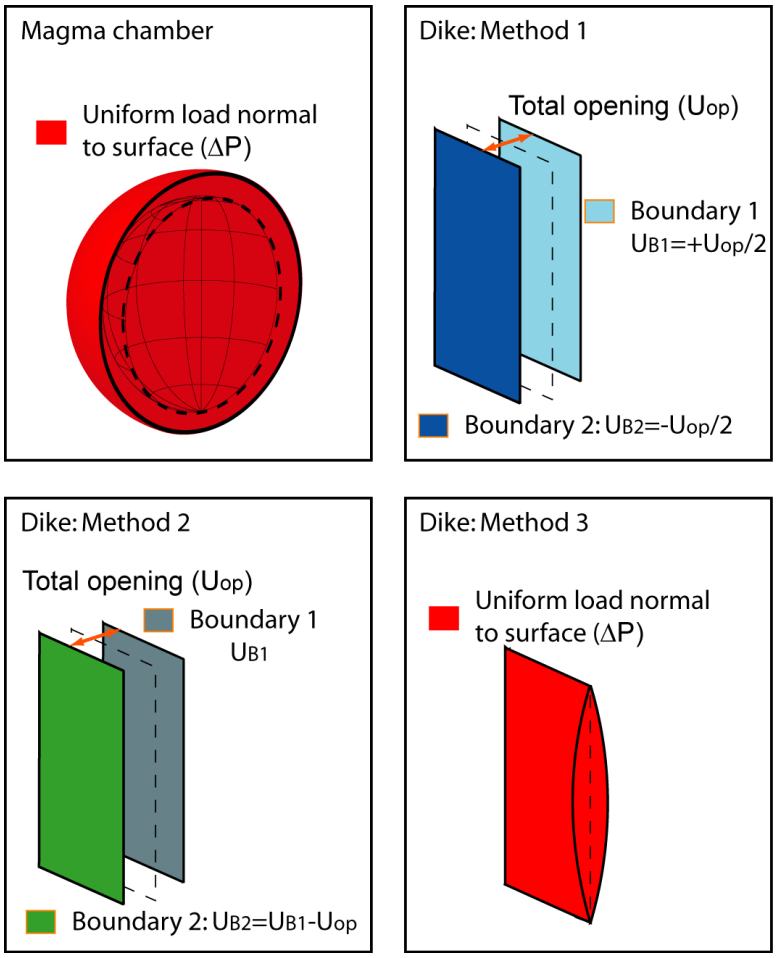

Figure 3.5: Finite element numerical methods employed to model a spherical pressurized source and a dike source equivalent to the analytical Mogi and Okada sources. Magma chamber: a load is applied normal to the surface of the spherical source. The dike is modelled with three different methods. Method 1: a constant normal displacement of $\pm U_{op}/2$ is applied to the dike walls; Method 2: a constant displacement U_{op} is applied between the two dike walls without fixing their location; Method 3: a pressure normal to the dike walls is applied such that its volume change corresponds to the volume of the analytical Okada source.

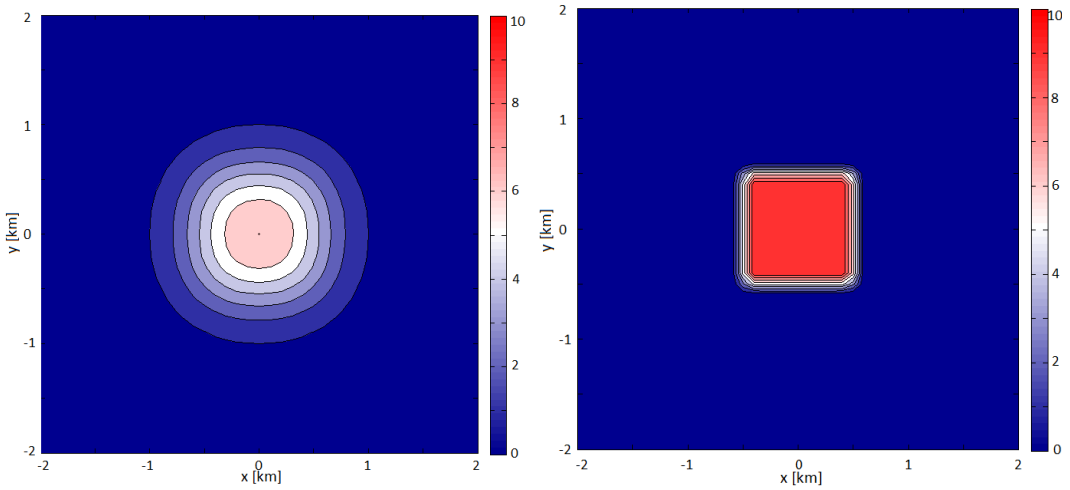

(a) Sill depth 500 m (b) Sill depth 15 m

Figure 3.6: Surface total displacements due to an horizontal 1×1 km Okada source opening by 10 m at a depth $d = 500$ m *(a)* and at a depth $d = 15$ m *(b)*. In the latter case the deformation of almost 10 m demonstrates that the central plane is shifted towards the free surface. This can not be modelled numerically with Method 1 but with Method 2.

Davis (1983) the dike is elliptical.

In COMSOL Multiphysics®, for Method 1 and Method 3, a 'Prescribed displacement' or a 'Load' boundary conditions are applied normal to the dike walls, respectively. For Method 2, a function is defined to make available the displacements of one dike wall on the other dike wall, while solving the model. A 'Prescribed displacement' is then imposed on this second boundary, which equals to the first boundary displacement minus U_{op} (Table 3.1).

3.3.2 Calibration

The analytical solution of the Okada dislocation source is employed to validate all the FE dike models (Currenti et al., 2008; Pulvirenti et al., 2009). The effect of the domain size and of the mesh size are investigated for a 1×1 km dike with depth-to-top $d = 1$ km, and opening $U_{op} = 1$ m. In the medium, the Poisson's ratio is set to $\nu = 0.25$, and the Young's modulus to $E = 30$ GPa, which is a common value for the crustal rigidity of volcanic environments (Albino et al., 2010; Beauducel et al., 2000; Palano et al., 2008). As for the magma chamber model, a smaller 'inner' surface of 6×6 km is designed above the source around the origin. The central boundaries surrounding the dike are defined as an *identity pair*, on which the nodes are automatically located at the same coordinates, improving the quality of the final solution. Table 3.3 and Figure 3.7 below

give the main parameters of the mesh and the surface and local maximum discrepancies with the analytical solution. As for the Mogi model, the calibration emphasizes the need for a fine mesh above the source, in particular near the origin above the dike where the vertical gradient of the displacement is important, and on the source walls (models #5 and #7, Table 3.3 and Figure 3.7). Overall, the discrepancies are higher than those for the Mogi model. This is due to the introduction of the central surfaces surrounding the dike (Figure 3.1) and to the dike boundary conditions when it is modelled with Methods 1 & 2. Indeed, in these cases, a discontinuity is created at the edges of the dike, where the constant opening applied is inconsistent with the surrounding surfaces defined as identity pair (Figure 3.8). With Method 3, the displacements on the surrounding surfaces are three times smaller than those induced by Method 1-2 (Figure 3.8*(d)-(f)*), and are less extended. Despite these numerical errors introduced by the modelling methods, the discrepancies at the surface can be kept below 5%.

Finally, the solution of Methods 1-3 are compared for a 1×1 km dike opening by 1 m (or by a pressurization $\Delta P = 12$ MPa for Method 3) for several dike depth-to-top (Figure 3.9 and Table 3.4). When comparing with the solution of the Okada analytical dislocation source, Method 3 gives the strongest discrepancies for a very shallow dike. However, the surface and maximum local discrepancies calculated for the three methods are comparable for a depth-to-top larger than 1 km. This confirms the results of Pollard and Holzhausen (1979) that the surface displacements calculated by either a pressurized or a dislocation source are similar for a depth to half-length ratio of at least 1.25, which would correspond to a depth-to-top of 0.625 km for the parameters used here. Moreover, when the dike is deep enough, the discrepancies calculated for Method 3 are the smallest, because, in contrast to Methods 1 & 2, the dike boundary conditions and the surrounding surfaces boundary condition are not inconsistent.

3.4 Summary

In this Chapter, the steps that must be taken when using Finite Element numerical methods have been described. The definition of the structural model, including the correct design of the geometry and of the physical constraints corresponding to the physical problem considered is an important step. It has been described for a magma chamber and a dike model embedded in an homogeneous, isotropic, elastic medium. These two models are validated against the analytical solutions of the Mogi and the

Model #		**1**	**2**	**3**	**4**	**5**
Mesh statistics	Tetrahedra	65809	3203	35103	46634	9693
	Inner Surface$^{(2)}$	7200	132	2380	5049	800
	Dike$^{(2)}$	800	68	68	68	200
	Total mesh points	16160	1029	8009	10472	2751
Computing time [s]		467	3	147	275	17
Benchmarking [%]	ϵ_x	5.64	22.96	18.23	19.28	13.34
	ϵ_y	3.58	19.83	15.25	14.83	8.77
	ϵ_z	3.12	17.50	14.30	14.34	7.84
	$\Xi_x\big\vert_{\min} = \Xi_x\big\vert_{\max}$	3.62	20.26	15.08	15.47	9.18
	$\Xi_z\big\vert_{\min}$	4.53	15.89	15.58	15.94	8.27
	$\Xi_z\big\vert_{\max}$	3.08	21.89	13.98	14.89	8.53

Model #		**6**	**7**	**8**	**9**	**10**	**11**
Mesh statistics	Tetrahedra	77445	6374	11863	29471	47465	81004
	Inner Surface$^{(2)}$	20000	800	800	4586	9074	20000
	Dike$^{(2)}$	200	50	50	620	620	800
	Total mesh points	19606	1758	2855	8118	12631	81215
Computing time [s]		1240	10	21	57	214	1434
Benchmarking [%]	ϵ_x	7.77	18.14	18.60	6.12	5.53	5.04
	ϵ_y	7.14	16.23	15.11	4.37	4.09	4.03
	ϵ_z	6.11	14.65	13.85	3.60	3.47	3.31
	$\Xi_x\big\vert_{\min} = \Xi_x\big\vert_{\max}$	7.45	16.26	15.71	4.64	4.27	4.20
	$\Xi_z\big\vert_{\min}$	7.83	14.83	16.19	5.40	5.06	5.01
	$\Xi_z\big\vert_{\max}$	7.80	14.53	14.80	4.56	3.78	3.52

Table 3.3: FE model of a dike: Models statistics and benchmarking of the various test models ran, against Okada (1992) solution. In all models, the 1×1 km dike opens by 1 m, with its depth-to-top at 2 km. The medium elastic parameters are $\nu = 0.25$ and $E = 30$ GPa. The domain is $50 \times 50 \times 35$ km and the inner surface with a denser mesh, located above the source at the surface, is 6×6 km; $^{(2)}$Elements are triangular. See also Figure 3.7.

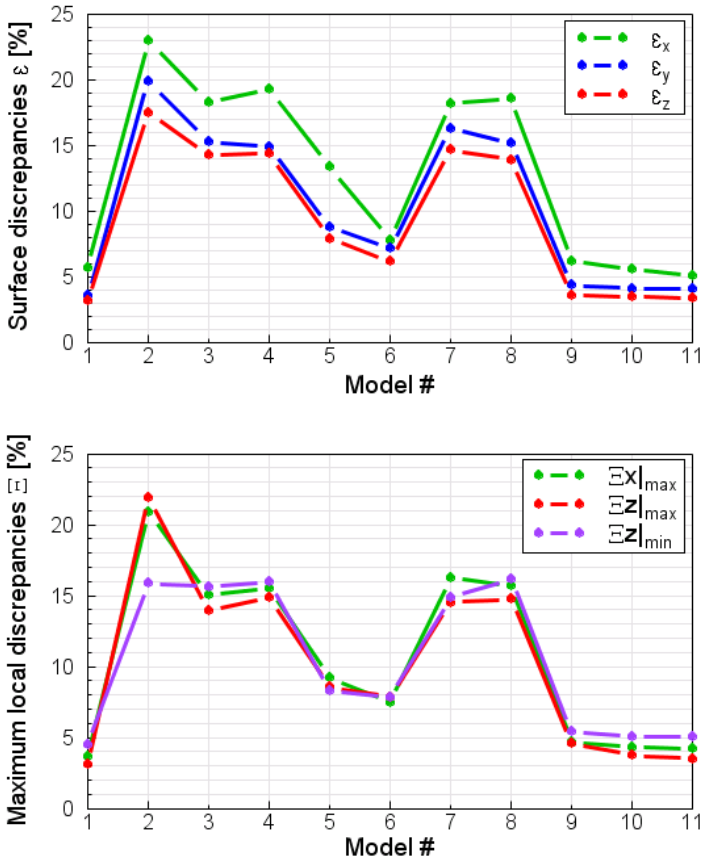

Figure 3.7: Horizontal and vertical surface discrepancies ϵ_x, ϵ_y, and ϵ_z (*top*) and maximum local discrepancies Ξ_x, and Ξ_z (*bottom*) obtained for the domain geometries and meshes of the models tested in Table 3.3, when compared to an equivalent Okada source solution. The 1×1 km is opening by 1 m, with its depth-to-top $d = 2$ km, in a medium with Young's modulus $E = 30$ GPa and Poisson's ratio $\nu = 0.25$. See also Table 3.3.

Dike depth-to-top	Modelling method	ϵ (%)			Ξ (%)			
		ϵ_x	ϵ_y	ϵ_z	$\Xi_x\|_{min}$	$\Xi_x\|_{max}$	$\Xi_z\|_{min}$	$\Xi_z\|_{max}$
2 km	M1	2.6	2.6	2.8	1.0	3.3	3.5	1.2
	M2	2.0	2.6	2.8	2.2	2.1	3.5	1.2
	M3	0.6	0.8	3.4	0.4	0.3	1.0	1.0
1 km	M1	4.0	3.0	2.0	5.0	0.3	2.5	2.3
	M2	2.5	2.9	2.3	2.4	2.6	2.6	2.1
	M3	0.8	1.3	1.9	0.4	0.8	0.0	0.2
0.2 km	M1	3.0	3.0	2.0	4.0	4.0	2.0	3.0
	M2	2.9	3.1	2.3	3.7	3.5	2.1	2.8
	M3	5.0	10.0	10.0	1.0	1.0	10.0	7.0

Table 3.4: Surface and local maximum discrepancies for a dike with depth-to-top at 0.2 km, 1 km and 2 km modelled with the numerical Methods 1-3. The dike opens by 1 m and its height and width are 1 km. Note that in the absence of a secondary source and for a depth-to-top larger than 1 km all three methods yield similar results matching the analytical Okada solution. See also Figure 3.9.

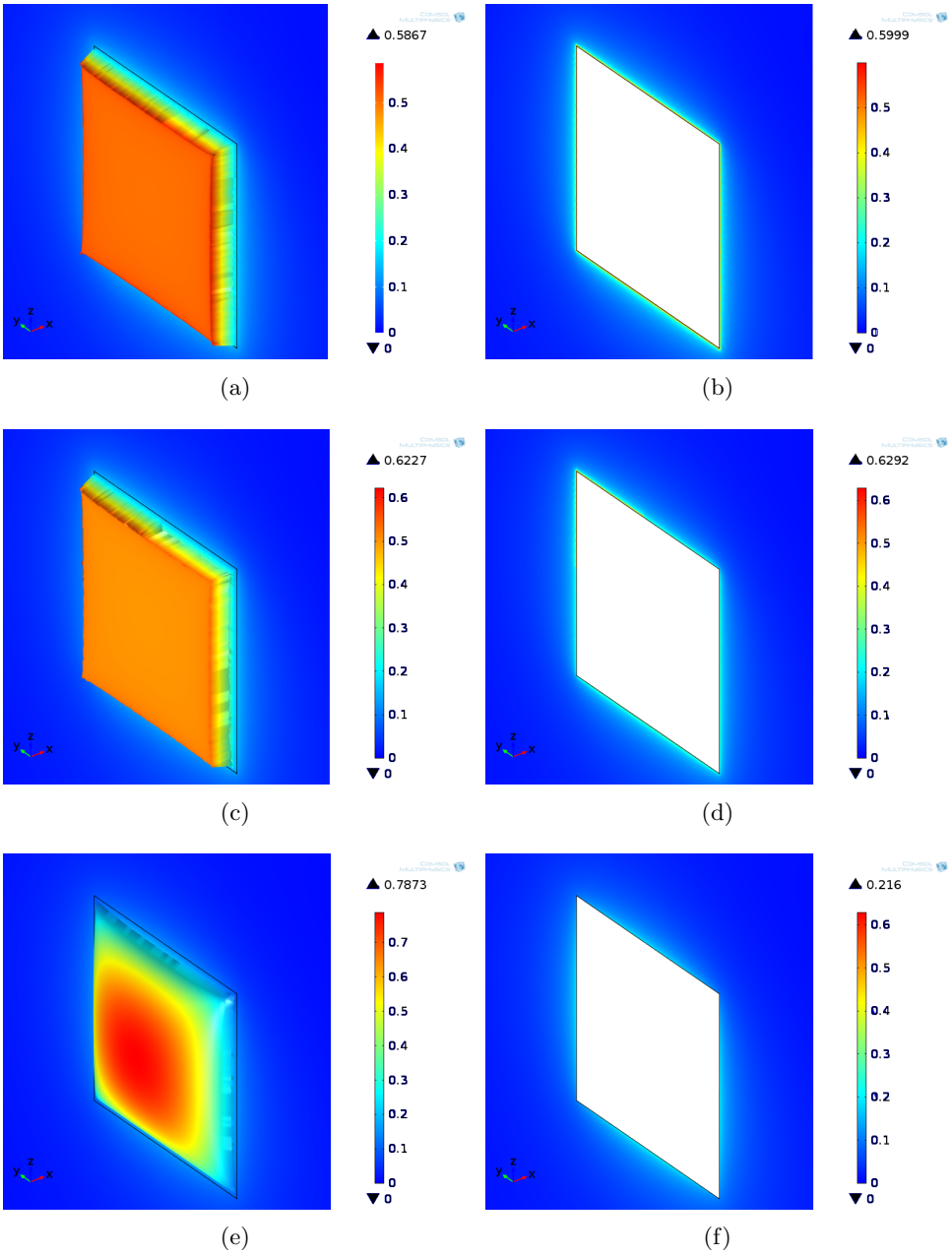

Figure 3.8: FE dike models: 3D perspective of the total displacements imposed on the dike walls (*left*) and computed next to the dike (*right, note that the dike is here hidden and its location is marked by the white rectangle*). The dike is either modelled with Method 1 *(a)-(b)*, Method 2 *(c)-(d)*, in which case the opening is 1 m, or with Method 3 *(e)-(f)*, in which case the dike is overpressurized by $\Delta P = 12$ MPa. For Methods 1-2, the dike opening is modelled through a displacement prescribed on the dike walls. The dislocation imposed on the dike boundaries and edges is inconsistent with the *identity pair* condition imposed on the surrounding surfaces, keeping them welded. This inconsistency introduces an error close to the source, highlighted here by total displacements ([m]) larger than 0.5 m in some places along the dike edges (*(a)* and *(c)*), and of non-zero displacements on the surrounding surfaces, whose maximum are significantly smaller with Method 3 (0.216 m, *(f)*) than with Methods 1-2 (≈ 0.6 m, *(b)* and *(d)*. Note that the displacements maximum is given above the color-scale.

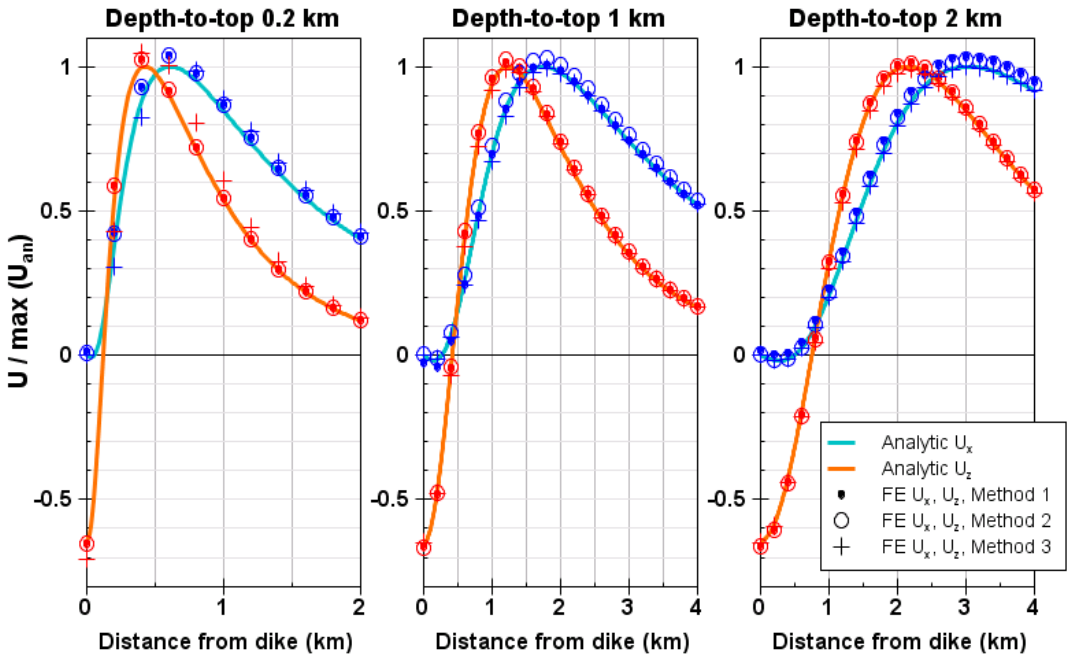

Figure 3.9: Surface displacement profiles for a dike with depth-to-top at 0.2 km (*left*), 1 km (*centre*) and 2 km (*right*) calculated either analytically or computed using Methods 1-3. The dike height and width are 1 km. When modelled with either the Okada model or with the FE Method 1 and Method 2 (represented here with filled circles and circles, respectively), the dike **opens** by 1 m. When modelled with Method 3 (represented with crosses), the dike is **pressurized** by 12 MPa, such that its volume change is similar to the dike volume change obtained with the other methods. The horizontal U_x and vertical U_z surface displacements are normalized by $U_x^{An}\Big|_{\max}$ and $U_z^{An}\Big|_{\max}$, respectively. Note that in the absence of a secondary source and for a depth-to-top larger than 1 km all three methods yield similar results matching the analytical Okada solution. See also Table 3.4.

Okada models, respectively. During the calibration process, I have determined for the various models the domain size and mesh density that reduce the numerical error to an acceptable level. The appropriate domain size and mesh density depend on the model parameters, including the source dimensions, the source pressurization or opening, and the elastic properties of the medium. For example, I have found that for the models considered, a dense mesh on the wall of the deformation source and above it at the surface, and a domain with lateral extent 200 times the magma chamber radius, or 50 times the dike width (*i.e.* 50000 times the dike opening) induce numerical errors of less than 5%. Smaller errors were achieved for the Mogi source models, with Ξ and ϵ less than 3%.

The calibration of the dike modelled as either a dislocation tensile source (Methods 1 & 2) or as a pressurized tabular crack (Method 3) confirms that the results of the surface displacements of the three methods are similar to the Okada analytical solutions despite the different dike shapes for depth-to-top of 1 and 2 km (Figure 3.9). Although Method 1 is employed by some authors (*e.g.* Currenti et al., 2008; Pulvirenti et al., 2009), Method 2 corresponds more closely to the Okada model, in the sense that it accounts for the presence of the free surface.

In Chapter 4, the effect of the source interactions is quantified in a system combining several magma chamber(s) and a dike. In such cases, several Mogi and Okada sources are simply combined, and the discrepancies between the sum of the analytical solutions are evaluated against the corresponding complete numerical solutions.

Chapter 4

On precisely modelling surface deformation due to interacting magma chambers and dikes

As stated in the introduction, most magmatic systems are composed of a network of reservoirs, sills, dikes, or conduits, *e.g.* Soufrière Hills Volcano (Elsworth et al., 2008; Foroozan et al., 2010), Eyjafjallajoküll, Iceland (Sigmundsson et al., 2010a), *etc.* In those cases, the surface deformation is often studied via models combining Mogi and Okada analytical sources. In general, their respective deformation fields are simply summed, violating the homogeneity condition (Section 2.4), and hence neglecting the interaction between the sources. In this Chapter, I quantify the effect of neglecting the source interaction, comparing the combined analytical models with the corresponding FE models. My purpose is to define the limitations of combining analytical models, and hence to provide guidance when and under which conditions the superposition of analytical models induces a large error and when it does not. First, I describe the various model scenarios designed and calibrate the FE models, next I analyse the discrepancies between analytical and FE models. Lastly, I employ the same methodology for three case studies, two adapted from models of the volcanic plumbing system of Soufrière Hill volcano, Montserrat, West Indies, and the other from the magmatic system of the Dabbahu segment, Afar, Ethiopia.

4.1 Method

4.1.1 Description of models scenarios A-D

The surface displacements induced by Mogi and Okada sources are controlled by the geometry, the volume change of the source(s), and by the elastic properties of the medium. In this study I focus on the effect of the model geometry and show results from more than 150 configurations in which I vary:

- source geometry (spherical and/or rectangular sources)
- source separation
- relative source position
- ratio between radius and depth of spherical sources
- pressure difference between spherical sources and medium.

Two main types of models are considered, with either two spherical sources (Models A and B) or one spherical and one rectangular source (Models C and D). Geometrically, the sources are arranged such that their centres are either lined-up vertically (Models A & C), horizontally along the x-axis (Model B), horizontally in the strike-perpendicular direction of the dike (Model DI), and horizontally in the strike-parallel direction of the dike (Model DII). In the following, I will refer to these three geometries as models with 'superposed', 'juxtaposed' and 'aligned' sources, respectively. All models are schematized in Figure 4.1 and their geometrical and physical parameters are listed in Table 4.1. I choose crustal elastic parameters representative of a volcanic environment, and fix in all models the medium Poisson's ratio and Young's modulus to $\nu = 0.25$ and $E = 10$ GPa, respectively as found at Soufrière Hill volcano (Linde et al., 2010).

In Models A and B, the two sources, identical in size, are either superposed (Models A) or juxtaposed (Models B). The Mogi source radius (a) is set to 50 m or 500 m. I vary the depth (d) of the upper source (source 1) such that its radius/depth ratio is either 0.1 (Groups G1 & G1'), 0.05 (Group G2), or 0.5 (Group G3). In the last case of $a/d = 0.5$, the source is too close to the surface (McTigue, 1987), violating the point source assumption of the Mogi model, thus I have employed the finite source analytical solution given by McTigue (1987). Various pressure differences have been tested, *e.g.* in Model A $\Delta P_1 = \pm\Delta P_2 = 20$ MPa or $\Delta P_1 = \Delta P_2 = 200$ MPa, where ΔP_1 and ΔP_2

Model	Group	Source radius a [m]	a/d ratio	Source separation (a to f) [radii]	Source 1 $\Delta P1$ [MPa]	Source 2 $\Delta P2$ or opening U_{op}
A	G1a-f	50	0.1	2.5, 3, 4, 5, 8, 10	Upper source	Lower source
	G1'a-f	500	0.1	2.5, 3, 4, 5, 8, 10	20	20 MPa
	G2a-f	50	0.05	2.5, 3, 4, 5, 8, 10	20	-20 MPa
	G3a-f	500	0.5	2.5, 3, 4, 5, 8, 10	200*	200* MPa
B	G1a-f	50	0.1	2.5, 3, 4, 5, 8, 10	Upper source	Right-hand s.
	G1'a-f	500	0.1	2.5, 3, 4, 5, 8, 10	20	20 MPa
	G2a-f	50	0.05	2.5, 3, 4, 5, 8, 10	20	-20 MPa
	G3a-f	500	0.5	2.5, 3, 4, 5, 8, 10		
C	a-f	500	< 0.2	1.5, 2, 3, 4, 7, 9	Lower source	Upper source
					20 MPa	1 m
					-20 MPa	1 m
DI	M1a-f	500	0.2	1.5, 2, 3, 4, 7, 9	Right-hand s.	Left-hand s.
					20	1 m
					-20	1 m
	M2a-f	500	0.2	1.5, 2, 3, 4, 7, 9	20	1 m
					-20	1 m
	M3a-f	500	0.2	1.5, 2, 3, 4, 7, 9	20	12 MPa
					-20	12 MPa
DII					Right-hand s.	Left-hand s.
	a-f	500	0.2	1.5, 2, 3, 4, 7, 9	20	1 m
					-20	1 m

Table 4.1: Geometry and physical parameters for Models A-D (* tested with Model A-G1 only). In all models, a Poisson's ratio of $\nu = 0.25$ and a Young's modulus of $E = 10$ GPa are used. The dike, of width and length 1 km, is modelled in the FEM with Methods 1-3 described in text. Note: Model 'A-G2d' refers to superposed sources ('A'), source with radius of 50 m and the upper source radius-to-depth ratio of 0.05 ('G2'), and a source separation of 5 radii ('d'). Model 'DI-M2a' refers to a spherical source juxtaposed to a dike ('DI') at a distance of 1.5 radii ('a'), the dike being modelled numerically with Method 2 (one of the dike walls is displaced relative to the other). See also Table 4.2 for more details on numerical models and their benchmarking.

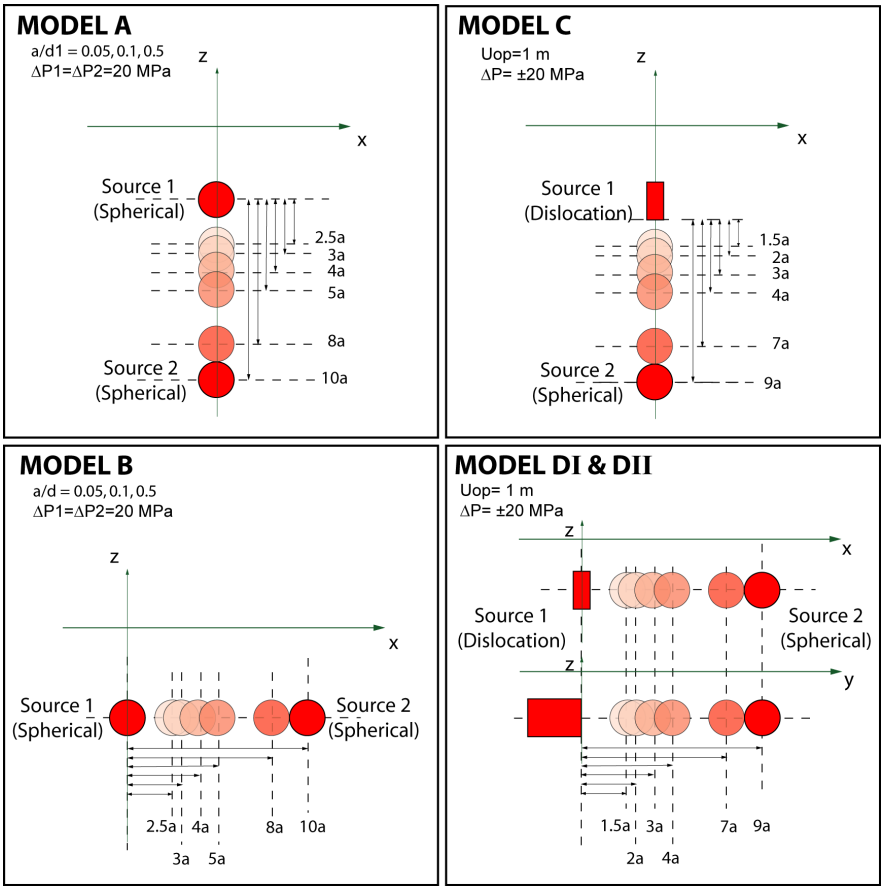

Figure 4.1: Model scenarios. Two spherical sources superposed (Model A) or juxtaposed (Model B); One spherical and one dike sources superposed (Model C), or one spherical source offset to a dike in strike-perpendicular and strike-parallel directions referred to in text as 'juxtaposed' and 'aligned', respectively (Models DI & DII). The separation between the sources is increased from 2.5 to 10 radii (Models A and B) or 1.5 to 9 source radius unit (Models C and D). Geometry and physical parameters are listed in Table 4.1.

is the overpressure of the upper and the bottom sources, respectively.

In Models C & D (Figure 4.1) the Mogi and Okada sources are either superposed (Model C), juxtaposed (Model DI), or aligned (Model DII). The dimensions of the Okada source are set to 1×1 km with an opening of 1 m and depth-to-top of 1 km (Model C), or 2 km (Models D). The Mogi source radius is set to 500 m, and the pressure difference $\Delta P = \pm 20$ MPa.

The centre-to-centre distance separating the sources ranges from 2.5 to 10 times the source radius in Models A-B and the separation between the Mogi source centre and the closest boundary of the Okada source varies from 1.5 to 9 source radii in Models C-D.

4.1.2 Estimation of discrepancies and model calibration

Throughout this study, I calibrate the FE models of the individual sources and quantify the effect of the source interaction by calculating the discrepancies between the displacements of corresponding analytical and FE models at the surface (ϵ, Equation 3.1), and at the maximum (Ξ, Equation 3.2), as defined in Section 3.1.3.

I employ the same calibration procedure as described in Chapter 3 for the spherical source (Models A-D) and the dike source (Models C & D). In order to ensure that I use the domain size and the mesh density which bring the numerical error to an acceptable level, for all model scenarios and source separations considered, I validate models corresponding to the shallowest spherical sources in Models A-D (scenarios 'a', Table 4.1), and sources closest to the lateral or bottom boundaries (scenarios 'f', Table 4.1). As observed in Chapter 3, the appropriate mesh density and domain size depend on the sources type, geometry and physical parameters. The domain dimensions and main features of the mesh employed later in this study are listed in Table 4.2, with the discrepancies calculated during the validation process. Overall, these domain size and mesh density yield a maximum error of 5%.

Furthermore, although imposed on the surface and on the source walls, the repartition of the nodes is not controlled within the entire domain and, when a second geometry is added to the domain, the mesh differs from the mesh generated during the calibration with one source only. In order to investigate the effect of the addition of a second geometry in the domain, I use the source parameters of Model A-G1a (Table 4.1), calibrate Source 1 adding a ('*full*') spherical subdomain, identical to Source 2, with physical properties identical to those of the main domain, such that the medium is homogeneous. Table 4.3 lists the mesh parameters with and without the full sphere, as well as the misfits obtained compared to the equivalent analytical solutions. The discrepancies for a spherical source are similar to the discrepancies for a model with a spherical source and the additional subdomain, demonstrating that no significant error is introduced with the addition of a second spherical subdomain, as far as the mesh is concerned.

Finally, the sum of the analytical solutions of models combining Mogi and Okada sources have been compared with the sum of the individual numerical solutions of each source, yielding also negligible discrepancies ('M1+M2' and 'M+0 (DIa)' in Table 4.2).

According to the various tests described above, discrepancies larger than 5% will

be considered as significant, and caused by the presence of a second deformation source and the resulting source interaction.

Model #		A					B				C	
Group		G1a-f	G1'a-f		G2a-f	G3a-f	G1a-f	G1'a-f	G2a-f	G3a-f	a-f	
a/d ratio		0.1			0.05	0.5	0.1		0.05	0.5	< 0.2	
Source radius a [m]		50	500		50	500	50	500	50	500	500	
Source 1 depth-to-centre [m]		500	5000		1000	1000	500	5000	1000	1000	2750-5000	
Source separation	[m]	125-500	1250-5000		125-500	1250-5000	125-500	1250-5000	125-500	1250-5000	750-4500	
	[radii]	2.5(a), 3(b), 4(c), 5(d), 8(e), 10(f)									1.5(a), 2(b), 3(c), 4(d), 7(e), 9(f)	
Source 1 / Source 2 pressurization or opening		20 MPa / 20 MPa; 20 MPa / -20 MPa; 200 MPa / 200 MPa (G1a-f only)					20 MPa / 20 MPa; 20 MPa / -20 MPa				20 MPa / 1 m; -20 MPa / 1 m	
Domain dimensions[1] [km]		20× 20× 10	200×200×100		20× 20× 10	200×200×100	20× 20× 10	40× 40× 15	20× 20× 10	20× 20× 10	$50^{(*)} \times 50^{(*)} \times 60$	
Mesh statistics	Tetrahedra	25826	50326	58774	24316	36264	26893	14594	26893	37268	22122	
	Elements[2]	113235	130567	169352	104396	158606	107029	84956	107029	152452	86129	
	A.E.Q [3]	0.66	0.88	0.89	0.66	0.68	0.60	0.78	0.60	0.67	0.71	
Benchmarking [%]	Source (M/O)	M(a-f)	M1+M2	M(a-f)	M(a-f)	M(a-f)	M(a-f)	M(a-f)	M(a-f)	M(a-f)	M(f)	O(a-f)
	ε_x	0.4	0.6	0.6	0.4	0.9	0.6	3.0	0.6	3.0	0.6	0.3
	ε_y	0.3	0.6	0.6	0.3	0.5	0.3	1.5	0.3	1.4	0.5	0.5
	ε_z	1.3	1.9	0.6	1.3	1.4	1.2	1.5	1.2	3.1	1.5	1.3
	$\Xi_x\|_{min}$	0.2	0.1	0.0	0.2	0.5	0.4	2.9	0.4	0.9	0.0	4.3
	$\Xi_x\|_{max}$	0.3	0.0	0.0	0.3	0.5	0.5	2.9	0.5	0.9	0.5	0.1
	$\Xi_z\|_{min}$	n/a	n/a	n/a	n/a	n/a	n/a	n/a	n/a	n/a	n/a	0.1
	$\Xi_z\|_{max}$	0.6	0.2	0.2	0.6	1.2	1.4	0.2	1.4	1.8	0.6	0.0

Table 4-3: Models A-D source parameters, models statistics, and benchmarking. On this page are presented parameters and results for Models A-C.
Continued on Next Page...

Model #		DI							DII					
Group		a-f							a-f					
a/d ratio		0.2							0.2					
Source radius a [m]		500							500					
Source 1 depth-to-centre [m]		2500							2500					
Source separation	[m]	750-4500							1250-5000					
	[radii]	1.5(a), 2(b), 3(c), 4(d), 7(e), 9(f)							1.5(a), 2(b), 3(c), 4(d), 7(e), 9(f)					
Source 1 / Source 2 pressurization or opening		20 MPa / 1 m (M1, 2); 20 MPa / 12 MPa (M3); -20 MPa / 1 m (M1, 2); -20 MPa / 12 MPa (M3)							20 MPa / 1 m; -20 MPa / 1 m					
Domain dimensions[1] [km]		110× 100× 35							120× 50[*] × 50					
Mesh statistics	Tetrahedra Elements[2]	50665							21876					
		184356							67078					
	A.E.Q [3]	0.63							0.66					
Benchmarking [%]	Source (M/O)	M+0 (DIa)	M(DIa)	M(DIf)	M(DIIf)	O (d_T =0.2 km)			O (d_T =1 km)			O (d_T =2 km)		
	Method	M1	n/a	n/a	n/a	M1	M2	M3	M1	M2	M3	M1	M2	M3
	ε_x	2.3	2.8	0.6	0.4	3.0	2.9	5.0	4.0	2.5	0.8	2.6	2.0	0.6
	ε_y	2.7	0.6	0.9	0.8	3.0	3.1	10.0	3.0	2.9	1.3	2.6	2.6	0.8
	ε_z	2.0	2.9	1.7	0.9	2.0	2.3	10.0	2.0	2.3	1.9	2.8	2.8	3.4
	$\Xi_x\|_{min}$	4.9	2.7	0.4	0.4	4.0	3.7	1.0	5.0	2.4	0.4	1.0	2.2	0.4
	$\Xi_x\|_{max}$	0.5	2.1	0.3	0.3	4.0	3.5	1.0	0.3	2.6	0.8	3.3	2.1	0.3
	$\Xi_z\|_{min}$	2.0	n/a	n/a	n/a	2.0	2.1	10.0	2.5	2.6	0.0	3.5	3.5	1.0
	$\Xi_z\|_{max}$	n/a	1.1	0.3	0.4	3.0	2.8	7.0	2.3	2.1	0.2	1.2	1.2	1.0

Table 4.2: *(Continued)* Models A-D: Description of the geometry and physical parameters of the combined models; Models statistics; Benchmarking of the various models individual spherical sources (M) and dike (0) modelled with Methods 1-3 against either Mogi (1958) and Okada (1992) solution. In all models, the medium elastic parameters are $\nu = 0.25$ and $E = 10$ GPa. The dike width and length are both 1 km. For Models DI and DII (juxtaposed and aligned spherical source and dike), the dike model benchmarked are located at a depth-to-top d_T. The 'M1+M2' (A) and 'M+0 (DIa)' columns correspond to the comparison between the sum of the two analytical sources against the sum of the two FEM sources displacement solutions. [1]Domain dimensions correspond to Width×Length×Height,[*] mark dimensions for which axisymmetry has been used to reduce computing time; [2]Elements are tetrahedral; [3]'A.E.Q' is the average elements quality, a dimensionless quantity between 0 and 1, where 0 and 1 represent a degenerated and a perfectly regular element, respectively.

Model #		**Without spherical subdomain**	**With spherical subdomain**
Domain dimensions[(1)] [km]		20×20×10	
Inner domain[(1)] [km]		2×2×1.5	
Lateral boundary		Fixed	
Mesh statistics	Tetrahedra	247111	467715
	Surface[(2)]	5216	5216
	Inner Surface[(2)]	2982	2982
	Cavity[(2)]	12732	12732 (×2)
	A.E.Q[(3)]	0.73	0.73
Degrees of Freedom		1044960	1929558
Computing time [s]		445	4842
Benchmarking [%]	$\epsilon_x = \epsilon_y$	1.13	1.14
	ϵ_z	1.07	1.10
	$\Xi_x\big\|_{\min} = \Xi_x\big\|_{\max}$	0.08	0.11
	$\Xi_z\big\|_{\max}$	0.47	0.52

Table 4.3: Calibration of combined sources models: error introduced by the addition of a second spherical subdomain. Description of the domain geometry, models statistics and benchmarking calculated for a model with one pressurized cavity (*i.e.* as in Chapter 3) and a model with a pressurized cavity and an additional spherical domain. In the latter case, the sphere, centred at depth 1125 m like in Model G1a (Table 4.1), has the same elastic properties as the elastic medium hence the medium is kept homogeneous. In all models, the medium elastic parameters are $\nu = 0.25$ and $E = 10$ GPa. The magma chamber is 50 m radius, its centre is located at 1 km depth, and is pressurized by $\Delta P = 20$ MPa. [(1)]Domain dimensions correspond to Width×Length×Height; [(2)]Elements are triangular; [(3)]'A.E.Q' is the average elements quality, a dimensionless quantity between 0 and 1, where 0 and 1 represent a degenerated and a perfectly regular element, respectively.

4.2 Results

In the following sections, I present the results for superposed or juxtaposed spherical sources (Models A & B, respectively) and for juxtaposed dike and spherical source (Model DI) that give significant discrepancies between analytical and FEM surface displacements. While I give here a subset of the results for Models A, B and DI, I list the full set of results in the Appendix A.

4.2.1 Effect of source types and relative position

Models C & DII: superposed or aligned spherical source and dike

Models C & DII always yield negligible discrepancies ($< 5\%$), as represented in Figures 4.2 & 4.3, and listed in Table A-3, and are not further described.

Model #	$\Delta P1$ [MPa]	$\frac{\Delta P1}{\Delta P2}$	U_{op}	Maximum discrepancies obtained [%]					D_{limit} (1) [radii]
				ϵ_x	ϵ_y	ϵ_z	Ξ_x	Ξ_z	
A, G1a	20	1	n/a	3.3	3.3	5.6	7.0	13.9	4
	200	1	n/a	3.3	3.3	5.6	7.0	13.9	4
	10	1	n/a	3.3	3.3	5.6	7.0	13.9	-
	20	1/2	n/a	3.6	3.6	5.7	7.3	16.1	-
	40	2	n/a	3.1	3.1	5.5	6.6	12.0	-
	20	-1	n/a	6.5	5.6	11.4	7.2	13.6	4
	200	-1	n/a	6.5	5.6	11.4	7.2	13.6	-
	20	-1/2	n/a	8.5	8.5	7.6	1.5	16.2	4
B,G1'a	20	1	n/a	5.3	5.8	4.6	1.4	6.3	4
	200	1	n/a	5.3	5.8	4.6	1.4	6.3	-
	20	-1	n/a	9.6	13.1	12.3	8.9	13.8	4
Ca	20	n/a	1	1.3	1.2	1.6	1.2	1.5	< 1.5
	-20	n/a	1	4.1	0.4	1.9	4.0	1.0	2
DI,m1	20	n/a	1 m	97.2	12.3	12.6	82.3	15.1	9+
	-20	n/a	1 m	553.7	9.8	22.5	298.8	5.3	9+
DI,m1	20	n/a	2 m	39.3	18.5	12.1	41.1	14.7	-
	-20	n/a	2 m	723.5	14.9	30.8	657.4	1.7	-
DI,m2	20	n/a	1 m	7.1	7.6	5.7	5.9	7.2	3
	-20	n/a	1 m	24.1	7.6	6.8	8.7	7.0	3
DI,m2	20	n/a	2 m	11.0	17.0	9.7	11.0	10.7	-
	-20	n/a	2 m	49.0	13.7	15.4	18.8	12.6	-
DI,m3	20	n/a	12 MPa	14.3	12.3	9.1	11.2	5.5	3
	-20	n/a	12 MPa	11.1	15.5	11.9	17.6	12.9	3
DI,m3	20	n/a	23 MPa	16.5	23.5	13.2	26.6	11.8	-
	-20	n/a	23 MPa	30.3	19.2	17.5	23.1	19.2	-
DII,m1	20	n/a	1	0.3	0.7	1.5	0.2	0.7	< 1.5
	-20	n/a	1	0.9	1.4	1.4	0.7	1.7	< 1.5

Table 4.4: Models A-D: Maximum discrepancies found either for various pressurization ($\Delta P1$, $\Delta P2$) of the two spherical sources in Models A-B or for various pressurization of the spherical source ($\Delta P1$) and various dike opening (U_{op}, Methods 1-2) or dike pressurization ($\Delta P2$, Method 3). D_{limit} (1) corresponds to the source separation where the discrepancies become negligible, that is smaller than 5% as defined in the calibration process. In all models, the Poisson's ratio $\nu = 0.25$ and the Young's modulus E=10 GPa. Models for which only the closest source separation was tested are indicated by '-'.

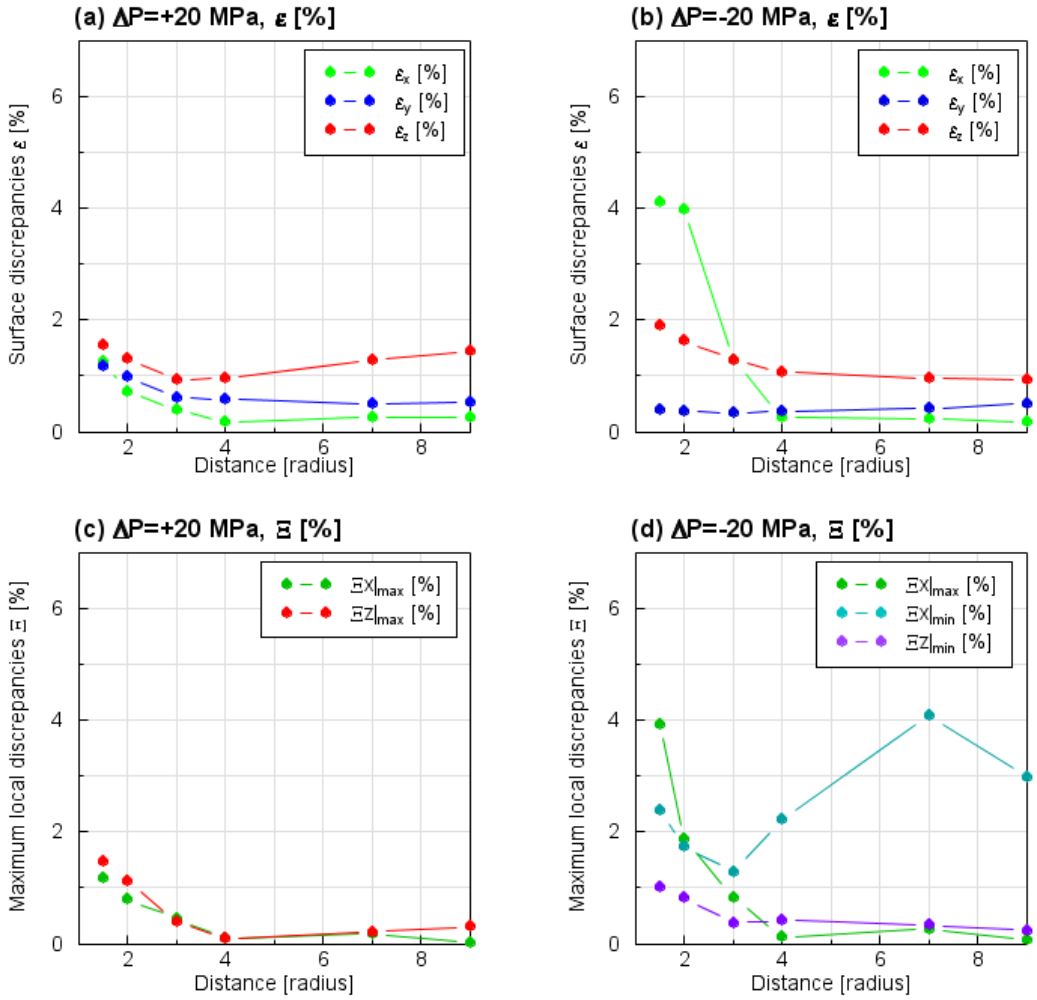

Figure 4.2: Model C: Surface (ϵ) and maximum local (Ξ) discrepancies *vs* source separation obtained for models combining a dike superposed to a spherical source. The dike is opening by 1 m and the spherical source is pressurized by either $\Delta P = +20$ MPa (*left column: a, c*) or by $\Delta P = -20$ MPa (*right column: b, d*). Corresponding discrepancies values are listed in Table A-3.

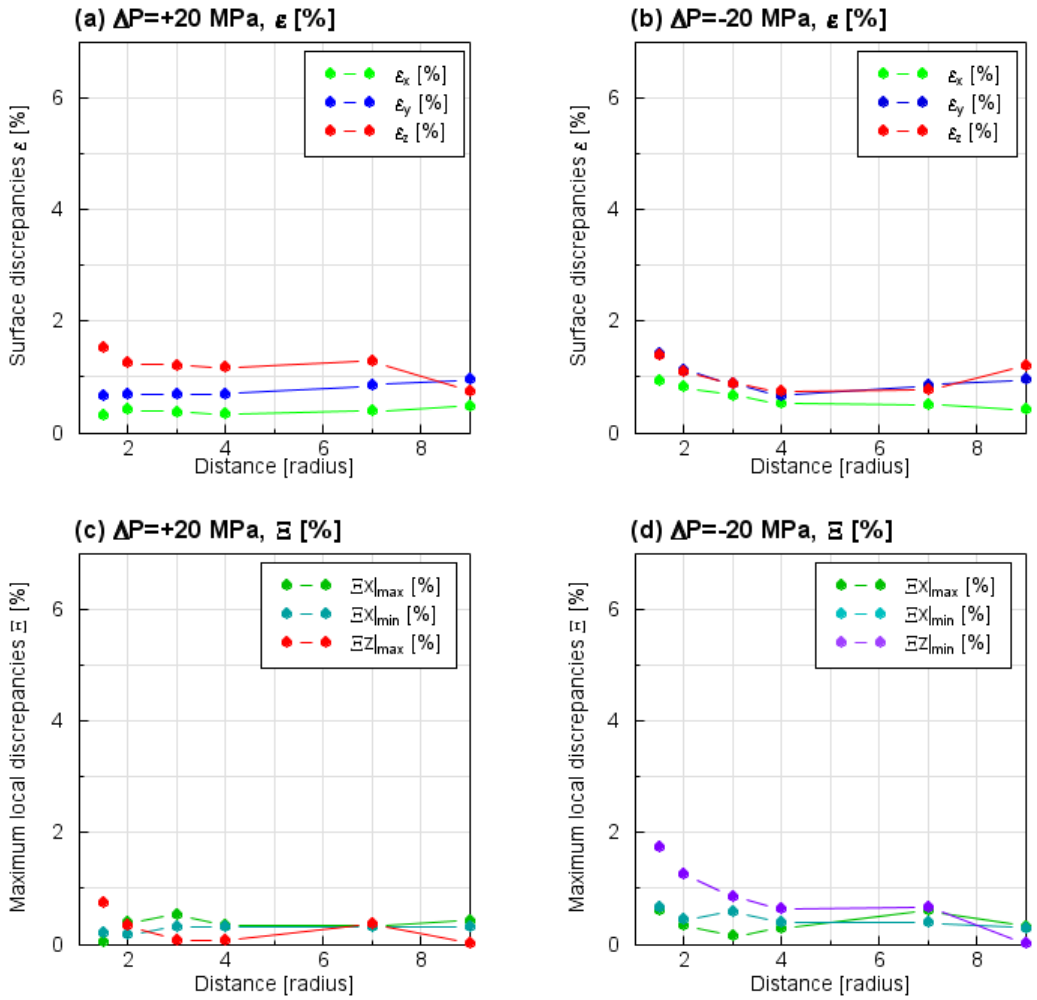

Figure 4.3: Model DII: Surface (ϵ) and maximum local (Ξ) discrepancies *vs* source separation obtained for models combining a dike aligned to a spherical source. The dike is opening by 1 m and the spherical source is pressurized by either $\Delta P = +20$ MPa (*left column: a, c*) or by $\Delta P = -20$ MPa (*right column: b, d*). Corresponding discrepancies values are listed in Table A-3.

Models A & B: superposed and juxtaposed spherical sources

The results of Model A and Model B highlight how the discrepancies between analytical and numerical models depend on both geometry and on the combination of inflating or deflating sources.

When the two sources are inflating, superposed sources (Model A) produce overall greater discrepancies than juxtaposed sources (Model B): *e.g.* for Model A, at 2.5 radii separation, ϵ, Ξ_x and Ξ_z are 9%, 7% and 14%, respectively, while for Model B ϵ reaches 7%, Ξ_x is always negligible, and Ξ_z is 10% (Figures 4.5 & 4.6 and Tables A-1 & A-2). However, when one of the sources is deflating, the discrepancies for both models are similar. For Models A and B, all discrepancies are negligible ($< 5\%$) beyond a source separation (centre-to-centre) of 4 radii.

Depending on the position of the sources and their pressurization (inflation or deflation) the analytical models either under- or overestimate the surface displacements (Figure 4.7). Two overpressurized sources 'shield' each other and their inflation is buffered where the sources are the closest (Figure 4.4a). However, when one of the two sources is inflating and the second deflating, the former expands into the space vacated by the latter, this effect being the strongest where the sources are the closest (Figure 4.4b). At the surface, for both Models A and B and the parameters chosen, the discrepancies are significant (5%) up to a horizontal distance of 3 km (U_x) and 5 km (U_z). In the case where two sources are superposed, the analytical solution overestimates both horizontal and vertical displacements for two inflating sources (Figure 4.7a), but underestimates them for one inflating and one deflating source (Figure 4.7b). In the scenario of two juxtaposed sources (Model B), the analytical model underestimates the surface displacements when the two sources are inflating or overestimates them when one of the sources is deflating (Figure 4.7c and d).

Finally, the discrepancies computed between the numerical solution and McTigue's finite spherical source solution (Group 3 in Models A & B) do not clearly differ from those calculated using Mogi's point source (Groups 1-2). The surface discrepancies ϵ are similar for Models A & B. In contrast, when the two spheres are superposed and inflating (Model A), the finite source solution reduces Ξ_x to 5% (Groups 1-2: 8%) and Ξ_z to 7% (Groups 1-2: 15%). In case of the juxtaposed sources (Model B), when one of the source is deflating, Ξ_x is similar to the discrepancies between analytical point source (Groups 1-2) and FE model, but McTigue's solution reduces Ξ_z to 7% (Groups

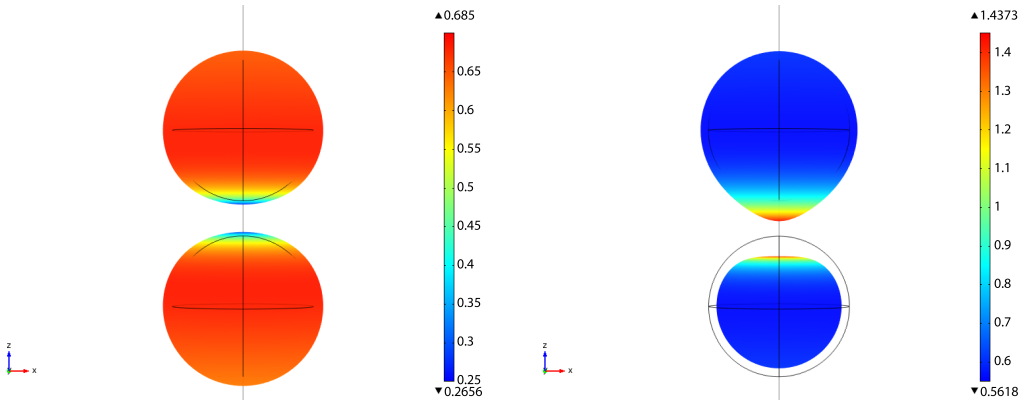

(a) Model A ($\Delta P1 = \Delta P2 = 20$ MPa) (b) Model A ($\Delta P1 = -\Delta P2 = 20$ MPa)

Figure 4.4: Models A (Group G1'a): 2D perspective of the displacement vector magnitude [m] deforming the walls of a spherical source pressurized by $\Delta P1 = 20$ MPa superposed to another spherical source pressurized by either $\Delta P2 = 20$ MPa (*left*) or $\Delta P2 = -20$ MPa) (*right*), in an homogeneous medium. Note that the source deformation is magnified by a factor of 100 and the difference in scale between *(a)* and *(b)*.

1-2: 14%).

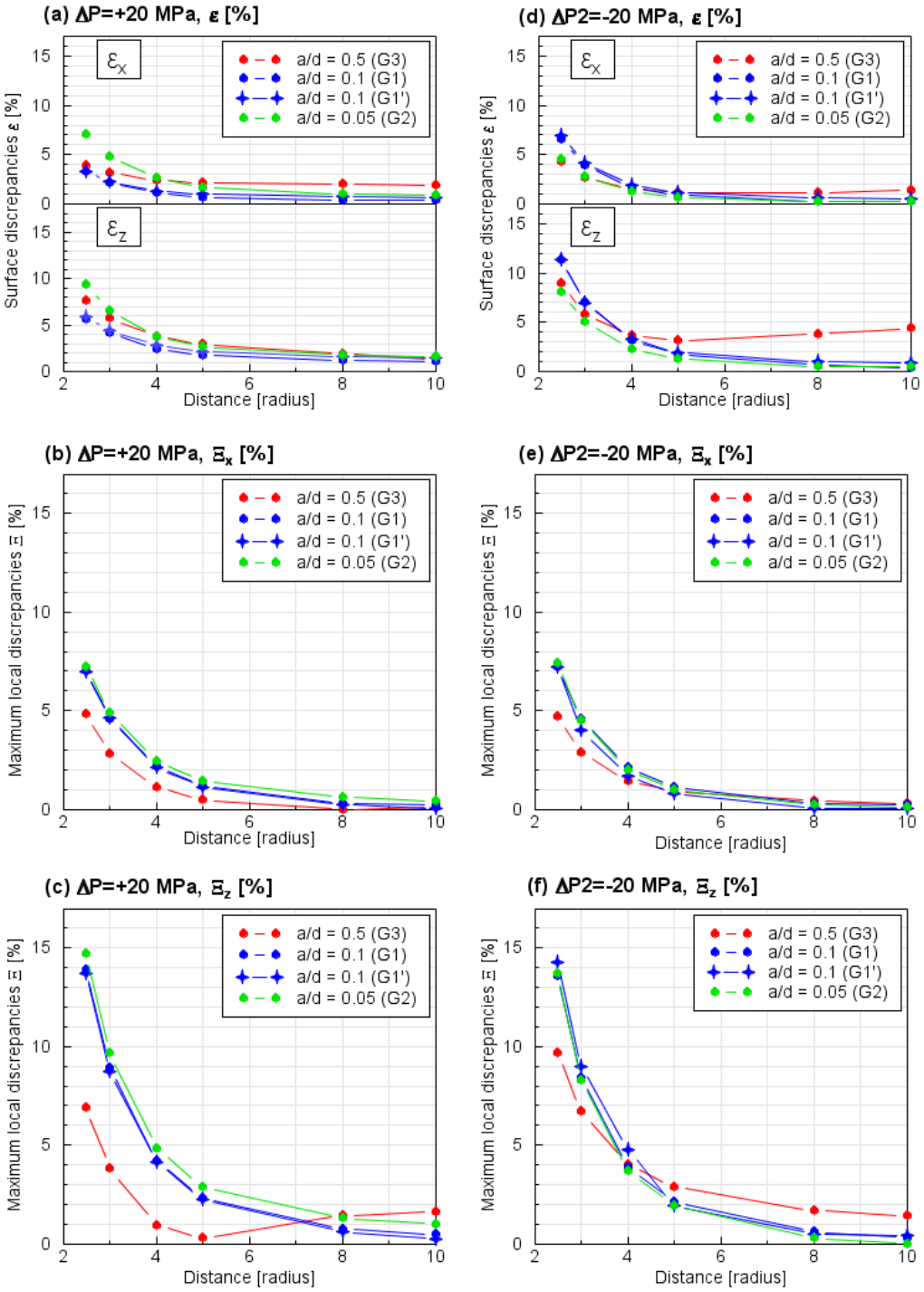

Figure 4.5: Model A: Surface (ϵ) and maximum local (Ξ) discrepancies *vs* source separation obtained for models combining two superposed spherical sources. The shallower source is pressurized by $\Delta P_1 = +20$ MPa and the deeper source is either pressurized by $\Delta P_2 = +20$ MPa (*left column: a, b, c*) or under-pressurized by $\Delta P_2 = -20$ MPa (*right column: d, e, f*). Corresponding discrepancies values are listed in Table A-1.

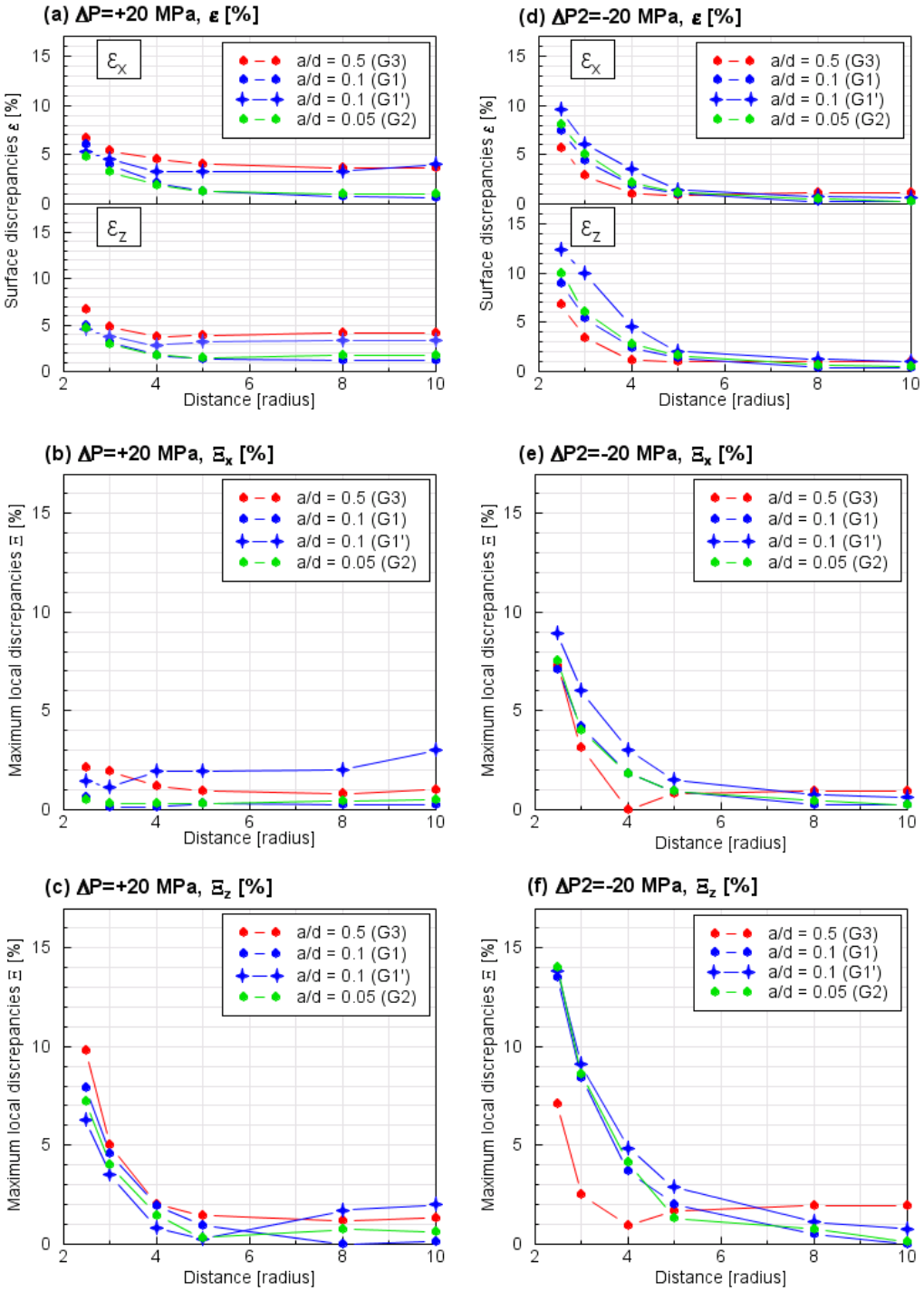

Figure 4.6: Model B: Surface (ϵ) and maximum local (Ξ) discrepancies *vs* source separation obtained for models combining two juxtaposed spherical sources, one of them being pressurized by $\Delta P_1 = +20$ MPa and the other one being either pressurized by $\Delta P_2 = +20$ MPa (*left column: a, b, c*) or pressurized by $\Delta P_2 = -20$ MPa (*right column: d, e, f*). Corresponding discrepancies values are listed in Table A-2.

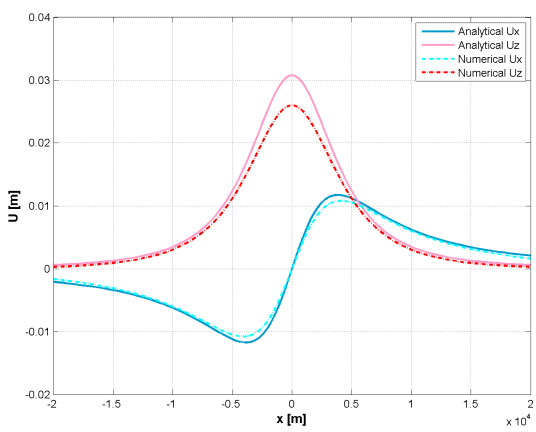

(a) Model A, $\Delta P2 = +20$ MPa, Distance 2.5 radii (G1'a)

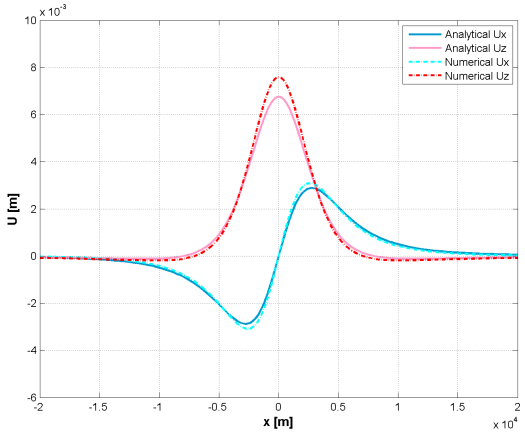

(b) Model A, $\Delta P2 = -20$ MPa, Distance 2.5 radii (G1'a)

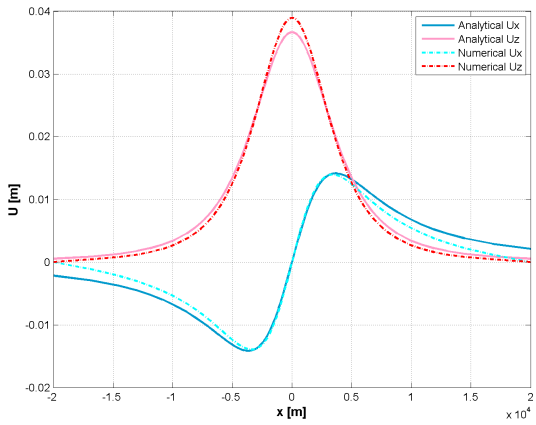

(c) Model B, $\Delta P2 = +20$ MPa, Distance 2.5 radii (G1'a)

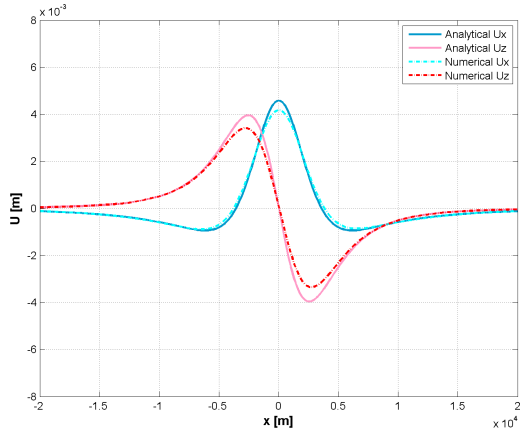

(d) Model B, $\Delta P2 = -20$ MPa, Distance 2.5 radii (G1'a)

Figure 4.7: Models A-B (Group G1'a): Surface displacements across the centre of the deformation sources for models with two superposed (Model A) or two juxtaposed sources (Model B) separated by a distance of 2.5 radii. The lower of right-hand source (Source 2) pressurization is either $\Delta P2 = 20$ MPa (*left column: a,c*) or $\Delta P2 = -20$ MPa (*right column: b, d*). The profiles for further source separation are presented in Figures A-2 & A-3.

Model DI, Methods 1-3: juxtaposed tensile rectangular and spherical sources

The discrepancies computed for Model DI strongly depend on the approach employed to model the opening dike (Figure 3.5). The results of the three approaches (Methods 1-3) are compared in Figure 4.8, in Figure A-1, and in Figure 4.9 (see also Table A-4). The conditions applied on the dike boundaries (displacements or pressure) are directly related to the way the sources can deform and influence each other (Figure 4.10).

Using Method 1, a fixed displacement prescribed on both dike walls immobilizes the dike, prevents further deformation, though the spherical source deforms. Method 1 gives analytical and numerical surface displacements that differ radically in the dike opening direction (the x direction for the models considered). Consequently, the discrepancies (ϵ and Ξ) in this direction are two orders of magnitude larger than in the other directions (see Table A-4 in Appendix). When the spherical source inflates, ϵ_x and Ξ_x reach 97% and 82% (Appendix, Figure A-1). They even reach 550% and 300%, respectively, when the spherical source deflates (Figure 4.8). The remaining discrepancies in vertical (ϵ_z) and strike (ϵ_y) directions are**,** however**,** of the same order of magnitude as those computed for Models A and B: ϵ_z and Ξ_z are up to 13% and 15% for an inflating sphere and up to 23% and 5% for a deflating source. All discrepancies become negligible beyond 9 radii separation.

In contrast to Method 1, when using Methods 2 and 3 (displacement of a flexible dike wall with constant opening, or pressurized tabular crack) all discrepancies are of comparable magnitude to models A & B. With these two methods (2 & 3), both the dike and the spherical source can deform (Figure 4.10). This is reflected in the magnitude of the surface discrepancies: while ϵ_y is on average lower than both ϵ_x and ϵ_z for a rigid dike (Method 1), all components of the surface discrepancies are within 2% for source separation of 3 radii and beyond. For both methods, neglecting the source interaction leads to significant discrepancies up to a horizontal distance of 5 km (U_x) and 3 km (U_z), with an underestimation of U_z and overall a slight overestimation of U_x (Figure 4.9).

With Method 2, the dike is simply 'pushed' away from or 'pulled' towards the inflating or deflating sphere, which in turn deforms in response to the dike opening, constant over the dike plane.

The discrepancies computed with Method 2, which is the closest to an Okada rectangular tensile dislocation, are on average the lowest calculated between the 3 methods,

and are significant only up to 2 radii source separation (Figure 4.8, and also Figure A-1). Regarding the surface discrepancies, ϵ_x is still larger than ϵ_z, with 7% *vs* 6% and 24% *vs* 7% for inflating and deflating sphere, respectively. However Ξ_x and Ξ_z are similar, with maximum values for Ξ_x and Ξ_z of 6% and 7%, respectively, for an inflating sphere, and 9% and 7% for a deflating source.

A pressurized tabular crack, Method 3, does not open uniformly as the Okada analytical model or Methods 1 or 2, but deformation of the dike walls results in a bulging shape (Figure 3.5). In the presence of an additional inflating or deflating source, the resulting shape will be more complex (Figure 4.10). The discrepancies are overall intermediate to those calculated with the two other methods and become negligible beyond 3 radii separation (Figure 4.8). This is the most realistic model for a pressurised dike.

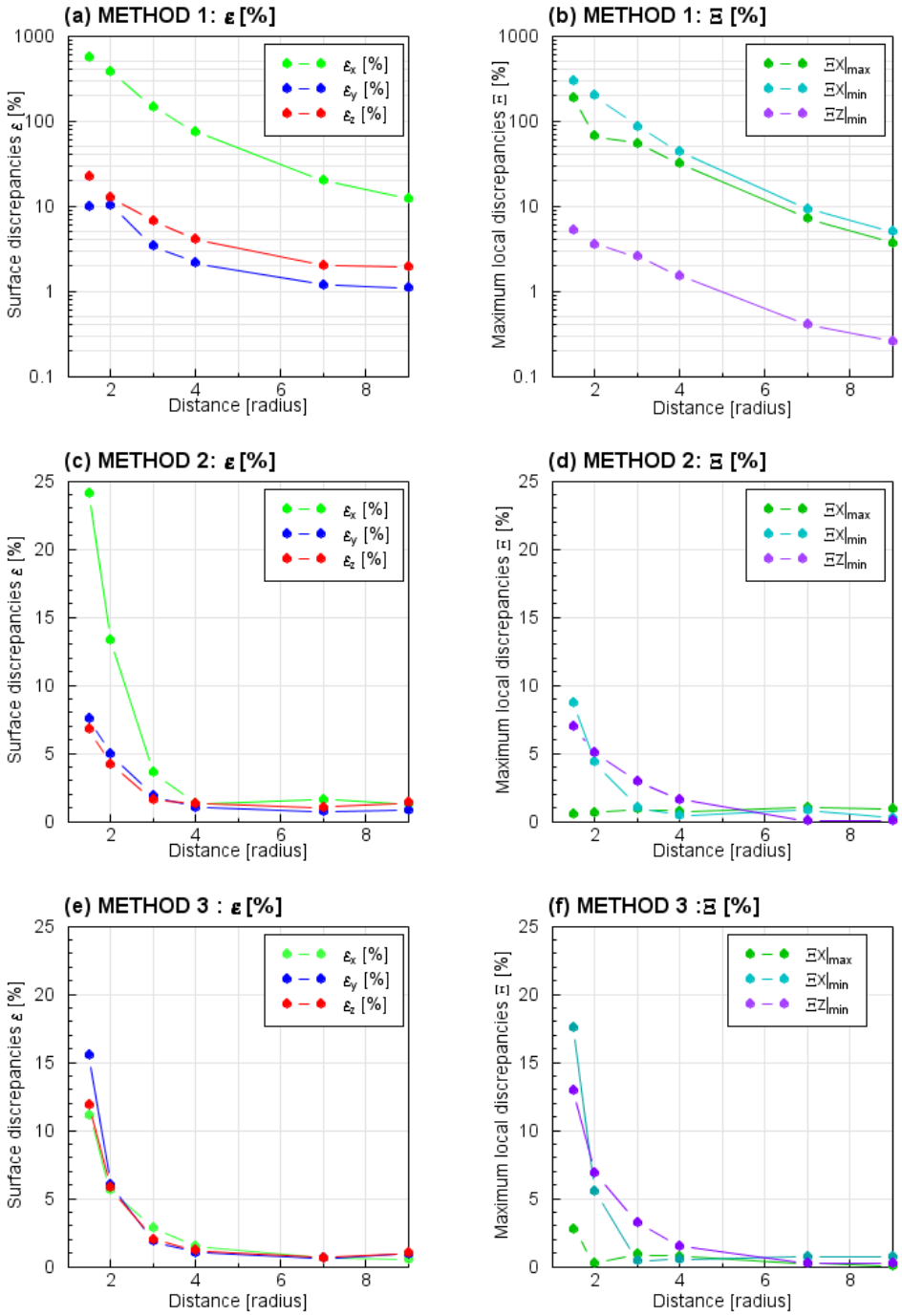

Figure 4.8: Model DI: Surface (ϵ) and maximum local (Ξ) discrepancies *vs* source separation obtained for models combining a spherical source pressurized by $\Delta P = -20$ MPa juxtaposed to a dike opening by 1 m, modelled with Methods 1-3 (*from top to bottom*). Corresponding discrepancies values are listed in Table A-4.

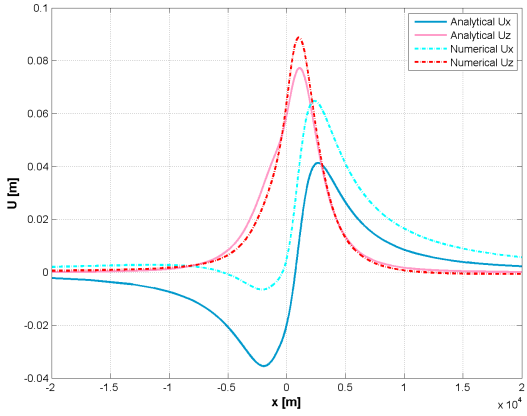

(a) Method 1, Distance 1.5 radii, $\Delta P = +20$ MPa

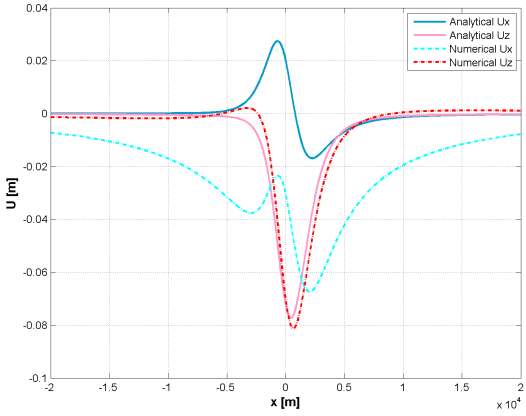

(b) Method 1, Distance 1.5 radii, $\Delta P = -20$ MPa

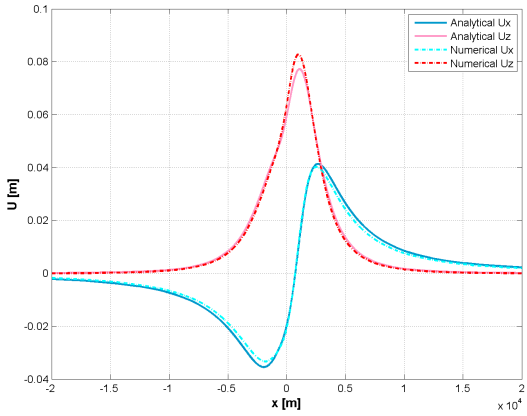

(c) Method 2, Distance 1.5 radii, $\Delta P = +20$ MPa

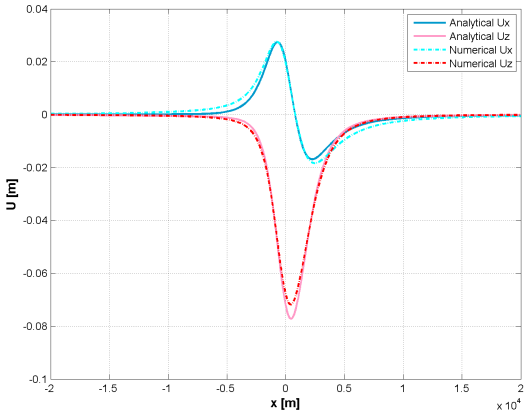

(d) Method 2, Distance 1.5 radii, $\Delta P = -20$ MPa

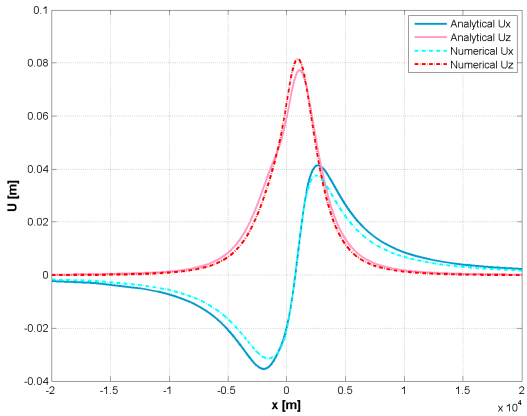

(e) Method 3, Distance 1.5 radii, $\Delta P = +20$ MPa

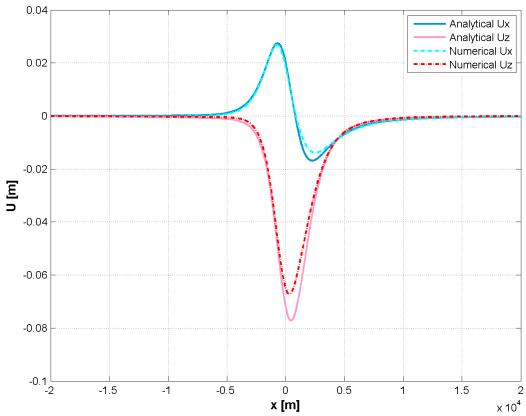

(f) Method 3, Distance 1.5 radii, $\Delta P = -20$ MPa

Figure 4.9: Model DIa: Surface displacements across the centre of the deformation sources for models of a dike opening by 1 m, modelled by Methods 1-3, juxtaposed to a spherical source pressurized by either $\Delta P2 = +20$ MPa (*left column: a, c, e*) or $\Delta P2 = -20$ MPa (*right column: b, d, f*). The sources are separated by a distance of 1.5 radii. The profiles for further source separation are presented in Figure A-4, Figures A-5 & A-6.

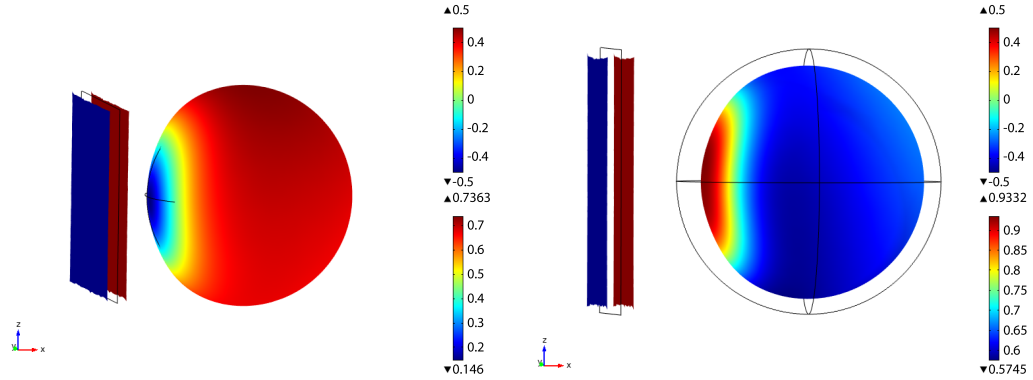

(a) Method 1 ($\Delta P = 20$ MPa)

(b) Method 1 ($\Delta P = -20$ MPa)

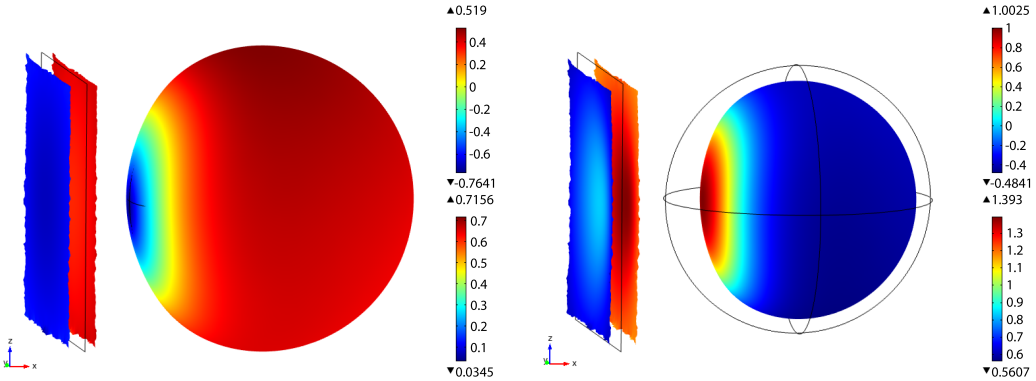

(c) Method 2 ($\Delta P = 20$ MPa)

(d) Method 2 ($\Delta P = -20$ MPa)

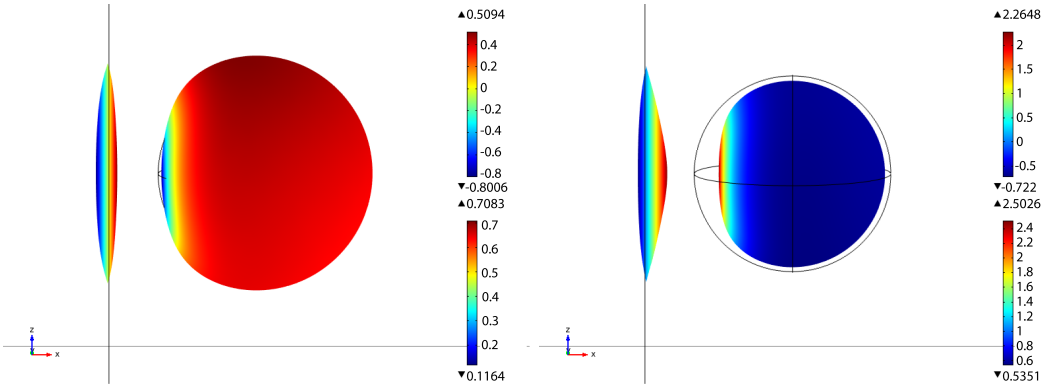

(e) Method 3 ($\Delta P = 20$ MPa)

(f) Method 3 ($\Delta P = -20$ MPa)

Figure 4.10: Models DI: 3D perspective of the displacement vector magnitude [m] on the walls of a dike opening by 1 m, modelled with Methods 1-3, juxtaposed to an inflating, $\Delta P = +20$ MPa (left), or a deflating, $\Delta P = -20$ MPa, spherical source (*right*), in an homogeneous medium. The distance between sources is 1.5 radii (Group DIa). The upper scale corresponds to the horizontal displacement of the dike walls, to emphasize how Methods 1-3 differ. The lower scale corresponds to the total deformation of the spherical source. The source deformation is magnified by a factor of 100. Note that, with Method 1 (*upper panel: a, b*), the dike opening is constant as imposed by the boundary conditions and only the spherical source is deforming.

4.2.2 Effect of the radius/depth ratio

In Models A and B, the effect of the distance between sources and free surface has also been tested with various (upper source) radius/depth ratios (a/d) and was found to generally have little influence on the magnitude of the discrepancies: the surface discrepancies computed for a/d =0.1 and 0.05 are all within 5%, and Ξ_x and Ξ_z differ less than 2%. For Model A, most of the discrepancies calculated for the two groups with same radius-to-depth ratio $a/d = 0.1$ (Models A-G1a and G1'a, Figures 4.5 & 4.6) differ by less than 1%. Overall, independent of the a/d ratio, the discrepancies always follow the same trend and are all negligible beyond 4 radii separation.

4.2.3 Effect of source strength and geometry (Models A + Models DI)

The results listed in Table 4.4 underline the fact that the discrepancies vary with the pressure difference or displacements applied to the spherical or dislocation source walls. For the three models A, B and DI, I found that the discrepancies are in general larger if one of the sources is deflating.

Table 4.4 also highlights how far the discrepancies depend on the geometry. Discrepancies are higher for Model DI than for Models A and B, although they decrease more rapidly and are only significant ($> 5\%$) for source separation of less than 3 radii for model DI (Methods 2 and 3), and 4 radii for Model A.

The various pressure differences tested in Model A indicate that the discrepancies are identical for all multiples of the chosen $\Delta P1/\Delta P2$ ratio. The magnitude of discrepancies increases with the magnitude of the deeper source pressurization ($\Delta P2$) for a constant pressurization of the upper source ($\Delta P1$).

The various openings or pressures applied on the dike wall in Model DI (Methods 2 and 3) also show that the closest results to the analytical solution are generally given when the dike is modelled with Method 2, with the exception of the surface discrepancies ϵ_x, which is closer to the analytical solution when modelled with Method 3.

4.3 Case studies

4.3.1 Models scenarios

In the following section, I apply our methodology to three examples (referred as Models CS1-3) where analytical models were combined. In line with Section 4.1.1, I construct FE models with geometries and physical parameters equivalent to the analytical models presented in these case studies, which are depicted in Figure 4.11, and their parameters are summarized in Table 4.5. I then calculate the discrepancies between FE and analytical models to estimate the effect of neglecting the source interactions.

I have adapted these cases from Elsworth et al. (2008) and Linde et al. (2010) who employed analytical models to represent the volcanic plumbing system of Soufrière Hill volcano, Montserrat, West Indies, for the first episode of unrest (15 Nov. 1995-10 March 1998) and an explosion during March 2004, respectively. In the third case study, Wright et al. (2006) modelled the magmatic system of the Dabbahu segment, Afar, Ethiopia, for the rifting episode that occurred between 14 Sept.-4 Oct. 2005.

Model CS1, representing Soufrière Hills Volcano (SHV), consists of 2 superposed spherical magma chambers, and corresponds to our Model A with two superposed Mogi sources, separated by 6 source radii and with a ratio of source radius to depth of 0.17 (upper source). In Model CS2, the SHV magmatic system composed of a dike (Okada source) superposed to a spherical pressure source (Mogi source).This model corresponds to our Model C, with a distance between the magma chamber centre and the bottom of the dike of 1.4 times the magma chamber radius. In Model CS3, I focus on the northern section of the Dabbahu-Gab'ho segment (Wright et al., 2006; Ayele et al., 2009), where two deflating magma chambers are located on either side of the dike. Compared to their original models, I focus merely on an opening dike without shear components. This scenario corresponds to our Model DI, where the dike has been modelled with Method 2 (see Section 4.1.1).

4.3.2 Results

The discrepancies computed for CS1-3, listed in Table 4.5, are in good agreement with our previous results. In Model CS2, as in Model C, both surface (ϵ) and maximum discrepancies (Ξ) are negligible ($< 5\%$). Models CS1 and CS3 have a set of geometrical

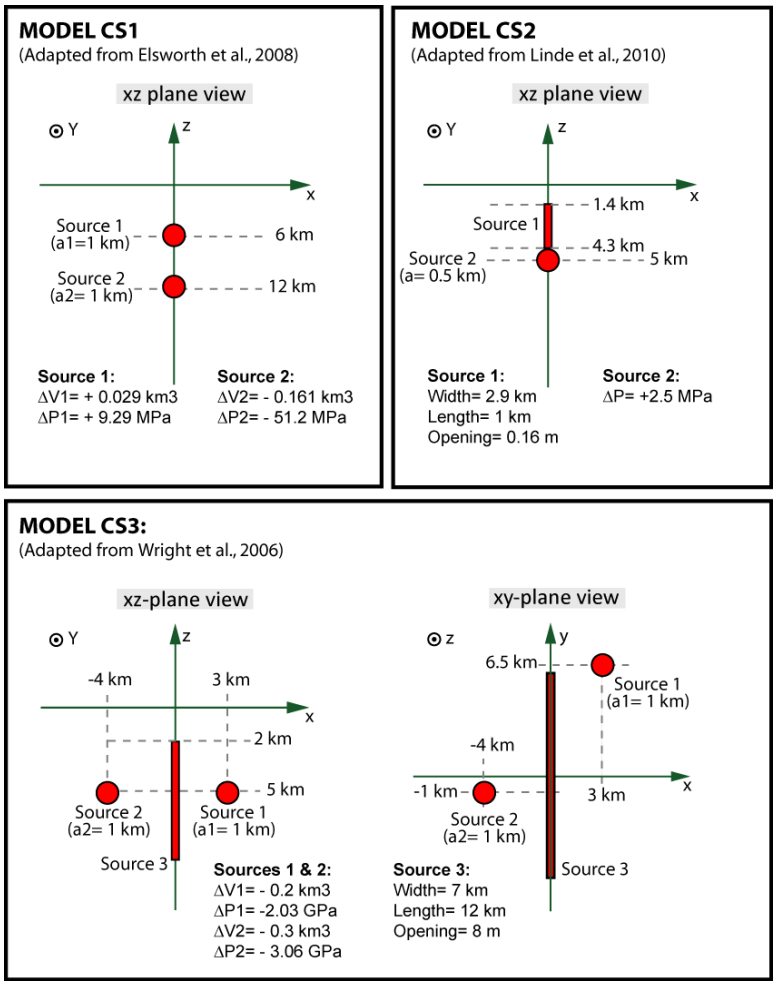

Figure 4.11: Case studies CS1-3. CS1 and CS2, corresponding to our Models A and C respectively, are adapted from Elsworth et al. (2008) and Linde et al. (2010) analytical models of the plumbing system of Soufrière Hills Volcano, Montserrat, West Indies. CS3, corresponding to our Model DI, is adapted from the Dabbahu segment, Afar, Ethiopia magmatic system as described by Wright et al. (2006). Geometry and physical parameters are listed in Table 4.5.

and physical parameters more complex than Models A and D1, henceforth producing a different, more intricate, deformation pattern (see *e.g.* Figure 4.12a). However, as expected from Model A and DI, the discrepancies of Model CS1 are weaker than those of Model CS3. In Model CS1, analytical and FEM solutions fit closely, with the exception of the near-field vertical displacements. Henceforth, the surface and horizontal ($\Xi_x\Big|_{\min}$ and $\Xi_x\Big|_{\max}$) discrepancies of Model CS1 are insignificant, but $\Xi_z\Big|_{\max}$ are significant and reach 18.5%. In Model CS3, horizontal and vertical surface discrepancies are up to 20%, and reflect how the analytical and FEM solutions differ by 10-15% over a 10 km^2 area encompassing the three sources, with maxima of 25% for U_z and U_x above or slightly offset of the spherical sources, respectively (Figure 4.11).

		Model CS1	Model CS2	Model CS3
Mogi source 1	Centre position [km]	(0,0,-6)	(0,0,-5)	(3,6.5,-5)
	radius [km]	1	0.5	1
	$\Delta P1$	9.29 MPa	-2.5 MPa	-2.03 GPa
	$\Delta V1$ $[km^3]$	0.03		-0.2
Mogi source 2	Centre position [km]	(0,0,-12)	n/a	(-4,-1,-5)
	radius [km]	1	n/a	1
	$\Delta P2$	51.25 MPa	n/a	-3.06 GPa
	$\Delta V2$ $[km^3]$	-0.16		-0.3
Okada source	Centre position [km]	n/a	(0,0,-2.85)	(0,0,-5.5)
	width × height [km]	n/a	2.9×1	12×7
	Opening [m]	n/a	0.16	8
Source separation [radii]		6	1.4	Mogi1-Ok.: 4 Mogi2-Ok.:: 3
Crustal properties	E [GPa]	2.5	10	80
	ν	0.25	0.25	0.25
Discrepancies [%]	ϵ_x	3.3	0.9	20.7
	ϵ_y	3.2	0.6	17.50
	ϵ_z	3.2	1.9	20.8
	$\Xi_x\|_{\min}$	0.1	2.2	2.4
	$\Xi_x\|_{\max}$	0.0	0.6	10.3
	$\Xi_z\|_{\min}$	2.4	1.0	13.7
	$\Xi_z\|_{\max}$	18.5	1.8	16.0

Table 4.5: Geometry, physical parameters and discrepancies obtained for Models CS1-3 (Figure 4.11 and Figure 4.12). Parameters are adapted from Elsworth et al. (2008), Linde et al. (2010) and Wright et al. (2006) for the volcanic plumbing system of Soufrière Hills Volcano, Montserrat, West Indies and from Wright et al. (2006) for the magmatic system of the Dabbahu-Gab'ho segment, Afar, Ethiopia. Overpressures are either given in the referenced works or, where indicated, derived from the source volume change (Delaney and McTigue, 1994). In CS3, I chose a common value of 1 km for the magma chambers radius, otherwise unknown. The Young's modulus of 80 GPa is taken from Hamling et al. (2010). In the FE model, dikes are modelled with Method 2, described in Section 3.3.1.

Model CS3			
Source 1 & 2 radii		0.5 km	1 km
Mogi source 2	$\Delta P1[GPa]$	-16.03	-2.03
	$\Delta V1\ [km^3]$	-0.2	-0.2
Mogi source 2	$\Delta P2[GPa]$	-24.50	-3.06
	$\Delta V2\ [km^3]$	-0.3	-0.3
Source distance (wall-to-wall [km])		Mogi1-Ok.: 2.5 Mogi2-Ok.: 3.5	Mogi1-Ok.: 2 Mogi2-Ok.: 3
Discrepancies [%]	ϵ_x	15.8	20.7
	ϵ_y	14.4	17.5
	ϵ_z	7.6	20.8
	$\Xi_x\|_{\min}$	3.4	2.4
	$\Xi_x\|_{\max}$	3.7	10.3
	$\Xi_z\|_{\min}$	4.6	13.7
	$\Xi_z\|_{\max}$	5.8	16.0

Table 4.6: Models CS3: discrepancies variations depending on the assumed radius of the magma chamber. The discrepancies calculated previously for magma chambers with a radius $a = 1$ km (Figure 4.11 and Figure 4.12) are compared with the discrepancies computed when the radius is decreased to $a = 0.5$ km. The models parameters, other than source radius and dependable variables, are identical to those listed for model CS3 in Table 4.5.

For both models CS1 and CS3, the significant discrepancies calculated contrast with the negligible discrepancies calculated for Models A and DI with similar source separations. This is particularly due to the 8 m opening of the dike in CS3, against only 1 m in DI, and to the high overpressures applied on most of the magma chambers walls in the two case studies, overpressures possibly too high for the deformation to remain elastic. In Model CS3, I chose a magma chamber radius of 1 km, as commonly observed (Marsh, 1989) and calculated the overpressure from the volume change given in Wright et al. (2006), and from the relation between radius, pressure and volume changes given in Delaney and McTigue (1994), where pressure and radius are inversely proportional. As shown in Table 4.6, increasing the magma chamber radii would induce a trade-off between decreasing the source interaction by decreasing the overpressure applied, and increasing the source interaction as the sources would grow closer.

4.4 Summary

In this chapter, I have quantified the effect of neglecting the interaction between sources in models combining several Mogi and Okada sources. It is difficult to deduce a general

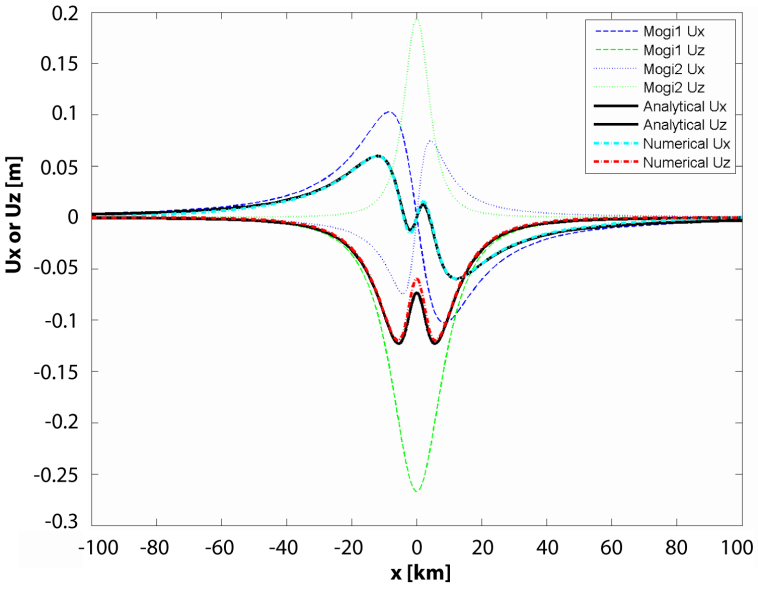

(a) Model CS1: Displacements profiles (m)

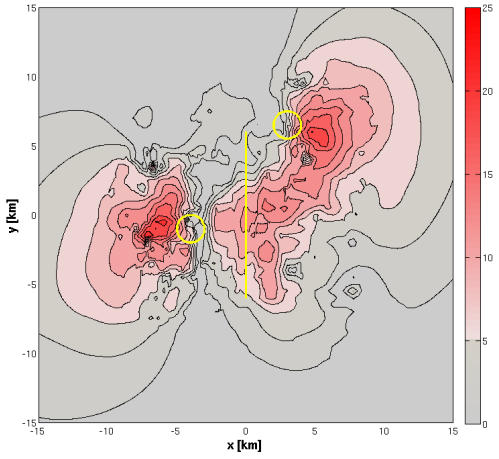

(b) Model CS3: discrepancies in U_x (%)

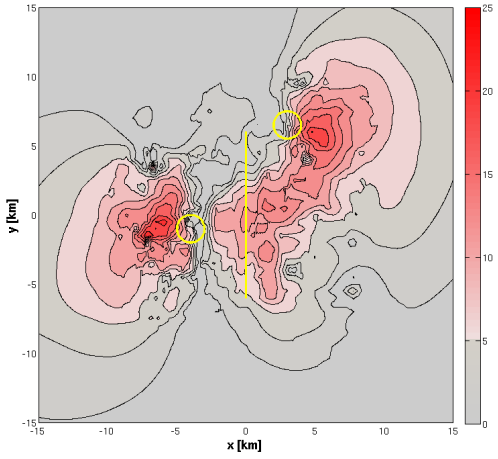

(c) Model CS3: discrepancies in U_z (%)

Figure 4.12: Model CS1 and CS3 (adapted from Elsworth et al., 2008 and Wright et al., 2006 for SHV, Montserrat, West Indies and the Dabbahu segment, Afar, Ethiopia, respectively). *Top: Model CS1.* Profiles of the analytical and numerical solutions for the two sources individually and combined. *Bottom: Model CS3.* Contourmaps of the horizontal (**b**) and vertical (**c**) discrepancies [%] between analytical and FE solutions, normalized by $U_z^{An}\Big|_{\max} U_z^{An}\Big|_{\max}$, respectively. Projection of the source position onto the surface is indicated in yellow. Negligible discrepancies ($< 5\%$) are mapped in grey. Corresponding geometry, physical parameters and discrepancies values are listed in Table 4.5.

rule for the discrepancies between analytical and FE solutions valid for all the geometries and parameters investigated. Nevertheless, I can extract the following findings from our models:

- The discrepancies induced when aligning and superposing a Mogi and an Okada source in Models C and DII (Figure 4.1) are always negligible ($< 5\%$).
- In contrast, models with superposed or juxtaposed Mogi sources (Models A and B) and models with juxtaposed Mogi and Okada sources (Models DI) result in analytical solutions differing from the numerical solution by up to 15%, 14%, and 25%, respectively. For these three models, the discrepancies are maximal when the sources are the closest, and are significant up to a horizontal distance of 5 km. All surface and maximum discrepancies computed for Models A & B become negligible when the sources are separated by 4 radii or more (Figure 4.5 to Figure 4.8).
- For model DI, in the case where the dike opening is modelled with relative displacements of the dike walls (Method 2) or pressure difference (Method 3), all discrepancies become insignificant for a source separation of more than 3 radii. However, when applying fixed displacements (Method 1), which implies that the medium is not elastic anymore at the dike boundaries, the discrepancies are up to 300% and significant for a source separation of at least 9 radii.
- When applying our methodology to three case studies adapted from the magmatic systems of Soufrière Hills Volcano, Montserrat, West Indies (Models CS1-2) and the Dabbahu segment, Afar, Ethiopia (Model CS3), I find discrepancies that are consistent with the above results. Indeed, employing model parameters adapted from studies on these three magma systems, the discrepancies calculated are also significant in the case of models with superposed magma chambers or juxtaposed dike and magma chamber, while they are negligible when a dike is superposed to a magma chamber. Additionally, these models highlight how the source interaction and the discrepancies are related to the trade-off between overpressure and radius.

In Chapter 5, I investigate how the estimation of model parameters is affected by neglecting the source interaction when two analytical models are combined, or in other words how the neglected source interaction is mapped into model parameters to be inverted for.

Chapter 5

Mapping the neglected source interaction into model parameters

Datasets of ground deformation are often inverted for geophysical model parameters, such as magma chamber pressure and volume, as well as its location. Therefore, in this chapter, I focus on evaluating how neglecting the source interaction, *i.e.* the discrepancies, affect the retrieval of the source parameters. Concentrating on Models A and DI where discrepancies are largest, I first investigate the sensitivity of the surface and maximum discrepancies to individual variations of ΔP, dike opening, and source separation. Then, I perform analytical inversions of the synthetic FE solutions of Models A and DI, to estimate to which extent the model parameters are affected by neglecting the source interaction when two analytical models are combined.

5.1 Sensitivity analysis

5.1.1 Method

I use the numerical solutions of Model A-G1'a and Model DIa as a reference where source interaction is accounted for (see Table 5.1 for a summary of the corresponding model parameters) and I vary in the combined analytical model where source interaction is neglected either the source separation, the Mogi source pressurization $\Delta P1$ or $\Delta P2$ (Figure 5.1), or the dike opening in order to match the numerical reference model (Figures 5.2 & 5.3 for Methods 1-2, and Figure 5.4 for Method 3). This misfit is quantified by the discrepancies as defined in Section 3.1.3 (Equations 3.1 & 3.2)

and therefore quantifies the error in the determination of the model parameters due to source interaction. I plot a grid of the discrepancies ϵ and Ξ as well as the mean of ϵ, calculated for a range of each of the three parameters: source separation, pressure ΔP_1 and ΔP_2 and dike opening. Red grid points correspond to negligible discrepancies hence to a best-fit between the numerically generated dataset (reference model) and the analytical combined model. The vertical red line indicates the parameter values of the reference numerical model, which the analytical models aim to retrieve. In this way, I can quantify how the interaction of deformation sources, neglected by the analytical models, maps into distorted model parameters. By varying one model parameter at the time, I assess the sensitivity of the model solution to this model parameter. Table 5.2 give a summary of the results.

5.1.2 Results

The sensitivity analysis of Model A-G1'a (Figure 5.1) shows that the discrepancies I try to minimize are, for the range of values chosen, more sensitive to the source separation than to the overpressure in the spherical sources, particularly for the shallower source ($\Delta P1$). Compared to the reference model, the discrepancies map into incorrect model parameters where $\Delta P1$ is underestimated by $10-20\%$, $\Delta P2$ by $20-35\%$, and the source separation is overestimated by $70-100\%$. The fact that the red grid points, calculated for the various discrepancies, overlap vertically, indicates that the solution of the respective model parameter satisfies all components of the surface displacement.

The sensitivity analysis of Model DIa (dike juxtaposed to chamber) is represented in Figure 5.4 for a dike modelled with Method 3, and in Figures 5.2 & 5.3 for a dike modelled with Method 1 and 2, respectively:

1. Method 1: The high discrepancies throughout Figure 5.2 demonstrate that no analytical model was found fitting the reference numerical surface displacements. The mean surface discrepancies are systematically larger than 70%, dominated by ϵ_x larger than 100%. Taken separately, the minima for ϵ_y and ϵ_z are still between $6-25\%$, and would yield a dike opening underestimated by up to 50%, a source separation overestimated by up to 45%, but a reasonable ΔP only 5% off its actual value (Table 5.1). The large values of $\Xi\Big|_{\text{min}}$ or $\Xi\Big|_{\text{max}}$ (*e.g.* $\Xi_x\Big|_{\text{max}} > 150\%$) emphasize how strongly the analytical and numerical surface displacements differ,

and that combining a Mogi and Okada solutions can never represent a scenario where the dike is fixed in space and the magma chamber accounts for all the deformation triggered by the interacting sources, such as was modelled through Method 1.

2. Method 2: Compared to the previous method, the dike modelled with Method 2 can now be deformed remaining at a constant opening of 1 m. In this case, the results depicted in Figure 5.3 show that an inversion using the analytical models would lead to an underestimation of the dike opening by 20% and to an incorrect estimation of ΔP and source separation by up to 10%, with a minimum mean(ϵ) of 10%. For the parameter range given, the spread of the smaller discrepancies points out that the model is more sensitive to the dike opening than to ΔP, but even more to the source separation.

3. Method 3: When the numerical model is realized by a tabular crack (Method 3), the volume change of the numerical pressurized crack is equivalent to the volume change of an Okada source of same dimensions and opening by 1 m. An inversion using the analytical models points to a source pressurization and a dike opening within 10% and 20% of their actual value, respectively, and a source separation overestimated by up to 25% (Figure 5.4). The minimum mean(ϵ) and ϵ are approximately equal to 7%. As for Method 2, the various discrepancies computed for Method 3 indicate that the model solution is more sensitive to a variation in dike opening and ΔP, but less sensitive to a change in source separation.

		Model A-G1'a	Model DIa		
			M1	M2	M3
Mogi source 1	Centre position [km]	(0,0,-5)	(0.75,0,-2.5)		
	radius [km]	0.5	0.5		
	$\Delta P1$ [MPa]	20	-20		
Mogi source 2	Centre position [km]	(0,0,-6.25)	n/a		
	radius [km]	0.5	n/a		
	$\Delta P2$ [MPa]	20	n/a		
Okada source	Centre position [km]	n/a	(0,0,-2.5)		
	width × height [km]	n/a	1×1		
	Opening [m]	n/a	1	1	n/a
	ΔP [MPa]	n/a	n/a	n/a	12
Source separation [radii]		2.5	1.5		
Discrepancies [%]	ϵ_x	11.6	553.7	24.1	11.1
	ϵ_y	11.4	9.8	7.6	15.5
	ϵ_z	14.1	22.5	6.8	11.9
	$\Xi_x\big\|_{\min}$	8.1	298.8	8.7	17.6
	$\Xi_x\big\|_{\max}$		185.1	0.5	2.7
	$\Xi_z\big\|_{\min}$	15.5	5.3	7.0	12.9
	$\Xi_z\big\|_{\max}$		n/a	n/a	n/a

Table 5.1: Summary of parameters and discrepancies for Models A-G1'a and DIa (Methods M1-3) used as references in the sensitivity analysis tests (Table 5.2, Figures 5.1-5.4). The results of the corresponding Monte-Carlo inversions are listed in Table 5.3. The domain elastic parameters are $E = 10$ GPa and $\nu = 0.25$.

		Model A-G1'a	Model DIa		
			Method 1	Method 2	Method 3
Mogi source 1	$\Delta P1$ [MPa]	16-18	(-21)-(-19)	(-21)-(-18)	(-22)-(-18)
	misfit to ref. model [MPa]	(-2)-(-4)	up to ± 1	(-1)-(+2)	up to ± 2
	misfit to ref. model [%]	(-10)-(-20)	up to ± 5	(-5)-(+10)	up to ± 10
Mogi source 2	$\Delta P2$ [MPa]	13-16	n/a	n/a	n/a
	misfit to ref. model [MPa]	(-4)-(-7)	n/a	n/a	n/a
	misfit to ref. model [%]	(-20)-(-35)	n/a	n/a	n/a
Okada source	Opening [m]	n/a	0.5-1	0.8	0.8-1.2
	misfit to ref. model [m]	n/a	0-(-0.5)	(-0.2)	up to ± 0.2
	misfit to ref. model [%]	n/a	0-(-50)	(-20)	up to ± 20
Source separation [radii]		4.2-5.1	1.5-2.2	1.5-1.6	1.3-1.9
Misfit to reference model [radii]		(+1.7)-(+2.6)	$\leq +0.7$	$\leq +0.1$	(+0.1)-(+0.4)
Misfit to reference model [%]		(+20)-(+30)	$\leq +45$	$\leq +7$	(+7)-(+27)
Discrepancies [%]	mean(ϵ)		≥ 150	$\leq 5-10$	$10-20$
	ϵ_x	< 5	≥ 150	$6-40$	$6-15$
	ϵ_y	$\lesssim 5$	$6-10$	$\leq 5-10$	$15-20$
	ϵ_z	$\lesssim 5$	$20-25$	$\leq 5-10$	$\leq 5-15$
	$\Xi_x\|_{\min}$	< 5	≥ 150	$\leq 5-30$	$\leq 5-10$
	$\Xi_x\|_{\max}$	< 5	≥ 150	$\leq 5-8$	$\leq 5-6$
	$\Xi_z\|_{\min}$	< 5 n/a	$\leq 5-10$	$\leq 5-10$	$\leq 5-15$
	$\Xi_z\|_{\max}$	< 5	n/a	n/a	n/a

Table 5.2: Summary of source parameters estimated from minimum discrepancies for Model A-G1'a and for Model DIa, Methods 1-3. In the former case, the estimations are based on Figure 5.1, while in the latter case they are based on Figures 5.2, 5.3 and 5.4, respectively. The source parameters range are primarily estimated looking at the minimum mean(ϵ) value, secondly at the minimum of all surface (ϵ) and maximum local (Ξ) discrepancies, simultaneously.

To summarize, when modelling a magmatic system composed of two Mogi sources, neglecting the source interaction ultimately leads to a significant underestimation of pressurization and an overestimation of the source separation by a factor of ≈2 if the original sources are as close as 2.5 radii.

When modelling a magmatic system composed of a dike juxtaposed to a magma chamber (Model DI), the discrepancies are enormous when Method 1 is employed, $\geq 150\%$ in x-axis direction, *i.e.* in the dike of the dike opening and alignment of the sources. This is due to the fact that the dike is fixed in space and the 'interaction' between the two sources results in the deformation of the spherical source only, while the dike acts as a rigid, pinned, barrier. When comparing the reference numerical model using Method 2 or 3, the discrepancies are much smaller and tend to be more sensitive to a variation in dike opening and ΔP, but less sensitive to source separation. When using Method 2, neglecting the source interaction is likely to lead to an underestimation of the dike opening by up to 20% and to give a comparatively better estimate of the source pressurization and the distance between sources. With Method 3, the discrepancies calculated for each parameter range indicate stronger dissimilarities between the numerical and analytical solutions than with Method 2. Given that Method 3 is the closest to a realistic, pressurized dike, the discrepancies between Method 3 and analytical solutions provide a measure of the error made when a real dike is modelled with a constant-opening dislocation.

5.2 Inversions

5.2.1 Method

While the 'grids' in Figures 5.1-5.4 give some valuable insight into how each of the deformation components contributes to the estimation of a model parameter such as ΔP, source separation and dike opening, a common inversion scheme will seek to minimize the misfit between input data and analytical model prediction in all data components simultaneously. Therefore, I take the scenarios of Model A-G1' & DIa and use their respective FE surface displacements as input data for the parameter inversion based on the solution of Mogi and Okada. In other words, I assume that the FE solutions represent the displacement fields for real cases where magma sources close to each other interact, and estimate how strongly this interaction affects the joint

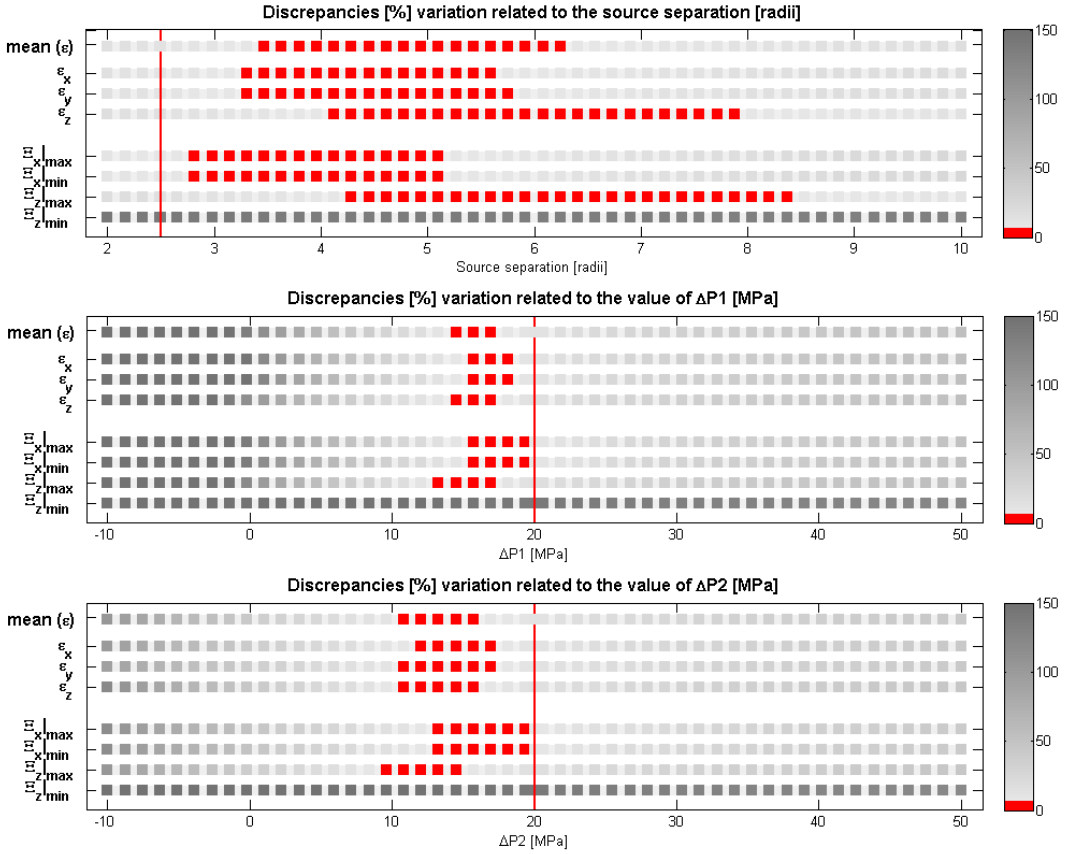

Figure 5.1: Sensitivity analysis for a model with two superposed Mogi sources of radii a =500 m and upper source radius-over-depth ratio a/d =0.1 (Model A-G1'a). The numerical solution is taken as reference and in the analytical model I vary either the source separation, $\Delta P1$, or $\Delta P2$ (*from top to bottom panel*). The red lines indicate the position of the reference model parameters (here A-G1'a). Reading each panel horizontally, the colour code refers to the value of the surface discrepancies (ϵ), their mean, and of the discrepancies at the extrema (Ξ). Values in red are discrepancies below 5% and indicate a good fit between the analytical and reference models. Reading the panels vertically gives an estimate of each discrepancy component for a give model parameter, indicating their respective sensitivity. Note that $\Xi_x\Big|_{\min} = \Xi_x\Big|_{\max}$ due to symmetry. Additionnally, the FEM $U_z\Big|_{\min}$ tend to zero hence $\Xi_z\Big|_{\min}$ results will not be taken into account. The parameter ranges showing the best-fit to the numerical model are listed in Table 5.2.

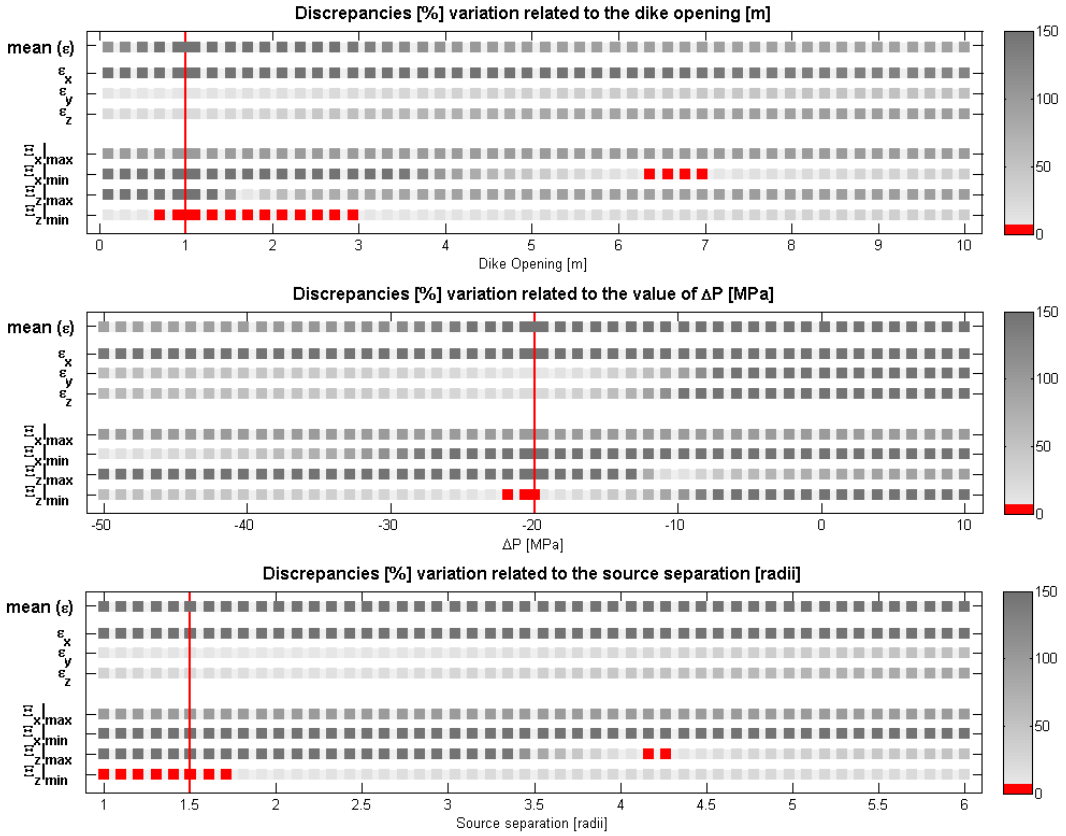

Figure 5.2: Sensitivity analysis for a model of a dike opening by 1 m, modelled with Method 1, juxtaposed to a deflating spherical source ($\Delta P = -20$ MPa). The sources are separated by a distance of 1.5 radii (Model DI -M1a). The numerical solution is taken as reference and in the analytical model I vary either the source separation, $\Delta P1$, or $\Delta P2$ (*from top to bottom panel*). The red lines indicate the position of the reference model parameters (here A-G1'a). Reading each panel horizontally, the colour code refers to the value of the surface discrepancies (ϵ), their mean, and of the discrepancies at the extrema (Ξ). Values in red are discrepancies below 5% and indicate a good fit between the analytical and reference models. Reading the panels vertically gives an estimate of each discrepancy component for a give model parameter, indicating their respective sensitivity. In this model the FEM $U_x\Big|_{\max}$ tend to zero hence $\Xi_x\Big|_{\max}$ results will not be taken into account. The parameter ranges showing the best-fit to the numerical model are listed in Table 5.2.

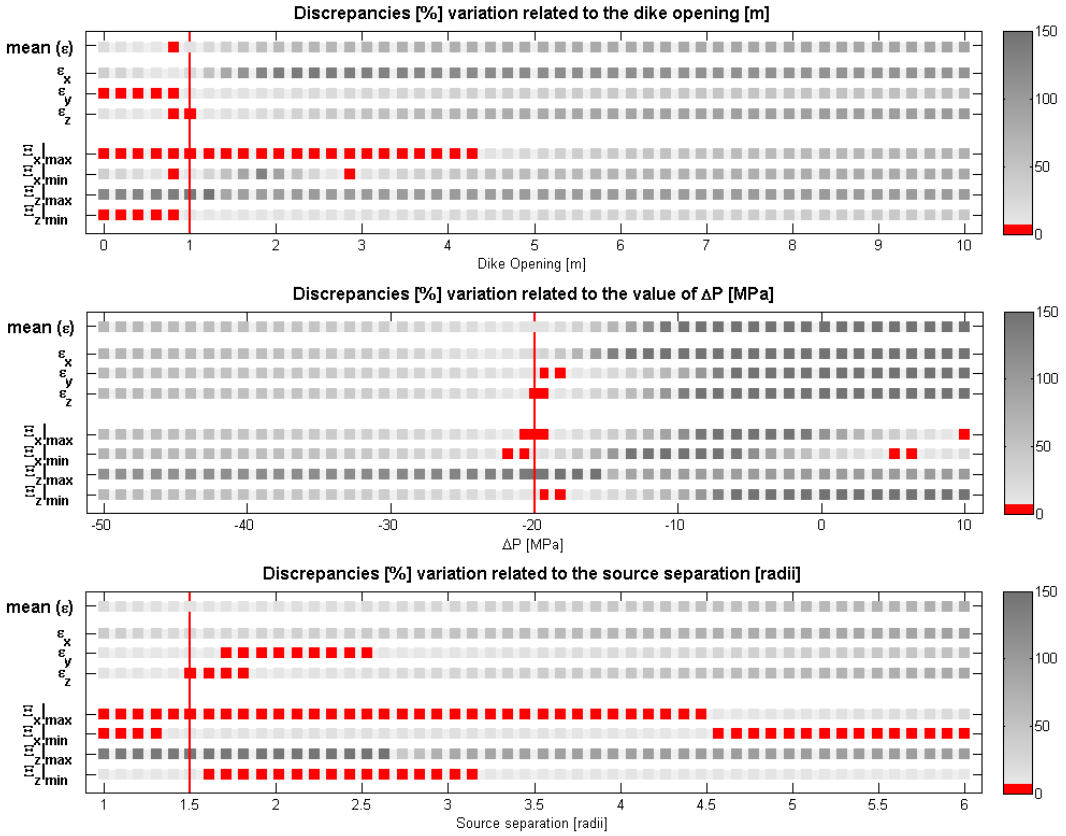

Figure 5.3: Sensitivity analysis for a model of a dike opening by 1 m, modelled with Method 2, juxtaposed to a deflating spherical source ($\Delta P = -20$ MPa). The sources are separated by a distance of 1.5 radii (Model DI-M2a). The numerical solution is taken as reference and in the analytical model I vary either the source separation, $\Delta P1$, or $\Delta P2$ (*from top to bottom panel*). The red lines indicate the position of the reference model parameters (here A-G1'a). Reading each panel horizontally, the colour code refers to the value of the surface discrepancies (ϵ), their mean, and of the discrepancies at the extrema (Ξ). Values in red are discrepancies below 5% and indicate a good fit between the analytical and reference models. Reading the panels vertically gives an estimate of each discrepancy component for a give model parameter, indicating their respective sensitivity. In this model the FEM $U_x\big|_{\max}$ tend to zero hence $\Xi_x\big|_{\max}$ results will not be taken into account. The parameter ranges showing the best-fit to the numerical model are listed in Table 5.2.

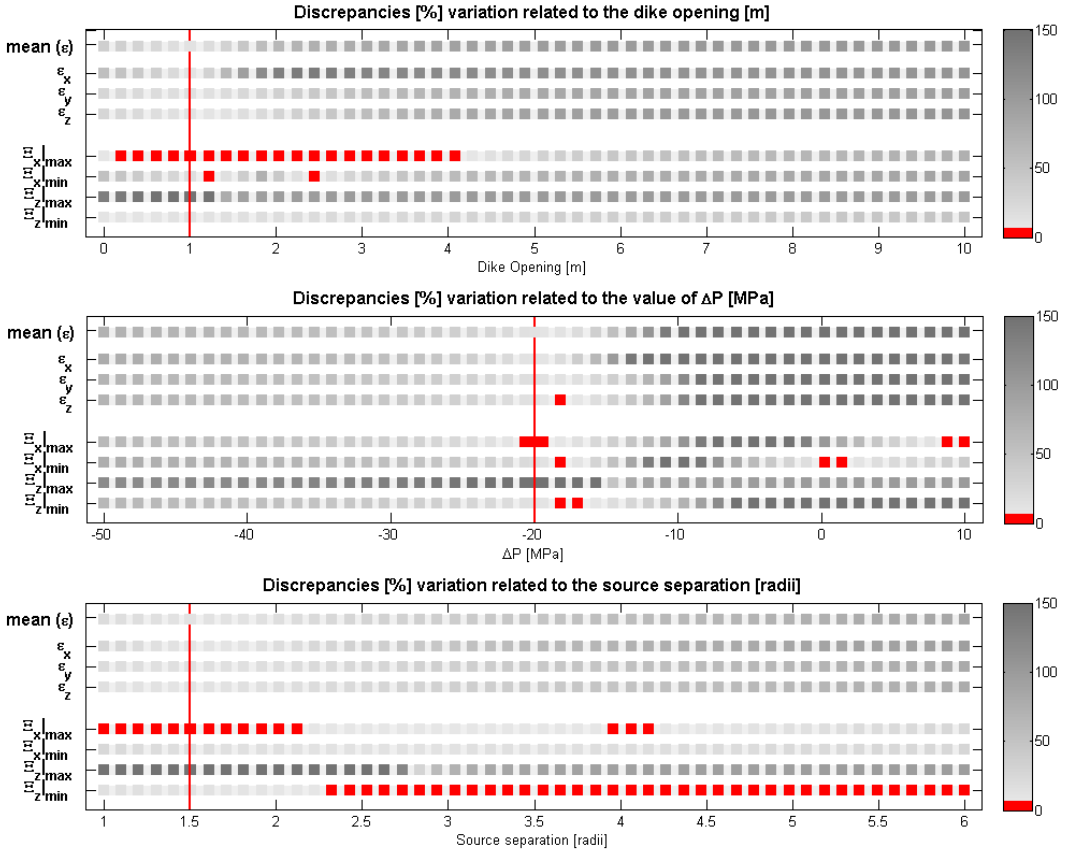

Figure 5.4: Sensitivity analysis for a model of a dike opening by 1 m, modelled with Method 3, juxtaposed to a deflating spherical source ($\Delta P = -20$ MPa). The sources are separated by a distance of 1.5 radii (Model DI-M3a). The numerical solution is taken as reference and in the analytical model I vary either the source separation, $\Delta P1$, or $\Delta P2$ (*from top to bottom panel*). The red lines indicate the position of the reference model parameters (here DI-M3a). Reading each panel horizontally, the colour code refers to the value of the variation of surface discrepancies (ϵ), their mean, and of the discrepancies at the extrema (Ξ). Values in red are discrepancies below 5% and indicate a good fit between the analytical and reference models. Reading the panels vertically gives an estimate of each discrepancy component for a give model parameter, indicating their respective sensitivity. In this model the FEM $U_x\Big|_{\max}$ tend to zero hence $\Xi_x\Big|_{\max}$ results will not be taken into account. The parameter ranges showing the best-fit to the numerical model are listed in Table 5.2.

retrieval of the model parameters by inversion of a model based on linear superposition of Mogi and Okada models with analytical models. I employ a hybrid Monte-Carlo, downhill simplex inversion scheme (Clarke, 1996; Wright et al., 1999, kindly provided by Prof T.Wright) to estimate volume change, dike opening and source location. With this method, calculation of the L2-norm allows to find the minimum misfit between the FE input and the analytically modelled displacements. To make sure the parameters retrieved do not correspond to local minima, I restart the inversion 2000 times with 200 randomly chosen starting parameter values. As previously, the full domain of the FE models are $200 \times 200 \times 100$ km for Model A and $110 \times 100 \times 35$ km for Model DI, in order to avoid including FEM boundary effects in the solution. However, I invert for all models the horizontal and vertical FE displacements only in a 30×30 km area in the centre of the models. The dimension of this area corresponds to the spatial extent of GPS or InSAR data often used during inversions. The source parameters inverted for are indicated in bold in Table 5.3. In Inversions #1, #2, and #3, I have tried to retrieve only one source parameter: the dike position, the dike opening, and the magma chamber volume change, respectively (Model DI), or the deeper magma chamber position (Source 2), Source 2 volume change, and Source 1 volume change, respectively (Model A). In Inversions #4, I have jointly inverted for dike opening and magma chamber volume change (Model DIa), or the two magma chambers volume change (Model A). In inversions #5, I have tried to retrieve both source positions, dike opening (Model DI) and/or the magma chamber(s) volume change.

5.2.2 Results

For Model DI (numerical Method 2), whether independently or jointly inverted for, the source deflation ΔV (ΔP) is similar to its reference value, the dike opening is under-estimated by 30 and the source separation is only slightly over-estimated (Table 5.3). Hence, when modelling magmatic system with a dike aside a magma chamber, it is possible to retrieve the parameters of the two sources relatively well when employing an inversion scheme based on the Mogi and Okada analytical solutions.

For Model A, I have run the inversions with source separation between 2.5 and 9 radii for the numerical model with interacting sources (rows a-f in Table 5.3). In order to separate the effect of the numerical noise in the FE models from the source interaction I also have added the individual FE displacements generated by each of

	Source parameters		Reference model	Inversions #				
				#1	#2	#3	#4	#5
DIa (M2)	Mogi source	ΔV [10^{-3} km^3]	-1.9	-1.9	-1.9	**-1.9**	**-1.9**	**-1.9**
		ΔP [MPa]	-20.0	-20.0	-20.0	-19.7	-18.9	-19.0
		x [m]	750	750	750	750	750	**744**
	Okada source	Opening [m]	1	1	**0.72**	1	**0.68**	**0.70**
		x [m]	0	**-238**	0	0	0	**-178**
	Source separation [radii]		1.5	**1.97**	1.5	1.5	1.5	**1.84**
A-G1'a	Mogi source 1	ΔV_1 [10^{-3} km^3]	1.9	1.9	1.9	**1.6**	**1.4**	**3.8**
		ΔP_1 [MPa]	20.0	20.0	20.0	16.4	13.9	38.2
		depth [km]	5.00	5.00	5.00	5.00	5.00	**5.72**
	Mogi source 2	ΔV_2 [10^{-3} km^3]	1.9	1.9	**1.4**	1.9	**2.3**	**-1.2**$\times 10^{14}$
		$\Delta P2$ [MPa]	20.0	20.0	14.8	20.0	23.6	-1.2$\times 10^{15}$
		depth [km]	6.25	**7.42**	6.25	6.25	6.25	**2.70**$\times 10^{8}$
	Source separation [radii]		2.5	**4.8**	2.5	2.5	2.5	**5.4**$\times 10^{8}$
A-G1'b	Mogi source 1	ΔV_1 [10^{-3} km^3]	1.9	1.9	1.9	**1.7**	**1.6**	**-25.2**
		ΔP_1 [MPa]	20.0	20.0	20.0	17.7	16.8	-256.4
		depth [km]	5.00	5.00	5.00	5.00	5.00	**5.09**
	Mogi source 2	ΔV_2 [10^{-3} km^3]	1.9	1.9	**1.6**	1.9	**2.1**	**28.7**
		$\Delta P2$ [MPa]	20.0	20.0	16.5	20.0	21.4	292.7
		depth [km]	6.50	**7.26**	6.50	6.50	6.50	**5.14**
	Source separation [radii]		3.0	**4.5**	3.0	3.0	3.0	**5.1**
A-G1'c	Mogi source 1	ΔV_1 [10^{-3} km^3]	1.9	1.9	1.9	**1.9**	**1.9**	**2.8**
		ΔP_1 [MPa]	20.0	20.0	20.0	18.9	18.9	29.1
		depth [km]	5.00	5.00	5.00	5.00	5.00	**5.38**
	Mogi source 2	ΔV_2 [10^{-3} km^3]	1.9	1.9	**1.8**	1.9	**2.0**	**0.8**
		$\Delta P2$ [MPa]	20.0	20.0	18.1	20.0	20.0	8.5
		depth [km]	7.00	**7.40**	7.00	7.00	7.00	**7.53**
	Source separation [radii]		4.0	**4.8**	4.0	4.0	4.0	**4.3**
A-G1'd	Mogi source 1	ΔV_1 [10^{-3} km^3]	1.9	1.9	1.9	**1.9**	**1.8**	**2.1**
		ΔP_1 [MPa]	20.0	20.0	20.0	19.4	18.6	21.2
		depth [km]	5.00	5.00	5.00	5.00	5.00	**5.12**
	Mogi source 2	ΔV_2 [10^{-3} km^3]	1.9	1.9	**1.8**	1.9	**1.9**	**1.7**
		$\Delta P2$ [MPa]	20.0	20.0	18.8	20.0	19.7	17.3
		depth [km]	7.50	**7.75**	7.50	7.50	7.50	**7.34**
	Source separation [radii]		5.0	**5.5**	5.0	5.0	5.0	**4.4**
A-G1'e	Mogi source 1	ΔV_1 [10^{-3} km^3]	1.9	1.9	1.9	**1.9**	**2.0**	**1.8**
		ΔP_1 [MPa]	20.0	20.0	20.0	19.8	20.0	18.0
		depth [km]	5.00	5.00	5.00	5.00	5.00	**4.92**
	Mogi source 2	ΔV_2 [10^{-3} km^3]	1.9	1.9	**1.9**	1.9	**1.9**	**2.0**
		$\Delta P2$ [MPa]	20.0	20.0	19.4	20.0	19.4	20.6
		depth [km]	9.00	**9.16**	9.00	9.00	9.00	**8.32**
	Source separation [radii]		8.0	**8.3**	8.0	8.0	8.0	**6.8**
A-G1'f	Mogi source 1	ΔV_1 [10^{-3} km^3]	1.9	1.9	1.9	**1.9**	**2.0**	**1.9**
		ΔP_1 [MPa]	20.0	20.0	20.0	19.8	20.0	19.20
		depth [km]	5.00	5.00	5.00	5.00	5.00	**4.97**
	Mogi source 2	ΔV_2 [10^{-3} km^3]	1.9	1.9	**1.9**	1.9	**1.9**	**1.9**
		$\Delta P2$ [MPa]	20.0	20.0	19.4	20.0	19.3	19.3
		depth [km]	10.00	**10.17**	10.00	10.00	10.00	**9.48**
	Source separation [radii]		9.0	**10.3**	9.0	9.0	9.0	**9.0**

Table 5.3: Inversions of the synthetic datasets (numerical reference model) using combined analytical models corresponding to Models A-G1'a-f, and DIa. In Model A, two spherical sources of radius $a = 500$ m, and pressurized by $\Delta P1 = \Delta P2 = 20$ MPa, are superposed by a distance of 2.5 (G1'a) to 10 radii (G1'f). In Model DI, a 1×1 km dike opening by 1 m is juxtaposed by 1.5 radii (*i.e.* 750 m) to a deflating source ($\Delta P = -20$ MPa). Note that inversions #1 through #3 retrieve only one parameter (in bold) while inversions #4 and #5 attempt to obtain several parameters simultaneously.

the sources for all source separations, and I have inverted the sum, in the following referred to as 'M1+M2'. This sum is identical to the analytical solution except for the numerical error introduced by the FE method (see 'M1+M2' in Table A-1). As a reference, I have furthermore inverted the sum of the analytical solutions for the same set of model parameters. In this case, the inversions have retrieved the original parameters, pointing out the fact that only the numerical error introduced by the FE method affects the results of inversions of the 'M1+M2' solutions. In Figure 5.5, I compare the normalized error between reference and retrieved parameters for both interacting and non-interacting source solutions. This figure therefore highlights how the results of the inversions are affected both by neglecting the surface interaction and by noise contamination. Overall, the influence of the source interaction on the retrieved parameters is significant until a minimum source separation of 8 radii is reached. When all but one parameters are fixed (Inversions #1-3 in Figure 5.5a), the error for the 'M1+M2' parameters only reach ±2%. The inversion results are in realistic ranges, but are affected by large or very large errors, in particular when one inverts for the depth of the deep source. The solutions for the full FE model confirm our previous results underestimating ΔV, hence ΔP, by up to 30% and overestimating the source separation by up to 20%. When $\Delta V1$ and $\Delta V2$ are simultaneously inverted for (Inversion #4, Figure 5.5b), neglecting the interaction between sources lead to underestimating the volume change of the upper source by 30% while overestimating the lower volume change by 20% when the distance between sources is 2.5 radii. When the sources are separated by more than 2.5 radii, the two volume changes can be retrieved with 5%. When depths and ΔV are jointly inverted for (Inversion #5, Figure 5.5c), the inversion is unstable for small source separation (< 4 radii) and still incorrectly estimated until 8 radii, when all parameters are retrieved within ±10%. This indicates that even small uncertainties in deformation data (here produced by the FE method) can lead to unrealistic source parameters if the inversion is based on source models which are in close vicinity to each other.

5.3 Summary

In this chapter, I have investigated how neglecting the source interaction by combining analytical models can affect the estimation of the source parameters, such as the

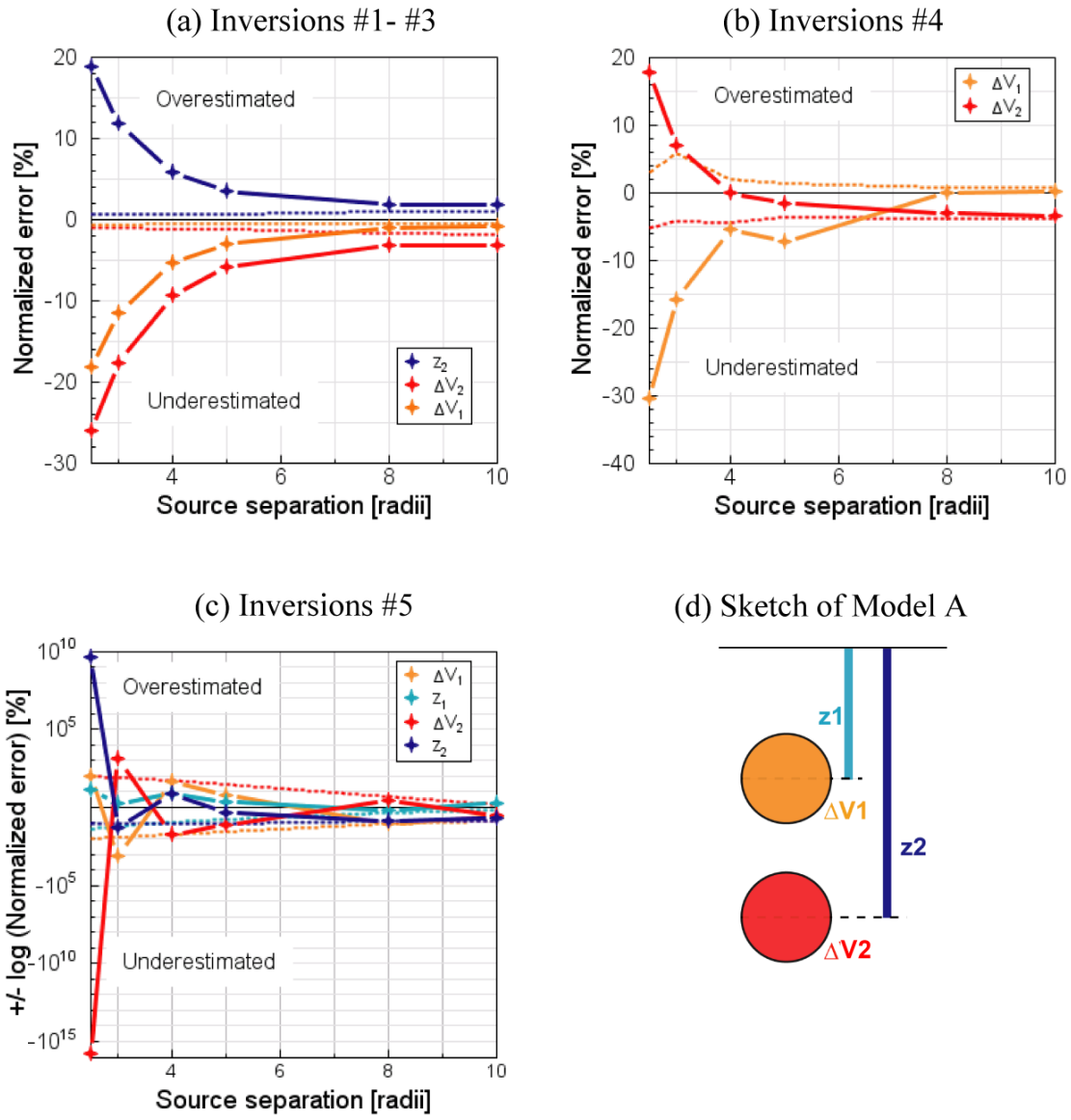

Figure 5.5: Inversions of the synthetic datasets (numerical reference model) using combined analytical models corresponding to Model A-G1'a to f. The reference models consist of two superposed spherical sources of radius a=500 m pressurized by $\Delta P1 = \Delta P2 = 20$ MPa. The errors obtained for the full FE model and for the 'M1+M2' summed model are indicated as a solid and dotted line, respectively. The sources are separated by a distance of 2.5, 3, 4, 5, 8, 9 radii. The error between reference and retrieved parameter normalized by the reference parameter is plotted against the reference model source separation. (a) Inversions #1 - #3 retrieve only one parameter at a time, (b) Inversions #4 retrieve both source volume change ΔV, (c) Inversions #5 retrieve all parameters, source volume changes and depths, (d) Sketch of Model A and source parameters inverted for.

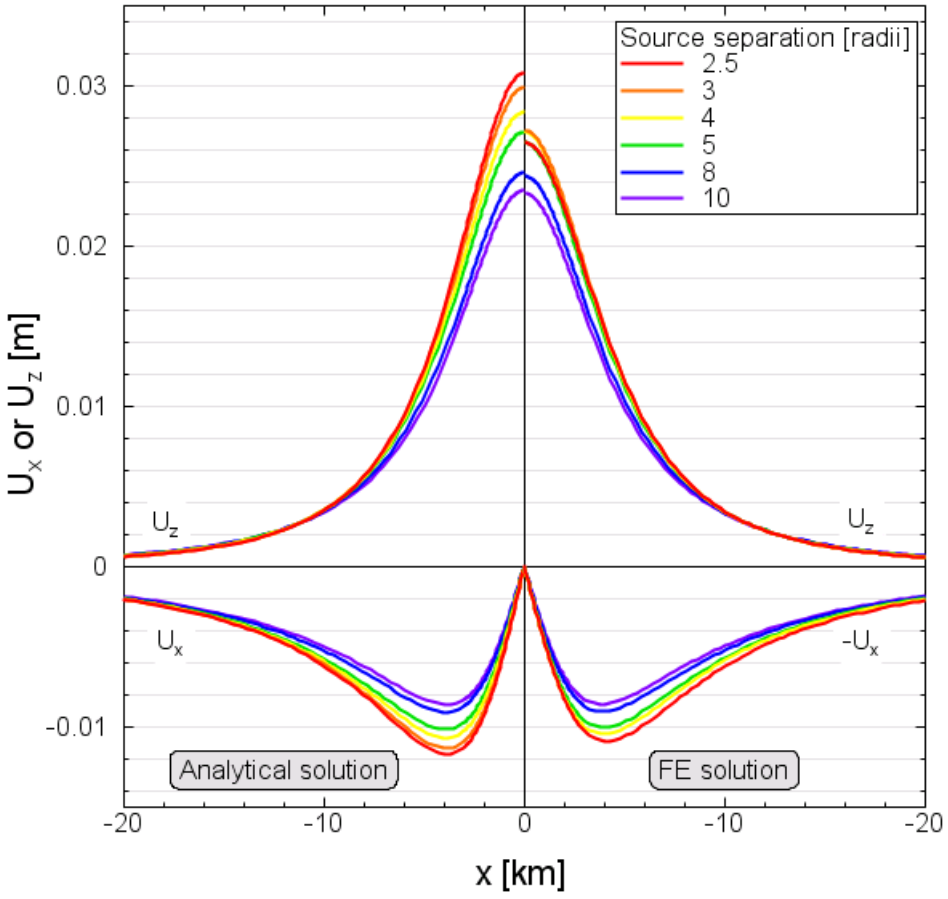

Figure 5.6: Profiles above the source centre comparing the analytical (*left*) and FE (*right*) vertical and horizontal surface displacements for models with two superposed spherical sources (Model A-G1') for source separations between 2.5-10 radii. For easier comparison, I mirrored the horizontal displacements of the FE solution.

magma chamber overpressure, the dike opening or the source separation. To that end, I have performed the sensitivity analysis of models with superposed magma chambers (Model A-G1') and with juxtaposed magma chamber and dike (Model DI). Using an inversion algorithm based on a linear addition of the Mogi and Okada solutions, I have also inverted the surface displacements computed with the FE models, and investigated the solutions when the source parameters are either individually or jointly inverted for. Overall, the deformation fields of Models A-G1' and DI, with source separation of 2.5 or 1.5 source radii, respectively, are less sensitive to a variation in overpressure or dike opening than to the source separation, for the range of parameter values searched. The sensitivity analysis shows that neglecting the source interaction leads to under- or overestimating the magmatic pressure, dike opening or overestimating the source separation. The inversion of the FE surface displacements of Model DI gives source parameters only slightly different to their set values. However, neglecting the source interaction in models with superposed spherical magma chambers, leads to an underestimation of the source pressurizations, and to an overestimation of the source separation, up to a source separation of 5 radii, when those parameters are inverted individually (Inversions #1-#3). Co-inverting the magma volume changes $\Delta V1$ and $\Delta V2$ (Inversion #4)leads to an underestimation of the lower source volume change but an overestimation of the upper source volume change, up to a source separation of about 3 radii. When the volume changes and depths of the two sources are co-inverted, the parameters retrieved are unrealistic for at least one of the sources, up to a separation of 8 source radii. In Inversions #4 and #5, it seems that the inversion scheme cannot solve for the parameters of two close sources, and 'attempts' to either merge the two imposed sources or to reducing the effect of one of them, *e.g.* increasing its depth or reducing its volume change.

In order to understand why source interaction affects heavily the inversion results, I have plotted the surface displacement solutions for different source separation in Figure 5.6, where I compare FEM and analytical models. The curves corresponding to the analytical solutions are well separated from each other and progressively less peaked for increasing source separation, while the numerical solutions overlap, or even show an inversion in the curve progression, for source separation up to 5-8 radii. This shows how source interaction induces a strong component of non-uniqueness to the displacement field.

Chapter 6

Discussion and conclusions

6.1 Summary

Analytical and Finite Element models are two complementary and widely employed methods to model volcano deformation data and retrieve source parameters. The deformation field of complex models can be solved with the Finite Element methods, that solve for the full elasticity equations at the nodes of the model. Analytical methods give the exact solution, at any location, of the elasticity equations simplified by a set of assumptions. The Mogi and Okada sources are the two analytical models that are the most frequently used to model the deformation field due to the pressure change in a magma chamber or due to a dike intrusion. The homogeneous, isotropic, elastic half-space assumption, inherent to these two models, implies the absence of topography, the uniformity of the elastic properties, such as the Young's modulus, and the absence of any external stress-field. The external stress-field can be a regional stress-field or can be introduced, in magmatic systems, by the presence of one or more additional deformation sources.

Various studies have shown that neglecting the topography or the crustal heterogeneities can lead to significant discrepancies when computing the surface displacements or the source parameters (*e.g.* Cayol and Cornet, 1998; Masterlark, 2007; Magni et al., 2008; Trasatti et al., 2003), and some authors have elaborated methods to correct for neglecting the topography (Williams and Wadge, 1998; Williams et al., 2000). However, when several analytical sources are combined to model a magmatic system, their interaction is usually neglected and their respective solutions for the surface displacements are simply summed.

In the present work, I have evaluated the limits of combining Mogi and Okada analytical sources for several model scenarios and studied the implications for numerical modelling of magma storage by employing various FE modelling methods.

The classic methodology to assess the impact of neglecting the analytical assumptions consists in comparing the analytical solutions with the solutions of equivalent numerical models (Boundary or Finite elements), and eventually to evaluate the errors. Following the same methodology, I have quantified the discrepancies introduced when neglecting the interaction between combined Mogi and Okada sources. For several model scenarios representing geometrical simplifications of magmatic systems, I have compared the analytical surface displacements with the equivalent numerical model solutions, which also account for the source interaction. I have carried out a series of synthetic tests combining either two spherical sources representing magma chamber models, or a magma chamber and an adjacent dike model. As model parameters I have used the relative source positions, dike opening and the source pressurization. I have modelled numerically the Mogi source by embedding a pressurized cavity (corresponding to a fluid-filled magma chamber) into a large numerical domain representing a half-space. To model numerically the Okada source, I have tested three approaches: applying a constant normal displacement on the dike walls (Method 1); imposing a constant displacement on one of the dike walls with respect to the other (Method 2); and applying a pressure normal to the dike walls (Method 3). To quantify the discrepancies between analytical and numerical solutions, I have estimated the differences in the surface displacements either by considering the entire surface (ϵ) or by examining the difference at the extrema of the surface displacement (Ξ).

I have demonstrated that discrepancies are negligible for all models with superposed or aligned dike and magma chamber (Models C & DII). However in all other cases tested, neglecting the source interaction introduces significant discrepancies whose magnitude depends on the source type, model geometry, and on the source strength (pressurization or dike opening). FE and analytical models differ the most in the near field, where volume or pressure estimates of magma intrusions are dominated by large amplitudes. The discrepancies decrease with increasing source separation, yet number and diversity of the parameters involved prevent the derivation of a simple mathemat-

ical expression to estimate these discrepancies. Instead I have considered the model scenarios separately.

Amongst these scenarios, I have found that when two pressurized sources are either superposed (Model A) or juxtaposed (Model B) they interact, for example, by shielding each other if they are both inflating. Neglecting this interaction causes discrepancies of up to 16% at 2.5 radii source separation. The discrepancies between analytical and numerical solutions become negligible for a source separation of more than 4 radii. Depending on the pressurization of the sources (inflation or deflation), and on their position, the analytical models either under- or over-estimate the surface displacements (Figures 4.7 & 4.9). Additionally, I have found that the discrepancies computed are overall similar for a particular model geometry and source pressurization, regardless of the radius-over-depth ratio (a/d) or the use of McTigue's expression for a finite source. In models with juxtaposed dike/magma chambers (Model DI), neglecting the source interaction will also lead to significant discrepancies in surface displacements, which, however, depend strongly on the approach taken to model the dike numerically. While large discrepancies ($> 550\%$) are calculated when modelling the dike with the numerical Method 1, employing Methods 2 and 3 induces discrepancies up to 25% and 18%, respectively, and become negligible beyond 3 radii separation.

In addition to these scenarios (Models A-D), I have applied the same approach to three case studies based on the magmatic systems of Soufrière Hills Volcano, Montserrat, West Indies (Models CS1 and CS2, similar to Models A and DII, respectively) and of the Dabbahu segment, Afar, Ethiopia (Models CS3, similar to Model DI). The results of these case studies are in agreement with the theoretical models, showing significant discrepancies for models with superposed magma chambers or with juxtaposed dike and magma chambers.

Moreover, in order to estimate how neglecting the source interaction map into source parameters, I have carried out analytical inversions of the FE solutions for models with superposed overpressurized spherical source separated by 2.5 to 10 source radii (Model A-G1'a-f). The parameters retrieved indicate that the fine structure of deep storage systems are 'intrinsically' impossible to determine by means of geodetic data only: when the vertical distance between different magma chambers is small, they interact and the solution is not unique, and when the distance is large, the magma chambers do not

interact much, but the signal of the deeper source will become too small to be resolved. When it is possible to invert for one source parameter only, or if the source location can be constrained and only the volume change of the two sources are co-inverted for, then the source parameters are within 5% when the source are separated by more than 4 radii. Additionally, when inverting jointly for all source volume changes and depths, the source interaction but also the noise contamination can make the solution unstable although all source parameters are retrieved within ±10% beyond the threshold distance of 8 radii.

6.2 Discussion

In this section, I am focusing on two findings and two limitations of the study, and I try to analyse in a broader context some of the results summarized above. These four focus points are (1) the importance of the chosen FE numerical methods; (2) the similar discrepancies obtained for a same, fixed, ratio of relative pressurization $\Delta P_1/\Delta P_2$; (3) the effect of source discrepancies in comparison with the effect of the crustal heterogeneities; and (4) the limitations of the inversion results for models with superposed spherical sources (Model A).

6.2.1 FE modelling methods: limitations and outcome

Pressurized magma chambers and opening dikes are often represented in 3D Finite Element models by, respectively, either pressurized cavities (Section 3.2) or by two surfaces representing the dike walls, on which is either applied a constant, normal, displacement or a constant pressure (respectively Methods 1 & 3, Section 3.3). In the case of a magma chamber, this modelling method ignores the compressibility of the magma in the magma chamber. Building on previous works (Delaney and McTigue, 1994; Johnson, 1992), Johnson et al. (2000) have emphasized that the deformation of the source depends on the compressibility of the magma, and have shown how, when a fixed volume of magma enters a magma chamber within an elastic domain, the surface displacements depend on the ratio between the shear modulus of the crust and the bulk modulus of the fluid. In the present study, I have shown that spherical deformation sources deform when adjacent to another deformation source and interact. On the one hand it is important to note that, for the model scenarios considered, my results are limited to calculations where the magma compressibility is ignored. On the other hand,

these results highlight the need for alternative FE models of magma chambers, where the magma compressibility is taken into account. In such models, the deformation of the source walls will diminish with magma compressibility, for a specified magma volume and crustal shear modulus. Consequently, it is expected that the interaction between sources and the misfit between the analytical Mogi solution and the FE solution will differ from those obtained in this study. In any cases, although the source interaction might be negligible, using an analytical inversion scheme not taking into account the compressibility of the deformation sources will lead to discrepancies between the source volumes changes, or between the source volume changes and the erupted volume (de Zeeuw-van Dalfsen et al., 2005; Mastin et al., 2008; Nobile et al., 2012; Pagli et al., 2007; Rivalta and Segall, 2008; Voight et al., 2010).

In the case of the dike, although Methods 1-3 give identical surface displacements when the dike is the only source in the FE model and is deep enough, the variations in the discrepancies obtained when two sources are combined, emphasize that each method represents a dike with a different physical behaviour and, therefore, a different interaction with the adjacent spherical source.
Method 1, limited to vertical dikes, is not realistic and should be avoided when modelling several interacting sources: the medium responds elastically to the dike walls, which are fixed in space. As demonstrated in Section 4.2 (*e.g.* Figure 4.8), modelling deformation sources embedded in such heterogeneous medium with the analytical Okada solution leads to large discrepancies ($> 550\%$). In contrast to Method 1, both Method 2 and Method 3 represent a non-rigid dike, with walls able to deform when subjected to the deformation field due to the combined sources. In Method 3, the static dike is subjected to a uniform internal pressure. When no other source is present, the regional stress is also uniform and the dike cross section is elliptical, as predicted by the equations of elasticity (Pollard and Muller, 1976). However, it opens asymmetrically when another source is present and, as with Method 2, the dike is either 'pushed away' from the spherical source when it is inflating, or 'pulled' towards it when it is deflating. The discrepancies induced when neglecting this deformation are up to 25% and 18% for Methods 2 and 3, respectively, but become negligible beyond 3 radii separation.

Although the physical model behind Method 1 is unrealistic, it is sometimes employed to model a dike (Currenti et al., 2008, 2011; Pulvirenti et al., 2009), in particular

because it is easily comparable with the Okada analytical model. It generates correct surface displacements when the dike is either the only deformation source or is far enough from other deformation sources such that it does not interact with them. However, the discrepancies summarized in Table 4.4 point out that modelling a dike with Method 1 when it is close enough to another deformation source, leads to very large errors. Moreover, the discrepancies, generally smaller for Method 2 than for Method 3, suggest that for a dike juxtaposed to a magma chamber, a flexible dike model can be represented by an Okada source, when it is further than 3 radii from the Mogi source.

6.2.2 Source proximity *vs* source strength

The results obtained for the various pressurization values listed in Table 4.4, specifically the equivalent discrepancies for the same ratio $\Delta P1/\Delta P2$, reveal that the discrepancies of Models A & B are do not depend on the pressurization applied to each individual source ($\Delta P1\&\Delta P2$), but rather on the pressurization ratio. This is because the overall stress field resulting from the source interaction and affecting their deformation is the same for a same $\Delta P1/\Delta P2$ ratio. Similarly, for models with similar sources, both sources are affected in the same manner by the elastic properties of the crust (as long as the medium is homogeneous).

This is demonstrated in Table 6.1 below, where I compare the discrepancies obtained for crustal Young's modulus $E = 10$ GPa and $E = 20$ GPa, for models with two inflating magma chambers either superposed or juxtaposed (Models A & B, respectively), and for model with an opening dike juxtaposed to a magma chamber (Model DI). For Models A & B, the surface and maximum discrepancies are independent of a variation of the Young's modulus E of the surrounding medium. On the contrary, the discrepancies obtained for Model DI vary depending on the Young's modulus E (Table 6.1), because the volume change of the two source types are not identical (McTigue, 1987; Davis, 1983).

Overall, for Models A & B, the discrepancies depend on the proximity of interacting surfaces rather than on the strength of the deformation sources. Hence, in order to avoid closely spaced deformation sources, one could decrease their radius and therefore increase the distance between the interacting surfaces, while maintaining the same strength by increasing the pressure, due to the trade-off between radius and pressure change ($a^3\Delta P$, Mogi, 1958). However, this relationship implies that a small change in

Model		ϵ (%)			Ξ (%)			
		ϵ_x	ϵ_y	ϵ_z	$\Xi_x\|_{\min}$	$\Xi_x\|_{\max}$	$\Xi_z\|_{\min}$	$\Xi_z\|_{\max}$
A-G1'	E=10 GPa	3.34	3.35	5.85	6.97	6.99	13.67	n/a
	E=20 GPa	3.34	3.35	5.85	6.98	6.99	13.66	n/a
B	E=10 GPa	4.5	4.4	3.8	1.4	1.5	4.7	n/a
	E=20 GPa	4.5	4.4	3.8	1.4	1.5	4.7	n/a
Model DI	E=10 GPa	7.1	7.6	5.7	5.9	2.7	n/a	7.2
	E=20 GPa	11.7	9.5	9.6	7.6	13.0	n/a	10.1

Table 6.1: Effect of Young's modulus on the surface (ϵ) and maximum (Ξ) discrepancies obtained for models with two superposed or juxtaposed inflating magma chambers (Models A & B, respectively), and for model with an inflating spherical source next to a dike opening by 1 m (Model DI, Method 2). For Models A & B the sources are separated by 2.5 source radii, and for Model DI by 1.5 source radius. In all cases, the magma chamber is pressurized by $\Delta P = 20$ and the Poisson's ratio of the crust is $\nu = 0.25$.

the radius must be compensated by a large increase in pressure, which will be limited by the strength of the crust.

6.2.3 Source interaction *vs* medium heterogeneities

As mentioned in Section 2.4.2, the Mogi and Okada models assume that deformation sources are embedded within an homogeneous crust, hence without any lateral or vertical variations of Young's modulus. This assumption being often violated for volcanic systems, several studies have shown that neglecting the crustal heterogeneities can introduce significant errors when modelling analytically the deformation field (Masterlark, 2003, 2007; Hautmann et al., 2010; Foroozan et al., 2010; Trasatti et al., 2003), the magnitude of which varies depending on the geometry of the heterogeneity body (or layer), on it's rigidity relative to the surrounding crust, and on the geometry and strength of the deformation source itself.

In order to compare the effect of neglecting the source interaction with the effect of neglecting the medium heterogeneity, I consider two models, referred to in the following as Models H1 & H2 (Figure 6.1), modified after Model A with two superposed spherical sources, with radii of $a = 500$ m and pressurized by $\Delta P_1 = \Delta P_2 = 20$ MPa (Figure 4.1, Model A-G1'). Model H1 consists of two superposed sources embedded in a medium with an upper softer layer with Young's modulus $E = 1$ GPa, which represents *e.g.* volcanic material weaker than bedrock. Model H2 consists of two superposed magma chambers located underneath a stiffer body, which could represent *e.g.* a previously emplaced sill, more rigid than the rest of the medium, as detected at Iwate volcano

(Aizawa et al., 2009). The Young's modulus of the sill is $E = 20$ GPa while the crust has a Young's modulus $E = 10$ GPa, as in Model H1. Additionally, a third set of tests, referred to 'Sum' in Figure 6.3 is created by computing two other models with the medium elastic properties of model H1: in the first one, only the upper source is embedded within the medium, and in the second one only the lower source is present. The solutions of model with the upper source and of the model with the lower source are then added. The same methodology is applied for model H2 crustal properties, such that a set of the 'Sum' solutions for all source separation for Model H1, and for all source separation for Model H2 are obtained. While the analytical solution neglects both the effect of medium heterogeneity and source interaction, the FE model solution accounts for both of them, and the summed solution allows to evaluate the effect of the heterogeneity alone. All numerical models are first calibrated against a corresponding Mogi solution, setting the same elastic properties to the lower and upper layer or to the crust and sill, such that the medium is homogeneous. For both Models H1 & H2, I calculate surface and maximum discrepancies between numerical and analytical solution for a source separation increasing from 2.5 to 10 radii. The displacement profiles of Models H1 and H2 are given in figure Figure 6.2. The discrepancies calculated for Models H1 and H2, as well as the results of the homogeneous model (Model A) are represented in Figure 6.3 and are summarized in Table B-1.

In the case of Model H1, the numerical horizontal and vertical displacements, which depend only weakly on the source separation, peak higher than the analytical solution in a narrow area above the source (here with 3 km^2 and 10 km^2 for U_z and U_x, respectively). These results are consistent with the results of Trasatti et al. (2003); Fernandez and Rundle (1994), who studied the effects of the presence of a weaker layer above one pressurized spherical source embedded in an elastic medium. On the contrary, in the case of Model H2, the numerical surface displacements are smaller than the analytical displacements until 3 radii source separation, and only slightly smaller than the numerical surface displacement obtained in the homogeneous Model A (Figures 5.6 & A-2). Consequently, the discrepancies obtained for Model H1 between numerical and analytical models are much stronger than those obtained for Model H2, for all source separation. The discrepancies of Model H1 'full' and 'summed' solution differ by a maximum of 20% when they are the closest, and beyond a distance of 3 radii, all discrepancies are approximately stable, reaching *e.g.* 55% and 15% for ϵ_x and ϵ_z,

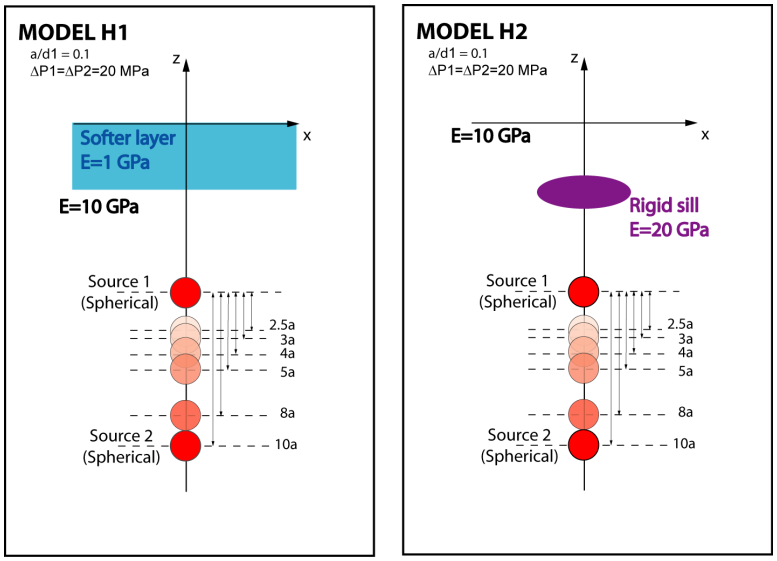

Figure 6.1: Effect of crustal heterogeneities: sketch of Models H1 and H2. In Model H1, the crust is heterogeneous, with a 2 km thick upper layer, relatively soft compared to the rest of the crust, with $E = 1$ GPa and $E = 10$ GPa, respectively. In Model H2, a $3 \times 3 \times 1$ km rigid sill, modelled as a prolate spheroid, with $E = 20$ GPa is located at 2 km depth, above the two spherical sources, in a crust with $E = 10$ GPa. In all models, the two spherical sources, with radii $a = 500$ m, are pressurized by $\Delta P_1 = \Delta P_2 = 20$ MPa, and the Poisson's ratio is $\nu = 0.25$. The upper source is located at 5 km depth and the lower source depth varies as in the homogeneous Model A, with the source separation increasing from 2.5 to 10 radii (Table 4.1). See also corresponding discrepancies in Figure 6.3

respectively (Figure 6.3a-c). In contrast to Model H1, the discrepancies obtained for Model H2 are similar within $\pm 3\%$ of the discrepancies for Model A, becoming negligible after a distance of 3-4 radii. The discrepancies obtained for the 'summed solution' are negligible for all source separations.

Again, it is important to note that these results depend on both the source and the medium parameters chosen. However, it is possible to conclude from these results that neglecting the source interaction can in some cases introduce significant discrepancies compared to those introduced by neglecting crust heterogeneities. While in Model H1, with a weaker surface layer, neglecting the heterogeneity of the medium affects the surface displacement more strongly than neglecting the source interaction, and 'hides' the effect of the source interaction. On the contrary, the presence of a stiff sill (Model H2) does not introduce significant discrepancies between numerical and analytical surface displacements, while the source interaction does.

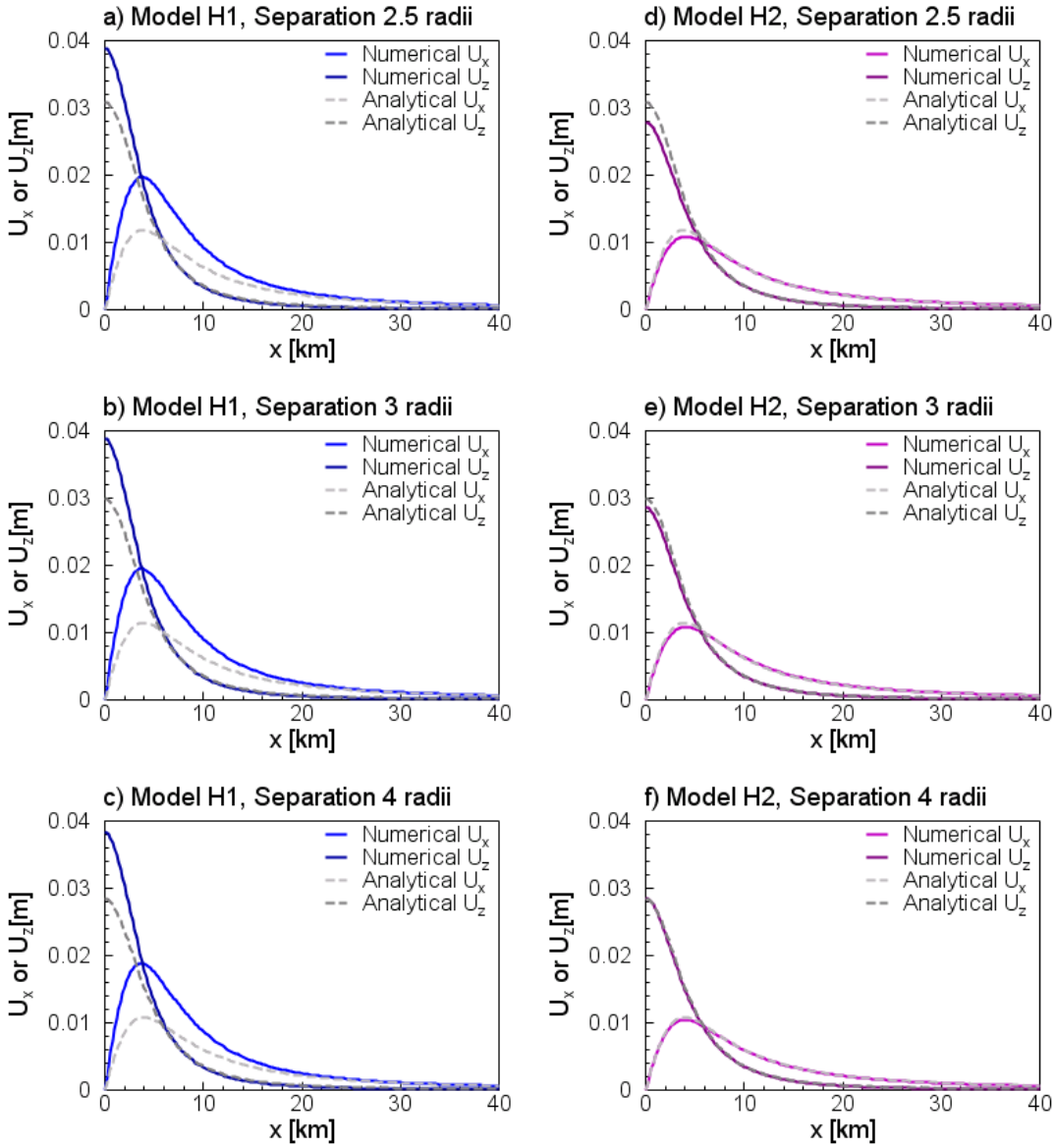

Figure 6.2: Effect of crustal heterogeneities: surface displacements profiles (U_x and U_z) of Models H1 and H2, compared with the analytical solutions, for models with source separations of 2.5, 3, and 4 source radii. In Model H1, the crust is heterogeneous, with a 2 km thick upper layer, relatively soft compared to the rest of the crust, with $E = 1$ GPa and $E = 10$ GPa, respectively. In Model H2, a $3 \times 3 \times 1$ km rigid sill, modelled as a prolate spheroid, with $E = 20$ GPa is located at 2 km depth, above the two spherical sources, in a crust with $E = 10$ GPa. In all models, the two spherical sources, with radii $a = 500$ m, are pressurized by $\Delta P_1 = \Delta P_2 = 20$ MPa, and the Poisson's ration is $\nu = 0.25$. The upper source is located at 5 km depth and the lower source depth varies depending on the source separation (Table 4.1). See also corresponding Figures 6.1 & 6.3 for corresponding models geometries & discrepancies, respectively.

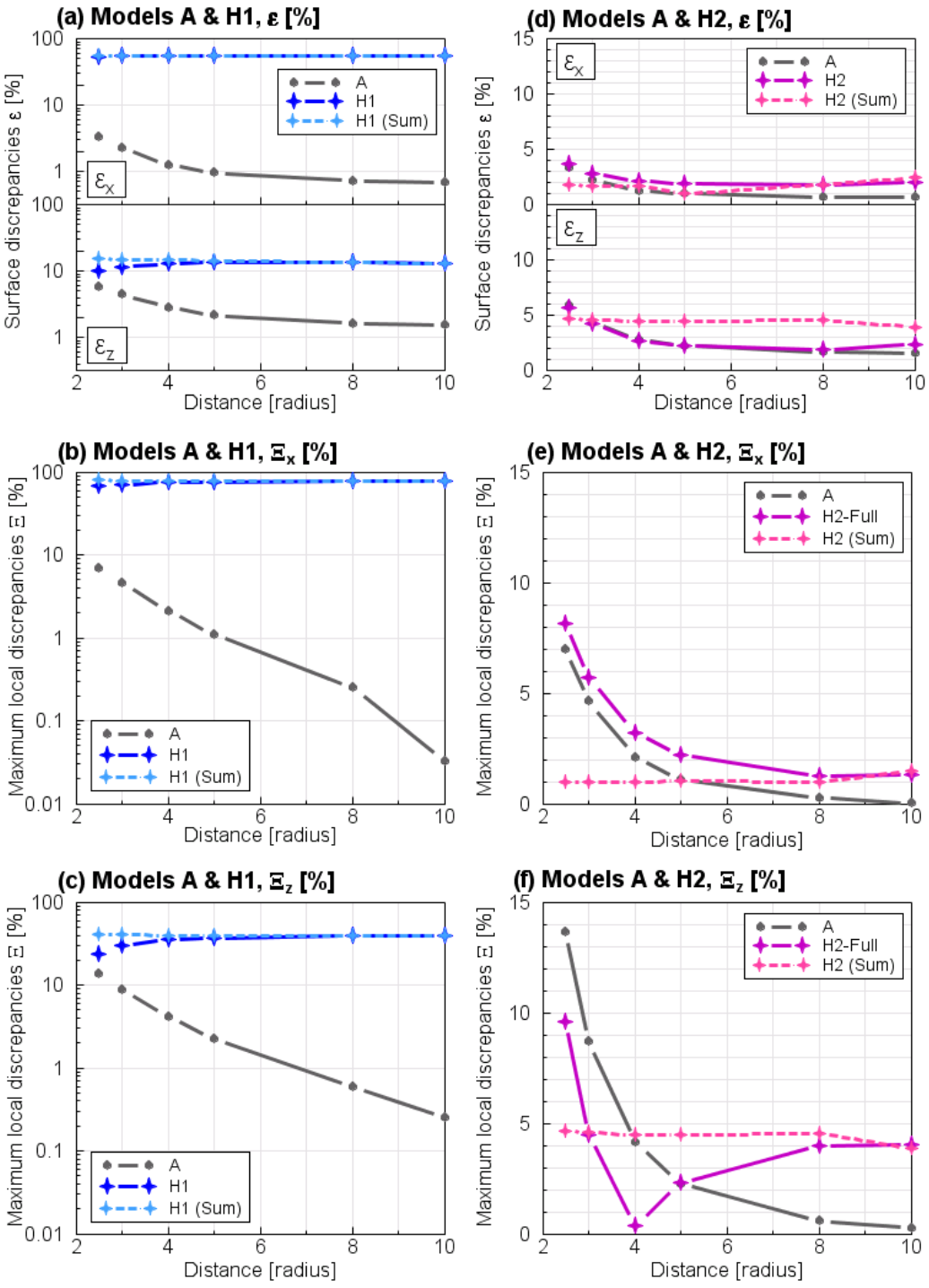

Figure 6.3: Effect of crustal heterogeneities: Model A-G1' compared to Models H1 and H2: Surface (ϵ) and maximum local (Ξ) discrepancies [%]. The 'Full solution' correspond to the solution of the FE model with the two sources. The 'Summed solution' correspond to the sum of the solution of two models, one with the upper source and the second one with the lower source. The comparison between the 'Full' and the 'Summed' solutions allow to isolate the effect of the source interaction. In all models, the two spherical sources, with radii $a = 500$ m, are pressurized by $\Delta P_1 = \Delta P_2 = 20$ MPa, and the Poisson's ratio is $\nu = 0.25$. In Model A, the crust is homogeneous, with Young's modulus $E = 10$ GPa. In Model H1, the crust is heterogeneous, with an 2 km thick upper layer, relatively soft compared to the rest of the crust with $E = 1$ GPa and $E = 10$ GPa, respectively. In Model H2, a $3 \times 3 \times 1$ km rigid sill with $E = 20$ GPa is located at 2 km depth, above the two spherical sources, in a crust with $E = 10$ GPa. See also Figure 6.1 for models geometries, and Table B-1 for discrepancies values.

6.2.4 Generalization of inversion results

In Section 5.2, I have shown that, for models with two overpressurized sources (Model A) separated by 2.5 to 10 source radii, the source parameters retrieved by an analytical inversion scheme neglecting the source interaction, can lead to erroneous model parameters of depths and volume change (*i.e.* pressurization). Depending on the number of parameters co-inverted for and on the source separation, the inversion results can be unrealistic. For joint inversions of all depths and volume changes (Inversion #5), I have also noticed that the analytical inversion scheme seems to attempt a minimization of the effect of one of the two sources by either merging it with the other source, or by increasing its depth, or by reducing its volume change. This behaviour indicates a trade-off between model parameters, and the corresponding problems of resolving single model parameters independently. While this trade-off was found considering only one single model, I present the following statistical tests to evaluate if my findings can be generalized and if they are applicable to 'real' deformation fields and associated analytical inversions. The results of the statistical study are given, describing the error on the source parameters retrieved during an analytical inversion of 100 synthetic datasets of the 'full' solution for two superposed spherical sources separated by 2.5, 3, 4, 5, 8 and 10 radii (Model A-G1'a-f). To generate the datasets, I have first added to the original synthetic dataset of Model A-G'1 Gaussian noise with a standard deviation equal to 1 cm, equivalent to data noise in *e.g.* GPS measurements. I have then applied a bootstrap method, commonly used for deformation datasets, to obtain the final 100 re-sampled synthetic datasets with added noise (Foroozan et al., 2010; Gottsmann et al., 2006; Efron and Tibshirani, 1986; Lisowski, 2007). As in Section 5.2, each dataset is either inverted for the lower source depth z_2 (Inversion #1) or volume change ΔV_2 (Inversion #2), and for the volume change of the upper source (Inversion #3). In Inversion #4 the volume changes of the two sources are inverted for, and in Inversion #5 the depth and the volume changes of the two sources are inverted for. Additionally, to be able to differentiate errors introduced by source interaction and those introduced by the added noise, I have also performed the same inversions on 100 synthetic datasets of the summed 'M1+M2' solutions (see Section 5.2). Finally, in order to evaluate if the accuracy of the source parameters retrieved is related to the number of data points, I have performed a second statistical study of 6000 inversions. As in the bootstrap study, I first add Gaussian noise with a standard deviation of 1 cm to the original synthetic

dataset and to the 'M1+M2' solution for each source separation. Then, instead of employing a bootstrap technique, I have produced, using as input these datasets with added noise, 100 samples with only 500 data points instead of the original 1600 data points. Note that in this case the datasets are not bootstrapped. Overall, both the bootstrap and downsampling studies have given similar results, hence only the results of the bootstrap study are shown below, while the results of the downsampled study are kept in Appendix C (Table C-2, Figures C-3-C-2).

In Table 6.2, I present only a subset of the results and give the mean and standard deviation of the maximum errors on the parameters retrieved in Inversions #1-5, obtained where the sources are the closest (2.5 radii distance). The distribution of the errors made on the retrieved parameters for all models and inversions are represented in Figure 6.4 for Inversions #1-3 and in Figures 6.5 & 6.6 for Inversions #4-5, along with the results obtained in Section 5.2. The corresponding numerical results are also given in Appendix C (Table C-1).

The results obtained in the statistical studies, either applying a bootstrapped or downsampling method, are consistent with our previous results of Section 5.2. When inverting for only one parameter (Inversions #1-3, Tables 6.2 & C-2, Figure 6.4 and Figure C-3), the depth of the lower source, *i.e.* the source separation, is overestimated by up to 16% ($\sigma \approx 2\%$), its volume change is in average underestimated by up to 23% ($\sigma \approx 3\%$) and the volume change of the upper source is in average underestimated by as much as 16% ($\sigma \approx 2\%$). When the source parameters were retrieved within 5% for source separation of more than 4 radii, here the comparison between full and summed solution shows that the source interaction can still introduce bigger errors, of up to 17% ($\sigma \approx 4\%$), at this distance. If the errors on the source parameters decrease with the source separation, however, when the sources are separated by more than 8 radii, the errors average and standard deviation on the lower source depth and volume change are, again unexpectedly high, for both full and summed solution, whether I use a bootstrap or a downsampling method. This demonstrates that, as the lower source is getting deeper and its effect on the surface deformation lessens, retrieving its parameters are hindered, particularly by the introduction of the noise.

While, when inverting the original FE model solution, the source parameters could still be retrieved within 10% for a source separation of more than 4 radii in Inversion #4, and 8 radii in Inversions #5, the calculations are unstable when inverting the noisy

re-sampled dataset (Figures 6.5 & 6.6, and Figures C-4 & C-5). For Inversions #4, the inverse linear relationship between the error on ΔV_1 and on ΔV_2 is highlighted in Figure 6.7a, together with the fact that the inversion scheme tries to retrieve an overall ΔV consistent with the surface displacements, rather than solving for the individual ΔV_1 and ΔV_2 (see also Figure C-6 in appendix). For Inversions #5 where the depths and volume changes of the two sources are co-inverted, Figure 6.7c shows a similar process, and the inversion results can be divided in two parameters combinations: one representing a source at 5 km (*i.e.* close to z_1 or z_2) and either a very deep or a very shallow source causing barely any deformation. Hence, neither the very deep or the very shallow source have a significant effect on the surface deformation. Note that in Inversions #5, carried out on the downsampled data sets, a third combination of source parameters consists of two sources close to each other and overall $\Delta V \approx \Delta V_1 + \Delta V_2$, where ΔV_1 and ΔV_2 taken separately can be unrealistic (Figure C-6c).

Overall, the statistical studies presented show that the errors obtained when inverting the original solution of the FE model (Section 5.2) are coherent with the errors which could be made when inverting a real deformation dataset with Gaussian noise of $\sigma = 1$ cm, either with a minimum of 500 data points, or using a bootstrap re-sampling technique for 1600 data points. Hence these results imply that for magmatic systems with a complex, fine structure, with two or more storage zones at different depths (i.e. smaller deformation sources within a same magma reservoir, rather than distinct bigger magma chambers, *e.g.* Sigmundsson et al., 2010b, on Eyjafjallajokull Volcano, Iceland), it would be difficult, at the very least, to invert for source depth and volume change at once, and independent information on source depth, for example petrological constraints, should be integrated in the procedure as an additional constraint.

Model		Distribution of errors on retrieved parameters							
		A ('full') Noisy, Bootstrapped				A (Summed 'M1+M2') Noisy, Bootstrapped)			
Inversions		Mean	σ	Min.	Max.	Mean	σ	Min.	Max.
#1	z_2	16.2	2.3	10.4	22.7	3.8	2.4	-2.7	9.0
#2	ΔV_2	-23.1	2.7	-30.4	-15.9	-4.9	3.8	-13.3	7.3
#3	ΔV_1	-16.2	1.9	-21.3	-11.2	-3.8	2.6	-9.6	4.4
#4	ΔV_1	-32.2	19.3	-78.1	-32.2	-37.5	23.0	-102.1	21.1
	ΔV_2	22.9	28.1	-41.4	88.1	48.4	32.8	-26.0	140.6
#5	ΔV_1	-1235.58	2540.08	-7451.55	7653.59	-1761.4	3602.6	-7538.4	6809.6
	Δz_1	10.68	22.37	-31.24	63.68	-1815.2	2284.1	-7694.3	2721.1
	ΔV_2	1197.69	2526.16	-7699.64	7427.02	34.1	34.1	-95.3	85.7
	Δz_2	-51.98	46.75	-99.10	34.50	1746.4	2250.1	-2788.5	7602.2

Table 6.2: Inversion #1-5, Model A-G1'a (2.5 radii separation): distribution of the errors on the parameters retrieved in the 100 inversions of the synthetic (FE) solution. An additional Gaussian noise with standard deviation 1 cm was added to the numerical solution, which has been then bootstrapped. The mean, the standard deviation (*sigma*), the minimum and the maximum error on each parameters are given for each Inversions of the 'full' solution of Model A, and of the summed 'M1+M2' solution and relative parameters to which was added some Gaussian noise and bootstrapped. The errors distribution is also represented in Figure 6.4, Figures 6.5 & 6.6. See Tables C-1 & C-2 for the entire set of the error distribution of the synthetic solution with added noise and either bootstrapped or downsampled.

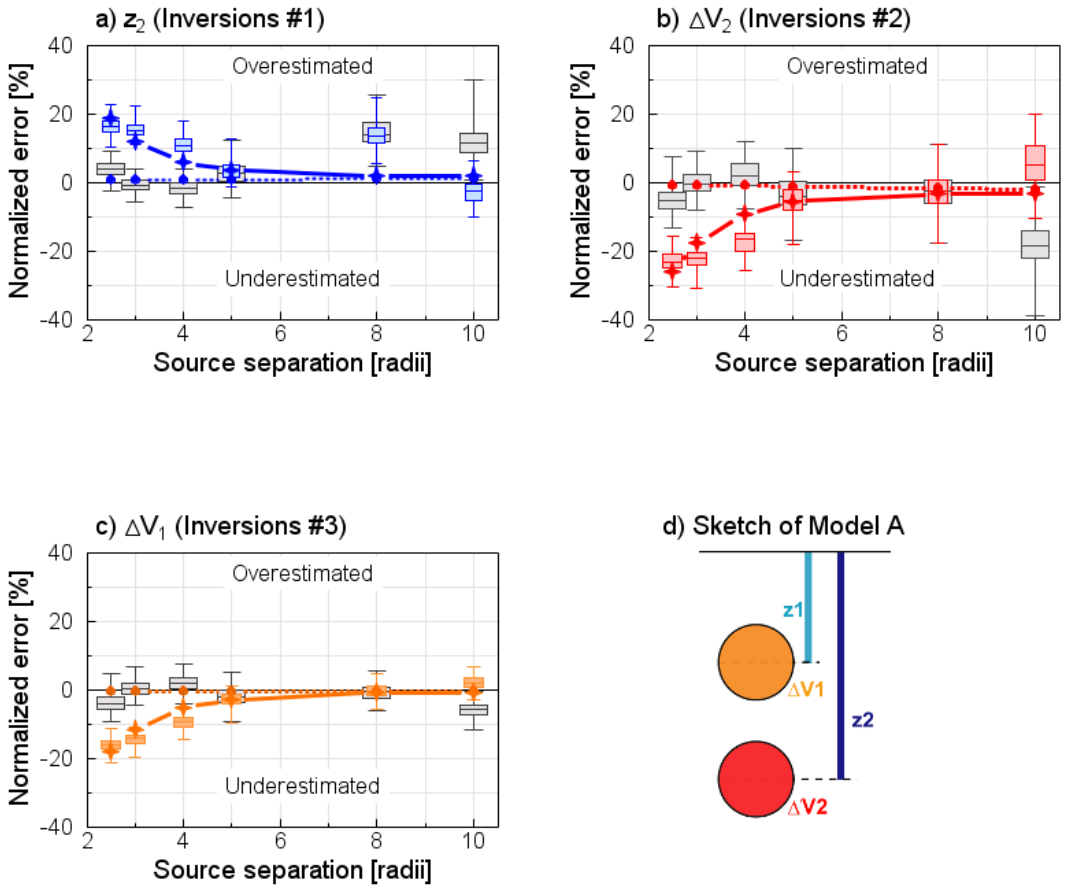

Figure 6.4: Inversions #1-3: errors between original and retrieved parameters values obtained for a population of 100 inversions of the solution of the synthetic datasets (numerical reference model), using combined analytical models corresponding to Model A-G1'a to f. The reference models consist of two superposed spherical sources of radius a=500 m pressurized by $\Delta P1 = \Delta P2 = 20$ MPa. A Gaussian noise with standard deviation 1 cm has been added to the synthetic solution, which has then been bootstrapped. The population of error between reference and retrieved parameter normalized by the reference parameter is plotted against the reference model source separation. The error distribution obtained for the full FE model and for the 'M1+M2' summed model are indicated in coloured and grey, respectively. The box-and-whiskers plot indicate the minimum, the first quartile, the median, the third quartile and the maximum of the error population. The errors obtained in Chapter 5 for the original synthetic dataset are indicated with a solid line for the full FE model and with a dotted line for the 'M1+M2' summed model. The sources are separated by a distance of 2.5, 3, 4, 5, 8, 9 radii. Inversions #1 - #3 retrieve only one parameter at a time: (a) the deeper source depth z_2, (b) the deeper source volume change ΔV_2, (c) the shallower source volume change ΔV_1. (d) Sketch of Model A and source parameters inverted for.

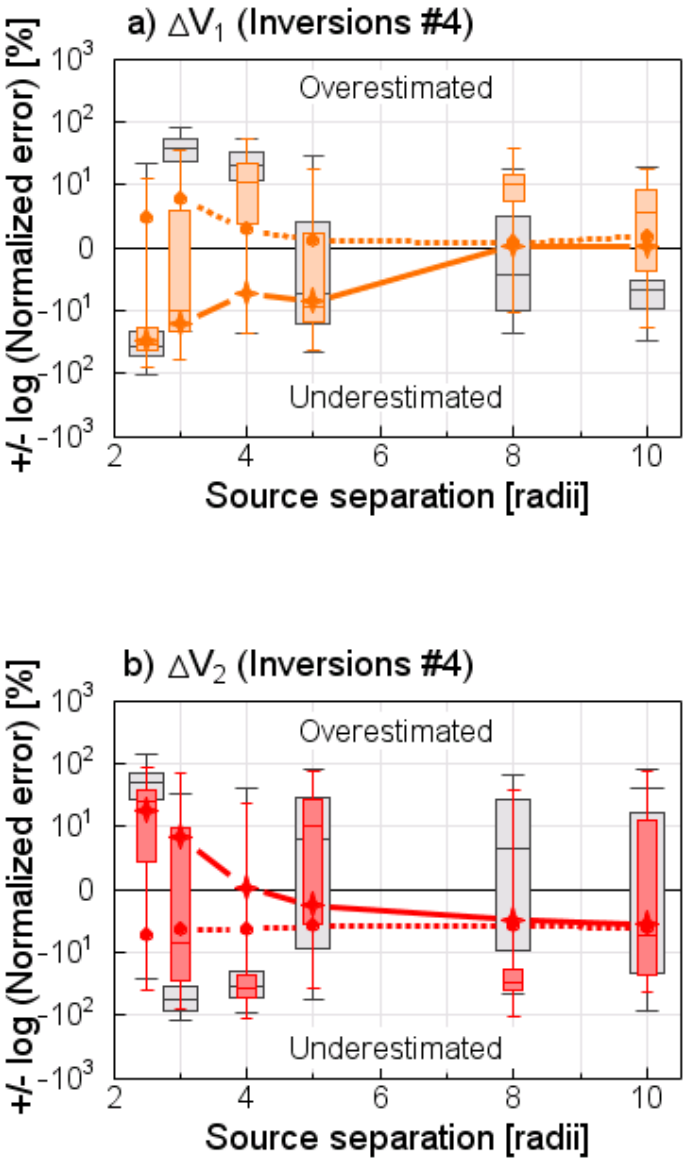

Figure 6.5: Inversions #4: errors between original and retrieved parameters values obtained for a population of 100 inversions of the solution of the synthetic datasets (numerical reference model), using combined analytical models corresponding to Model A-G1'a to f. The reference models consist of two superposed spherical sources of radius a=500 m pressurized by $\Delta P1 = \Delta P2 = 20$ MPa. A Gaussian noise with standard deviation 1 cm has been added to the synthetic solution, which has then been bootstrapped. The population of error between reference and retrieved parameter normalized by the reference parameter is plotted against the reference model source separation. The error distribution obtained for the full FE model and for the 'M1+M2' summed model are indicated in coloured and grey, respectively. The box-and-whiskers plot indicate the minimum, the first quartile, the median, the third quartile and the maximum of the error population. The errors obtained in Chapter 5 for the original synthetic dataset are indicated with a solid line for the full FE model and with a dotted line for the 'M1+M2' summed model. The sources are separated by a distance of 2.5, 3, 4, 5, 8, 9 radii. Inversions #4 retrieve both source volume change: (a) the deeper source volume change ΔV_2, and (b) the shallower source volume change ΔV_1.

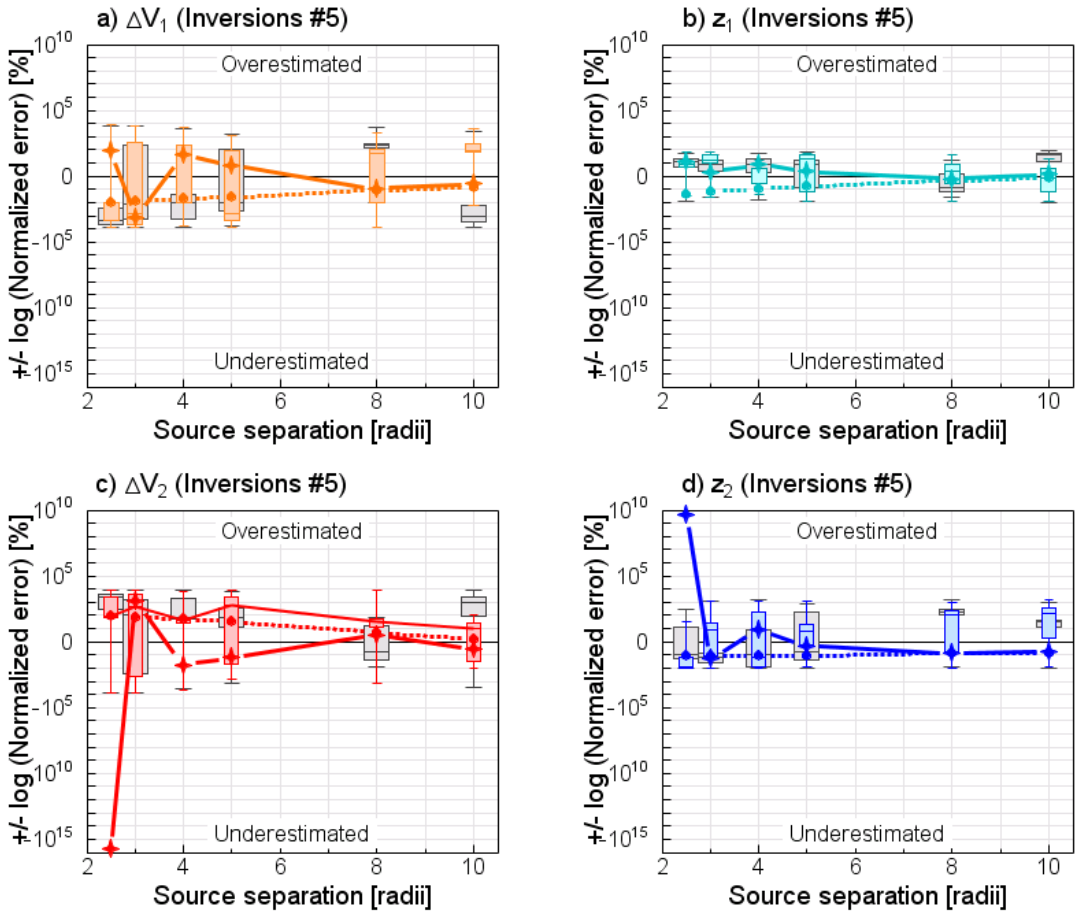

Figure 6.6: Inversions #5: errors between original and retrieved parameters values obtained for a population of 100 inversions of the solution of the synthetic datasets (numerical reference model), using combined analytical models corresponding to Model A-G1'a to f. The reference models consist of two superposed spherical sources of radius a=500 m pressurized by $\Delta P1 = \Delta P2 = 20$ MPa. A Gaussian noise with standard deviation 1 cm has been added to the synthetic solution, which has then been bootstrapped. The population of error between reference and retrieved parameter normalized by the reference parameter is plotted against the reference model source separation. The error distribution obtained for the full FE model and for the 'M1+M2' summed model are indicated in coloured and grey, respectively. The box-and-whiskers plot indicate the minimum, the first quartile, the median, the third quartile and the maximum of the error population. The errors obtained in Chapter 5 for the original synthetic dataset are indicated with a solid line for the full FE model and with a dotted line for the 'M1+M2' summed model. The sources are separated by a distance of 2.5, 3, 4, 5, 8, 9 radii. Inversions #5 retrieve all parameters, source volume changes and depths: (a) the deeper source volume change ΔV_2 and (b) depth Δz_2, and (c) the shallower source volume change ΔV_1 and (d) depth z_1.

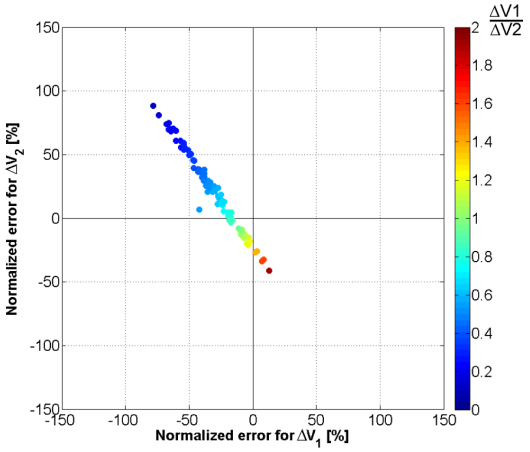

(a) Inv #4: Errors for ΔV_1 and ΔV_2

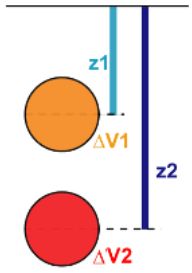

(b) Sketch of Model A

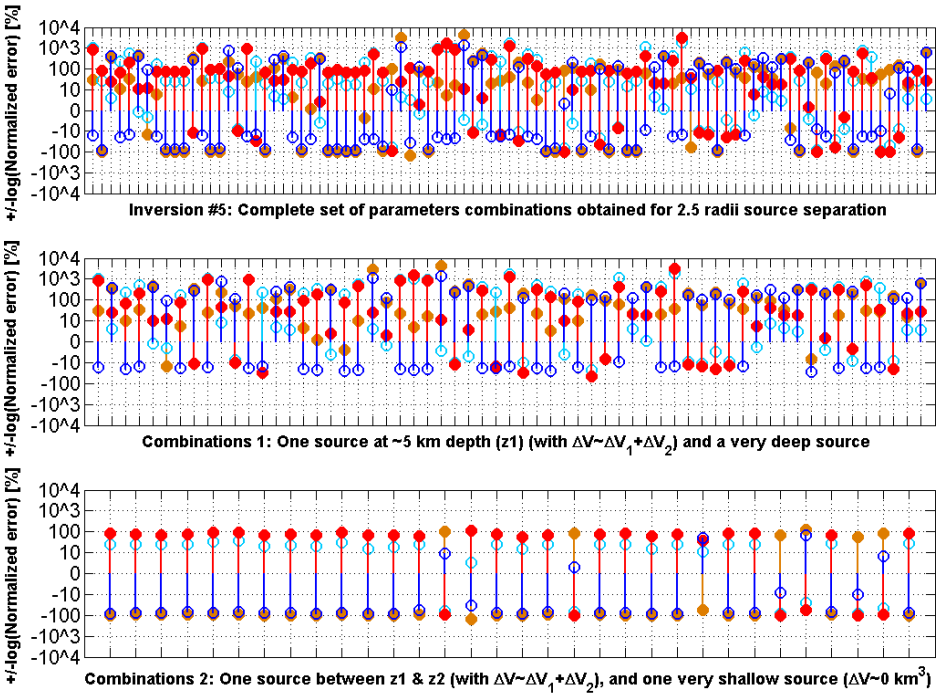

(c) Distribution of the errors obtained for ΔV_1, z_1, ΔV_2 and z_2

Figure 6.7: Summary of the results of Inversions #4-5: relationship between the errors obtained for 100 co-inversions of either the volume changes ΔV_1 and ΔV_2 (Inversion #4), or volume changes and depths of the two sources (see also Figures 6.5 & 6.6. The reference models consist of two superposed spherical sources of radius a=500 m, at a distance of 2.5 radii, pressurized by $\Delta P1 = \Delta P2 = 20$ MPa (Model A-G1'a). A Gaussian noise with standard deviation 1 cm has been added to the synthetic solution, which has then been bootstrapped. (a) Relationship between the errors obtained during the co-inversion of the two sources volume change (Inversion #4, Figure 6.5). The colour scale give the ratio between the volume of the upper and the lower source ($\Delta V_1/\Delta V_2$), (b) Sketch of Model A and source parameters inverted for, (c) Errors obtained for the volume change and depth (*circle*) of the two sources (*filled circle*): ΔV_1 (*orange*), z_1 (*clear blue*), ΔV_2 (*red*) and z_2 (*dark blue*). While all the inversions results are represented in the upper subfigure, the middle and lower subfigures show that there is two types of models obtained, both with a source at approximately 5 km depth and volume $\Delta V \approx \Delta V_1 + \Delta V_2$. The second source is either very shallow and weak (Combination 2), or very deep with variable strength (Combination 1). In both cases the second source has a negligible effect on the surface deformation.

6.3 Conclusions

This study has been concerned with accurately modelling surface deformation when magmatic systems are composed of several reservoirs, employing either analytical solutions or the Finite Elements method.

The main focus of this work has been to evaluate the effect of neglecting the source interaction when jointly employing two widely used analytical models, the Mogi point source and the Okada source, and simply adding their solutions. First I have calculated the discrepancies between analytical and numerical solutions introduced on the surface displacements, to determine the overall error. Then I have estimated how these discrepancies map into source parameters, when inverting the synthetic FE displacements with an inversion code based on the analytical solutions, *i.e.* neglecting the source interaction. Additionally, I have explored the importance of the choice of the modelling method testing a finite spherical analytical source (McTigue, 1987), and three different FE methods to model a dike-like structure.

In Chapter 4, I have compared the analytical summed solutions and the comprehensive FE solutions of four model scenarios. I have shown that, within the source parameters investigated, the discrepancies introduced by neglecting the source interaction are always negligible in systems where a magma chamber is located below a dike or aligned along its strike direction. However, the discrepancies are significant ($> 5\%$) when two magma chambers are located above each other, side by side, or when a dike and a magma chamber are located side by side. In these cases, the discrepancies reach $\approx 20\%$ when the sources are separated by a distance of 1.5 or 2.5 radii (magma chamber and dike, or two magma chambers, respectively) and become negligible after a source separation of about 4 radii. Additionally, I adapted three case studies, two related to the Soufrière Hills Volcano, Montserrat, and one to the Dabbahu-Gab'ho segment, with similar geometries to the scenarios previously tested, but with different source dimensions and pressurization or dike opening. On the one hand, these three models have confirmed the previous results, in the sense that *e.g.* the discrepancies were negligible for models with a dike superposed to a magma chamber. On the other hand, these models have pointed out that the discrepancies calculated are extremely variable, depending on the sources geometry, on the source physical parameters, but

also on the crust elastic properties. In Section 6.2.2, I have shown that the discrepancies depend on the elastic properties of the crust if the source types differ, while, for a same model geometry, they depend only on the ratio between the chamber pressurizations $\Delta P_1/\Delta P_2$. This is because two identical source are affected (and deform) in the same way by a same pressure change or respond on the same way to the elastic properties of the crust as long as it is homogenous. Their interaction and induced discrepancies remain constant. It is beyond the scope of this study, if at all possible, to find a general relation between those parameters and the discrepancies introduced by the source interaction. However, the calculated discrepancies highlight that care needs to be taken when the surface deformation is interpreted as resulting from either two distinct, close, magma chambers, or perhaps more realistically from two zones of the same magma chamber. Similarly, care should also be taken when the surface deformation is interpreted as resulting from *e.g.* a magma chamber feeding a dike, juxtaposed in its strike-perpendicular direction.

In Chapter 5, I have evaluated the effect of neglecting the source interaction when the surface displacements are inverted analytically to retrieve the source parameters, *i.e.* the depth and volume change, for models with superposed magma chamber and juxtaposed magma chamber and dike. Again my results vary with the model geometry and the parameter(s) inverted for. For a model with a magma chamber juxtaposed to a dike, the error between original and retrieved value was insignificant, independently of the number of parameters inverted for. However, the inversions of the surface displacements for models with two superposed magma chambers have demonstrated the difficulty to solve for a finely structured magmatic system with stacked deforming sources. This trade-off problem has been confirmed in Chapter 6 with a statistical analysis: when only the depth of the lower source or the volume change of the sources is inverted for, they are still over- or underestimated by up to 30%, but can be recovered within 5% if the sources are separated by more than 4 radii. However, as the lower source gets deeper, its impact on the surface deformation at the surface decreases and even a small contribution of measurement noise can prevent the retrieval of the deeper source parameters. When several source parameters are jointly inverted for, the results obtained cannot be trusted.

In parallel, I have found that the discrepancies induced when using an analytical finite source model are similar to those obtained when employing an analytical point source model, which only confirms the fact that the discrepancies are introduced by the source interaction and are not related to the distance to the surface. However, this study has also demonstrated how important the choice of the Finite Element modelling method is when the sources are close enough to interact. Although the three methods tested to model the dike numerically - *i.e.* applying a fix displacement or a pressure on each boundary, or a relative displacement between boundaries - have given identical displacements when the dike is the only source in the FE model, they represent different physical conditions. Although applying fixed displacements (opening) on the dike boundary is not a realistic dike model as the dike is then rigid, this method can be used as long as no significant external stress-field causes the dike to deform, *e.g.* a second magmatic source, the load of the edifice, or regional tectonic stresses. On the contrary, with the two other methods, the dike can deform and interact with another deformation source. Hence, on one side the discrepancies calculated show that the source interaction can in some cases be significant enough to lead to over- or under-estimate the source parameters, but also that when the source are close enough to interact the source surfaces of the numerical models employed should both be able to deform under external stresses.

6.3.1 Future research

The focus of the study has evolved around quantifying the discrepancies affecting the deformation field by neglecting the source interaction when combining the Mogi and Okada model. The difficulty of formulating a general relationship between model parameters and discrepancies at the surface is a unsatisfying aspect of this study. However, I showed in Section 6.2.2 that for models combining two magma chambers, the discrepancies seem to depend only on the geometry of the model and on the ratio between magma chamber pressurization. Varying the geometry of the model and the pressurization ratio even further, although limited to models with two spherical magma chambers, will provide an extended and useful catalogue of discrepancies depending on the position of the magma chambers relatively to the free surface, on their relative position, and on the pressurization ratio.

The emphasis of the thesis was restricted to comparing Finite Element and analyt-

ical models, henceforth designing numerical source and domain constraints equivalent to the simple analytical model assumptions. However, one of the strengths of the Finite Element methods is to be able to solve problems with complex geometry and physics. Hence in future research, this strength could be exploited to compare the effect of neglecting the source interaction simultaneously to *e.g.* the topography, the medium heterogeneities (as piloted in Section 6.2.3), which could mask the presence of a second magmatic source or can lead to under- or over-estimate of the surface deformation, and ultimately the source parameters. Furthermore, most models neglect the magmatic conduit connecting one magma reservoir with the other, although some studies have already highlighted that shear stresses along conduits can cause significant surface displacements (Nishimura, 2009; Anderson and Segall, 2011). Similarly, significant surface displacement can also be related to surface processes such as the loading/unloading history of the volcanic edifice in relation to *e.g.* erupted material (Grapenthin et al., 2010; Odbert et al., 2013) or icecap retreat (Auriac et al., 2013; Pagli et al., 2007), or by lava flow cooling and contraction at the surface (Toombs and Wadge, 2009) or at depth (de Zeeuw-van Dalfsen et al., 2005; Sigmundsson et al., 1997). In other words, while this thesis separated the effect of source interaction, future FEM modelling could advance deformation modelling in a wider context. Such a widened approach has to rely on other types of data available, *e.g.* tomography for crustal heterogeneities or petrological data including the compressibility of the source, which I consider of high priority in future research. As discussed, one of the interesting results of this study is the fact that sources do interact when they are close enough to each other, and that in those cases the deformation of the source and of the surface is related in particular to the properties of the magma within the reservoir. While some analytical expressions exists to relate surface deformation and the magma input into spherical compressible magma chambers for an elastic medium, analytical and numerical models are mostly still treating the magma as incompressible, and compressibility has yet to be integrated into numerical models. Developing a numerical method to relate the deformation of a compressible magma chamber and the surface deformation, and hence trying to integrate more systematically geophysical and geological data, would with no doubt lead us towards more realistic results, improving significantly volcano deformation models, and ultimately volcano deformation monitoring.

References

Abidin, H. Z., H. Andreas, and M. Gamal (2005), The Deformation of Bromo Volcano (Indonesia) as Detected by GPS Surveys Method, *Journal of Global Positioning Systems*, *3*(1-2), 16–24.

Aizawa, K., Y. Ogawa, M. Mishina, K. Takahashi, S. Nagaoka, N. Takagi, S. Sakanaka, and T. Miura (2009), Structural controls on the 1998 volcanic unrest at Iwate volcano: Relationship between a shallow, electrically resistive body and the possible ascent route of magmatic fluid, *Journal of Volcanology and Geothermal Research*, *187*(1-2), 131–139, doi:10.1016/j.jvolgeores.2009.08.009.

Albino, F., V. Pinel, and F. Sigmundsson (2010), Influence of surface load variations on eruption likelihood: application to two Icelandic subglacial volcanoes, Grímsvötn and Katla, *Geophysical Journal International*, pp. 1510–1524, doi:10.1111/j.1365-246X.2010.04603.x.

Albino, F., V. Pinel, H. Massol, and M. Collombet (2011), Conditions for detection of ground deformation induced by conduit flow and evolution, *Journal of Geophysical Research*, *116*, B06,201, doi:10.1029/2010JB007871.

Anderson, E. M. (1936), The dynamics of formation of cone sheets, ring dykes and cauldron subsidence, *Proceedings of the Royal Society of Edinburgh*, *56*, 128–163.

Anderson, K., and P. Segall (2011), Physics-Based Models of Ground Deformation and Extrusion Rate at Effusively Erupting Volcanoes , Part I : Model Development & Analysis, *Journal of Geophysical Research-solid Earth*, *116*, B07,204.

Anderson, K., M. Lisowski, and P. Segall (2010), Cyclic ground tilt associated with the 20042008 eruption of Mount St. Helens, *Journal of Geophysical Research*, *115*(B11), 1–29, doi:10.1029/2009JB007102.

Arnadóttir, T., F. Sigmundsson, and P. T. Delaney (1998), Source of crustal deformation associated with the Krafla, Iceland, eruption of September 1984, *Geophys. Res. Lett.*, *25*(7), 1043–1046.

Auriac, A., K. Spaans, F. Sigmundsson, A. Hooper, P. Schmidt, and B. Lund (2013), Iceland rising: solid Earth response to ice retreat inferred from satellite radar interferometry and viscoelastic modeling, *Journal of Geophysical Research - Solid Earth*, *118*, 1–14, doi:10.1002/jgrb.50082.

Ayele, A., D. Keir, C. Ebinger, T. J. Wright, G. W. Stuart, W. R. Buck, E. Jacques, G. Ogubazghi, and J. Sholan (2009), September 2005 mega-dike emplacement in the Manda-Harraro nascent oceanic rift (Afar depression), *Geophysical Research Letters*, *36*(20), 1–5, doi:10.1029/2009GL039605.

Beauducel, F., F. Cornet, E. Suhanto, T. Duquesnoy, and M. Kasser (2000), Constraints on magma flux from displacements data at Merapi volcano , Java , Indonesia, *Journal of Geophysical Research*, *105*(B4), 8193–8203.

Bianchi, R., A. Coradini, C. Federico, G. Giberti, P. Lanciano, and R. Scandone (1987), Modeling of surface deformation in volcanic areas: the 1970-1972 and 1982-1984 crises of Campi Flegrei, Italy, *Journal of Geophysical Research - Solid Earth*, *92*(B13), 14,139–14,150.

Bonaccorso, A. (2006), Explosive activity at Mt. Etna summit craters and source modeling by using high-precision continuous tilt, *Journal of Volcanology and Geothermal Research*, *158*(3-4), 221–234, doi:10.1016/j.jvolgeores.2006.05.007.

Bonaccorso, A., and P. M. Davis (1999), Models of ground deformation from vertical volcanic conduits with application to eruptions of Mount St. Helens and Mount Etna, *Journal of Geophysical Research*, *104*(B5), 10,531–10,542.

Bonaccorso, A., S. Gambino, F. Guglielmino, M. Mattia, G. Puglisi, and E. Boschi (2008), Stromboli 2007 eruption: Deflation modeling to infer shallow-intermediate plumbing system, *Geophysical Research Letters*, *35*(6), L06,311, doi:10.1029/2007GL032921.

Bonafede, M., and C. Ferrari (2009), Analytical models of deformation and residual gravity changes due to a Mogi source in a viscoelastic medium, *Tectonophysics*, *471*(1-2), 4–13, doi:10.1016/j.tecto.2008.10.006.

Bonforte, A., A. Bonaccorso, F. Guglielmino, M. Palano, and G. Puglisi (2008), Feeding system and magma storage beneath Mt. Etna as revealed by recent inflation/deflation cycles, *Journal of Geophysical Research*, *113*(B5), B05,406, doi:10.1029/2007JB005334.

Camacho, A. G., P. J. González, J. Fernández, and G. Berrino (2011), Simultaneous inversion of surface deformation and gravity changes by means of extended bodies with a free geometry: Application to deforming calderas, *Journal of Geophysical Research*, *116*(B10), B10,401, doi:10.1029/2010JB008165.

Cayol, V., and F. H. Cornet (1998), Effects of topography on the interpretation of the deformation field of prominent volcanoes - Application to Etna, *Geophysical Research Letters*, *25*(11), 1979–1982.

Cayol, V., J. H. Dieterich, A. T. Okamura, and A. Miklius (2000), High Magma Storage Rates Before the 1983 Eruption of Kilauea, Hawaii, *Science*, *288*(5475), 2343–2346, doi:10.1126/science.288.5475.2343.

Celâl Sengôr, A. (2003), *The large wavelength deformations of the lithosphere: Materials for a history of the evolution of thought frm the earliest times to plate tectonics*, 347 pp., Geological Society of America.

Clarke, P. J. (1996), Tectonic Motions and Earthquake Deformation in Greece from GPS Measurements, Ph.D. thesis, University of Oxford.

Cole, P. D., T. Christopher, S. Melander, K. Pascal, P. Smith, R. Stewart, A. Stinton, and R. Syers (2012), MVO scientific report for volcanic activity between 1 May 2012 and 12 October 2012 ; Open File Report OFR 12-02, *Tech. rep.*, Montserrat Volcano Observatory.

Collinson, A., and J. Neuberg (2012), Gas storage, transport and pressure changes in an evolving permeable volcanic edifice, *Journal of Volcanology and Geothermal Research*, *243-244*, 1–13, doi:10.1016/j.jvolgeores.2012.06.027.

Currenti, G., C. Del Negro, G. Ganci, and D. Scandura (2008), 3D numerical deformation model of the intrusive event forerunning the 2001 Etna eruption, *Physics of the Earth and Planetary Interiors*, *168*(1-2), 88–96, doi:10.1016/j.pepi.2008.05.004.

Currenti, G., R. Napoli, A. Di Stefano, F. Greco, and C. Del Negro (2011), 3D integrated geophysical modeling for the 2008 magma intrusion at Etna: Constraints on rheology and dike overpressure, *Physics of the Earth and Planetary Interiors*, *185*(1-2), 44–52, doi:10.1016/j.pepi.2011.01.002.

Davis, P. M. (1983), Surface Deformation Associated With a Dipping Hydrofracture, *Journal of Geophysical Research*, *88*(B7), 5826–5834, doi:10.1029/JB088iB07p05826.

Davis, P. M. (1986), Surface deformation due to inflation of an arbitrarily oriented triaxal ellipsoidal cavity in an elastic half-space, with reference to Kilauea Volcano, Hawaii, *Journal of Geophysical Research*, *91*(B7), 7429–7438.

de Zeeuw-van Dalfsen, E., H. Rymer, F. Sigmundsson, and E. Sturkell (2005), Net gravity decrease at Askja volcano, Iceland: constraints on processes responsible for continuous caldera deflation, 19882003, *Journal of Volcanology and Geothermal Research*, *139*(3-4), 227–239, doi:10.1016/j.jvolgeores.2004.08.008.

de Zeeuw-van Dalfsen, E., R. Pedersen, A. Hooper, and F. Sigmundsson (2012), Subsidence of Askja caldera 2000-2009: Modelling of deformation processes at an extensional plate boundary, constrained by time series InSAR analysis, *Journal of Volcanology and Geothermal Research*, *213-214*, 72–82, doi:10.1016/j.jvolgeores.2011.11.004.

Decker, R., R. Y. Koyanagi, J. J. Dvorak, A. Lockwood, A. Okamura, K. Yamashita, and W. Tanigawa (1983), Seismicity and Surface Deformation of Mauna Loa Volcano , Hawaii, *EOS*, *64*(37).

Delaney, P. T., and D. F. McTigue (1994), Volume of magma accumulation or withdrawal estimated from surface uplift or subsidence, with application to the 1960 collapse of Kilauea volcano, *Bulletin of Volcanology*, *56*(6-7), 417–424, doi:10.1007/BF00302823.

Dragoni, M., and C. Magnanensi (1989), Displacement and stress produced by a pressurized , spherical magma chamber , surrounded by a viscoelastic shell, *Physics of the Earth and Planetary Interiors*, *56*, 316–328.

Dvorak, J. J., and D. Dzurisin (1997), Volcano geodesy: the search for magma reservoirs and the formation of eruptive vents, *Reviews of Geophysics*, *35*(3), 343–384.

Dzurisin, D. (1992a), Geodetic Leveling as a Tool for Studying Restless Volcanoes, in *Monitoring Volcanoes : Techniques and Strategies Used by the Staff of the Cascades Volcano Observatory , 1980-90*, chap. 12, pp. 125–134, U.S. G. P. O., U.S.G.S. Bulletin 1966.

Dzurisin, D. (1992b), Electronic Tiltmeters for Volcano Monitoring: Lessons from Mount St. Helens, in *Monitoring Volcanoes : Techniques and Strategies Used by the Staff of the Cascades Volcano Observatory , 1980-90*, chap. 7, pp. 69–84, U.S. G. P. O., U.S.G.S. Bulletin 1966.

Dzurisin, D. (2000), Volcano geodesy: challenges and opportunities for the 21st century, *Philosophical Transactions of the Royal Society A: Mathematical, Physical and Engineering Sciences*, *358*(1770), 1547–1566, doi:10.1098/rsta.2000.0603.

Dzurisin, D. (2003), A comprehensive approach to monitoring volcano deformation as a window on the eruption cycle, *Reviews of Geophysics*, *41*(1), 1001, doi:10.1029/2001RG000107.

Efron, B., and R. Tibshirani (1986), Bootstrap Methods for Standard Errors, Condidence Intervals, and Other Measures of Statistical Accuracy, *Statistical science*, *1*(1), 54–75.

Elsworth, D., G. S. Mattioli, J. Taron, B. Voight, and R. Herd (2008), Implications of magma transfer between multiple reservoirs on eruption cycling, *Science*, *322*(5899), 246–8, doi:10.1126/science.1161297.

Fernandez, J., and J. B. Rundle (1994), Gravity changes and deformation due to a magmatic intrusion in a two-layered crustal model, *Journal of Geophysical Research - Solid Earth*, *99*(B2), 2737–2746.

Fialko, Y., M. Simons, and Y. Khazan (2001a), Finite source modelling of magmatic unrest in Socorro, NewMexico, and Long Valley, California, *Geophysical Journal International*, *146*(1), 191–200, doi:10.1046/j.1365-246X.2001.00453.x.

Fialko, Y., Y. Khazan, and M. Simons (2001b), Deformation due to a pressurized horizontal circular crack in an elastic half-space, with applications to volcano geodesy, *Geophysical Journal International*, *146*(1), 181–190, doi:10.1046/j.1365-246X.2001.00452.x.

Foroozan, R., D. Elsworth, B. Voight, and G. S. Mattioli (2010), Dual reservoir structure at Soufrière Hills Volcano inferred from continuous GPS observations and heterogeneous elastic modeling, *Geophysical Research Letters*, *37*(19), n/a–n/a, doi:10.1029/2010GL042511.

Fournier, T. J., M. E. Pritchard, and S. N. Riddick (2010), Duration, magnitude, and frequency of subaerial volcano deformation events: New results from Latin America using InSAR and a global synthesis, *Geochemistry Geophysics Geosystems*, *11*(1), Q01,003, doi:10.1029/2009GC002558.

Fournier, T. J., M. E. Pritchard, and S. N. Riddick (2012), Global compilation of deforming volcanoes (updated table).

Galland, O., and J. Scheibert (2013), Analytical model of surface uplift above axisymmetric flat-lying magma intrusions: Implications for sill emplacement and geodesy, *Journal of Volcanology and Geothermal Research*, *253*, 114–130, doi:10.1016/j.jvolgeores.2012.12.006.

Gdoutos, E. (1981), Interaction effects between a crack and a circular inclusion, *Fibre Science and Technology*, *15*(3), 173–185, doi:10.1016/0015-0568(81)90002-6.

Genco, R., and M. Ripepe (2010), Inflation-deflation cycles revealed by tilt and seismic records at Stromboli volcano, *Geophysical Research Letters*, *37*(12), 1–5, doi:10.1029/2010GL042925.

Gorbatikh, L., S. Lomov, and I. Verpoest (2007), On Stress Intensity Factors of Multiple Cracks at Small Distances in 2-D Problems, *International Journal of Fracture*, *143*(4), 377–384, doi:10.1007/s10704-007-9070-9.

Gottsmann, J., A. Folch, and H. Rymer (2006), Unrest at Campi Flegrei: A contribution to the magmatic versus hydrothermal debate from inverse and finite element modeling, *Journal of Geophysical Research*, *111*(B7), B07,203, doi:10.1029/2005JB003745.

Grapenthin, R., B. G. Ófeigsson, F. Sigmundsson, E. Sturkell, and A. Hooper (2010), Pressure sources versus surface loads: Analyzing volcano deformation signal composition with an application to Hekla volcano, Iceland, *Geophysical Research Letters*, *37*(20), 3–7, doi:10.1029/2010GL044590.

Grechka, V., and M. Kachanov (2006), Effective elasticity of rocks with closely spaced and intersecting cracks, *Geophysics*, *71*(3), D85, doi:10.1190/1.2197489.

Green, D. N., J. Neuberg, and V. Cayol (2006), Shear stress along the conduit wall as a plausible source of tilt at Soufrière Hills volcano, Montserrat, *Geophysical Research Letters*, *33*(10), 2–6, doi:10.1029/2006GL025890.

Hamling, I. J., T. J. Wright, E. Calais, L. Bennati, and E. Lewi (2010), Stress transfer between thirteen successive dyke intrusions in Ethiopia, *Nature Geoscience*, *3*(10), 713–717, doi:10.1038/ngeo967.

Hautmann, S., J. Gottsmann, R. S. J. Sparks, G. S. Mattioli, I. S. Sacks, and M. H. Strutt (2010), Effect of mechanical heterogeneity in arc crust on volcano deformation with application to Soufrière Hills Volcano, Montserrat, West Indies, *Journal of Geophysical Research*, *115*(B9), B09,203, doi:10.1029/2009JB006909.

Hughes, G. R. (2011), Reinvestigation of the 1989 Mammoth Mountain, California seismic swarm and dike intrusion, *Journal of Volcanology and Geothermal Research*, *207*(3-4), 106–112, doi:10.1016/j.jvolgeores.2011.07.001.

Huppert, H. E., and A. W. Woods (2002), The role of volatiles in magma chamber dynamics., *Nature*, *420*(6915), 493–5, doi:10.1038/nature01211.

Iguchi, M., H. Yakiwara, T. Tameguri, M. Hendrasto, and J. Hirabayashi (2008), Mechanism of explosive eruption revealed by geophysical observations at the Sakurajima, Suwanosejima and Semeru volcanoes, *Journal of Volcanology and Geothermal Research*, *178*(1), 1–9, doi:10.1016/j.jvolgeores.2007.10.010.

Iwatsubo, E. Y., and D. A. Swanson (1992), Trilateration and Distance-Measuring Techniques Used at Cascades and Other Volcanoes, in *Monitoring Volcanoes : Techniques and Strategies Used by the Staff of the Cascades Volcano Observatory , 1980-90*, chap. 10, pp. 103–114, U.S. G. P. O., U.S.G.S. Bulletin 1966.

Jaeger, J., N. Cook, and R. Zimmerman (2007), *Fundamentals of Rock Mechanics*, vol. 470, 4th editio ed., 488 pp., John Wiley & Sons, doi:10.1016/j.tecto.2008.12.009.

Janssen, V. (2007), Volcano deformation monitoring using GPS, *Journal of Spatial Science*, *52*(1), 41–54, doi:10.1080/14498596.2007.9635099.

Johnson, D. J. (1992), Dynamics of Magma storage in the summit reservoir of kilauea volcano, Hawaii, *Journal of Geophysical re*, *97*(B2), 1807–1820.

Johnson, D. J., F. Sigmundsson, and P. T. Delaney (2000), Comment on " Volume of magma accumulation or withdrawal estimated from surface uplift or subsidence, with application to the 1960 collapse of Klauea volcano" by P. T. Delaney and D. F. McTigue, *Bulletin of Volcanology*, *61*(7), 491–493, doi:10.1007/s004450050006.

Kachanov, M. (1987), Elastic solids with many cracks: a simple method of analysis, *International Journal of Solids and Structures*, *23*(1), 23–43.

Kachanov, M. (2003), On the problems of crack interactions and crack coalescence, *International Journal of Fracture*, *120*, 537–543.

Kavanagh, J. L., and R. S. J. Sparks (2011), Insights of dyke emplacement mechanics from detailed 3D dyke thickness datasets, *Journal of the Geological Society*, *168*(4), 965–978, doi:10.1144/0016-76492010-137.

Kohno, Y., T. Matsushima, and H. Shimizu (2008), Pressure sources beneath Unzen Volcano inferred from leveling and GPS data, *Journal of Volcanology and Geothermal Research*, *175*(1-2), 100–109, doi:10.1016/j.jvolgeores.2008.03.022.

Linde, A. T., K. Agustsson, I. S. Sacks, and R. Stefansson (1993), Mechanism of the 1991 eruption of Hekla from continuous borehole strain monitoring, *Nature*, *365*, 737–740.

Linde, A. T., S. Sacks, D. Hidayat, B. Voight, A. Clarke, D. Elsworth, G. S. Mattioli, P. Malin, E. Shalev, R. S. J. Sparks, and C. Widiwijayanti (2010), Vulcanian explosion at Soufrière Hills Volcano, Montserrat on March 2004 as revealed by strain data, *Geophysical Research Letters*, *37*, 1–5, doi:10.1029/2009GL041988.

Lipman, P. W., D. R. Mullineaux, and Geological Survey (U.S.) (1981), *The 1980 eruptions of Mount St. Helens, Washington*, 1981 ed., 844 pp., U.S. Dept. of the Interior, U.S. Geological Survey, Geological Survey professional paper.

Lisowski, M. (2007), Analytical volcano deformation source models, in *Volcano Deformation*, chap. 8, pp. 279–304, Springer Praxis, Chichester, U.K.

Long, S. M., and E. B. Grosfils (2009), Modeling the effect of layered volcanic material on magma reservoir failure and associated deformation, with application to Long Valley caldera, California, *Journal of Volcanology and Geothermal Research*, *186*(3-4), 349–360, doi:10.1016/j.jvolgeores.2009.05.021.

Lu, Z., D. Mann, J. T. Freymueller, and D. J. Meyer (2000), Synthetic aperture radar interferometry of Okmok volcano, Alaska: Radar observation, *Journal of Geophysical Research*, *105*(B5), 10,791–10,806.

Lu, Z., C. W. Jr, D. Dzurisin, J. A. Power, S. C. Moran, and W. Thatcher (2002), Magmatic inflation at a dormant stratovolcano : 1996 1998 activity at Mount Peulik volcano , Alaska , revealed by satellite radar interferometry, *Journal of Geophysical Research - Solid Earth*, *107*(B7), ETG 4–1– ETG 4–13.

Lungarini, L., C. Troise, M. Meo, and G. Denatale (2005), Finite element modelling of topographic effects on elastic ground deformation at Mt. Etna, *Journal of Volcanology and Geothermal Research*, *144*(1-4), 257–271, doi:10.1016/j.jvolgeores.2004.11.031.

Magni, V., A. Manconi, P. Tizzani, M. Battaglia, and T. Walter (2008), Heterogeneous Axial Symmetric Crustal Deformation Model for Long Valley Caldera , California, in *Excerpt from the Proceedings of the COMSOL Conference*.

Marsh, B. D. (1989), Magma chambers, *Annu. Rev. Earth Planet. Sci.*, *17*, 438–474, doi:10.1126/science.212.4494.528.

Massonnet, D., P. Briole, and A. Arnaud (1995), Deflation of Mount Etna monitored by spaceborne radar interferometry, *Nature*, *375*, 567–570.

Masterlark, T. (2003), Finite element model predictions of static deformation from dislocation sources in a subduction zone: Sensitivities to homogeneous, isotropic, Poisson-solid, and half-space assumptions, *Journal of Geophysical Research*, *108*(B11), doi:10.1029/2002JB002296.

Masterlark, T. (2007), Magma intrusion and deformation predictions: Sensitivities to the Mogi assumptions, *Journal of Geophysical Research*, *112*(B6), 1–17, doi:10.1029/2006JB004860.

Mastin, L. G., E. Roeloffs, N. M. Beeler, and J. E. Quick (2008), Constraints on the Size , Overpressure , and Volatile Content of the Mount St . Helens Magma System from Geodetic and Dome-Growth Measurements During the 2004 2006 + Eruption, *Holocene*, (early 2006), 2004–2006.

Mattioli, G. S., R. a. Herd, M. H. Strutt, G. Ryan, C. Widiwijayanti, and B. Voight (2010), Long term surface deformation of Soufrière Hills Volcano, Montserrat from GPS geodesy: Inferences from simple elastic inverse models, *Geophysical Research Letters*, *37*, L00E13, doi:10.1029/2009GL042268.

McTigue, D. F. (1987), Elastic stress and deformation near a finite spherical magma body: resolution of the point source paradox, *Journal of Geophysical Research*, *92*, 12,931–12,940.

McTigue, D. F., and P. Segall (1988), Displacements and tilts from dip-slip faults and magma chambers beneath irregular surface topography, *Geophysical Research Letters*, *15*(6), 601–604.

Melan, E. (1932), Point force at internal point in a semi-infinite plate (in German), *Z. Angew. Math. Mech.*, *12*, 343–346.

Meo, M., U. Tammaro, and P. Capuano (2008), Influence of topography on ground deformation at Mt. Vesuvius (Italy) by finite element modelling, *International Journal of Non-Linear Mechanics*, *43*(3), 178–186, doi:10.1016/j.ijnonlinmec.2007.12.005.

Mindlin, R. (1936), Force at a point in the interior of a semi-infinite solid, *Physics*, *7*, 195–202.

Mogi, K. (1958), Relations between the eruptions of various volcanoes and the deformations of the ground surfaces around them, *Bulletin of the Earthquake Research Institute*, *36*, 99–134.

Montgomery-Brown, E. K., D. K. Sinnett, M. Poland, P. Segall, T. Orr, H. Zebker, and A. Miklius (2010), Geodetic evidence for en echelon dike emplacement and concurrent slow slip during the June 2007 intrusion and eruption at Kilauea volcano, Hawaii, *Journal of Geophysical Research*, *115*(B7), 1–15, doi:10.1029/2009JB006658.

Murray, J. B., and L. K. Wooller (2002), Persistent summit subsidence at Volcan de Colima, México, 1982-1999: strong evidence against Mogi deflation, *North*, *117*, 69–78.

Nishimura, T. (2009), Ground deformation caused by magma ascent in an open conduit, *Journal of Volcanology and Geothermal Research*, *187*(3-4), 178–192, doi:10.1016/j.jvolgeores.2009.09.001.

Nishimura, T., S. Ozaway, M. Murakami, T. Sagiya, T. Tada, M. Kaidzu, and M. Ukawa (2001), Crustal deformation caused by magma migration in the northern Izu Islands, Japan, *Geophysical Research Letters*, *28*(19), 3745–3748.

Nobile, A., C. Pagli, D. Keir, T. J. Wright, A. Ayele, J. Ruch, and V. Acocella (2012), Dike-fault interaction during the 2004 Dallol intrusion at the northern edge of the Erta Ale Ridge (Afar, Ethiopia), *Geophysical Research Letters*, *39*(19), n/a–n/a, doi:10.1029/2012GL053152.

Odbert, H., B. Taisne, and S. Tait (2013), Volcanic ground deformation due to surface loading of erupted material on Montserrat, in *EGU General Assembly*.

Okada, Y. (1985), Surface deformation due to shear and tensile faults in a half-space, *Bulletin of the Seismological Society of America*, *75*(4), 1135–1154, doi:10.1016/0148-9062(86)90674-1.

Okada, Y. (1992), Internal deformation due to shear and tensile faults in a half-space, *Bulletin of the Seismological Society of America*, *82*(2), 1018–1040.

Pagli, C., F. Sigmundsson, R. Pedersen, P. Einarsson, T. Árnadóttir, and K. L. Feigl (2007), Crustal deformation associated with the 1996 Gjálp subglacial eruption, Iceland: InSAR studies in affected areas adjacent to the Vatnajökull ice cap, *Earth and Planetary Science Letters*, *259*(1-2), 24–33, doi:10.1016/j.epsl.2007.04.019.

Palano, M., G. Puglisi, and S. Gresta (2007), Ground deformation at Mt . Etna : a joint interpretation of GPS and InSAR data from 1993 to 2000, *Bollettino di Geofisica Teorica ed Applicata*, *48*, 18pp.

Palano, M., G. Puglisi, and S. Gresta (2008), Ground deformation patterns at Mt. Etna from 1993 to 2000 from joint use of InSAR and GPS techniques, *Journal of Volcanology and Geothermal Research*, *169*(3-4), 99–120, doi:10.1016/j.jvolgeores.2007.08.014.

Palano, M., E. Guarrera, and M. Mattia (2012), GPS ground deformation patterns at Mount St. Helens (Washington, USA) from 2004 to 2010, *Terra Nova*, *24*(2), 148–155, doi:10.1111/j.1365-3121.2011.01049.x.

Peltier, A., T. Hurst, B. Scott, and V. Cayol (2009), Structures involved in the vertical deformation at Lake Taupo (New Zealand) between 1979 and 2007: New insights from numerical modelling, *Journal of Volcanology and Geothermal Research*, *181*(3-4), 173–184, doi:10.1016/j.jvolgeores.2009.01.017.

Piombo, A., A. Tallarico, and M. Dragoni (2007), Displacement, strain and stress fields due to shear and tensile dislocations in a viscoelastic half-space, *Geophysical Journal International*, *170*(3), 1399–1417, doi:10.1111/j.1365-246X.2007.03283.x.

Pollard, D. D., and G. Holzhausen (1979), On the mechanical interaction between a fluid-filled fracture and the earth's surface, *Tectonophysics*, *53*, 27–57.

Pollard, D. D., and O. H. Muller (1976), The Effect of Gradients in Regional Stress and Magma Pressure on the Form of Sheet Intrusions in Cross Section, *Journal of Geophysical Research*, *81*(5), 975–984, doi:10.1029/JB081i005p00975.

Pollard, D. D., P. T. Delaney, W. A. Duffield, E. T. Endo, and A. T. Okamura (1983), Surface deformation in volcanic rift zones, *Tectonophysics*, *94*, 541–584.

Price, E. J. (2004), Dynamic deformation of Seguam Island, Aleutian Islands, Alaska, 19932000: Implications for magmatic and hydrothermal processes, *Journal of Geophysical Research*, *109*(B4), B04,202, doi:10.1029/2003JB002671.

Pritchard, M. E., and M. Simons (2002), A satellite geodetic survey of large-scale deformation of volcanic centres in the central Andes., *Nature*, *418*(6894), 167–71, doi:10.1038/nature00872.

Pulvirenti, F., M. Aloisi, G. De Guidi, and M. Mattia (2009), A finite element test of the 2002-2003 Etna eruption, in *Geoitalia 2009 VII, Italian Forum of Earth Sciences, September 9-11, 2009, Rimini, Italy*, Milan.

Rivalta, E., and P. Segall (2008), Magma compressibility and the missing source for some dike intrusions, *Geophysical Research Letters*, *35*(4), 0–4, doi:10.1029/2007GL032521.

Roman, D., S. De Angelis, J. Latchman, and R. White (2008), Patterns of volcanotectonic seismicity and stress during the ongoing eruption of the Soufrière Hills Volcano, Montserrat (19952007), *Journal of Volcanology and Geothermal Research*, *173*(3-4), 230–244, doi:10.1016/j.jvolgeores.2008.01.014.

Sanderson, R., J. Johnson, and J. Lees (2010), Ultra-long period seismic signals and cyclic deflation coincident with eruptions at Santiaguito volcano, Guatemala, *Journal of Volcanology and Geothermal Research*, *198*(1-2), 35–44, doi:10.1016/j.jvolgeores.2010.08.007.

Schmid, A., J. R. Grasso, D. Clarke, V. Ferrazzini, P. Bachèlery, and T. Staudacher (2012), Eruption forerunners from multiparameter monitoring and application for eruptions time predictability (Piton de la Fournaise), *Journal of Geophysical Research*, *117*(B11), B11,203, doi:10.1029/2012JB009167.

Segall, P. (2010), *Earthquake and volcano deformation*, 517 pp., Princeton University Press.

Segall, P. (2013), Volcano deformation and eruption forecasting, *Geological Society, London, Special Publications*, *380*, doi:10.1144/SP380.4.

Segall, P., and J. L. Davis (1997), Gps Applications for Geodynamics and Earthquake Studies, *Annual Review of Earth and Planetary Sciences*, *25*(1), 301–336, doi:10.1146/annurev.earth.25.1.301.

Shepherd, J. B., R. a. Herd, P. Jackson, and R. Watts (1998), Ground deformation measurements at the Soufriere Hills Volcano, Montserrat: II: Rapid static GPS measurements June 1996June 1997, *Geophysical Research Letters*, *25*(18), 3413, doi:10.1029/98GL01655.

Sigmundsson, F., H. Vadon, and D. Massonnet (1997), Readjustment of the Krafla Spreading Segment to crustal rifting measured by satellite radar interferometry, *Geophysical Research Letters*, *24*(15), 1843–1846, doi:10.1029/97GL01934.

Sigmundsson, F., S. Hreinsdóttir, A. Hooper, T. Arnadóttir, R. Pedersen, M. J. Roberts, N. Oskarsson, A. Auriac, J. Decriem, P. Einarsson, H. Geirsson, M. Hensch, B. G. Ofeigsson, E. Sturkell, H. Sveinbjörnsson, and K. L. Feigl (2010a), Intrusion triggering of the 2010 Eyjafjallajökull explosive eruption., *Nature*, *468*(7322), 426–30, doi:10.1038/nature09558.

Sigmundsson, F., V. Pinel, B. Lund, F. Albino, C. Pagli, H. Geirsson, and E. Sturkell (2010b), Climate effects on volcanism: influence on magmatic systems of loading and unloading from ice mass variations, with examples from Iceland., *Philosophical transactions. Series A, Mathematical, physical, and engineering sciences*, *368*(1919), 2519–34, doi:10.1098/rsta.2010.0042.

Sparks, R. S. J. (2003), Forecasting volcanic eruptions, *Earth and Planetary Science Letters*, *210*(1-2), 1–15, doi:10.1016/S0012-821X(03)00124-9.

Steketee, J. A. (1958), On Volterra's dislocation in a semi-infinite elastic medium, *Can. J. Phys.*, *36*, 192–205.

Stiros, S. C., P. Psimoulis, G. Vougioukalakis, and M. Fyticas (2010), Geodetic evidence and modeling of a slow, small-scale inflation episode in the Thera (Santorini) volcano caldera, Aegean Sea, *Tectonophysics*, *494*(3-4), 180–190, doi:10.1016/j.tecto.2010.09.015.

Sturkell, E. (2003), Recent unrest and magma movements at Eyjafjallajökull and Katla volcanoes, Iceland, *Journal of Geophysical Research*, *108*(B8), 1–13, doi:10.1029/2001JB000917.

Tiampo, K. F., J. Rundle, J. Fernandez, and J. Langbein (2000), Spherical and ellipsoidal volcanic sources at Long Valley caldera, California, using a genetic algorithm inversion technique, *Journal of Volcanology and Geothermal Research*, *102*(3-4), 189–206, doi:10.1016/S0377-0273(00)00185-2.

Toombs, A., and G. Wadge (2009), Removing lava flow subsidence signals from deformation interferograms at Nyamuragira Volcano, in *Proceedings of the FRINGE 2009 Workshop, ESA ESRIN*, pp. SP–677, Frascatti, Italy.

Trasatti, E., C. Giunchi, and M. Bonafede (2003), Effects of topography and rheological layering on ground deformation in volcanic regions, *Journal of Volcanology and Geothermal Research*, *122*(1-2), 89–110, doi:10.1016/S0377-0273(02)00473-0.

Trasatti, E., M. Bonafede, C. Ferrari, C. Giunchi, and G. Berrino (2011), On deformation sources in volcanic areas: Modeling the Campi Flegrei (Italy) 198284 unrest, *Earth and Planetary Science Letters*, *306*(3-4), 175–185, doi:10.1016/j.epsl.2011.03.033.

Tryggvason, E. (1986), Multiple magma reservoirs in a rift zone volcano: ground deformation and magma transport during the september 1984 eruption of Krafla, Iceland, *Journal of Volcanology and Geothermal Research*, *28*, 1–44.

Voight, B., R. Hoblitt, A. B. Clarke, A. B. Lockhart, A. D. Miller, L. Lynch, and J. Mcmahon (1998), Remarkable cyclic ground deformation monitored in real-time on Montserrat, and its use in eruption forecasting, *Geophysical Research Letters*, *25*(18), 3405–3408.

Voight, B., R. S. J. Sparks, A. D. Miller, R. Stewart, R. P. Hoblitt, A. Clarke, J. Ewart, W. Aspinall, B. Baptie, E. Calder, P. Cole, T. Druitt, C. Hartford, R. A. Herd, P. Jackson, A. M. Lejeune, A. B. Lockhart, S. C. Loughlin, R. Luckett, L. Lynch, G. E. Norton, R. Robertson, I. M. Watson, R. Watts, and S. R. Young (1999), Magma Flow Instability and Cyclic Activity at Soufriere Hills Volcano, Montserrat, British West Indies, *Science*, *283*(5405), 1138–1142, doi:10.1126/science.283.5405.1138.

Voight, B., C. Widiwijayanti, G. S. Mattioli, D. Elsworth, D. Hidayat, and M. Strutt (2010), Magma-sponge hypothesis and stratovolcanoes: Case for a compressible reservoir and quasi-steady deep influx at Soufrière Hills Volcano, Montserrat, *Geophysical Research Letters*, *37*, 0–4, doi:10.1029/2009GL041732.

Wadge, G., G. S. Mattioli, and R. Herd (2006), Ground deformation at Soufrière Hills Volcano, Montserrat during 19982000 measured by radar interferometry and GPS, *Journal of Volcanology and Geothermal Research*, *152*(1-2), 157–173, doi:10.1016/j.jvolgeores.2005.11.007.

Watson, I., C. Oppenheimer, B. Voight, P. W. Francis, A. Clarke, J. Stix, A. Miller, D. M. Pyle, M. R. Burton, S. R. Young, G. Norton, S. Loughlin, B. Darroux, and M. Staff (2000), The relationship between degassing and ground deformation at Soufriere Hills Volcano, Montserrat, *Journal of Volcanology and Geothermal Research*, *98*(1-4), 117–126, doi:10.1016/S0377-0273(99)00187-0.

Williams, C. A., and G. Wadge (1998), The effects of topography on magma chamber deformation models: Application to Mt. Etna and radar interferometry, *Geophysical Research Letters*, *25*(10), 1549–1552.

Williams, C. A., N. York, and G. Wadge (2000), An accurate and efficient method for including the effects of topography in three-dimensional elastic models of ground deformation with applications to radar interferometry, *Journal of Geophysical Research*, *105*, 8103–8120.

Wright, T. J., B. Parsons, J. Jackson, M. Haynes, E. Fielding, P. England, and P. J. Clarke (1999), Source parameters of the 1 October 1995 Dinar (Turkey) earthquake from SAR interferometry and seismic bodywave modelling, *Earth and Planetary Science Letters*, *172*(1-2), 23–37, doi:10.1016/S0012-821X(99)00186-7.

Wright, T. J., C. Ebinger, J. Biggs, A. Ayele, G. Yirgu, D. Keir, and A. Stork (2006), Magma-maintained rift segmentation at continental rupture in the 2005 Afar dyking episode., *Nature*, *442*(7100), 291–4, doi:10.1038/nature04978.

Yang, B. Y. X., and P. M. Davis (1986), Deformation due to a rectangular tension crack in an elastic half-space, *Bulletin of the Seismological Society of America*, *76*(3), 865–881.

Yang, B. Y. X., and P. M. Davis (1992), Geodetic analysis of dike intrusion and motion of the magma reservoir beneath the summit of Kilauea volcano, Hawaii: 1970-1985, *Journal of Geophysical Research*, *97*, 3305–3324.

Yang, X.-m., P. M. Davis, and J. H. Dieterich (1988), Deformation from inflation of a dipping finite prolate spheroid in an Elastic Half-space as a model for volcanic stressing, *J. Geophys. Res.*, *93*(B5), 4249–4257.

Zellmer, G. F., and C. Annen (2008), An introduction to magma dynamics, *Geological Society, London, Special Publications*, *304*(1), 1–13, doi:10.1144/SP304.1.

Appendices

Appendix A

Additional material for Chapter 4

Model	$\Delta P_1 = \Delta P_2 = 20$ MPa					$\Delta P_1 = \Delta P_2 = 200$ MPa					$\Delta P_1 = -\Delta P_2 = 20$ MPa				
	ϵ_x	ϵ_y	ϵ_z	Ξ_x	Ξ_z	ϵ_x	ϵ_y	ϵ_z	Ξ_x	Ξ_z	ϵ_x	ϵ_y	ϵ_z	Ξ_x	Ξ_z
G1a	3.3	3.3	5.6	7.0	13.9	3.3	3.3	5.6	7.0	13.9	6.5	5.6	11.4	7.2	13.6
G1b	2.2	2.2	4.1	4.6	8.9	2.2	2.2	4.1	4.6	8.9	3.9	3.9	7	4.6	8.4
G1c	1.1	1.1	2.4	2.2	4.2	1.1	1.1	2.4	2.2	4.2	1.7	1.7	3.2	2.1	3.9
G1d	0.7	0.7	1.7	1.1	2.3	0.7	0.7	1.7	1.1	2.3	0.9	0.9	1.8	1.1	2.1
G1e	0.4	0.4	1.2	0.3	0.7	0.4	0.4	1.2	0.3	0.7	0.3	0.3	0.6	0.3	0.6
G1f	0.4	0.4	1.1	0.2	0.5	0.4	0.4	1.1	0.2	0.5	0.2	0.2	0.4	0.2	0.3
G1'a	3.3	3.3	5.9	7.0	13.7	–	–	–	–	–	6.9	6.9	11.3	7.6	14.3
G1'b	2.2	2.2	4.4	4.6	8.7	–	–	–	–	–	4.2	4.1	6.9	4.0	9.0
G1'c	1.2	1.2	2.8	2.1	4.1	–	–	–	–	–	1.9	1.9	3.3	2.0	3.7
G1'd	1.0	1.0	2.2	1.1	2.3	–	–	–	–	–	1.1	1.1	1.9	1.1	1.9
G1'e	0.7	0.7	1.6	0.2	0.6	–	–	–	–	–	0.6	0.6	1.0	0.3	0.5
G1'f	0.7	0.7	1.5	0.1	0.2	–	–	–	–	–	0.5	0.5	0.9	0.1	0.4
G2a	7	7	9.4	7.2	14.7	–	–	–	–	–	4.6	4.6	8.1	7.4	13.7
G2b	4.8	4.8	6.6	4.9	9.7	–	–	–	–	–	2.8	2.8	5	4.5	8.3
G2c	2.6	2.6	3.8	2.5	4.8	–	–	–	–	–	1.3	1.3	2.3	2	3.7
G2d	1.7	1.7	2.7	1.4	2.9	–	–	–	–	–	0.7	0.7	1.3	1	1.9
G2e	1	0.9	1.8	0.5	1.3	–	–	–	–	–	0.2	0.2	0.5	0.2	0.3
G2f	0.9	0.9	1.6	0.4	1.1	–	–	–	–	–	0.2	0.2	0.5	0.1	0
G3a	3.9	3.7	7.6	4.8	6.9	–	–	–	–	–	4.3	4.2	8.9	4.7	9.7
G3b	3.1	2.9	5.7	2.8	3.8	–	–	–	–	–	2.7	2.6	5.8	2.9	6.7
G3c	2.4	2.1	3.7	1.1	0.9	–	–	–	–	–	1.5	1.4	3.6	1.4	4
G3d	2.1	1.8	2.9	0.5	0.3	–	–	–	–	–	1.2	1.1	3.2	0.9	2.9
G3e	2.0	1.7	1.9	0.0	1.4	–	–	–	–	–	1.2	1.1	3.8	0.4	1.7
G3f	1.9	1.6	1.4	0.1	1.6	–	–	–	–	–	1.4	1.2	4.4	0.3	1.4

Table A-1: Model A, Groups 1-3: Surface (ϵ) and maximum local (Ξ) discrepancies [%] obtained for $\Delta P_1 = \Delta P_2 = 20$ MPa, $\Delta P_1 = -\Delta P_2 = 20$ MPa (Groups G1-3), and $\Delta P_1 = \Delta P_2 = 200$ MPa (Group G1). Depending on the model, $\Xi_z = \Xi_z\Big|_{\max}$ or $\Xi_z\Big|_{\min}$, and similarly for Ξ_x. Elastic parameters are $\nu = 0.25$ and $E = 10$ GPa. See also Figure 4.5.

Model	$\Delta P_1 = \Delta P_2 = 20$ MPa					$\Delta P_1 = -\Delta P_2 = 20$ MPa				
	ϵ_x	ϵ_y	ϵ_z	Ξ_x	Ξ_z	ϵ_x	ϵ_y	ϵ_z	Ξ_x	Ξ_z
G1a	6.0	5.3	4.9	0.6	7.9	7.4	9.7	8.9	7.1	13.5
G1b	6.4	5.6	5.3	1.4	9.0	4.4	5.6	5.4	4.2	8.4
G1c	2.1	1.6	1.8	0.1	1.9	1.9	2.6	2.4	1.8	3.7
G1d	1.3	0.9	1.3	0.3	0.9	1.0	1.5	1.4	0.9	2.0
G1e	0.8	0.4	1.2	0.2	0.0	0.3	0.5	0.4	0.2	0.5
G1f	0.7	0.4	1.2	0.2	0.1	0.2	0.4	0.4	0.2	0.0
G1'a	5.3	5.8	4.6	1.4	6.3	9.6	13.1	12.3	8.9	13.8
G1'b	4.5	4.7	3.8	1.1	3.5	6.0	8.2	10.0	6.0	9.1
G1'c	3.3	2.6	2.8	1.9	0.8	3.5	5.2	4.6	3.0	4.8
G1'd	3.3	2.1	3.2	1.9	0.2	1.4	1.8	2.0	1.5	2.9
G1'e	3.3	1.5	3.4	2	1.7	0.8	1.4	1.3	0.7	1.1
G1'f	4	2.0	3.4	3.0	2.0	0.7	1.2	1.0	0.6	0.7
G2a	4.8	5.5	4.7	0.5	7.2	8.1	10.9	10.0	7.5	14.0
G2b	3.3	3.5	3.0	0.3	4.0	5.0	6.2	6.0	4.0	8.6
G2c	1.9	1.8	1.8	0.3	1.4	2.1	3.3	2.8	1.8	4.1
G2d	1.3	1.2	1.5	1.3	0.3	1.2	1.8	1.7	0.9	1.3
G2e	1.0	0.7	1.7	0.4	0.7	0.5	0.7	0.7	0.4	0.7
G2f	1.0	0.7	1.7	0.5	0.6	0.3	0.6	0.5	0.2	0.1
G3a	6.7	5.9	6.7	2.1	9.8	5.7	8.0	6.8	7.3	7.1
G3b	5.4	3.6	4.8	1.9	5.0	2.9	4.0	3.4	3.1	2.5
G3c	4.5	1.6	3.7	1.2	2.0	1.0	1.9	1.2	0.0	0.9
G3d	4.1	1.4	3.9	0.9	1.4	0.9	1.2	1.0	0.8	0.9
G3e	3.7	1.6	4.1	0.8	1.2	1.2	0.8	1.0	0.9	1.9
G3f	3.7	1.7	4.2	1.0	1.3	1.2	0.7	1.0	0.9	1.9

Table A-2: Model B, Groups 1-3: Surface (ϵ) and maximum local (Ξ) discrepancies [%] obtained for $\Delta P_1 = \Delta P_2 = 20$ MPa. Elastic parameters are $\nu = 0.25$ and $E = 10$ GPa. See also Figure 4.6.

Model		ϵ (%)			Ξ (%)			
		ϵ_x	ϵ_y	ϵ_z	$\Xi_x\|_{\min}$	$\Xi_x\|_{\max}$	$\Xi_z\|_{\min}$	$\Xi_z\|_{\max}$
ΔP=20 MPa	Ca	1.3	1.2	1.6	n/a	1.2	n/a	1.5
	Cb	0.7	1.0	1.3	n/a	0.8	n/a	1.1
	Cc	0.4	0.6	0.9	n/a	0.4	n/a	0.4
	Cd	0.2	0.6	1.0	n/a	0.1	n/a	0.1
	Ce	0.2	0.5	1.3	n/a	0.2	n/a	0.2
	Cf	0.3	0.5	1.4	n/a	0.01	n/a	0.3
ΔP=-20 MPa	Ca	4.1	0.4	1.9	2.4	4.0	1.0	n/a
	Cb	4.0	0.4	1.6	1.7	1.9	0.8	n/a
	Cc	1.3	0.4	1.3	1.3	0.8	0.4	n/a
	Cd	0.3	0.4	1.1	2.2	0.1	0.4	3.8
	Ce	0.2	0.4	0.9	4.1	0.2	0.5	0.3
	Cf	0.2	0.5	0.9	3.0	0.1	0.2	0.1
ΔP=20 MPa	DIIa	0.3	0.7	1.5	0.2	0.1	n/a	0.7
	DIIb	0.4	0.7	1.3	0.2	0.4	n/a	0.3
	DIIc	0.4	0.7	1.2	0.3	0.5	n/a	0.1
	DIId	0.4	0.7	1.2	0.3	0.3	n/a	0.1
	DIIe	0.4	0.9	1.3	0.3	0.3	n/a	0.4
	DIIf	0.5	1.0	0.7	0.3	0.4	0.5	n/a
ΔP=-20 MPa	DIIa	0.9	1.4	1.4	0.7	0.6	1.7	n/a
	DIIb	0.8	1.1	1.1	0.5	0.3	1.3	n/a
	DIIc	0.7	0.9	0.9	0.6	0.2	0.9	n/a
	DIId	0.5	0.7	0.8	0.4	0.3	0.6	n/a
	DIIe	0.5	0.9	0.8	0.4	0.6	0.7	n/a
	DIIf	0.4	1.0	1.2	0.3	0.3	n/a	0.3

Table A-3: Model C and D2: Surface (ϵ) and maximum local (Ξ) discrepancies obtained for an dike opening by 1 m superposed (Model C) or horizontaly aligned (Model DII, see Figure 4.1) to either an inflating ($\Delta P = 20$ MPa) or a deflating spherical source ($\Delta P = -20$ MPa). Elastic parameters are $\nu = 0.25$ and $E = 10$ GPa.

Model			ϵ (%)			Ξ (%)			
			ϵ_x	ϵ_y	ϵ_z	$\Xi_x\|_{\min}$	$\Xi_x\|_{\max}$	$\Xi_z\|_{\min}$	$\Xi_z\|_{\max}$
Model DI,dike op. 1 m	ΔP=20 MPa	DIa	97.2	12.3	12.6	82.3	57.5	n/a	15.1
		DIb	87.7	9.6	9.0	61.4	42.6	n/a	11.5
		DIc	45.8	4.2	6.1	42.3	27.0	n/a	6.9
		DId	28.3	2.3	4.1	26.5	16.0	n/a	4.1
		DIe	12.0	1.8	2.2	13.0	6.1	n/a	1.5
		DIf	8.7	2.2	2.4	8.4	3.9	n/a	0.6
	ΔP=-20 MPa	DIa	553.7	9.8	22.5	298.8	185.1	5.3	n/a
		DIb	382.5	10.1	12.6	200.2	65.8	3.6	n/a
		DIc	148.0	3.4	6.6	86.5	54.3	2.6	468.6
		DId	74.5	2.2	4.1	43.1	31.6	1.5	83.9
		DIe	19.8	1.2	2.0	9.2	7.1	0.4	16.5
		DIf	12.0	1.1	1.9	5.1	3.7	0.3	12.1
Model DI,rel. dike op. 1 m	ΔP=20 MPa	DIa	7.1	7.6	5.7	5.9	2.7	n/a	7.2
		DIb	4.5	5.4	4.2	4.1	0.8	n/a	5.7
		DIc	1.8	2.0	2.4	1.8	0.7	n/a	3.4
		DId	0.8	0.7	1.8	0.2	1.1	n/a	2.2
		DIe	0.8	1.2	1.4	0.3	1.0	n/a	1.1
		DIf	0.8	1.8	1.9	1.0	0.9	n/a	0.5
	ΔP=-20 MPa	DIa	24.1	7.6	6.8	8.7	0.5	7.0	n/a
		DIb	13.3	5.0	4.2	4.4	0.6	5.1	n/a
		DIc	3.6	1.9	1.6	1.0	0.9	2.9	n/a
		DId	1.3	1.0	1.3	0.4	0.7	1.6	n/a
		DIe	1.6	0.7	1.0	0.8	1.0	0.1	6.4
		DIf	1.3	0.8	1.4	0.2	0.9	0.1	6.0
Model DI, crack 12 MPa	ΔP=20 MPa	DIa	14.3	12.3	9.1	11.2	9.3	n/a	5.5
		DIb	9.2	6.9	6.6	8.6	5.9	n/a	4.2
		DIc	3.9	3.0	3.1	4.8	1.9	n/a	2.4
		DId	2.0	1.3	2.0	0.2	0.6	n/a	1.5
		DIe	1.0	0.7	1.5	0.2	0.0	n/a	0.8
		DIf	1.1	1.2	2.2	1.6	0.1	n/a	0.3
	ΔP=-20 MPa	DIa	11.1	15.5	11.9	17.6	2.7	12.9	n/a
		DIb	5.6	6.0	5.7	5.5	0.2	6.9	n/a
		DIc	2.8	1.9	2.0	0.4	0.9	3.2	n/a
		DId	1.5	1.0	1.2	0.5	0.7	1.5	n/a
		DIe	0.6	0.6	0.6	0.7	0.2	0.2	0.9
		DIf	0.5	0.9	1.0	0.7	0.1	0.2	1.6

Table A-4: Model DI, Methods 1-3: Discrepancies obtained for a spherical source pressurized by $\Delta P = 20$ MPa or $\Delta P = -20$ MPa and a dike opening by 1 m modelled applying on its walls either a fixed displacements (Method 1), relative displacements (Method 2), or an overpressure of 12 MPa (Method 3). Elastic parameters are $\nu = 0.25$ and $E = 10$ GPa. See also corresponding Figures 4.8 & A-1

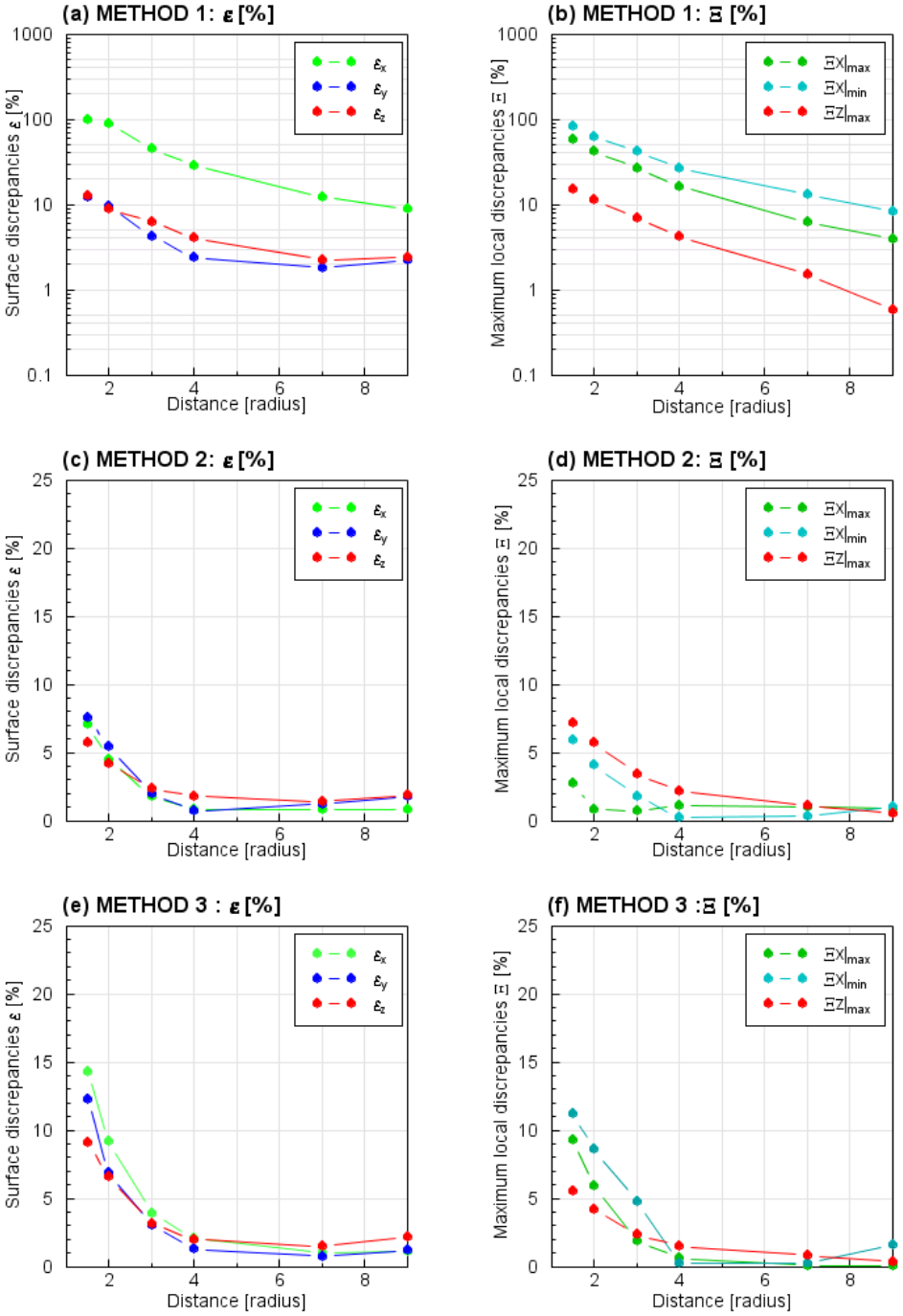

Figure A-1: Model DI: Surface (ϵ) and maximum local (Ξ) discrepancies obtained for models combining a spherical source pressurized by $\Delta P = +20$ MPa juxtaposed to a dike opening by 1 m, modelled with Methods 1-3 (*from top to bottom*). Corresponding discrepancies values are listed in Table A-4.

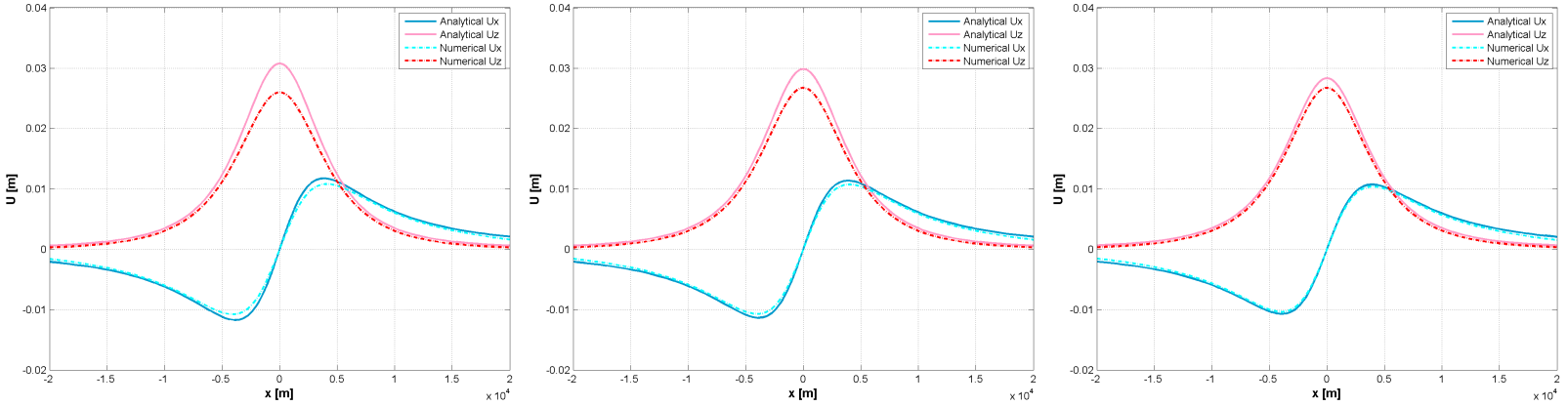

(a) Model A, $\Delta P2 = 20$ MPa, Distance 2.5 (G'1a)

(b) Model A, $\Delta P2 = 20$ MPa, Distance 3 (G'1b)

(c) Model A, $\Delta P2 = 20$ MPa, Distance 4 (G'1c)

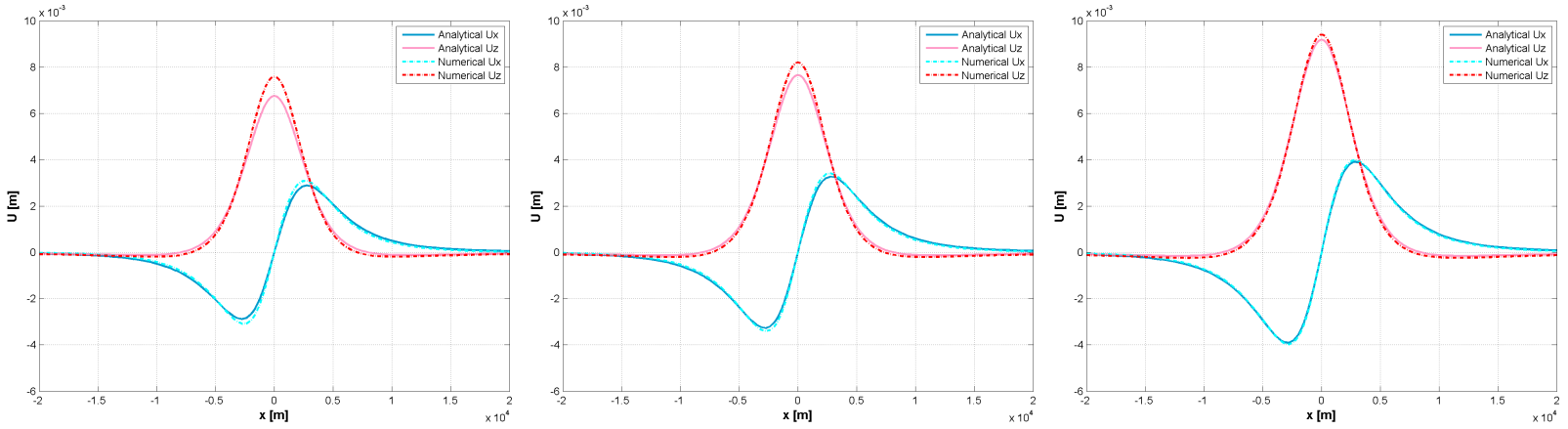

(d) Model A, $\Delta P2 = -20$ MPa, Distance 2.5 (G'1a)

(e) Model A, $\Delta P2 = -20$ MPa, Distance 3 (G'1b)

(f) Model A, $\Delta P2 = -20$ MPa, Distance 4 (G'1c)

Figure A-2: Models A (Group G1'a): Surface displacements across the centre of the deformation sources for models with two superposed sources separated by a distance of 2.5, 3 and 4 radii. The upper source pressurization is $\Delta P1 = 20$ MPa (*top*) and the lower source pressurization is $\Delta P2 = \pm 20$ MPa (*bottom*).

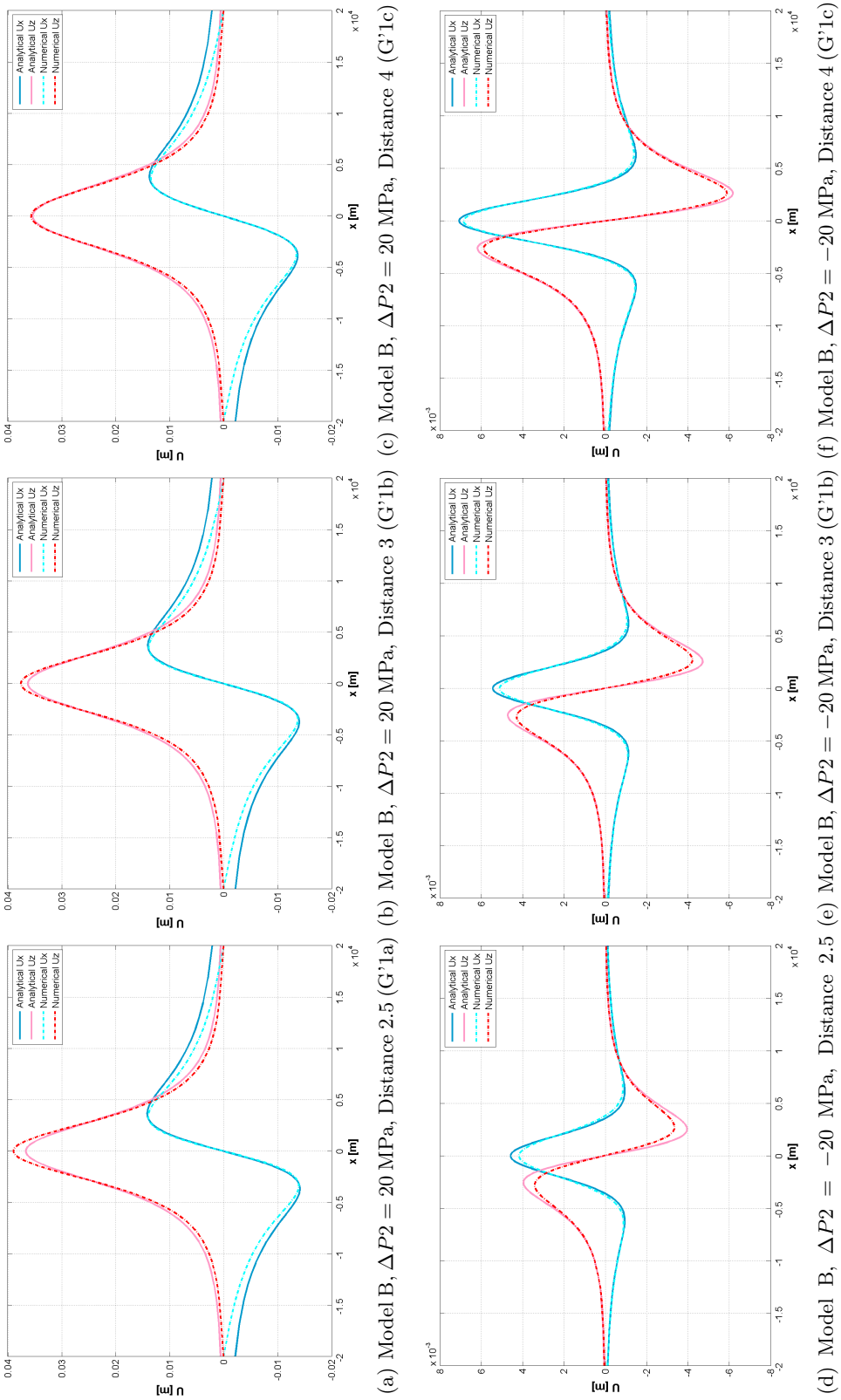

(a) Model B, $\Delta P2 = 20$ MPa, Distance 2.5 (G'1a) (b) Model B, $\Delta P2 = 20$ MPa, Distance 3 (G'1b) (c) Model B, $\Delta P2 = 20$ MPa, Distance 4 (G'1c)

(d) Model B, $\Delta P2 = -20$ MPa, Distance 2.5 (e) Model B, $\Delta P2 = -20$ MPa, Distance 3 (G'1b) (f) Model B, $\Delta P2 = -20$ MPa, Distance 4 (G'1c) (G'1a)

Figure A-3: Models B (Group G1'a): Surface displacements across the centre of the deformation sources for models with two superposed sources separated by a distance of 2.5, 3 and 4 radii. The left-hand source pressurization is $\Delta P1 = 20$ MPa (*top*) and the right-hand source pressurization is $\Delta P2 = \pm 20$ MPa (*bottom*).

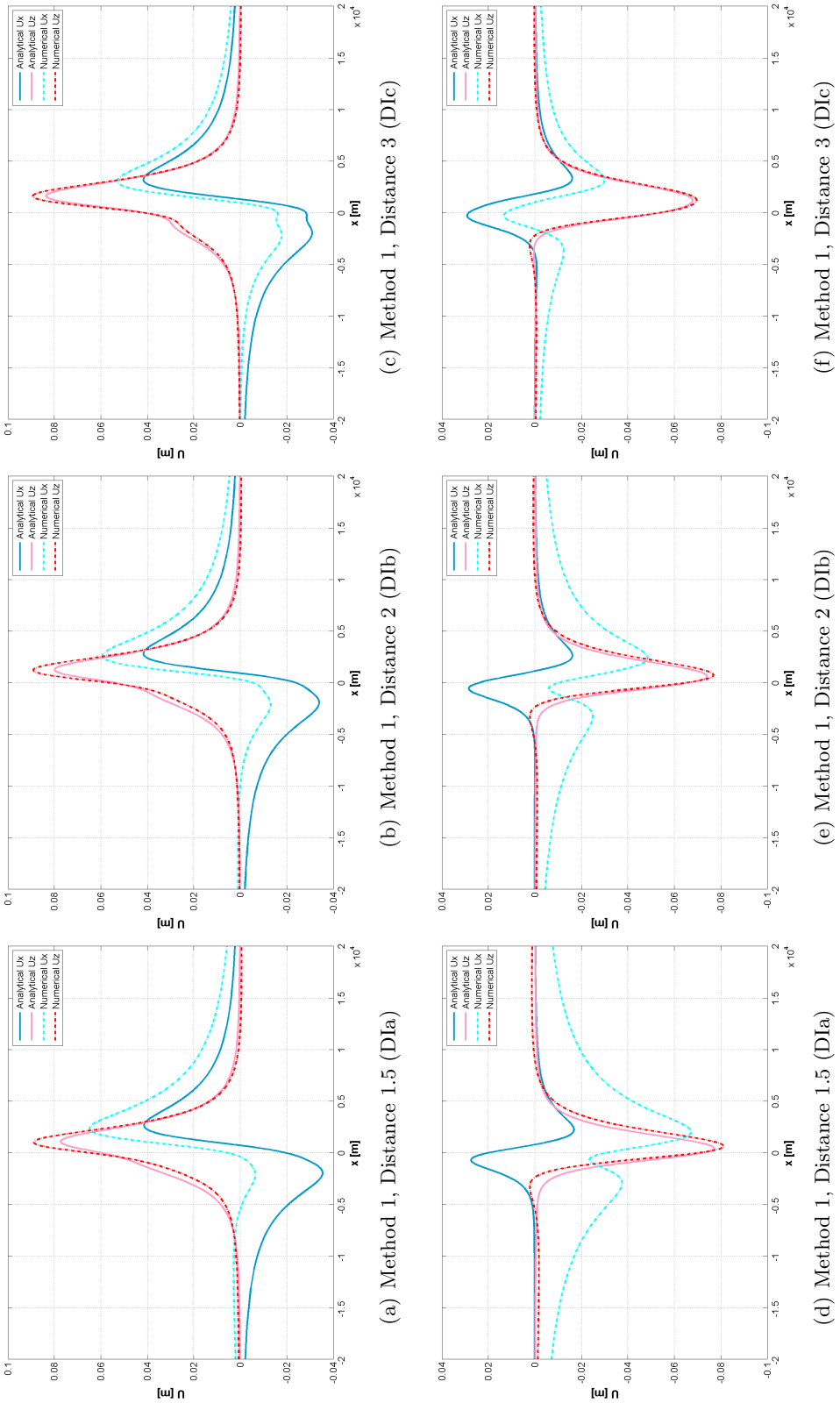

(a) Method 1, Distance 1.5 (DIa)
(b) Method 1, Distance 2 (DIb)
(c) Method 1, Distance 3 (DIc)
(d) Method 1, Distance 1.5 (DIa)
(e) Method 1, Distance 2 (DIb)
(f) Method 1, Distance 3 (DIc)

Figure A-4: Model DIa,b,c (Method 1): Surface displacements across the centre of the deformation sources for models of a dike opening by 1 m, modelled by Method 1, juxtaposed to a spherical source pressurized by either $\Delta P2 = +20$ MPa (*top*) or $\Delta P2 = -20$ MPa (*bottom*). The sources are separated by a distance of 1.5 radii, 2 and 3 radii.

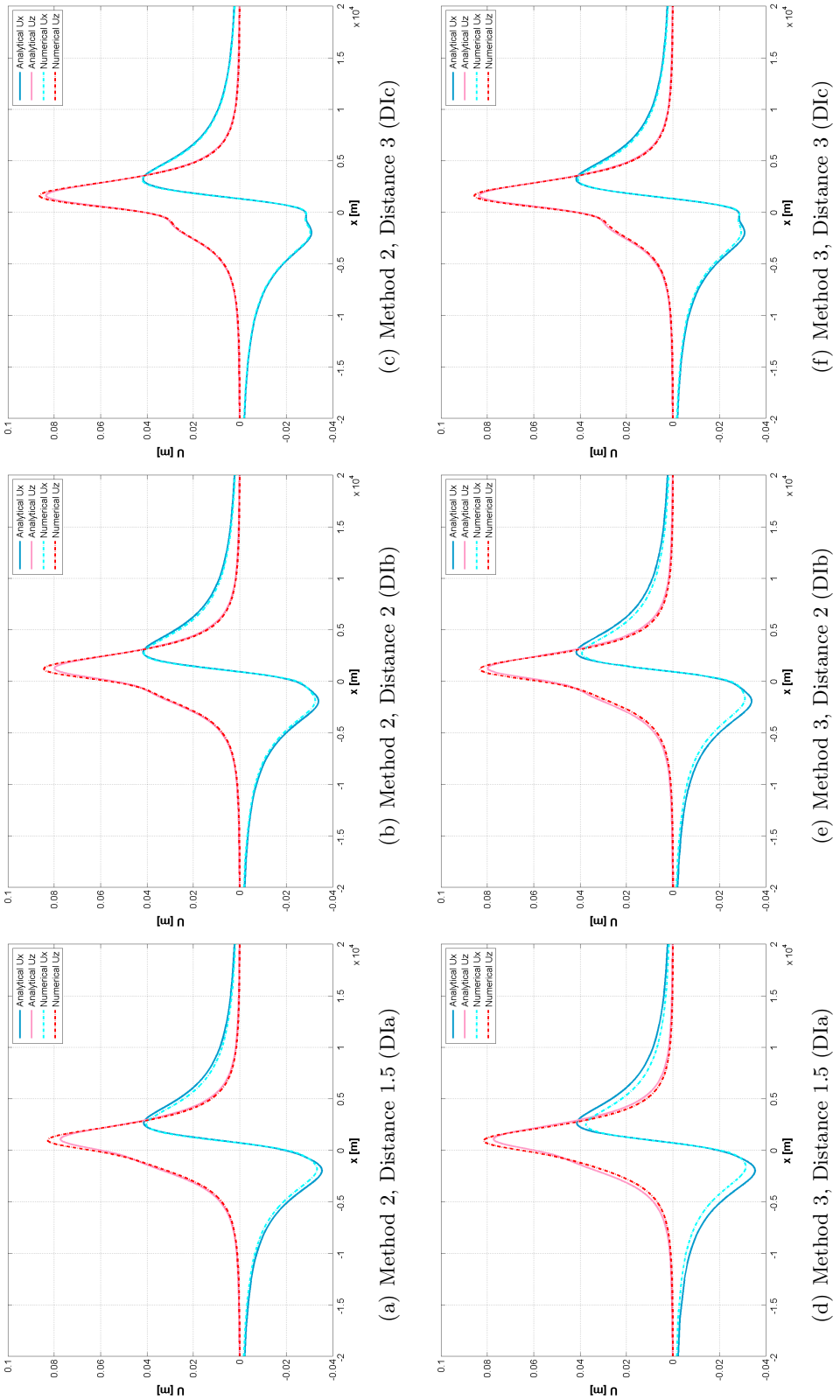

(a) Method 2, Distance 1.5 (DIa)
(b) Method 2, Distance 2 (DIb)
(c) Method 2, Distance 3 (DIc)
(d) Method 3, Distance 1.5 (DIa)
(e) Method 3, Distance 2 (DIb)
(f) Method 3, Distance 3 (DIc)

Figure A-5: Model DIa,b,c: Surface displacements across the centre of the deformation sources for models of a dike opening by 1 m, modelled by Method 2 (*top row*) or Method 3 (*bottom row*), juxtaposed to a spherical source pressurized by $\Delta P2 = +20$ MPa. The sources are separated by a distance of 1.5 radii, 2 and 3 radii.

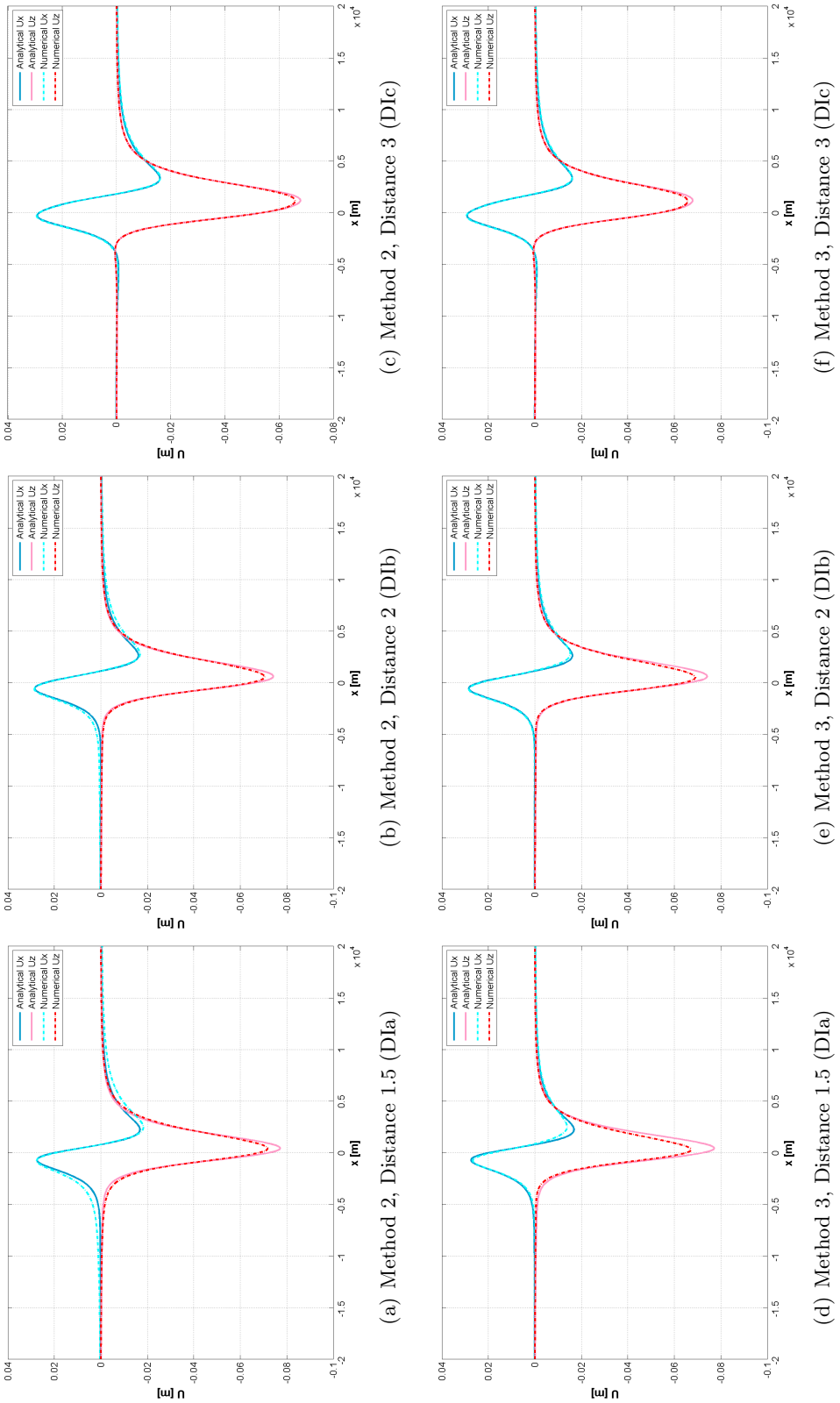

(a) Method 2, Distance 1.5 (DIa)
(b) Method 2, Distance 2 (DIb)
(c) Method 2, Distance 3 (DIc)
(d) Method 3, Distance 1.5 (DIa)
(e) Method 3, Distance 2 (DIb)
(f) Method 3, Distance 3 (DIc)

Figure A-6: Model DIa,b,c: Surface displacements across the centre of the deformation sources for models of a dike opening by 1 m, modelled by Method 2 (*top row*) or Method 3 (*bottom row*), juxtaposed to a spherical source pressurized by $\Delta P2 = -20$ MPa. The sources are separated by a distance of 1.5 radii, 2 and 3 radii.

Appendix B

Additional material for models H1-H2 (Chapter 6)

Model	'Full solution'				'Summed solution'			
	ϵ_x	ϵ_z	Ξ_x	Ξ_z	ϵ_x	ϵ_z	Ξ_x	Ξ_z
G1a	3.3	5.6	7.0	13.9	–	–	–	–
G1b	2.2	4.1	4.6	8.9	–	–	–	–
G1c	1.1	2.4	2.2	4.2	–	–	–	–
G1d	0.7	1.7	1.1	2.3	–	–	–	–
G1e	0.4	1.2	0.3	0.7	–	–	–	–
G1f	0.4	1.1	0.2	0.5	–	–	–	–
H1a	54.1	9.9	67.2	23.5	56.3	15.2	79.2	40.7
H1b	54.4	11.6	70.9	29.6	56.1	15.0	78.9	40.4
H1c	54.9	13.0	74.8	35.0	55.8	14.6	78.4	39.9
H1d	55.1	13.4	76.2	36.9	55.6	14.2	78.1	39.7
H1e	55.0	13.3	77.5	38.9	55.0	13.5	78.1	39.5
H1f	54.8	13.1	78.2	39.7	54.9	13.2	78.3	39.8
H2a	3.7	5.7	8.2	9.6	1.7	1.9	1.0	4.6
H2b	2.8	4.2	5.7	4.5	1.7	1.9	1.0	4.6
H2c	2.2	2.7	3.2	0.4	1.7	1.9	1.0	4.5
H2d	1.9	2.2	2.2	2.3	1.0	1.9	1.0	4.5
H2e	1.8	2.0	1.3	4.0	1.7	1.9	1.0	4.5
H2f	2.0	2.3	1.3	4.1	2.4	2.8	1.5	3.9

Table B-1: Effect of crustal heterogeneities: Model A-G1' compared to Models H1 and H2: Surface (ϵ) and maximum local (Ξ) discrepancies [%]. The 'Full solution' correspond to the solution of the FE model with the two sources. The 'Summed solution' correspond to the sum of the solution of two models, one with the upper source and the second one with the lower source. The comparison between the 'Full' and the 'Summed' solutions allow to isolate the effect of the source interaction. In all models, the two spherical sources, with radii $a = 500m$, are pressurized by $\Delta P_1 = \Delta P_2 = 20$ MPa, and the Poisson's ration is $\nu = 0.25$. In Model A, the crust is homogeneous, with Young's modulus $E = 10$ GPa. In Model H1, the crust is heterogeneous, with an 2 km thick upper layer, relatively soft compared to the rest of the crust with $E = 1$ GPa and $E = 10$ GPa, respectively. In Model H2, a $3x3x1$ km rigid sill with $E = 20$ GPa is located at 2 km depth, above the two spherical sources, in a crust with $E = 10$ GPa. See also Figures 6.1 & 6.3.

Appendix C

Additional material for inversions (Chapter 6)

Model #	Inv. #		Full Mean	Full σ	Full Min.	Full Q1	Full Median	Full Q3	Full Max.	Sum Mean	Sum σ	Sum Min.	Sum Q1	Sum Median	Sum Q3	Sum Max.
A-G1'a (2.5 radii)	1	z_2	16.2	2.3	10.4	14.7	16.2	17.8	22.7	3.8	2.4	-2.7	2.2	4.0	5.3	9.0
	2	ΔV_2	-23.1	2.7	-30.4	-25.0	-23.2	-21.1	-15.9	-4.9	3.8	-13.3	-7.7	-5.3	-2.8	7.3
	3	ΔV_1	-16.2	1.9	-21.3	-17.5	-16.3	-14.9	-11.2	-3.8	2.6	-9.6	-5.6	-4.1	-2.4	4.4
	4	ΔV_1	-32.2	19.3	-78.1	-42.5	-34.0	-18.8	12.7	-37.5	23.0	-102.1	-53.3	-37.8	-21.8	21.1
		ΔV_2	22.9	28.1	-41.4	2.6	24.5	38.1	88.1	48.4	32.8	-26.0	26.4	51.1	70.1	140.6
	5	ΔV_1	-1235.58	2540.08	-7451.55	-2497.98	-100.56	-100.31	7653.59	-1761.4	3602.6	-7538.4	-4450.7	-2381.0	-267.3	6809.6
		z_1	10.68	22.37	-31.24	4.47	8.34	13.83	63.68	12.2	19.9	-83.5	4.7	14.3	21.9	54.7
		ΔV_2	1197.69	2526.16	-7699.64	74.22	85.39	2442.18	7427.02	1762.7	3601.3	-6804.0	262.4	2384.9	4449.8	7510.6
		z_2	-51.98	46.75	-99.10	-93.07	-77.12	-16.41	34.50	-7.0	42.7	-100.0	-16.9	-8.5	12.0	319.3
A-G1'b (3 radii)	1	z_2	15.5	2.3	10.8	13.8	14.9	16.8	22.2	-1.0	2.1	-5.9	-2.1	-1.0	0.4	3.7
	2	ΔV_2	-22.6	2.8	-30.8	-24.3	-22.3	-20.6	-16.1	-0.1	3.6	-8.3	-2.7	-0.4	2.2	9.2
	3	ΔV_1	-14.7	1.8	-19.6	-15.6	-14.4	-13.4	-10.8	0.5	2.3	-4.6	-1.2	0.3	1.8	6.5
	4	ΔV_1	-10.2	18.0	-58.7	-22.0	-9.9	3.8	36.3	37.7	22.1	-21.1	23.3	38.3	52.9	80.5
		ΔV_2	-7.1	27.9	-79.0	-27.8	-7.2	9.8	69.7	-57.3	33.7	-124.1	-82.8	-58.1	-35.4	32.7
	5	ΔV_1	-1446.32	3655.67	-7651.35	-4619.19	-726.84	393.64	6793.18	-506.2	2897.4	-7762.8	-1741.7	-136.0	251.5	6934.4
		z_1	24.54	17.52	-38.98	10.38	18.46	38.89	63.23	7.9	17.1	-34.5	2.4	7.8	14.8	46.4
		ΔV_2	1360.40	3648.87	-6804.99	-421.73	493.82	4577.15	7605.95	447.1	2892.2	-6925.6	-256.3	100.4	1608.1	7717.3
		z_2	32.04	158.65	-96.59	-11.76	8.92	23.81	1213.71	4.2	141.5	-95.2	-41.3	-14.0	0.1	1177.0
A-G1'c (4 radii)	1	z_2	10.7	2.9	5.5	9.0	10.5	12.7	17.8	-1.9	2.4	-7.2	-3.4	-1.9	-0.3	4.0
	2	ΔV_2	-17.2	3.7	-25.6	-20.1	-16.7	-15.1	-9.9	2.1	4.4	-7.7	-0.8	1.9	5.5	11.9
	3	ΔV_1	-9.4	2.1	-14.5	-11.0	-9.3	-8.2	-5.2	1.7	2.5	-4.0	0.1	1.7	3.4	7.5
	4	ΔV_1	11.8	14.2	-22.6	2.4	11.2	21.5	52.2	21.0	16.1	-22.4	11.8	20.4	32.3	52.7
		ΔV_2	-38.4	23.4	-110.6	-52.7	-38.0	-22.8	22.9	-33.7	27.7	-90.7	-51.9	-34.7	-19.7	41.0
	5	ΔV_1	-321.53	1578.23	-6437.40	-102.02	-100.15	217.33	4628.14	-875.5	2600.4	-8103.1	-1886.4	-100.1	-22.4	3942.1
		z_1	-0.22	7.51	-23.10	-3.53	-0.23	3.61	15.34	10.9	17.6	-65.4	1.9	8.4	19.0	50.8
		ΔV_2	459.63	1481.49	-4683.66	26.50	46.11	60.47	6401.48	871.1	2568.2	-3964.6	55.6	75.4	1858.6	8038.9
		z_2	109.55	288.03	-97.01	-79.29	-14.84	193.31	1096.36	-3.4	171.2	-99.1	-75.4	-10.2	7.5	1471.1

Table C-1: Inversion #1-5, model with two superposed inflating source (Model A-G1'a-c, 2.5 to 4 radii separation): distribution of the error on the parameters retrieved in the 100 inversions of the synthetic (FE) solution. A Gaussian noise with 1 cm standard deviation was added to the original FE solution, and a bootstrapped method was applied to obtain the 100 synthetic dataset.

Continued on Next Page...

			'Full' solution							Summed 'M1+M2' solution						
Model #	Inv. #		Mean	σ	Min.	Q1	Median	Q3	Max.	Mean	σ	Min.	Q1	Median	Q3	Max.
A-G1'd (5 radii)	1	z_2	3.4	2.5	-1.3	1.5	3.5	5.0	12.6	2.6	3.2	-4.7	0.3	2.4	4.5	12.2
	2	ΔV_2	-5.4	4.0	-18.2	-8.1	-5.5	-2.3	3.2	-3.8	5.1	-17.0	-6.4	-4.1	0.0	9.7
	3	ΔV_1	-2.9	2.0	-9.9	-4.2	-3.0	-1.3	1.2	-2.1	2.7	-9.5	-3.6	-2.1	-0.2	4.8
	4	ΔV_1	9.9	8.2	-10.5	5.3	10.3	14.5	37.3	-3.0	9.2	-23.7	-10.2	-2.7	3.1	18.1
		ΔV_2	-29.0	22.9	-105.6	-40.9	-29.5	-18.9	36.5	6.3	25.8	-45.3	-9.4	4.5	27.1	66.9
	5	ΔV_1	-1406.66	2064.78	-8127.84	-2456.79	-648.80	81.53	1357.96	-425.8	1193.3	-6132.5	-408.0	-98.9	115.1	1547.1
		z_1	8.70	35.21	-73.72	-13.32	18.97	38.47	52.05	-1.9	35.2	-89.3	-7.4	8.3	18.3	64.6
		ΔV_2	1412.23	2027.74	-654.91	-48.45	599.69	2432.93	8102.75	511.0	1123.7	-1357.9	12.9	72.5	347.6	6102.0
		z_2	30.29	151.80	-81.60	-1.66	7.10	22.69	1134.05	84.8	201.1	-99.8	-26.6	0.2	164.9	808.8
A-G1'e (8 radii)	1	z_2	13.5	3.3	5.3	11.2	13.6	15.8	24.6	14.4	4.0	4.7	11.9	13.9	17.3	25.3
	2	ΔV_2	-2.5	5.1	-17.9	-6.1	-2.5	0.7	11.1	-2.5	5.1	-17.9	-6.1	-2.5	0.7	11.1
	3	ΔV_1	-0.4	1.8	-5.8	-1.7	-0.4	0.9	4.6	-0.7	2.2	-6.3	-2.4	-0.6	0.7	5.2
	4	ΔV_1	-8.1	11.3	-43.4	-15.5	-8.7	-0.6	17.8	-6.6	14.8	-45.7	-16.2	-5.5	2.5	29.4
		ΔV_2	10.4	21.9	-37.8	-3.7	10.4	26.4	75.7	8.8	28.0	-55.2	-8.5	6.4	28.0	83.4
	5	ΔV_1	-510.54	1952.42	-8186.92	-100.11	50.94	101.31	2193.69	392.2	720.5	-100.7	127.6	227.4	324.7	5620.4
		z_1	2.02	21.96	-75.83	-3.62	2.65	8.20	42.82	-7.9	10.8	-40.5	-13.6	-6.8	-0.7	16.4
		ΔV_2	592.87	1880.68	-1286.36	12.95	32.47	56.69	8094.05	-5.1	30.8	-81.5	-24.0	-6.0	15.6	73.5
		z_2	129.22	202.09	-97.46	-5.69	101.20	243.30	1052.18	266.5	263.4	-86.4	116.3	191.4	304.4	1483.9
A-G1'f (10 radii)	1	z_2	-2.6	3.5	-10.2	-5.3	-2.7	-0.4	6.3	11.6	5.3	0.7	8.6	11.5	14.3	29.8
	2	ΔV_2	5.4	6.7	-10.6	0.8	5.1	10.4	19.9	-18.2	6.9	-39.1	-22.1	-18.5	-14.3	-1.5
	3	ΔV_1	1.8	2.1	-2.8	0.4	1.7	3.3	6.7	-5.8	2.2	-11.6	-7.2	-5.7	-4.5	-0.7
	4	ΔV_1	2.9	7.4	-19.2	-2.4	3.7	8.0	17.1	-5.0	8.9	-30.9	-9.4	-4.6	0.3	18.4
		ΔV_2	-3.9	23.9	-44.0	-22.4	-5.3	12.3	72.8	-2.8	27.9	-87.1	-20.8	0.0	16.2	78.8
	5	ΔV_1	313.85	671.91	-152.21	69.44	92.82	308.13	4429.06	-1815.2	2284.1	-7694.3	-2864.3	-1016.8	-171.1	2721.1
		z_1	-14.07	29.44	-80.20	-14.05	-1.49	3.85	19.74	34.1	34.1	-95.3	13.7	40.3	58.2	85.7
		ΔV_2	-7.10	54.68	-98.93	-33.94	10.03	28.04	111.35	1746.4	2250.1	-2788.5	86.4	951.0	2758.4	7602.2
		z_2	250.29	331.57	-89.66	1.99	137.88	343.91	1476.54	56.9	137.8	-99.9	12.9	31.6	45.6	874.2

Table C-1: *(Continued)* Inversion #1-5, Model A-G1'a-f (2.5 to 10 radii separation): distribution of the errors on the parameters retrieved in the 100 inversions of the synthetic (FE) solution. A Gaussian noise with 1 cm standard deviation was added to the original FE solution, and a bootstrap method was applied to obtain the 100 synthetic datasets. The mean, the standard deviation (*sigma*), the minimum, the first and third quartile (Q1 and Q3), the median, and the maximum error of each parameters are given for Inversions #1 to #5 of the 'full' solution of Model A, and of the summed 'M1+M2' solution. The errors distribution is also represented in Figure 6.4, Figures 6.5 & 6.6.

			Full							Sum						
Model #	Inv. #		Mean	σ	Min.	Q1	Median	Q3	Max.	Mean	σ	Min.	Q1	Median	Q3	Max.
A-G1'a (2.5 radii)	1	z_2	16.40	3.67	9.18	3.67	16.28	19.03	25.50	3.93	2.58	-1.79	2.39	4.28	5.81	10.07
	2	ΔV_2	-23.19	4.46	-33.99	-26.37	-22.72	-20.37	-12.93	-5.11	3.93	-13.99	-8.03	-5.70	-2.74	4.94
	3	ΔV_1	-16.26	3.04	-23.26	-18.42	-16.18	-14.38	-9.47	-3.95	2.80	-10.28	-5.99	-4.30	-2.29	2.80
	4	ΔV_1	-31.69	28.96	-97.35	-52.05	-26.87	-13.21	43.00	-38.27	29.33	-115.73	-57.26	-42.01	-17.81	40.41
		ΔV_2	22.43	42.50	-87.84	-4.81	19.29	49.54	123.16	49.36	41.32	-63.26	18.52	55.78	75.28	157.86
	5	ΔV_1	-965.80	2868.89	-12855.57	-2390.38	-100.76	-100.28	6594.76	-1304.65	3508.57	-7578.22	-3961.25	-760.15	126.34	6840.46
		z_1	10.57	22.00	-37.07	0.94	8.20	14.29	71.43	9.82	28.01	-93.88	3.59	10.00	17.79	63.57
		ΔV_2	676.15	2317.90	-6594.30	63.28	84.63	2297.21	6493.38	1328.53	3492.68	-6829.97	34.83	739.49	3960.13	7561.17
		z_2	12.51	352.00	-99.86	-91.52	-40.64	-11.72	2576.13	22.66	112.81	-98.76	-16.74	-7.77	16.25	651.17
A-G1'b (3 radii)	1	z_2	15.92	3.64	7.66	3.64	15.67	18.41	25.44	-0.97	2.60	-7.91	-2.80	-0.82	0.70	6.11
	2	ΔV_2	-23.05	4.24	-33.44	-26.02	-22.85	-19.81	-12.32	-0.15	4.48	-12.37	-3.26	-0.84	3.13	12.72
	3	ΔV_1	-23.05	4.24	-33.44	-26.02	-22.85	-19.81	-12.32	0.49	2.96	-7.33	-1.58	0.05	2.62	8.65
	4	ΔV_1	-10.84	24.23	-72.21	-29.53	-11.15	6.36	38.47	40.70	22.47	-5.09	22.46	40.97	57.42	104.53
		ΔV_2	-6.40	37.01	-85.29	-32.77	-6.62	19.82	86.06	-61.85	34.05	-161.68	-88.04	-59.75	-34.40	3.82
	5	ΔV_1	-1429.71	3986.99	-24405.29	-2315.39	-559.39	-95.17	6823.82	-54.64	2394.86	-7775.37	-572.26	-99.90	255.98	6137.96
		z_1	19.03	25.66	-54.60	8.21	13.26	39.04	95.94	7.42	20.12	-51.34	-4.25	7.58	17.82	59.77
		ΔV_2	954.12	3075.31	-6839.19	64.89	396.11	2072.75	7566.97	-4.94	2380.18	-6174.76	-294.15	75.52	507.02	7727.18
		z_2	99.68	427.95	-96.88	-13.30	-1.29	34.13	3201.15	5.96	115.43	-98.20	-44.49	-12.06	20.06	743.56
A-G1'c (4 radii)	1	z_2	10.67	3.58	2.78	3.58	10.55	12.73	20.39	-1.48	2.60	-7.02	-3.37	-1.09	0.23	4.05
	2	ΔV_2	-16.86	4.68	-27.89	-19.75	-16.79	-14.08	-6.67	1.64	4.70	-8.45	-1.53	0.92	5.10	13.99
	3	ΔV_1	-9.33	2.69	-15.98	-10.94	-9.26	-7.67	-3.21	1.35	2.72	-4.07	-0.36	0.92	3.40	7.94
	4	ΔV_1	8.54	20.46	-39.24	-5.69	10.23	24.16	59.80	18.07	16.89	-35.17	9.50	18.17	27.40	63.87
		ΔV_2	-31.71	35.55	-124.48	-53.72	-34.45	-8.28	50.53	-29.25	29.19	-109.36	-47.10	-30.23	-13.69	54.86
	5	ΔV_1	46.83	1006.94	-2980.56	-101.48	-100.05	221.32	4141.27	-151.33	1992.27	-6393.18	-273.33	-98.83	264.22	4881.07
		z_1	0.69	10.72	-25.13	-5.00	-0.62	7.96	19.41	6.84	20.34	-59.48	-0.79	8.51	17.21	58.79
		ΔV_2	166.05	712.06	-1673.54	5.55	49.31	64.78	2978.17	173.86	1966.48	-4924.12	-263.16	65.29	206.16	6249.87
		z_2	108.31	301.09	-100.00	-83.61	-9.06	131.56	1202.50	16.79	183.49	-99.84	-70.11	-10.19	1.21	926.18

Table C-2: Inversion #1-5, model with two superposed inflating source (Model A-G1'a-c, 2.5 to 4 radii separation): distribution of the error on the parameters retrieved in the 100 inversions of the synthetic (FE) solution. A Gaussian noise with 1 cm standard deviation was added to the original FE solution, and a 100 synthetic dataset by downsampling the orginal dataset to 500 data points.
Continued on Next Page...

			'Full' solution							Summed 'M1+M2' solution						
Model #	Inv. #		Mean	σ	Min.	Q1	Median	Q3	Max.	Mean	σ	Min.	Q1	Median	Q3	Max.
A-G1'd (5 radii)	1	z_2	3.57	3.49	-4.41	3.49	3.44	6.21	12.58	2.29	3.55	-6.72	0.13	1.78	5.02	12.69
	2	ΔV_2	-5.40	5.86	-19.13	-9.54	-6.06	-1.42	7.07	-3.02	5.76	-17.61	-7.09	-2.90	0.65	13.33
	3	ΔV_1	-2.94	2.92	-9.62	-5.14	-2.98	-1.27	4.02	-1.83	3.04	-9.97	-4.22	-1.58	0.01	6.72
	4	ΔV_1	-9.28	16.29	-58.42	-20.31	-8.47	1.26	24.43	-9.28	17.82	-58.32	-21.49	-8.98	2.29	42.39
		ΔV_2	12.73	32.76	-54.35	-9.85	10.36	33.68	111.30	14.71	33.94	-82.54	-8.27	15.55	38.07	104.27
	5	ΔV_1	-1449.52	2221.94	-8095.83	-2686.72	-102.39	107.48	1570.79	-828.06	2107.33	-8865.34	-846.15	92.21	124.97	2574.66
		z_1	1.67	49.74	-99.56	-46.27	19.10	46.29	68.49	-14.39	47.51	-98.34	-75.04	1.27	19.43	78.91
		ΔV_2	1518.95	2115.87	-130.64	-91.83	107.53	2642.39	8053.23	895.86	2046.12	-2545.09	-98.36	49.77	804.15	8844.38
		z_2	278.28	1076.70	-83.41	-0.33	18.27	23.54	5427.54	56.57	172.00	-98.66	-5.66	1.50	22.61	669.00
A-G1'e (8 radii)	1	z_2	1.00	4.11	-6.71	4.11	0.11	3.94	11.09	1.97	4.71	-7.26	-1.19	0.96	5.49	16.41
	2	ΔV_2	-2.42	7.05	-19.03	-7.71	-1.37	3.26	13.38	-1.79	7.84	-23.10	-8.02	-0.38	3.65	15.62
	3	ΔV_1	-0.36	2.60	-6.41	-2.23	0.05	1.34	4.99	-0.79	2.91	-7.89	-2.93	-0.48	1.34	5.55
	4	ΔV_1	9.45	11.93	-18.07	-0.20	10.31	17.09	42.39	-2.28	11.70	-29.52	-11.12	-1.12	6.53	20.81
		ΔV_2	-27.62	32.42	-115.06	-50.83	-25.57	-5.83	37.86	4.10	31.56	-60.15	-17.33	0.87	27.49	76.13
	5	ΔV_1	-477.02	1866.23	-8175.32	-100.19	29.80	165.37	2411.20	426.25	782.99	-100.66	110.37	218.70	372.35	5361.17
		z_1	3.37	22.33	-80.18	-4.93	3.02	11.64	50.63	-8.63	10.90	-37.86	-15.66	-7.04	-1.19	13.44
		ΔV_2	565.14	1790.42	-655.62	-2.09	27.61	60.76	8087.79	-6.09	29.90	-71.15	-25.71	-3.82	16.22	70.48
		z_2	120.31	207.85	-98.99	-7.40	37.84	232.33	1060.33	270.54	282.31	-93.43	112.86	196.09	293.02	1540.57
A-G1'f (10 radii)	1	z_2	-2.87	4.69	-13.60	4.69	-3.21	-0.34	9.67	12.66	6.30	0.81	8.45	11.63	15.59	30.20
	2	ΔV_2	6.20	9.46	-14.61	0.81	5.34	13.26	30.94	-19.38	8.30	-39.24	-23.73	-19.36	-13.47	0.25
	3	ΔV_1	2.04	2.70	-4.58	0.43	2.01	3.93	9.52	-6.22	2.47	-12.37	-7.46	-5.95	-4.89	-0.87
	4	ΔV_1	3.50	11.04	-32.77	-3.58	5.80	11.22	27.68	-5.57	10.00	-31.81	-12.29	-4.78	2.43	13.13
		ΔV_2	-4.99	38.45	-97.00	-32.09	-8.40	20.64	111.09	-2.15	33.32	-60.36	-27.28	-3.49	21.08	86.72
	5	ΔV_1	326.44	2901.47	-6066.87	68.40	117.66	241.73	23104.12	-1506.77	2153.72	-7694.61	-2311.73	-1000.05	-100.28	3617.51
		z_1	-16.86	32.42	-91.84	-28.71	-7.26	2.04	43.07	28.71	39.31	-100.00	8.11	31.74	57.62	86.08
		ΔV_2	203.78	1068.19	-308.85	-60.46	-2.95	23.72	5997.46	1431.39	2131.15	-3682.95	59.87	919.03	2143.59	7626.41
		z_2	223.55	422.95	-95.50	10.82	104.11	257.73	2992.86	27.61	81.61	-96.48	-2.70	29.74	38.84	335.64

Table C-2: *(Continued)* Inversion #1-5, Model A-G1'a-f (2.5 to 10 radii separation): distribution of the errors on the parameters retrieved in the 100 inversions of the synthetic (FE) solution. A Gaussian noise with 1 cm standard deviation was added to the original FE solution, and the 100 datasets were obtained by downsampling to 500 data points the solution with added noise. The mean, the standard deviation (*sigma*), the minimum, the first and third quartile (Q1 and Q3), the median, and the maximum error on each parameters are given for each Inversions #1 to #5 of the 'full' solution of Model A, and of the summed 'M1+M2' solution. The error distribution is also represented in Figure C-3 Figures C-4 & C-5, and Figures C-1 & C-2 give examples of the geographic repartition of the 'full' and summed 'M1+M2' downsampled dataset.

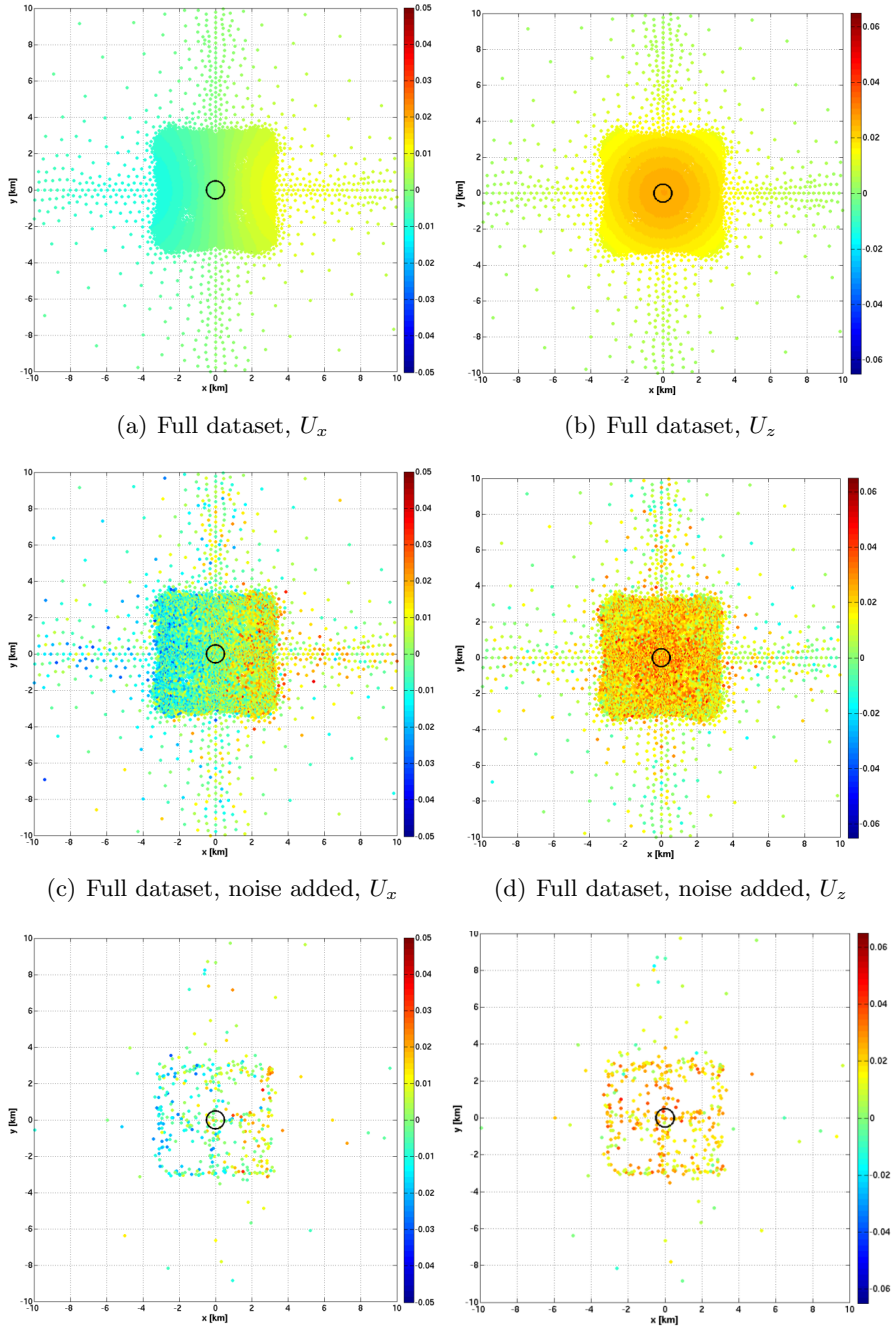

(a) Full dataset, U_x

(b) Full dataset, U_z

(c) Full dataset, noise added, U_x

(d) Full dataset, noise added, U_z

(e) Full dataset, noise added and downsampled, U_x

(f) Full dataset, noise added and downsampled, U_z

Figure C-1: Inversions of Models A, 'full' model: example of the noise introduced on the synthetic data and comparison of the data distribution for the complete and the downsampled solution. The model consists of two superposed sources Models A (Group G1'a), separated by a distance of 2.5 and pressurized by $\Delta P1 = \Delta P2 = 20$ MPa. The distribution of the complete 'original' synthetic dataset without any added noise is shown (*top*), after the addition of A Gaussian noise with 1 cm standard deviation (*middle*), and thirdly after having been downsampled from 1600 to 500 data points (*bottom*) are represented. The colour scheme indicates the magnitude of the surface displacements (U_x or U_z, respectively *left* and *right*)) and the position of the sources is represented (*black circle*).

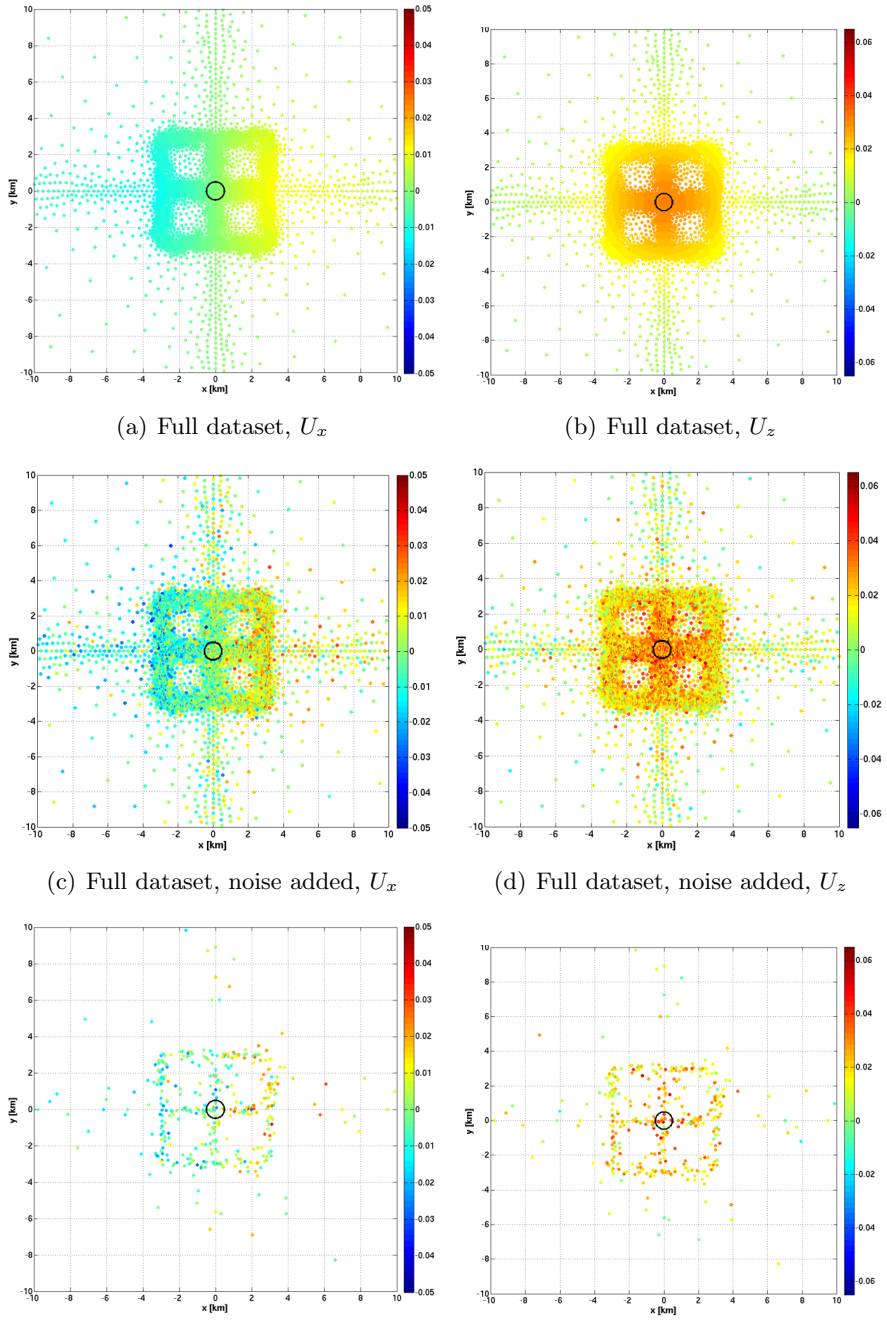

(a) Full dataset, U_x

(b) Full dataset, U_z

(c) Full dataset, noise added, U_x

(d) Full dataset, noise added, U_z

(e) Full dataset, noise added and downsampled, U_x

(f) Full dataset, noise added and downsampled, U_z

Figure C-2: Inversions of Models A, summed 'M1+M2' model: example of the noise introduced on the synthetic data and comparison of the data distribution for the complete and the downsampled solution. The model consists of two superposed sources Models A (Group G1'a), separated by a distance of 2.5 and pressurized by $\Delta P1 = \Delta P2 = 20$ MPa. The distribution of the complete 'original' synthetic dataset without any added noise is shown (*top*), after the addition of A Gaussian noise with 1 cm standard deviation (*middle*), and thirdly after having been downsampled from 1600 to 500 data points (*bottom*) are represented. The colour scheme indicates the magnitude of the surface displacements (U_x or U_z, respectively *left* and *right*)) and the position of the sources is represented (*black circle*).

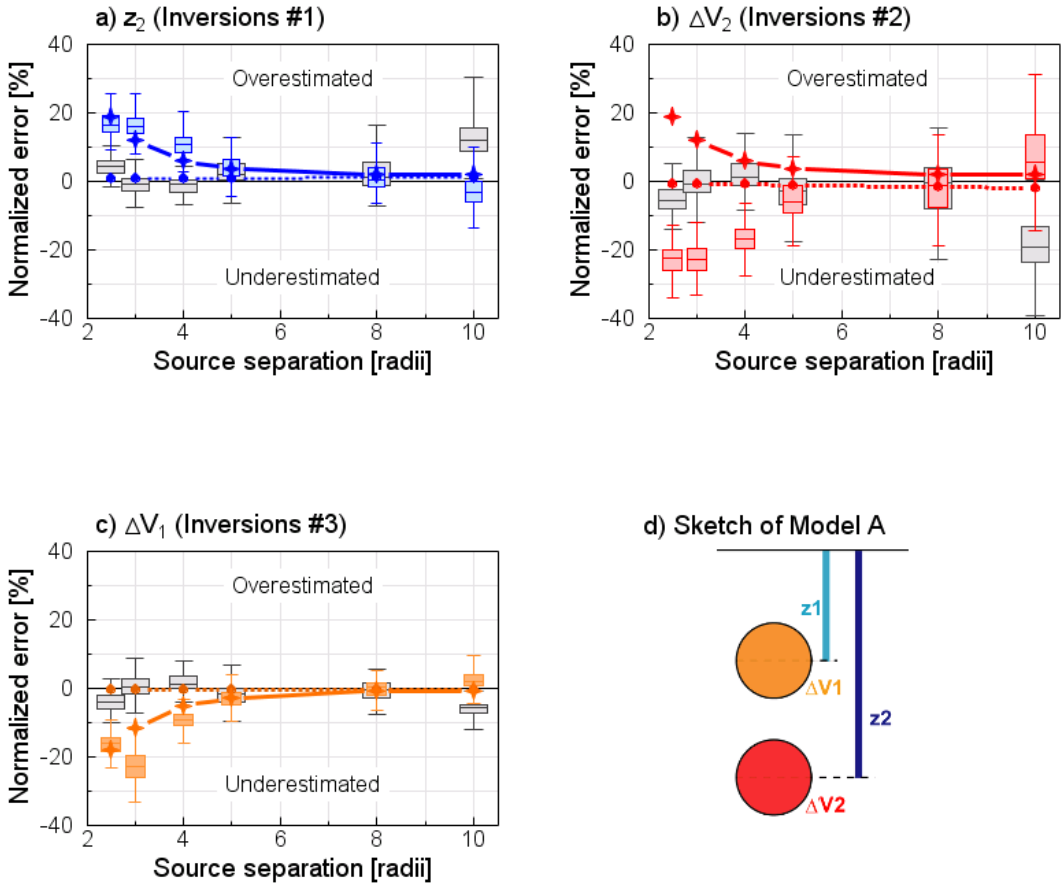

Figure C-3: Inversions #1-3: errors between original and retrieved parameters values obtained for a population of 100 inversions of the solution of the synthetic datasets (numerical reference model), using combined analytical models corresponding to Model A-G1'a to f. The reference models consist of two superposed spherical sources of radius a=500 m pressurized by $\Delta P1 = \Delta P2 = 20$ MPa. A Gaussian noise with $\sigma = 1$ cm has been added to the synthetic solution, which has then been downsampled from 1600 to 500 data points. The population of error between reference and retrieved parameter normalized by the reference parameter is plotted against the reference model source separation. The error distribution obtained for the full FE model and for the 'M1+M2' summed model are indicated in coloured and grey, respectively. The box-and-whiskers plot indicate the minimum, the first quartile, the median, the third quartile and the maximum of the error population. The error obtained in Chapter 5 for the original synthetic dataset are indicated with a solid line for the full FE model and with a dotted line for the 'M1+M2' summed model. The sources are separated by a distance of 2.5, 3, 4, 5, 8, 9 radii. Inversions #1 - #3 retrieve only one parameter at a time: (a) the deeper source depth z_2, (b) the deeper source volume change ΔV_2, (c) the shallower source volume change ΔV_1. (d) Sketch of Model A and source parameters inverted for.

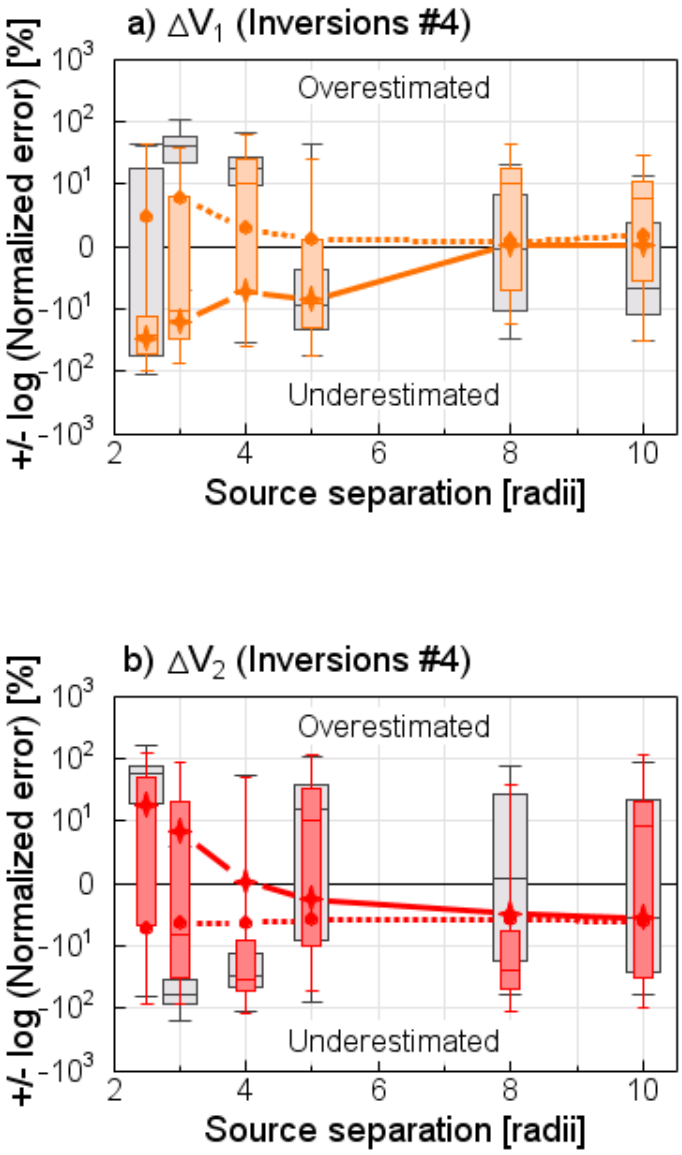

Figure C-4: Inversions #4: errors between original and retrieved parameters values obtained for a population of 100 inversions of the solution of the synthetic datasets (numerical reference model), using combined analytical models corresponding to Model A-G1'a to f. The reference models consist of two superposed spherical sources of radius a=500 m pressurized by $\Delta P1 = \Delta P2 = 20$ MPa. A Gaussian noise with $\sigma = 1$ cm of up to 1 cm has been added to the synthetic solution, which has then been downsampled from 1600 to 500 data points. The population of error between reference and retrieved parameter normalized by the reference parameter is plotted against the reference model source separation. The error distribution obtained for the full FE model and for the 'M1+M2' summed model are indicated in coloured and grey, respectively. The box-and-whiskers plot indicate the minimum, the first quartile, the median, the third quartile and the maximum of the error population. The error obtained in Chapter 5 for the original synthetic dataset are indicated with a solid line for the full FE model and with a dotted line for the 'M1+M2' summed model. The sources are separated by a distance of 2.5, 3, 4, 5, 8, 9 radii. Inversions #4 retrieve both source volume change: (a) the deeper source volume change ΔV_2, and (b) the shallower source volume change ΔV_1.

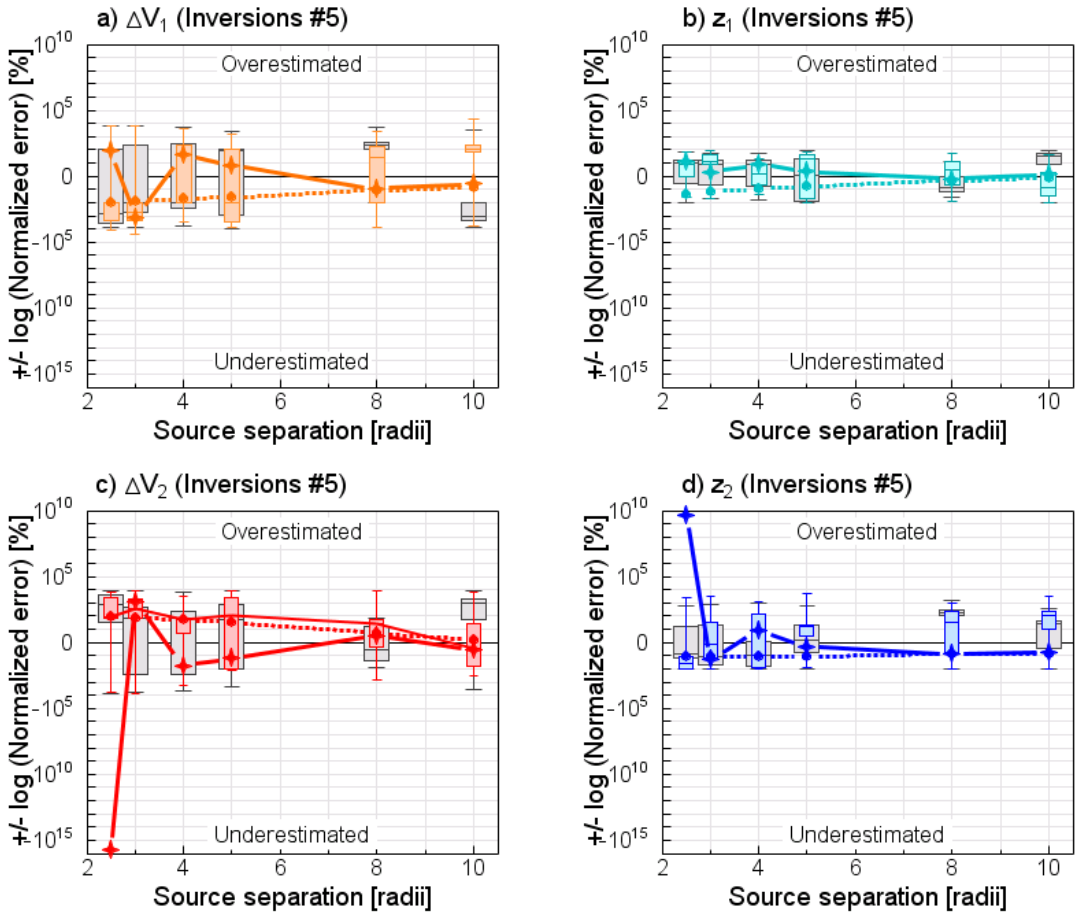

Figure C-5: Inversions #5: errors between original and retrieved parameters values obtained for a population of 100 inversions of the solution of the synthetic datasets (numerical reference model), using combined analytical models corresponding to Model A-G1'a to f. The reference models consist of two superposed spherical sources of radius a=500 m pressurized by $\Delta P_1 = \Delta P_2 = 20$ MPa. A Gaussian noise with $\sigma = 1$ cm has been added to the synthetic solution, which has then been downsampled from 1600 to 500 data points. The population of error between reference and retrieved parameter normalized by the reference parameter is plotted against the reference model source separation. The error distribution obtained for the full FE model and for the 'M1+M2' summed model are indicated in coloured and grey, respectively. The box-and-whiskers plot indicate the minimum, the first quartile, the median, the third quartile and the maximum of the error population. The error obtained in Chapter 5 for the original synthetic dataset are indicated with a solid line for the full FE model and with a dotted line for the 'M1+M2' summed model. The sources are separated by a distance of 2.5, 3, 4, 5, 8, 9 radii. Inversions #5 retrieve all parameters, source volume changes and depths: (a) the deeper source volume change ΔV_2 and (b) depth Δz_2, and (c) the shallower source volume change ΔV_1 and (d) depth z_1.

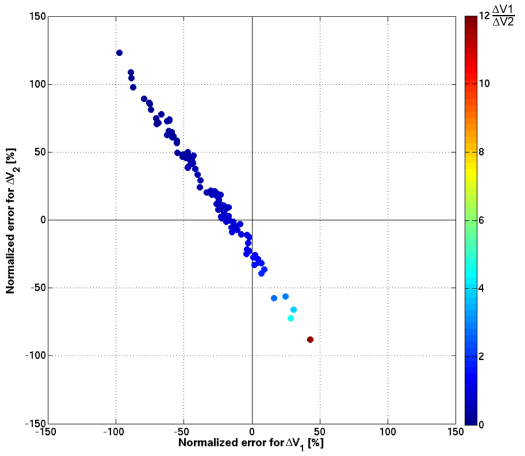

(a) Inv #4: Errors for ΔV_1 and ΔV_2

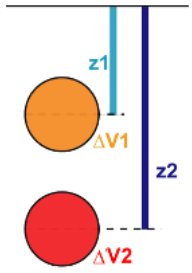

(b) Sketch of Model A

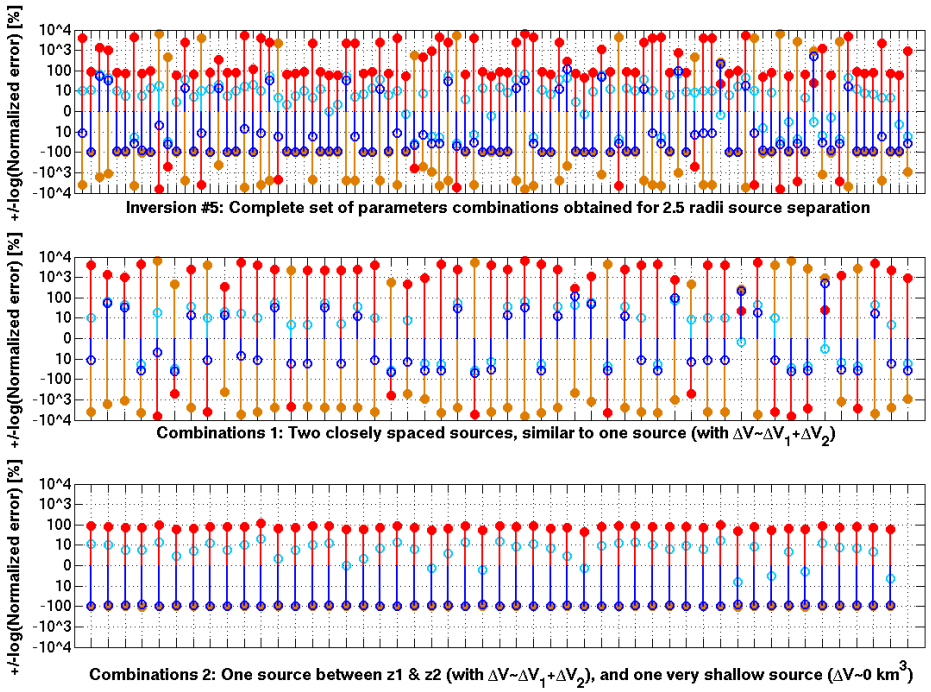

(c) Distribution of the errors obtained for ΔV_1, z_1, ΔV_2 and z_2

Figure C-6: Summary of the results of Inversions #4-5: relationship between the errors obtained for 100 co-inversions of either the volume changes ΔV_1 and ΔV_2 (Inversion #4), or volume changes and depths of the two sources (see also Figures C-4 & C-5). The reference model consists of two superposed spherical sources of radius a=500 m, at a distance of 2.5 radii, pressurized by $\Delta P1 = \Delta P2 = 20$ MPa (Model A-G1'a). A Gaussian noise A Gaussian noise with $\sigma = 1$ cm has been added to the synthetic solution, which has then been downsampled from 1600 to 500 data points. (a) Relationship between the errors obtained during the co-inversion of the two sources volume change (Inversion #4, Figure 6.5). The colour scale give the ratio between the volume of the upper and the lower source ($\Delta V_1/\Delta V_2$), (b) Sketch of Model A and source parameters inverted for, (c) Errors obtained for the volume change and depth (*circle*) of the two sources (*filled circle*): ΔV_1 (*orange*), z_1 (*clear blue*), ΔV_2 (*red*) and z_2 (*dark blue*). While all the inversions results are represented in the upper subfigure, the middle and lower subfigures show that there is two types of models obtained, both with a source at approximately 5 km depth and volume $\Delta V \approx \Delta V_1 + \Delta V_2$. The second source is either very shallow and weak (Combination 2), or very deep with variable strength (Combination 1). In both cases the second source as a negligible effect on the surface deformation.